R-12-09

Detailed description of TRUE Block Scale Structure #20 based on intercepts in boreholes and intercepts in the TASS tunnel

Anders Winberg, Conterra

Aaron Fox, Anders Pettersson
Golder Associates

Henrik Drake, Isochron Geoconsulting

September 2013

Svensk Kärnbränslehantering AB
Swedish Nuclear Fuel
and Waste Management Co

Box 250, SE-101 24 Stockholm
Phone +46 8 459 84 00

SKB

ISSN 1402-3091
SKB R-12-09
ID 1389690

Detailed description of TRUE Block Scale Structure #20 based on intercepts in boreholes and intercepts in the TASS tunnel

Anders Winberg, Conterra

Aaron Fox, Anders Pettersson
Golder Associates

Henrik Drake, Isochron Geoconsulting

September 2013

Summary

The primary goal of this study, targeted on the TRUE Block Scale Structure #20, was to produce an integrated description of a deformation zone at the centimetre to decimetre length scale, by combining observations from cored boreholes, image logging, tunnel mapping, fracture mineralogical sampling, hydraulic testing and hydraulic pressure responses. The resulting composite description includes comments on the lithologies associated with the deformation zone, a description of the visible fracturing, descriptions of relationships in the ductile fabric at macro and micro scales, the hydraulic connectivity and hydraulic properties of the deformation zone, and detailed mineralogical descriptions of brittle and ductile fabrics.

The lithology of Structure #20 is dominated by a mix of Äspö diorite and fine-grained granite. The structure consists of a mix of fault rock; mylonite, cataclasite, fault gouge, occasional breccia and of various open, partly open, and sealed fractures. The structure is also found to show at least weak association with fine-grained granite intrusions which suggests attention needs to be paid to igneous intrusions, as they may follow pre-existing ductile shear zones or may be coincident with ongoing ductile shearing.

Three categories of fracturing associated with Structure #20 are assumed to be applicable to deformation zones in general within the Äspö/Laxemar/Simpevarp region; brittle deformation in the core of the deformation zone; increased fracture intensity in the damage zones surrounding the deformation zone core; and epidote-filled fractures that form so-called “marker beds” for the structure. Structure #20 constitutes an oblique-slip fault with predominantly sinistral displacements developed from a ductile shear zone pre-cursor. Mineralogical kinematic indicators suggest both dextral and pure dip-slip. These kinematic indicators are mostly of ductile character so this statement is incomprehensive. However, brittle indicators exist as well and numerous generations of fracture fillings indicate multiple brittle reactivation. Structure #20 exhibits a fairly typical deformation zone configuration including a relatively narrow core composed of both ductile and brittle structures, surrounded by a damage zone largely characterized by increased fracture intensity. Results indicate that, at least over the scale of the investigation area, Structure #20 is largely planar, with only local-scale undulation.

Mineralogical analysis of intercepts of Structure #20 in boreholes and the TASS tunnel show similar general features regarding the fracture re-activation history and deformation events. This is evidenced by small deviations in fracture mineral assemblages and whole-rock and mineral chemistry. The overall characteristics were similar between borehole intercepts but showed some heterogeneity. Wall rock alteration showed very similar features (alteration of Fe-Mg-minerals, fragmentation of feldspars, re-crystallisation of quartz). The extent of the alteration varied from decimetre to metre scale, depending on the intercepts.The thickness and amount of mylonite and cataclasite varied between different intercepts. The general mineral assemblages were; mylonite (ductile deformation) and cataclasite and extensional fractures (brittle deformation).

Apart from geometrical extrapolation the intercept of Structure #20 with the TASS tunnel was also interpreted from pressure responses observed in the TRUE Block Scale borehole array during drilling of the TASS tunnel pilot boreholes. The resulting intercept corresponds well with the geometrically extrapolated intercept, suggesting that Structure #20 can be regarded as an essentially planar structure across its known extent. Transmissivity data evaluated from hydraulic tests performed in the TRUE Block Scale borehole array, the TASS tunnel pilot boreholes and short TASS grouting holes transecting Feature A were analysed. Analysis of statistics based on various means of pooling the data showed that the geometric mean and variance of the transmissivity of Structure #20 based on the TASS pilot and probe boreholes were close to those established based on on all available data on the structure, suggesting that the statistical sample for Structure #20 from the TASS pilot boreholes (representing a length scale of metres) may be regarded as representative of the “global statistical properties” of the structure (over length scale of several decametres). It was however noted that at best, this relationship is indicative for this type of NW conductive structures at Äspö (and possibly in the neighbouring Laxemar-Simpevarp area).

A simple flowchart was deviseded to distinguish and describe similar structures as a preliminary method of screening borehole data to determine if a particular fracture intercept is worthy of additional investigation as a potential “large fracture”, the latter affecting the positioning of deposition holes/waste canisters through the (Full tunnel Perimeter Intersection) FPI-related design criteria.

The results of the detailed geological and structural mapping were presented in conceptual synthesis images that add additional detail and structural-geological context. The synthesis is compatible with, and lend additional support to, the original micro-structural conceptualization reported by the TRUE Block Scale and TRUE Block Scale Continuation projects.

Characterization efforts on individual major structures (MDZs/fractures) of the kind and type described in this work may turn out to be prohibitive in terms of time and costs. However, repeated targeted campaigns on representative type structures (and fractures) (e.g. representing typical orientations) may provide an important basis for constructing generalised conceptual models and may also help define a data base based on which “large fractures”, related to the FIP-related design criteria, may be identified. It was also noted that techniques employed in this work, HDR photography, UV photography and mineralogical kinematic indicators, may prove as valuable contribution to planned detailed site investigations.

Contents

1 Introduction

1.1 Background

The current study involves a detailed follow-up of a hydraulically conductive structure comprehensively investigated in the TRUE Block Scale rock volume using information from pilot boreholes for the TASS tunnel and from the TASS tunnel itself.

The TRUE Block Scale experiment (Andersson et al. 2002a, 2007, Winberg et al. 2003) had as its principal aim to investigate the retention of radionuclides in fractured rock at depth in the Äspö HRL. The experiment involved an extensive site characterisation of the 3D geometries and properties of conductive structures; this effort resulted in a deterministic hydrostructural model of the TRUE Block Scale experimental volume, and of its connections to other structures of regional hydrogeologic significance at Äspö. The developed hydrostructural model formed the basis for packing off selected intervals in the boreholes, facilitating performance of comprehensive tracer experiments using radioactive tracers (Andersson et al. 2002b), producing a basis for assessing the retention of radioactive tracers in the studied flow paths (Poteri et al. 2002, Andersson et al. 2002a, b, 2004, 2007, Cvetkovic 2010a, b, Cvetkovic et al. 2010, Cvetkovic and Frampton 2010).

The Tunnel Sealing Project involved construction of an 80 m long tunnel (the TASS tunnel) at repository depth in the Äspö HRL to demonstrate the ability to seal a tunnel to prevent significant water inflows at repository depth. Tunnel construction was preceded by drilling of three pilot boreholes along the tunnel perimeter (Hardenby et al. 2008, Hardenby and Sigurdsson 2010). The tunnel development featured pre-grouting using low alkaline cement-based grouts and silica sol resin (Funehag and Emmelin 2011).

The performed site descriptive modelling at Forsmark (SKB 2008) and Laxemar (SKB 2009) involved DFN-based hydraulic modelling where the stochastically-assigned transmissivity of modelled fractures was assumed to be constant across their lateral extents. This analysis, along with the results of a subsequent safety analysis (SKB 2011) identified a need for an improved description of the heterogeneity of material and hydraulic properties (mainly transmissivity) of modelled fractures.

Work on the TASS tunnel at Äspö also provided the possibility to further investigate structures identified in the TRUE Block Scale rock volume across a larger portion of their extents, as well as the opportunity to assess the structures for heterogeneity at multiple scales, making use of the information from boreholes and the tunnel. The techniques and conclusions of this study are directly applicable to the detailed site investigation to be performed during the construction of the repository for spent fuel repository at Forsmark.

1.2 Objectives and scope

The objective of this project is to describe in detail the geological and hydrogeologic heterogeneity of Structure #20, as seen in its intercept inside the TASS tunnel and in the various boreholes which intersect the structure. This is achieved through geometrical, geological and hydrogeological analysis of available data. A key objective of this study is the integrated description of Structure #20 in terms of a synthesis between geology, geochemistry, and hydrogeology. A second major objective of this study is to perform an integrated description at a very high (decimetre to centimetre scale) resolution, such that the resulting updated conceptual model of Structure #20 is made useful for generic and site-specific transport modelling.

The hydrogeological analysis includes the assessment of pressure responses recorded in the instrumented borehole array during drilling of the TASS pilot boreholes and an assessment of the variability in hydraulic material properties obtained from hydraulic tests in boreholes.

1.3 TRUE Block Scale hydrostructural model

The geological features used for both injection and extraction of tracers during the TRUE Block Scale project tracer experiments are steeply-dipping northwest-striking discontinuities: Structure #20 (near the centre of the TRUE Block volume) and Structure #19 (near the outer edge of the volume). The conductive hydraulic network within the TRUE Block volume is mainly composed of Structures #20, #21, #22, #13 and #19 (Andersson et al. 2002a), cf. Figure 1-1. The model was developed and updated in the SKB RVS system; the evolution of the hydrostructural model is described through a series of Äspö progress reports (Hermanson 2001a, b, Hermanson and Doe 2000). Conceptual micro-structural models of typical structures involved in the tracer experiments are described in Andersson et al. (2002a) and Dershowitz et al. (2003).

Deformation zones in crystalline Precambrian bedrock tend to have very complicated and variable geometries, representing repeated periods of ductile deformation and polyphase re-activation in both the brittle-ductile and brittle fracture regimes. The complex tectonic and metamorphic history of these rocks has produced structures with variable thicknesses and character along their length (cf. Figure 1-2), such that multiple drill core intersections are necessary to enable estimation of the uncertainty in the thickness and character of the deformation zone. Therefore, the use of existing data from the TRUE Block Scale project in conjunction with new data available from TASS tunnel pilot boreholes and the walls of the TASS tunnel are crucial for producing an accurate updated conceptual model of Structure #20.

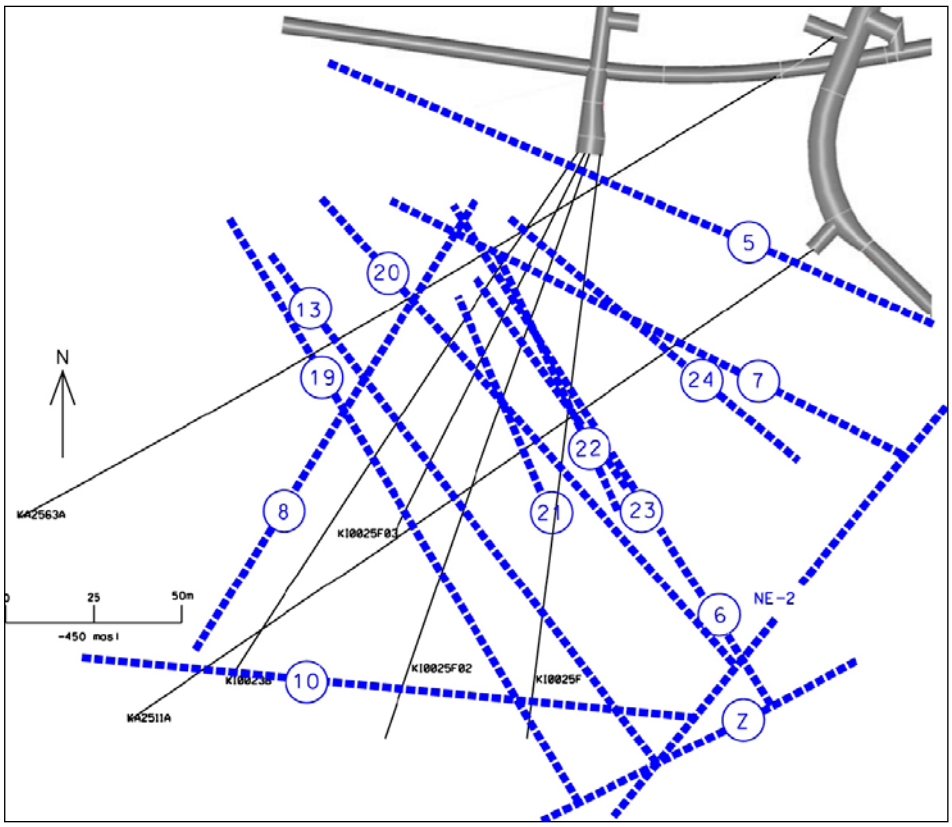

Figure 1-1. *Plan view of the final 3D hydrostructural model of the TRUE Block Scale rock volume during the tracer test stage of the experiment. Figure is from Andersson et al. (2002a).*

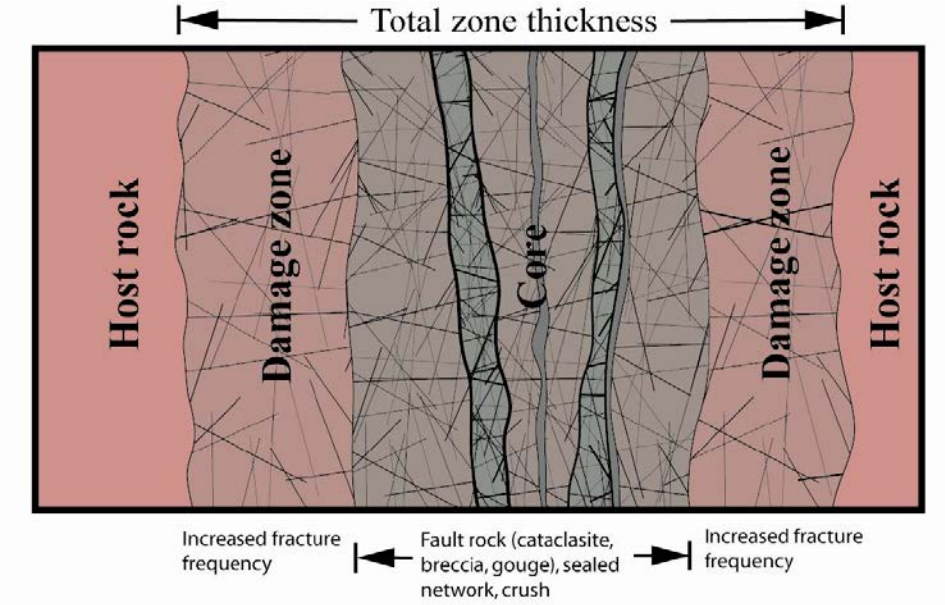

Figure 1-2. *Idealised cross-section through a deformation zone (DZ) typical to the Forsmark and Laxemar sites (after Munier et al. 2003). The figure shows the core of the deformation zone, which is typically characterized by intense fracturing, brecciation, and sometimes the presence of fault rock (mylonite, cataclasite, and clay-rich gouge). The deformation zone core is surrounded on both sides by damage zones (formerly known as "transition zones" in older SKB reports); these volumes are characterized by mechanically- and/or hydrothermally-induced alteration along with increased intensity of fracturing relative to the host rock (Kim et al. 2004).*

1.4 Extrapolation of TRUE Block scale structures

The TRUE Block Scale 3D RVS model of the conductive structures was combined with the corresponding RVS model of the approximately 80.7 m long TASS tunnel and pilot boreholes so that projected intercepts of TRUE Block Scale structures could be calculated (Table 1-1). These projected intercepts serve as the basis for targeted investigations (review of BIPS imagery, targeting of relevant drill core boxes and areas of the TASS tunnel to focus mapping efforts) of the actual geometry of the studied discontinuities.

Table 1-1. Intercepts in the TASS tunnel based on projection of structures included in the TRUE Block Scale deterministic hydrostructural model and based on interpretation of TASS information (Hardenby and Sigurdsson 2010).

TRUE Block Scale structure ID	Projected intercept with TASS tunnel (TASS tunnel length coordinate, m)	Interpreted intercept with the TASS tunnel (R-10-35) (m)	Comment
#5	20.5	c. 20	
#6	49.0		
#7	53.6	c. 55	
#13	99.8	NA	Beyond the end of the tunnel
#19	106.7	NA	Beyond the end of the tunnel
#20	75.3	c. 76	
#22	43.2	c. 43	

1.5 Characterisation of TRUE Block Scale structures in conjunction TASS tunnel development

The emphasis of the characterisation in the TASS pilot boreholes has been to provide a basis for a suitable pre-grouting strategy. However, consideration has also been taken to correlate mapped deformation zones and associated hydraulic anomalies with TRUE Block scale structures, see Hardenby et al. (2008, Chapter 4–6). Accordingly, care was also taken to document the intercepts of TRUE Block Scale structures during the TASS tunnel mapping (Hardenby and Sigurdsson 2010).

1.6 Selection of structures for further analysis

The TRUE Block Scale structures initially selected for a detailed follow-up using existing drill cores, borehole logs and tunnel mapping information are Structures #20 and #22. The argumentation for this selection is as follows:

Structure #20: This structure, although showing a degree of variability along its interpreted extent in the TRUE Block Scale characterisation boreholes (Andersson et al. 2002a), has a "relatively simple" geometry that is strongly associated with a precursor ductile structure (mylonite). From a safety assessment perspective, this structure belongs to the group of fractures and structures which are not allowed to intersect a canister deposition hole. Additional quantification of the heterogeneity of the structure, with a focus on deformation zone core thickness, damage zone thickness, and unique mineral assemblages, is directly useful to detailed characterization efforts at other sites.

Structure #22: This structure, which does not show up in all TRUE Block Scale characterisation boreholes, has an interpreted extent that is much smaller than Structure #20, and does not exhibit the same clear association with a mylonitic precursor. Its geometrical arrangement is also more complicated than Structure #20. Previous work (Andersson et al. 2002a) has associated this structure with one or more visible open fractures with a 10 cm to 20 cm band of cataclasite around the deformation zone core. Initial impressions of Structure #22 in the TASS tunnel, however, are less clear; there are several candidate fractures within an approximately 5 m 'band' along the tunnel that possess similar characteristics.

The selection of these two discontinuities provides the opportunity for more detailed study of one of the principal structures of the TRUE Block scale tracer experiments (Structure #20) and of a nearly parallel structure of lesser extent (Structure #22) that provides connectivity to the studied fracture network of the studied rock volume. Improved understanding of the heterogeneity in the structural appearance and properties of these two structures is considered relevant from a site-specific Äspö/TRUE/TASS perspective, from a more general site descriptive modelling standpoint, and from a methodological standpoint in support of planned detailed site investigations at Forsmark.

Due to the limited amount of time available during the field investigation combined with the more obscure nature of Structure #22, a decision was, however, made to focus the modelling and characterisation efforts on Structure #20. Structure #20 is a clearly-defined, well-delimited structure within the minor local deformation zone (MDZ) size ranges presented in the discrete-fracture network models at Forsmark and Laxemar (Fox et al. 2007, Follin et al. 2007, Rhén et al. 2008, La Pointe et al. 2008). An increased understanding of the variability of the geometry and hydraulic properties of structures in this size range is a significant contribution to the modelling of similar structures elsewhere in SKB's repository programme.

2 Methods

2.1 Analysis of hydrogeological information

The hydrogeological database associated with the TRUE Block Scale and TASS work is extensive. Hydraulic pressure response data from the drilling of pilot boreholes for the TASS tunnel provides basis for geometrical inference and substantiation/verification of deformation zone geometry defined on purely geological/geometrical grounds. Furthermore, a large database of hydraulic test results provides basis for assessment of material property and its variability. Work performed does not involve any additional field work, nor has transmissivity of hydraulic tests been reinterpreted.

Performed work includes 1) review of pressure responses registered in the TRUE Block Scale borehole array during drilling of the TASS pilot boreholes, 2) compilation, structuring/pooling of data followed by calculation of univariate statistics of transmissivity data.

In the first case pressure events in the existing TRUE Block Scale array of boreholes instrumented with multiple packer piezometers have been correlated with the advance of the drilling of the TASS pilot boreholes. Ideally, assuming a planar structure geometry, a notable pressure event (drawdown) of hydraulic pressure in borehole sections containing a given interpreted structure/zone can be geometrically correlated with a corresponding intercept with the given zone in the borehole being drilled. It should be noted that geometrical inference can be significantly distorted by network effects, conveying the pressure response in a much more intricate 3D path. Notable is that the experience from the TRUE Block Scale rock volume (Andersson et al. 2002a, Andersson et al. 2007) is that such 3D effects were insignificant and pressure responses could be used effectively in building the deterministic model of conductive structures in the rock volume.

The analysis of transmissivity data from the various boreholes intersecting Structure #20 is followed by an assessment of the representativity of (local) TASS pilot borehole information compared with statistics based on multiple borehole intercepts collected in the larger volume including data from the TRUE Block Scale borehole array. In total, 21 test data have been analysed in various combinations. The location of the tests in the respective boreholes, the type of test performed and type of evaluation employed is indicated in Table 3-2.

2.2 Structural-geological mapping of drill cores

All drill cores collected at the Äspö Hard Rock Laboratory for both the TRUE Block Scale experiment and the pilot boreholes of the TASS tunnel, have undergone extensive scientific analysis, including detailed description of primary lithology, dike and vein lithology, rock fabric, fracture and vein mineralogy, and properties of individual fractures and sealed fracture networks. Geological logging of an individual borehole is done using a combination of physical examination of drill core and BIPS downhole image logging; the resulting interpretation process is known as Boremap. The resulting geological analysis of the borehole (both image log and drill core) is then entered into SKB's database (Sicada).

Of the data recorded in Sicada for boreholes at Äspö, the following tables/reports are most relevant for the study of the lithology and structural geology of deformation zone features:

- *object_location*: Describes the location of boreholes in 3D space, and provides geometrical information necessary to reconstruct borehole paths for modelling or to reference geological features along the hole to a spatial record frame.
- *p_fract_core*: Detailed description of fractures visible in image logs or drill core, including fracture orientation, morphology, aperture, presence of flowing water, mineralogy, and spatial reference information.
- *p_fract_crush*: Describes sections of a drillhole where the rock mass, either in core or along the hole walls, has been brecciated or crushed to an extent that more formal mapping of fractures cannot be made.

- *p_fract_sealed_nw*: Sealed fracture networks are zones where the intensity (count) of closed mineralized fractures is so large it is impossible to map every single fracture. Sealed networks often map past fluid flow paths, and may represent locations where brittle deformation was concentrated.
- *p_rock*: Primary lithology encountered along the borehole/drill core.
- *p_rock_occur*: Description of the location, type, orientation, and structure of subordinate rock types encountered along the borehole or drill core. Subordinate rock types include veins, igneous dikes, mafic enclaves and inclusions of country rock.
- *p_rock_alter*: Description of the location, type, and intensity of weathering or hydrothermal alteration encountered along the borehole or drill core.
- *p_core_loss*: Description of the location and amount of core missing from drilling runs. Often core loss can be a sign of less-cohesive formations or intense fracturing, such that the core is not intact enough to stay within the core barrel.

Boremap data from nine cored boreholes at Äspö (six from within the TRUE Block Scale volume, and the three TASS tunnel pilot boreholes) were available for use in this study. The boreholes utilized in this study are KA2511A, KA2563A, KI0025F, KI0023B, KI0025F02, KI0025F03, KI0010B01, KI0014B01 and KI0016B01.

Primary data available from Sicada are used in several standard fracture parameter analyses commonly used in the development of discrete-fracture network (DFN) models, as a first method of understanding the properties of fractures associated with Structure #20. These analyses include:

- Cumulative Fracture Intensity (CFI) analysis: The intensity of fracturing along a drill core or wellbore is recorded as a cumulative number, usually as a function of elevation or borehole length. Changes in slope of the CFI curve represent changes in fracture intensity in the host rock, while gaps in the CFI curve can indicate mechanical layer boundaries (a function of lithology and rock-mechanical properties). CFI plots are more effective than traditional moving-average fracture-frequency plots for identifying fracture domain and deformation zone boundaries.
- Polar stereonet plots: The trend and plunge of the poles to fracture surfaces are plotted on lower-hemisphere equal-area stereo nets. These figures are used to look for changes in fracture orientations inside and outside of Structure #20 that might indicate secondary fracture orientations that might suggest or confirm direction of shear across the deformation zone, or to determine the boundaries of the zone itself.

In addition to numerical data from Sicada, a review of existing BIPS images from all nine boreholes was performed. The goal of the review of BIPS imagery was not to re-map features previously logged, but to re-evaluate the boundaries of Structure #20 employing new methodology and understandings about (minor) deformation zones obtained from the Forsmark and Laxemar site investigations. All BIPS images were reviewed on a desktop PC using the BIPS Viewer software package.

The structural geologic mapping of TRUE Block Scale and TASS pilot bore cores takes into account lessons learned from the Site Descriptive Model efforts at both Forsmark and Laxemar. In particular, the Single Hole Interpretation project, which is designed to integrate data from multiple investigations and logs into a coherent geological picture of an entire borehole, produced several key insights into the delineation of deformation zones within crystalline rocks typical to Forsmark and Laxemar. In addition, results from the Minor Deformation Zone re-identification project at Forsmark (Fox and Hermanson 2006) and Boremap mapping of MDZ-boreholes during SDM Laxemar (Mattsson et al. 2007) also influenced the thinking about the characterization of deformation zones and their geometry. The structural characterization of deformation zones in the Laxemar area from the Oskarshamn site investigation performed by the Geological Survey of Norway (Viola and Venvik Ganerød 2008) is an excellent introduction to the type of structural analysis necessary for deformation zone reconstruction.

The wealth of knowledge and experience regarding the geometry and characteristics of deformation zones collected by SKB during the site investigations at Forsmark and Laxemar is used as a methodological starting point for the current study. In general, many of the minor deformation zones at Laxemar (and to an extent Forsmark, although Fox and Hermanson (2006) suggested that Forsmark MDZs might have slightly different morphological characteristics) can be identified by:

1. Presence of increased intensity of bedrock alteration, in particular the so-called “red staining”;
2. Increase in open and sealed fracture intensity. These structures have been active numerous times in both the brittle-ductile and brittle regimes, and the effects of past phases of deformation (i.e. large numbers of clustered sealed fracture s) are strong indicators of potential deformation zones. In particular, zones of sealed epidote-filled fractures are often found at the boundaries of deformation zones and minor deformation zones;
3. Presence of fault rocks, e.g. cataclasite, breccia, or clay-rich fault gouge, which often marks the core or presence of multiple cores of the deformation zone;
4. Increase in the intensity of foliation in the bedrock. This reflects a possible ductile precursor of most minor deformation zones; and
5. Presence of kinematic indicators such as shear movement along fracture surfaces (as shown by mineral lineations and growth fibres, slicken lines and conjugate fracture sets).

2.3 Photographical documentation in the TASS tunnel and associated analysis

A key component of the geological mapping of the structures in the TASS tunnel was to evaluate several techniques for the photographic documentation of excavated features seen on tunnel walls. SKB has invested a significant amount of effort into developing a methodology, the Rock Characterisation System (RoCS), for documenting lithology, discontinuities, geologic structure, hydrogeologic, and rock mechanical characteristics of excavations, tunnels, shafts, and deposition holes (Magnor et al. 2006). RoCS is designed to replace SKB’s existing methodologies for mapping tunnels at the Äspö HRL.

The RoCS system consists of the integration of high-resolution digital laser scanning and digital photography of the walls and faces of the advancing tunnels and shafts and physical mapping of exposed surfaces. Following entry in Sicada the information is readily available for modelling in SKB´s geologic CAD systems (RVS). The advantage of laser scanning is that a three-dimensional surface (similar to a digital elevation model) is created by the scanning process. High-resolution photographic imagery can be georeferenced and draped over the resulting mesh model, resulting in a high-quality working model on which additional geoscientific analyses can be performed. Photographic mesh-draped images have been used to develop fracture models (Gaich et al. 2006), assist in the design and engineering of rock fall-prevention structures and assessment of slope stability (Turner et al. 2006), and to allow for safer mapping of tunnels and rock slopes (Kemeny et al. 2006).

Photographic documentation conducted during the photographical mapping of Structures #20 and #22 in the TASS tunnel consisted of the following efforts:

- High-resolution (cm to mm/pixel scale) visible light photography and production of image mosaics. The goal was to evaluate techniques for the rapid and detailed documentation of small-scale features so as to produce better-quality tunnel maps and reduce the amount of time needed to be spent mapping in the tunnel (thereby avoiding slowing down the construction work).
- High Dynamic Range (HDR) photography, to determine if additional information dimensions could be opened up by the use of this technique. In particular, HDR was tested to assess its ability to increase edge-detection (for mapping fractures) and for removing shadows and dark spots present in the images even after extensive illumination (lighting).
- Ultraviolet (UV) light photography, to determine if this technique may provide any additional value to the mapping process. Many minerals and substances fluoresce (emit visible light) when stimulated by ultraviolet radiation; the hope was that images created using UV illumination would make it easier to visualize mineralized (sealed) fractures from those fractures merely ‘closed’ tight. In addition, since groundwater generally possesses some amount of calcium carbonate (same as the mineral calcite, which fluoresces under both longwave and shortwave UV), photography using UV light is likely to produce a better estimate of which fractures are flowing in the tunnel.

2.3.1 Camera equipment and setup

All images were collected by Golder Associates staff, with coordinate survey assistance and construction light illumination provided by Äspö Hard Rock Laboratory staff.

- **Camera**: Nikon D200 with a remote shutter release.
- **Lens**: Nikkor 50mm f/1.8D, Nikkor 35mm f/2D, Tokina AT-X 124 AF PRO DX.
- **Flash**: All Nikon, 1x SB900, 1x SB800, and 1x SB600.
- **Tripod**: Aluminium total station tripod.
- **Tripod head**: Manfrotto 400 Geared Head combined with a Manfrotto 303Plus Precision Panoramic Head.
- **External Lighting**: 8×high-intensity LED construction lights for lighting up the photographed area.
- **Handheld UV-light** (combined shortwave and long wave emissions). It was initially planned to use larger-scale UV emitters rented specifically for this project. However, cost and technical limitations precluded their use.

Software used during image post-processing includes Photoshop LightRoom 3 from Adobe Systems, which was used for organizing the raw images and converting between image formats (NEF to JPG/TIFF), and the Graphical User Interface for Panorama Tools (PTGui) from New House Internet Services.

All digital images were saved as RAW files, which is a collective name for several different vendor-specific formats common to high-end digital camera. The common property of these formats is that they all contain image sensor data, camera equipment metadata (colour profiles, size and resolution of the image sensor), and image metadata (exposure settings, camera model, date and location). RAW files are the digital equivalent of a film negative; they contain image information before the camera applies white balance, sharpening and other corrections that are parts of the process to create a finished image.

The use of RAW images allows photographers to avoid the use of a digital camera's built-in processing routines for image processing, gives a significantly finer degree of control over the final images, and avoids the limited colour depth and artefacts present in JPEG-formatted images so common to consumer-level digital cameras. Nikon's version of the RAW standard is called NEF (Nikon Electronic Format). The main benefit to NEF as a storage medium is that it contains more information than can be used in the finished image. This information can be used when converting NEF to more common image formats to recreate details from faint information in highlights and shadows. It is also easy to set the white balance in the conversion from NEF to other formats, a process that otherwise is hard to do on finished RGB images.

2.4 Mineralogical sampling an analyses

Samples were collected from drill cores or from the tunnel using rock hammer and/or rock saw. Samples used for thin sections were cut to small rock chips and then prepared by Minoprep AB, Sweden. Thin sections were analysed using a petrographic microscope (Leica) equipped with a microscope camera, as well as on a SEM-EDS, at the Earth Sciences Centre, University of Gothenburg, Sweden, accordingly: An Oxford Instruments energy dispersive system mounted on a Hitachi S-3400N scanning electron microscope was used. Polished thin-sections were coated with carbon for electron conductivity. The acceleration voltage was 20 kV, the working distance 9.9 mm and the specimen current was about 1nA. The instrument was calibrated at least twice every hour using a cobalt standard linked to simple oxide and mineral standards, to confirm that the drift was acceptable and the stability of the beam current was measured regularly using a Faraday cage mounted to the sample holder. X-ray spectrometric corrections were made by an on-line computer system. These quantitative analyses give reliable mineral compositions but Fe^{2+} and Fe^{3+} are not distinguished and the H_2O content is not calculated. Detection limits for major elements are better than 0.1 oxide %. Note that the SEM-EDS analyses used in this report show the Fe_{tot}-content as "FeO" (78% Fe) in contrast to the chemical analyses which gives the Fe content as Fe_2O_3 (70% Fe).

Samples used for fracture surface samples were first cut into smaller pieces with the fracture surface horizontal and then analysed using stereo microscope and the same SEM-EDS unit described above. Only exception was that low vacuum mode was used and no quantitative analyses were carried out (due to the relatively uneven surface).

Samples for whole rock chemical analysis were first cut into smaller pieces with a rock saw and then ground with a swing mill and then analysed for major, minor and trace elements by the ALS laboratory (Luleå, Sweden) accordingly:

The sample was dried at 105°C. 0.1 g sample was fused with 0.375 g $LiBO_2$ and dissolved in dilute HNO_3. LOI (Loss on ignition) was carried out at 1,000°C. Concentrations of the elements are determined by ICP-AES and ICP-QMS. Analyses are carried out according to EPA methods (modified) 200.7 (ICP-AES) and 200.8 (ICP-QMS).

Calcite used for stable isotope analysis was first examined with stereo microscope and then scraped off using a chisel and then analysed for stable isotopes by Institute for Energy Technology (IFE), Norway, accordingly:

About 100 µm of the sample was transferred to a 10 ml vacutainer, put in a temperature controlled ALU block and flushed with He for 5 min. 0.1 ml 100% H_3PO_4 was added and the reaction was controlled at 30.0°C for 2 hours. The produced CO_2 gas (calcite fraction) was then flushed out with He flow on to a Poraplot Q GC column and analysed directly on a Finnigan MAT Delta XP, Isotope Ratio Mass Spectrometer. Based on the repeated analysis of laboratory standards, the precision reported is as follows: $\delta^{13}C \pm 0.1‰$ (2sigma) and $\delta^{18}O \pm 0.2‰$ (2sigma). Results are reported in ‰ relative to PDB. IAEA-CO-1 reference material from IAEA was analysed as unknown together with the samples and gave $\delta^{13}C$: 2.41 ± 0.04‰ (2.49 recommended by IAEA) and $\delta^{18}O$ –2.6 ± 0.05‰ (–2.5 recommended by IAEA).

2.4.1 Samples for fracture mineralogical investigations

Samples and methods used are listed below in Table 2-1, and described in Sections 4.5.1 (cored boreholes) and 5.5.1 (tunnel). Additional thin sections from the TRUE Block Scale experiment (Andersson et al. 2002a) were investigated using microscope and SEM. Descriptions for these samples, which were originally sampled during the TRUE Block Scale project by Eva-Lena Tullborg, are included in Section 4.5.2.

Table 2-1. Samples and methods used.

Tunnel samples	x	y	Wall	Thin section (SEM and microscope)	Stable isotopes	SEM (fracture surface)	Whole rock chemistry
#1	0.800	75.210	A	1			
#2	1.130	75.340	A				
#3	2.360	75.890	B	1			
#4	2.290	76.080	B	1	1		
#5	2.220	75.990	B				
#6	1.120	76.180	B				
#7	0.900	76.120	B	1		1	
#8	3.850	76.150	B	1	1		1
#9	2.830	75.200	A	1		1	1
#10	0.900	76.140	B		1		
#11	1.250	76.200	B	1			1
Borehole samples	**Secup**	**Seclow**					
KI0010B01	75.354	75.426		1	1	2	1
KI0014B01	72.162	72.289		2	1	2	1
KI0016B01	70.328	70.838		3	2	2	1

Note: Samples #2, #5 and #6 were not analysed.

2.5 Structural-geological tunnel mapping

After a better understanding of the nature of the Structure #20 intercept had been obtained through the analysis of drill cores from the pilot boreholes and the TRUE Block Scale boreholes, a limited structural geological mapping effort was performed at the (interpreted) intersection of Structure #20 with the TASS tunnel. The mapping was complementary to the photographic imaging efforts described in Section 2.3; while that effort was focused on a 'whole tunnel' level of detail, the structural-geological tunnel mapping was focused on characterizing the full-perimeter intersection of Structure #20 in the tunnel.

Remaining "half pipes" of blast holes (Figure 2-1) from tunnel excavation were used as makeshift scanlines; this allowed for the characterization of locations of fractures, veins, and other features as a 'length', with the opportunity to convert to 3D coordinates at a later date through optical survey methods. A number of blast holes (23) across both walls and the roof of the TASS tunnel were used to quantify the thickness of the core and damage zone of Structure #20. All distances measured along the tunnel walls during the survey are relative to tunnel chainage 00+76 m. The mapping was conducted manually, and, due to the difficulty of measuring distances on steep and sloping walls, the accuracy of the length measurements is estimated at ± 20 cm in terms of survey position along the tunnel centreline, and ± 5 cm in terms of element thickness, structure length or total deformation zone structure width (as interpreted along the sampling line, e.g. a borehole).

The data recorded during the mapping included:

- Orientation of fractures inside Structure #20 (where possible);
- Limits (in terms of lengths along the scanline) of the core and damage zone of the deformation zone;
- Fracture mineralogy (including rock and fracture mineral samples taken for geochemistry and SEM analysis);
- Observation of shear indicators (slicken lines, slip-fibre mineral growth) where possible;
- Fracture openness (open or sealed) and a measurement of the mechanical aperture where possible.
- Linear fracture intensity (P_{10}); and
- Geologic description of the Structure #20 intercept, using the same methodology as employed in the BIPS and drill core re-examinations.

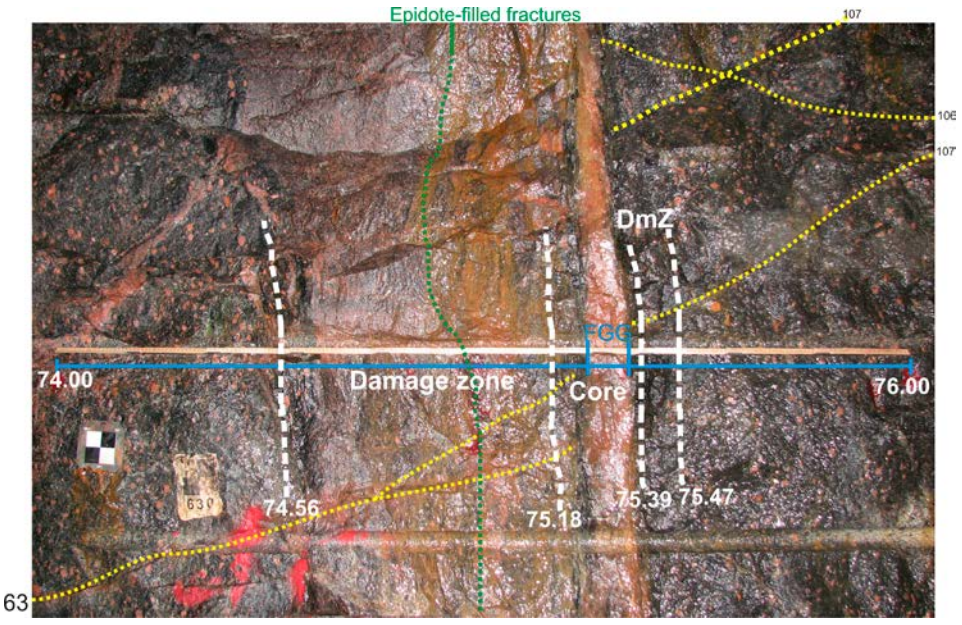

Figure 2-1. *Example of mapping along remaining "half pipes" of blast holes at the Structure #20 interface in the TASS tunnel. As the start and endpoints of each blast hole were easily surveyed in, and the paths of the blast holes were at a favourable angle to Structure #20, they effective serve as fracture scan lines. Tunnel coordinates (m) are shown at extreme left and right.*

In addition to mapping fracture traces along blast holes, the high-resolution photographic images taken of the TASS tunnel at the Structure #20 intercept were used as a base map for the digitization of fracture trace maps. The normal light, HDR, and UV fluorescence images were imported to ArcGIS as flat, non-georeferenced images. It is not currently possible to georeference the fracture trace maps in ArcGIS; its projection tools do not handle multiple-Z values, as it is fundamentally a 2D software package. In addition, there was a strong desire to present the traces as true 3D objects, rather than as a panelised 2D representation similar to that of CAD drawings of fracture trace maps. Consequently, georeferencing of the fracture traces can be performed by SKB staff at a later date with the same systems used in RoCS to generate 3D images of the tunnel walls from laser scanning.

All fractures clearly visible in the tunnel images were digitized. The fractures were mapped in ArcGIS in terms of whether their aperture was visible and whether the fracture was open or sealed. A comments field contains geological and structural notes about individual fractures (blast-induced fracturing, termination relationships with other features/fractures, visible mineralogy or water inflow). The resulting ESRI shape files will be provided to SKB, such that both the photographic images and the polyline shape files can be draped over the 3D TIN mesh of the tunnel surface produced from laser scanning, such that the fractures are brought into a proper coordinate reference frame.

It is important to note that the trace mapping does not directly correspond to, and is not to be regarded as a replacement for the RoCS-based geological maps of the TASS tunnel. Instead, it should be seen as an experiment to investigate how high resolution images could be used to augment existing mapping procedures without adversely affecting the rate of tunnel construction. The use of high-resolution images, combined with laser-swath mapping of the tunnel surface, has the potential to allow collection of important information with a minimum of disruption to construction activities.

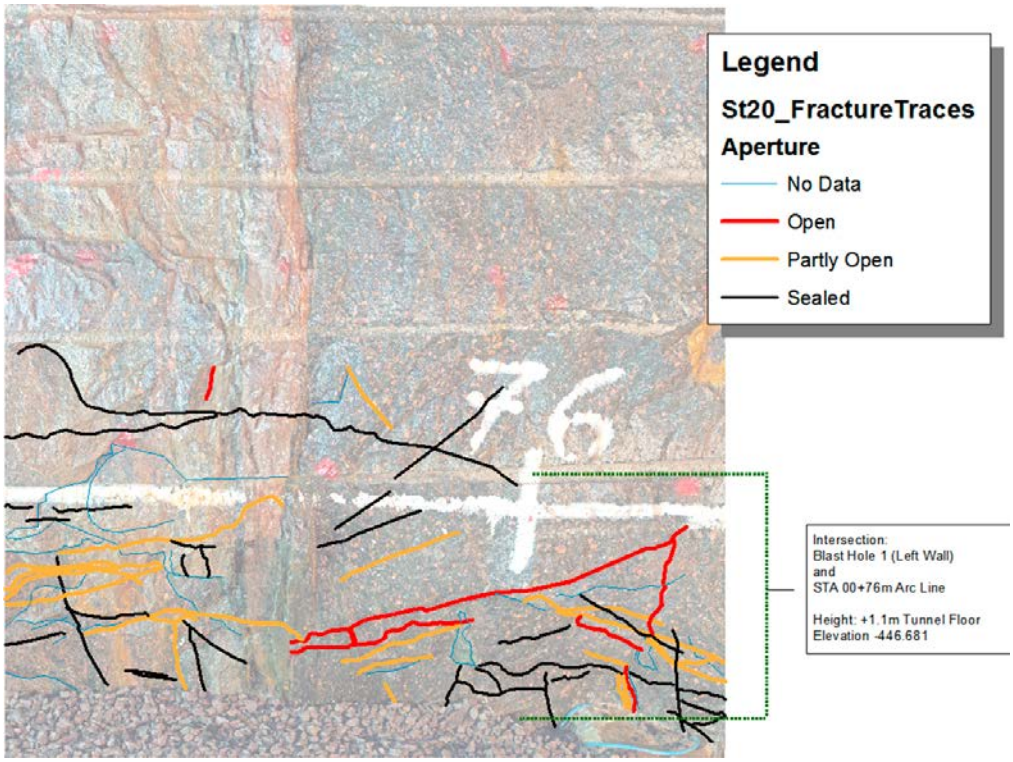

Figure 2-2. *Example of digitization of fracture traces along the "A" wall of the TASS tunnel on high-resolution photography. This figure was created at a very early stage of digitization. "No Data" indicates fractures for which it is impossible to determine their aperture from photography alone. The green bracket along the right side of the image illustrates the scale of the image: the intersection of tunnel chainage 76+00m and the first blast hole is 1.1 m above the elevation of the tunnel floor.*

3 Identification and characterisation of structures from hydrogeology

The TRUE Block Scale hydrostructural model was developed through an iterative approach where each new borehole was the basis for a new update of the block-scale hydrostructural model. Given that each borehole was strategically instrumented with multi-packer systems (up to 9 sections) with pressure transducers, pressure responses obtained during drilling of a new borehole were used to verify and develop further the model. Further refinement of the geometrical model was performed through the analysis of data from BIPS borehole imaging, Posiva flow logging and pressure build-up tests. Verification of connectivity (to flow) was obtained through a combination of interference and tracer dilution tests. The results of the latter tests were instrumental in identifying source points for tracer injection, and for tailoring the input tracer signal and pump rate at the extraction borehole (Andersson et al. 2002a).

As the boreholes drilled during the TRUE Block Scale project remain packed off and instrumented, a natural extension of the above procedure is to analyse the pressure responses in the instrumented borehole array to the drilling of the three pilot boreholes that preceded excavation of the TASS tunnel. Furthermore, to incorporate the quantification of hydraulic properties and characteristics, as obtained from the characterisation of the pilot boreholes, into a unified assessment of the hydraulic properties of the studied structure.

3.1 Objectives and scope

The objectives of the hydrogeological analysis were:

- Estimation of Structure #20 intercepts with the TASS pilot boreholes on the basis of recorded pressure responses in sections of the TRUE Block Scale Array interpreted to contain Structure #20. Comparison with projected Structure #20 intercept with the TASS tunnel made purely on geometrical grounds by extrapolation of Structure #20 geometry, as modelled in 3D using RVS.
- Grouping of transmissivity data attributed to Structure #20 followed by calculation of univariate statistics. Comparison of “global” and “local” variability in hydraulic properties as obtained statistics of different groupings of boreholes (TASS pilot vs. TRUE Block Scale + TASS pilot borehole data).

3.2 Overview of existing work

3.2.1 Tunnel sealing project

The geological characterisation of the TASS pilot boreholes included BIPS logging followed by Boremap core-logging. This mapping resulted in illustrations of lithology and illustrations of various fractures and fracture properties including the physical apertures of fractures as seen in BIPS. The lithology of the boreholes is dominated by Äspö diorite, with minor amounts of fine-grained diorite-gabbro and occasional dikes and veins of pegmatite and fine-grained granite (Hardenby et al. 2008). The average strike of mapped fractures in the boreholes is approximately 135°, and most fractures are steeply dipping. However, it is important to recognize that there is a strong sampling bias due to the orientations of the pilot holes; as horizontal boreholes, they systematically under-sample subhorizontal- to gently-dipping structures.

The hydraulic characterisation included registrations of groundwater pressure in the surrounding borehole array during drilling of the three TASS pilot boreholes, but also in the completed pilot boreholes themselves. Furthermore, the boreholes were logged with double-packer flow logging and Posiva flow logging (PFL; in pilot borehole KI0010B01 only). Results of the hydraulic tests (including inflow observed during drilling) were reported in terms of transmissivity (T) and equivalent hydraulic aperture (b_{eq}), cf. Figure 3-1. Anomalously high transmissivity/hydraulic aperture could for the most part be attributed to the intersection of TRUE Block Scale structures with the TASS tunnel.

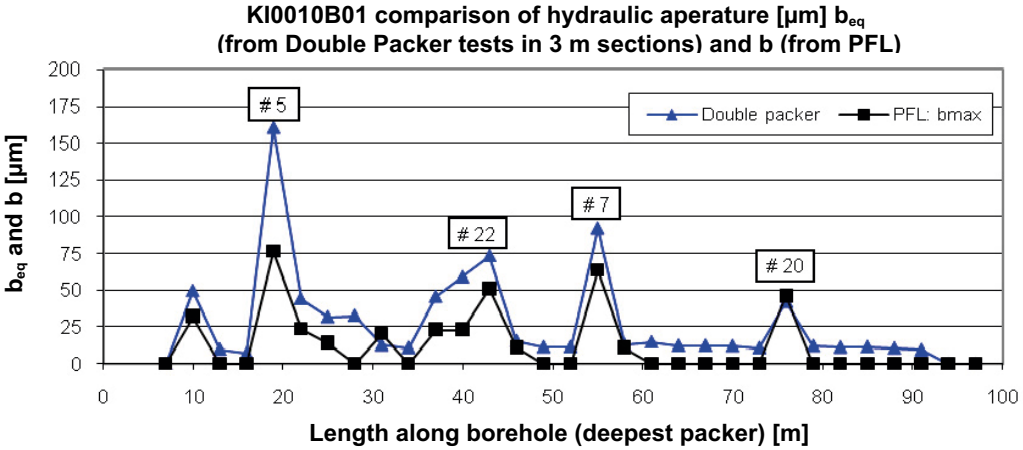

Figure 3-1. *Comparison for KI0010B01 between the largest aperture (b) from the PFL within each 3m section and the equivalent aperture b_{eq} obtained from double packer flow logging, from Hardenby et al. (2008).*

Overall the results of the double packer and PFL tests in the same borehole (KI0010B01) show comparable results with regards to suggested TRUE Block Scale structures, whose extrapolated intercepts are good matches to data recorded during pilot hole and tunnel mapping.

3.2.2 Planning for SWIW tests

As part of a search for a suitable site for conducting a single borehole injection withdrawal (SWIW) test with synthetic groundwater, the potential for using the TRUE Block Scale Structures #19 and #20 for such tests was assessed by using records of pressure response due to drilling of the TASS pilot boreholes and the excavation of the TASS tunnel. The results showed strong responses in Structure #20 due to drilling, and even stronger responses during the excavation of the tunnel. The pressure registrations also showed a clear hydraulic connection between the TASS tunnel and Structure #19, albeit with a smaller pressure response than the Structure #20 intercepts; the latter structure is positioned beyond the end of the tunnel end, which suggests a well-connected fracture network adjacent to the TASS tunnel.

3.3 Drilling progress versus time

In order to enable the correlation of drilling advance rates with the pressure responses, graphs have been produced which illustrate the drilling progress of pilot bores KI001B01, KI0014B01 and KI0016B01 as tabulated in Sicada (Figure 3-2). Overall, the records show steady progress without any visible problems or drilling rate decreases. The cyclic patterns observed in the graphs are due to day-night contrasts of the drilling shifts.

The relationships between the collars of the respective TASS pilot boreholes and the start of the centreline of the TASS tunnel are listed in Table 3-1.

Table 3-1. Drilling time of TASS pilot boreholes and relative difference in length between TASS pilot borehole and tunnel collar coordinates.

Pilot borehole	Drilling time	Borehole collar relative to tunnel collar length coordinate (m)
KI0010B01	2007-04-11–2007-04-21	+0.76
KI0014B01	2007-06-14–2007-06-18	+3.34
KI0016B01	2007-06-01–2007-06-08	+4.75

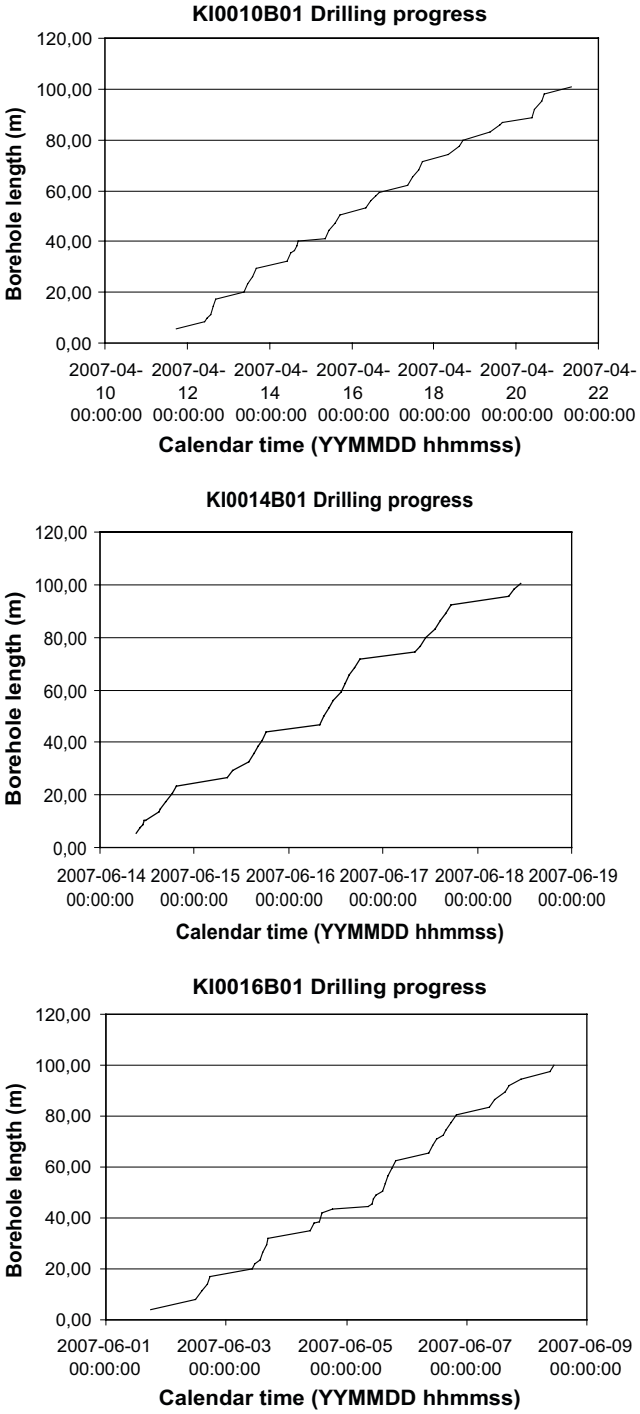

Figure 3-2. *Drilling advance vs. time for the TASS pilot boreholes KI0010B01, KI0014B01 and KI0016B01, respectively.*

3.4 Pressure responses observed during drilling

Pilot borehole KI0010B01 was drilled in April 2007 (Figure 3-1). This hole was kept shut-in after testing during the drilling of the remaining two boreholes. Borehole KI0016B01 was drilled in early June 2007 and was kept open after subsequent testing during the drilling of KI0014B01. The latter borehole was completed in mid-June 2007 and was kept open after logging and testing. Detailed accounts of the drilling procedures are presented in Hardenby et al. (2008, Section 4.1).

1. The procedure used to analyse the pressure response records was as follows:Using the intercept of Structure #20 with the TASS tunnel based on the TRUE Block Scale projection, cf. Table 1-1, a review of the pressure records was made. The time of the interpreted associated pressure drawdown event due to the respective intercept was recorded.
2. Using the tabulated drilling progress records, illustrated in Figure 3-2, the corresponding positions of the drill bit could be deduced. Subsequently, the borehole lengths were transformed to the corresponding tunnel lengths using the entries in Table 3-1. The interpreted intercepts, recorded times, associated borehole and tunnel lengths of intercepts are presented in Figure 3-3, Figure 3-4, and Figure 3-5.

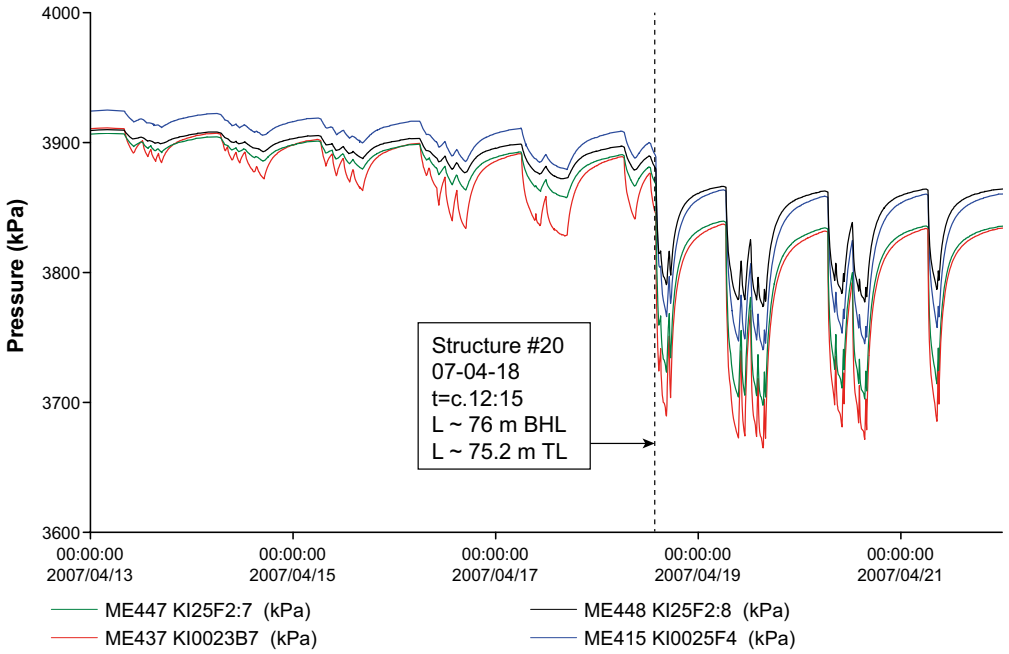

Figure 3-3. *Drawdown in selected TRUE Block Scale borehole sections due to drilling of borehole KI0010B01. Interpreted responses due to borehole intercepts with Structure #20 are indicated. Lengths are given as borehole length (BHL) and the corresponding TASS tunnel length (TL).*

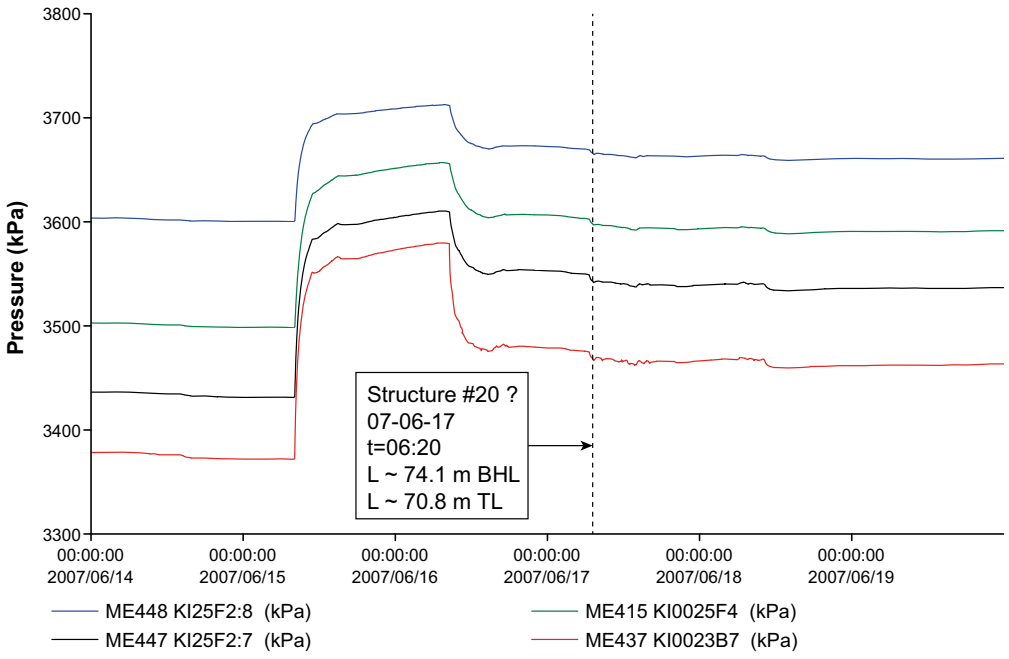

Figure 3-4. *Drawdown in selected TRUE Block Scale borehole sections due to drilling of borehole KI0014B01. Interpreted possible responses due to borehole intercept with Structure #20 are indicated. Lengths are given as borehole length (BHL) and the corresponding TASS tunnel length (TL).*

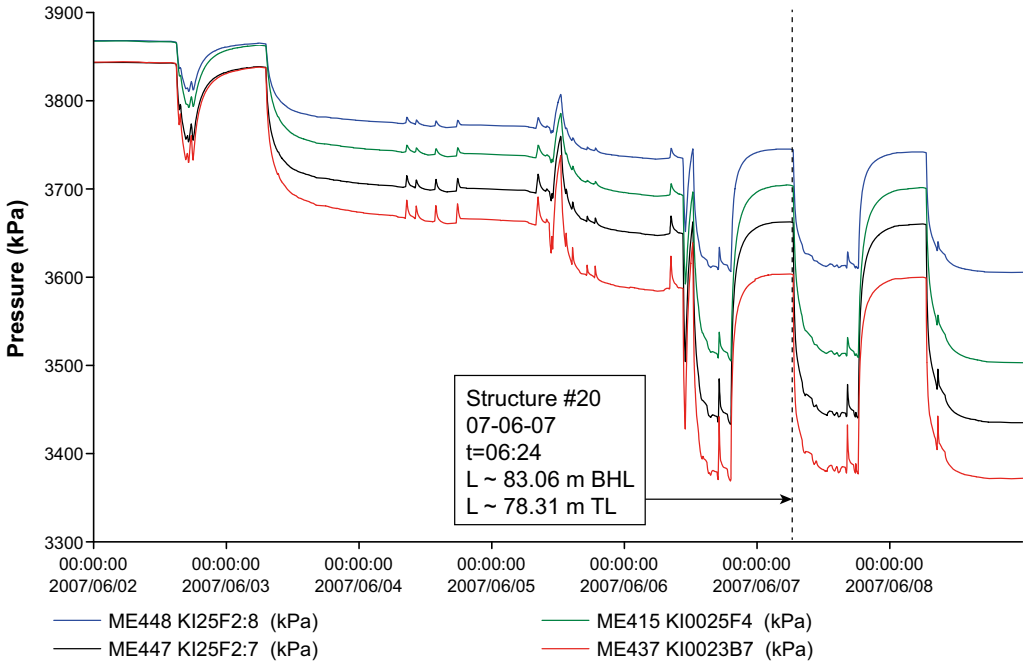

Figure 3-5. *Drawdown in selected TRUE Block Scale borehole sections due to drilling of borehole KI0016B01. Interpreted possible responses due to intercept with Structure #20 are indicated. Lengths are given as borehole length (BHL) and the corresponding TASS tunnel length (TL).*

It is clearly evident that the pressure record from KI0010B01 provides the most clear response pattern, and also shows an interpreted intercept with Structure #20 which is in agreement with the intercepts predicted by the TRUE Block Scale 3D RVS model, cf. Section 4.4.1 and Table 1-1, and also with the interpretation based on the hydraulic tests in the same borehole (Figure 3-1). The response pattern from the drilling of KI0016B01 is somewhat obscure, and that of KI0014B01 is even poorer. It is possible that following the drilling of the first pilot hole, the fact that one or two open holes provided close proximity short circuiting, disrupted the near-scale flow-field and connectivity to such an extent that pressure response transmission and identification was inhibited.

3.5 Hydraulic properties of selected structures

In the processing of the available hydraulic data, no new or complementary evaluations of performed hydraulic tests have been performed. In the statistical analysis, results from the TRUE Block Scale characterisation boreholes KA2511A, KA2563A, KI0025F, KI0025F02, and KI0025F03 were used (Andersson et al. 2002a). The data included results from PFL, pressure build-up tests and cross-hole interference tests. Results from the TASS construction and development stages included PFL logs and double-packer tests conducted in pilot boreholes KI0010B01, KI0014B01 and KI0016B01 (Hardenby et al. 2008) and test results from three probe holes SS0064F01, SS0064F02 and SS0064F04 employed during excavation of the TASS tunnel .

Hydraulic test results attributable to Structures #20 are available from the TRUE Block Scale project; readers are encouraged to view the compilation of results presented in Andersson et al. (2002a), and the Tunnel Sealing project (TASS) (Hardenby et al. 2008). In the former case results are available from a variety of different test methods (PBU = pressure build-up tests, PTSS = Posiva flow log tests, and PTT = Cross-hole interference tests, DPT = Double packer tests). All tests have been subject to either transient (PBU, PTT) or steady-state (PTSS, DPT) evaluation. The PBU and PTSS test results are useful in describing hydraulic conditions in the immediate neighbourhood of the test, while the PTT tests are useful in evaluating the hydraulic properties between observation and pumping boreholes. PTSS results are only available for the first TASS pilot borehole (KI0010B01, cf. Table 3-2). In order not to mix data of distinctly different nature, PTSS data from KI0010B01 has been treated as if it were part of the TRUE Block Scale borehole array.

Different groupings of data on transmissivity have been subjected to univariate statistical analysis. Evident in the analysis results of data related to Structure 20 (Table 3-2) is that the (geometric) mean transmissivity of TRUE Block Scale PTSS data is a factor of seven times smaller than the mean of the corresponding PBU data. It is also notable that there is good correspondence between the TRUE Block Scale PBU and the corresponding PTT statistic. Similarly, the mean of all TRUE Block Scale data is approximately 65% larger than the mean of all the TASS data. However, it is important to remember that the hydraulic data available from the TASS tunnel is quite limited (N=6).

The statistical analysis, although restricted by the smaller number of data from the TASS pilot boreholes, shows that the statistics for tests on Structure #20 based on the TASS pilot boreholes only differ within 45% in relation to the "global mean" established based on all available data on the structure.

These results suggests that the statistical samples for the two structures collected in the TASS pilot boreholes may be considered representative of the "global statistical properties" of the two studied structures (as interpreted from data from the TRUE Block Scale boreholes and the TASS pilot holes). This interim conclusion, based solely on hydraulic properties, is revisited and addressed further in the geological, structural geological and fracture mineralogical analyses presented in subsequent chapters.

Table 3-2. Compilation of hydraulic test results related to Structures #20 as obtained from the TRUE Block Scale project (Andersson et al. 2002a) and from the Tunnel sealing project (focused on the TASS tunnel) (Hardenby et al. 2008). PBU = pressure build-up tests, PTSS = Posiva flow log tests (Rouhiainen 2008), PTT = Cross-hole interference test, and DPT = Double packer test. Steady state evaluation of tranmissivity according to Thiem (1906) or Moye (1967). Transient evaluation according to Cooper and Jacob (1946).

Borehole: Test type	Transmissivity T (m^2/s) Structure #20	Comment
KI0025F:PBU	5.1E–07	L = 87.0–88.0 m Transient, Cooper-Jacob
KI0025:PTT	8.5E–07	Transient, Cooper-Jacob
KI0025F:PTSS	4.4E–08	Steady-state, Moye
KI0025F02:PBU	6.5E–07	L = 73.0–77.0 m Transient, Cooper-Jacob
KI0025F02:PTT	1.1E–06	Transient, Cooper-Jacob
KI0025F02:PTSS	> 1.2E–07	L = 73.0–77.0 m, Posiva flow log Steady-state, Moye
KI0025F03:PBU	6.1E–07	L = 72.0–74.0 m Transient, Cooper-Jacob
KI0025F03:PTT	6.1E–07	Transient, Cooper-Jacob
KI0025F03:PTSS	7.5E–08	L = 72.0–74.0 m, Posiva flow log Steady-state, Moye
KI0023B:PBU	9.6E–07	L = 68.4–69.4 m, Constant pressure withdrawal, Transient, Cooper-Jacob
KI0023B:PTT	1.4E–07	Transient, Cooper-Jacob
KI0023B:PTSS	8.9E–08	Steady-state, Moye
KA2563A:PBU	–	Not performed
KA2563A:PTT	8.7E–07	Transient, Cooper-Jacob
KA2563A:PTSS	> 1.9E–07	Steady-state, Moye
KI0010B01:PTSS	6.37E–08	L~ 75.5 m, Posiva flow log Steady state, Thiem's equation
KI0010B01:DPT	4.7E–08	L = 73.0–76.0m. Summed up thickness of two core sections (~ 10 cm each) + related damage zones: ~ 50 cm (67.7 cm in alternative BIPS interpretation). Intercepts at c. 75.0–75.5 m. Steady-state, Moye
KI0014B01:DPT	2.5E–08	L = 70.5–73.5. Thickness of core section+related damage zones: ~ 40–50 cm. Core section = ~ 15cm. Intercepts at c. 72.0–72.4 m. Steady state, Moye
KI0016B01:DPT	7.1E–06	L = 66.5–69.5 m. Thickness of core section+related damage zones: ~ 70–80 cm. Core section = ~ 13cm. Intercepts at c. 70.3–71.1 m.
SS0064F01	1.60E–07	Grouting screen : 6 Stuffinj, Tunnel chainage : 64.5 m, borehole length: 20 m, Steady State, Moye
SS0064F02	1.08E–07	Grouting screen : 6 Stuffinj, Tunnel chainage : 64.5 m, borehole length: 20 m, Steady State, Moye
SS0064F04	1.80E–07	Grouting screen : 6 Stuffinj, Tunnel chainage: 64.5 m, borehole length : 20 m, Steady State, Moye

Table 3-3. Compilation of statistics related to tests carried out on Structures #20 as obtained using results compiled in Table 3-2. Geometric mean values and associated standard deviation.

Sample	Log T_g (m^2/s)	Transmissivity T_g	Standard deviation	Number of data	Comments
TBS PBU	–6.18	6.64E–07	0.12	4	
TBS PTSS	–7.03	9.23E–08	0.24	5	
TBS PTT	–6.23	5.87E–07	0.36	5	
TASS DPT	–6.70	2.00E–7	1.34	3	
TASS Probe Inj	–6.84	1.44E–7	0.12	3	
TBS All data	–6.55	2.82E–07	0.50	15	Including one value from PFL in KI0010B01.
TASS All data (DBT + Probe Inj)	–6.77	1.70E–7	0.86	6	
TBS + TASS All data	–6.61	2.45E–7	0.60	21	

4 Geological information from cored boreholes

The objectives of the analysis of the geological characteristics of Structure #20 using drill cores and image logs are twofold:

1. Establish a baseline description using existing data re-interpreted using knowledge and experience gained from the site descriptive modelling efforts at Forsmark and Laxemar. The combination of extensive existing data and focused new analyses will allow for a comprehensive updated description at a scale (centimetre to decimetre) not frequently studied at Äspö Hard Rock Laboratory since the TRUE Block Scale experiment; and
2. Attempt to quantify the heterogeneity of minor deformation zones along their extent, with an eye towards trying to understand exactly how much information (number of drill holes, scale of investigation, types and numbers of data collected) is necessary to characterize such structures during future underground detailed site investigations in order to improve evaluations of long-term safety.

The focused re-analysis of existing data from previous geological models, Sicada, and BIPS is the first step in this process. The re-analysis consisted of two distinct activities:

- Re-examination of drill cores from the TRUE Block Scale boreholes and the TASS tunnel pilot boreholes. The analysis consisted of high-resolution drill core photography (cm to mm per pixel resolution) of all Structure #20 intercepts, measurements of sealed and open fracture intensity along the drill core, the collection of mineral samples for chemical and isotopic analysis, a re-identification/interpretation of the boundaries of the core and damage zone of the deformation zone, and the preparation of an integrated description of the Structure #20 intercepts through annotated image mosaics.
- Reinterpretation of Structure #20 intercepts using BIPS image logs. In most cases, the core of the deformation zone has been well-constrained by previous analyses, but the thicknesses of the damage zone (cf. Figure 1-2) is often under-estimated. This task includes calculating the length coordinates and thicknesses of the new core and damage zones in image logs for use in further analyses.

4.1 Review of mapping of Structure #20

In the following a résumé is given of the successive structural conceptualization and modelling of the TRUE Block Scale rock volume during the TRUE Block Scale project, with special emphasis on Structure #20. A sizeable amount of information exists on the geometry of Structure #20 resulting from activities of the TRUE Block Scale project, which utilized this deformation zone as a key structure for hydraulic characterisation and tracer tests. The development of a geological model for Structure #20 was an evolutionary process involving geometric extrapolation and hydraulic interference test analysis response during the initial stages of the TRUE Block Scale experiment (Hermanson et al. 1997, Hermanson 2001a, b) as new investigation boreholes were drilled and investigated.

Initially, Structure #20 was defined as a group of faults with visible apertures in the TRUE Block Scale boreholes KA2563A and KA2511A, with an inferred intercept or close connection in borehole KI0025F due to the hydraulic interference response (Hermanson 2001a). The structure was first mapped as either a single open fracture or a series of open fractures within “altered diorite”, and given an initial strike and dip of 318/85. Subsequent refinements were based on data from boreholes KI0023B (Hermanson 2001b) and KI0025F02.

The definitive geological basis for the majority of the TRUE Block Scale structures was the March 2000 hydraulic and structural model (Hermanson and Doe 2000), which incorporated new data from borehole KI0025F03, and a new conceptualization of the relationship between flowing fractures and the deformation zone structure. The importance of fault splays and interconnected fracture/fault swarms was re-enforced in this model revision through pressure response analysis (the same type of analysis previously described in Chapter 3). The March 2000 hydrostructural model recognizes the geometric complexity of Structure #20 within the TRUE Block, and describes the structure as a

highly fractured core inside 10 to 15 cm of mylonite surrounded by altered porphyritic diorite. The interpretation of the brittle core of Structure #20 was that it consisted of a double fault plane with calcite infilling (Hermanson and Doe 2000). It is in this model where Structure 20 is first recognized as a key feature within the TRUE Block Scale rock volume, in that it shows strong hydraulic connections across the entire volume to multiple structures (#6, #13, #21, #22, and #23). The actual extent of Structure #20 to the north is not clearly defined in the March 2000 TRUE Block hydrostructural model, but it was interpreted to extend at least as far as borehole KA2563A.

The best current summation of the geology of Structure #20 is the description presented in the final report of the TRUE Block Scale project (Andersson et al. 2002a, Appendix C). This report represents the "final" understanding of the geometry and hydraulic connections of structures in the TRUE Block, where Structure #20 is recognized as a significant hydraulic conductor with a highly variable geometry across the TRUE Block. The general appearance of the deformation zone core of Structure #20 is that of one to two open fractures within a thicker (10–15 cm) zone of mylonite, indicative of strong ductile shearing. Lenses of calcite-rich fault gouge and occasional breccia are also present. The deformation zone core is surrounded by a 20–30 cm rim made up of a mix of altered wall rock (largely Äspö diorite) and additional cataclasite. In one borehole (KA2563A), an association with fine-grained granite is noted. The possibility of fault splays associated with Structure #20 is also noted; in KI0025F02 the Structure #20 intercept takes the form of a double fault plane (Andersson et al. 2002a). Structurally, Structure #20 was characterized during the TRUE Block Scale project as a re-activated ductile shear zone precursor (mylonite). The zone was attributed a final modelled pole trend and plunge of 229/5, or, expressed as a strike and dip, 319/85.

4.2 Rock types

Table 4-1 illustrates the major rock types found on Äspö Island and within the TRUE Block Scale borehole volume as inferred from the borehole array; the table also presents the relevant rock type from the most recent site-descriptive modelling (SDM) effort, and the identifier code for the rock type in the Sicada database. Most drill cores are composed of a mix of Äspö diorite and Ävrö granite, which have been subdivided into different subcategories in Sicada in an attempt to bring geologic mapping at Äspö in line with the SDM efforts at Simpevarp and Laxemar.

Table 4-2 summarizes the rock types within a ± 2 m respect zone around Structure #20 in the TRUE Block Scale boreholes (using the measured depth limits of the deformation zone defined in Andersson et al. (2002a) and the TASS pilot boreholes (based on the authors' interpretation of the deformation zone thickness through drill core interpretation). The presence or absence of deformation-related rock types (mylonite, cataclasite, breccia or fault gouge) is also noted. Data from TRUE Block Scale boreholes in Table 4-2 have been taken from Appendix C of Andersson et al. (2002a).

Table 4-1. Translation table for relevant Äspö rock names to Sicada rock types and codes.

Äspö lithology	Description	Code
Äspö diorite	Quartz monzodiorite to granodiorite, porphyritic	501037
Ävrö granite	Granite to quartz monzodiorite, generally porphyritic	501044
Ävrö granodiorite	Granite to granodiorite, sparsely porphyritic to porphyritic	501056
Ävrö quartz monzodiorite	Quartz monzonite to quartz monzodiorite, generally porphyritic	501046
Gabbroid-dioritoid	Mafic rock, undifferentiated	508107
Mylonite	Mylonite	508004
Breccia	Breccia	508002
Fine-grained diorite-gabbro	Fine-grained mafic rock	505102
Fine-grained granite	Fine-grained granite	511058
Hybrid Rock[1]	Hybrid Rock	505105
Pegmatite	Pegmatite	501061

[1] The hybrid rock constitutes either a mixing (chemical) or mingling (physical), or a combination of the two, of two different magmas, e.g. felsic and basic. At the Äspö HRL, the hybrid rock is typically composed of either Ävrö granodiorite or Äspö diorite interacting with gabbroic/dioritic rock.

Table 4-2. Rock types associated with Structure #20 intercepts in cored boreholes.

Drillhole Idcode	Primary lithology	Secondary lithologies	Deformation features			
			Cataclasite	Mylonite	Breccia	Gouge
KA2511A	501037	511058	N	N	N	N
KA2563A	511058	n/a	Y	Y	Y	Y
KI0025F	501037	505102, 508107	N	N	N	N
KI0023B	501037	508107	Y	Y	Y	Y
KI0025F02	501037	511058, 508107	Y	Y	N	N
KI0025F03	501037	511058, 508107	Y	Y	Y	N
KI0010B01	501037	501061	Y	Y	N	N
KI0014B01	501037	501061, 511058	Y	Y	N	N
KI0016B01	501037	501044, 511058	Y	Y	N	N

The dominant rock type in the TASS tunnel is Äspö diorite, ranging from fresh to oxidized (Hardenby and Sigurdsson 2010). When Äspö diorite is oxidized, it displays a distinct reddish staining. The Äspö diorite is not a true diorite, but varies in composition from quartz monzodiorite to granodiorite on standard QAP plots (Hardenby and Sigurdsson 2010). In the TASS tunnel, the Äspö diorite is predominantly massive with large pink to reddish-white feldspar phenocrysts in a medium-grained, dark grey to almost black groundmass. Near the interpreted Structure #20 intercept, dikes of fine-grained granite are noted; this is consistent with results from borehole KA2563A (Table 4-2). The tunnel mapping effort (Section 5.3) suggests that the fine-grained granite dike functioned to concentrate strain at the boundary of the dike and the Äspö diorite host rock, resulting in a localization of both brittle and ductile deformation at the interface between the two lithologies.

4.3 Fracturing

Fractures are both the key component of deformation zones and the key identifier for their location in boreholes. During site descriptive modelling (SDM), both major and minor deformation zones were identified in drill cores based on changes in fracture intensities, fracture orientations, and fracture morphologies. Any integrated model of a deformation zone must include a description of the fracturing associated with the structure. This section of the report examines the fracture patterns observed in cored boreholes in both the TRUE Block Scale rock volume and along the TASS tunnel from drill core, BIPS image logs and from Boremap data from previous mapping exercises stored in Sicada. It is noted that these analyses may seem out of place, given that the Structure #20 is already relatively well-constrained in the boreholes and in the tunnel. However, their inclusion is designed to demonstrate a conceptual methodology for the identification of deformation zone and minor deformation zones from cored borehole data that could conceivably be used during the detailed site characterization efforts at Forsmark.

4.3.1 Fracture orientations

Fracture orientations can often be a key indicator of both the spatial limits of deformation zones and of the orientation of the zone itself, given the availability of information (or, failing the presence of direct data, a geological conceptual model of deformation and rupture) on the sense of shear along the deformation zone and the relative timing of brittle deformation events. While the global, and often linear, geometry of deformation zones within the TRUE Block Scale rock volume are largely manifested by hydraulic response data on connectivity (cf. Chapter 3), local variability of the orientation of the deformation zone can be seen in the orientations of fractures within the core and damage zone of the deformation zone. The effects of the deformation zone core on the damage zone can manifest as a secondary fracture set of Riedel shear fractures, an increased intensity of brittle fractures parallel to subparallel to the direction of slip, wing cracks perpendicular to the strike of the deformation zone near the tips, or the presence of extensional pull-apart joints in the transpressional zone between two overlapping strands of the deformation zone (Kim et al. 2004).

All fracture orientations are expressed as the trend and plunge of the normal (pole) to the fracture plane; all values are taken directly from Sicada. Data was obtained from Sicada table query *p_fract_core*, with a depth filter applied to extract only records within a certain distance of the deformation

zone intercept. For this analysis, the intercepts for TRUE Block Scale boreholes were taken from Andersson et al. (2002a), while the TASS tunnel report (Hardenby et al. 2010) was used to select intervals from the TASS pilot bore holes. A bounding threshold of plus or minus one or two metres from the calculated deformation zone core location (midpoint of the selected interval) was used to identify fractures inside the footprint of the deformation zone. The bounding threshold was used to ensure that there were sufficient fractures to allow for statistical analysis. The bounding thicknesses are on the upper end of potential damage zone thicknesses seen and/or hypothesized during SDM site modelling and from geologic judgement based on fault structures at similar scales in other locations. It was decided that, given the uncertainty in the precise location of the deformation zone intercepts, a conservative approach to selecting fracture data for analysis was appropriate. The intervals used to select data for orientation and intensity analysis are presented in Table 4-3.

In the Äspö HRL, all strikes and dips are referenced to the Äspö96 coordinate system north, which is rotated 11.1° counter-clockwise (west) from geographic north, and 12° west from mean magnetic north (Figure 4-1). Sicada automatically converts between the Äspö coordinate system and Swedish national grid coordinates for X, Y, and Z, but does not automatically convert angular measurements. No orientations were available for borehole KA2563A in Sicada (the records for strike and dip for this hole appear to be missing). In addition, records from borehole KA2511A have been intentionally excluded from the orientation analysis due to suspected corruption of the fracture orientations. The issue has been reported back to SKB. The counts and measured depths of fractures in KA2511A and KA2563A are assumed to be accurate for purposes of fracture intensity analysis.

For this study, a brief review of orientation stereo plots using fracture pole trends and plunges calculated from Sicada records was done. The goals were to determine what, if any, characteristic fracture orientations were associated with Structure #20. The results include probability distribution fits to data within the Structure #20 footprint using the ISIS analysis function of FracMan version 7.4 (Dershowitz et al. 1998), see Table 4-4. Fracture orientations are presented as polar stereo plots in Figure 4-2 through Figure 4-7.

Table 4-3. Locations of borehole sections used to provide data for fracture orientation and intensity analysis.

Drillhole Idcode	Zone delimit (m) Secup	Seclow	Number of fractures Total	Open	Sealed	No aperture	Intensity P_{10}_total (m^{-1})
KA2511A	121	124	14	14	0	0	4.67
KA2563A	188	190		0	0	0	0.00
KI0025F	86	89	5	1	0	4	1.67
KI0023B	68	71	7	3	0	4	2.33
KI0025F02	74	76	7	2	0	5	3.50
KI0025F03	72	74	12	3	0	9	6.00
KI0010B01	74	76	21	10	11	0	10.50
KI0014B01	71	73	14	7	7	9	7.00
KI0016B01	69	72	9	9	0	0	3.00

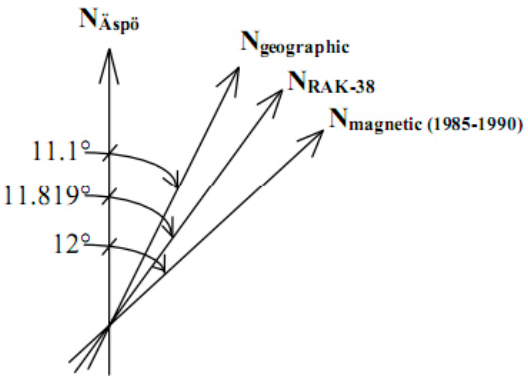

Figure 4-1. *Relationship of magnetic north and true north to the Äspö96 coordinate system (from Almén and Stenberg 2005, Section 3.2).*

Table 4-4. ISIS analysis results within ~ ± 1–2m of the interpreted intercept of Structure#20. All fracture orientations are in Äspö96 coordinates.

Set number	Set name	Count	Distribution	Mean pole Trend	Plunge	Dispersion K1	K2	K12	Goodness of fit K-S	Signif.
TRUE Block boreholes										
1	NW	14	Bivariate Bingham	61.2	1.7	–34.8	–6.3	n/a	0.08	99.9%
2	SH	5	Univariate Fisher	186.1	77.0	23.6	n/a	n/a	0.3	76.8%
3	EW	12	Elliptical Fisher	220.5	24.8	18.6	4.1	n/a	0.19	82.3%
TASS tunnel pilot boreholes										
1	NW	28	Elliptical Fisher	42.3	5.2	33.3	4.1	n/a	0.18	38.3%
2	SH	7	Univariate Fisher	202.4	69.4	8.5	n/a	n/a	0.23	88.1%
3	EW	2	Univariate Fisher	168.7	24.4	100.00	n/a	n/a	0.40	91.1%
4	NS	7	Elliptical Fisher	270.8	3	18.45	n/a	n/a	0.20	94.6%

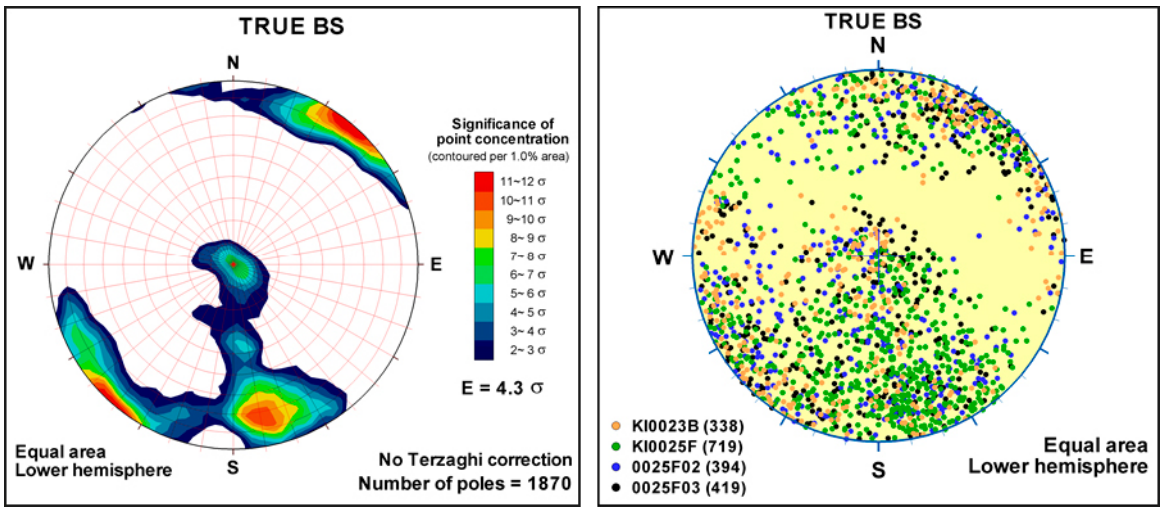

Figure 4-2. Orientations of all fractures within TRUE Block Scale boreholes, presented as Kamb-contoured stereonets (left) and as a pole plot coloured by borehole name (right). Note that boreholes KA2511A and KA2563A are excluded from the stereoplots due to suspected errors in fracture orientations or missing data in Sicada. All fracture orientations are in Äspö96 coordinates.

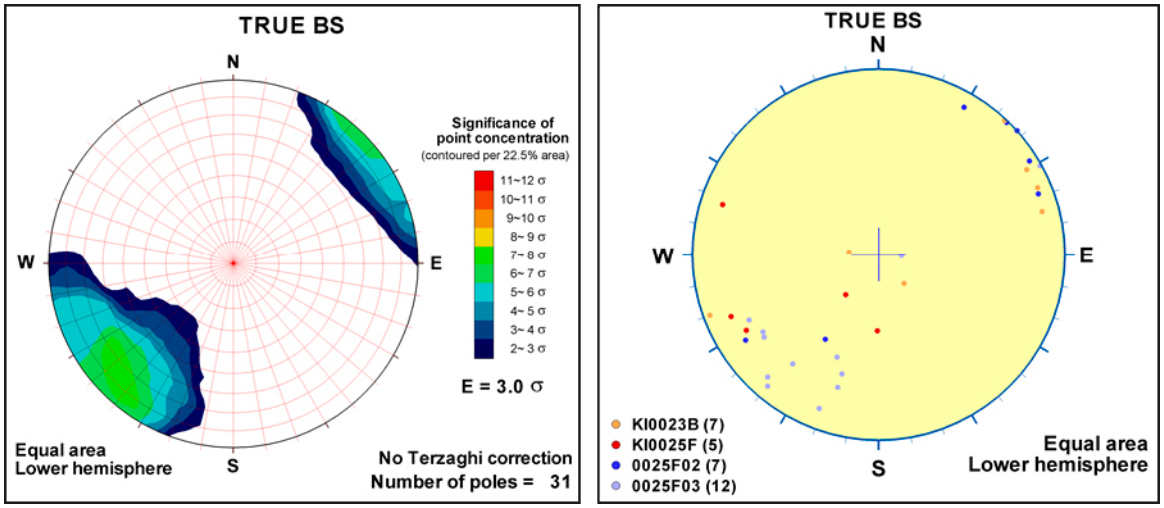

Figure 4-3. Orientations of fractures inside of or near (~ ± 2 m) the interpreted intercepts of Structure #20 with TRUE Block Scale boreholes. All fracture orientations are in Äspö96 coordinates.

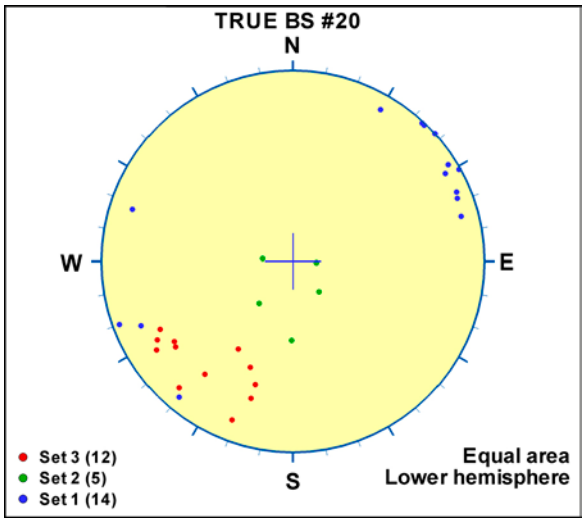

Figure 4-4. *ISIS analysis results for fractures inside of or near (~ ± 2 m) the interpreted intercepts of Structure #20 with TRUE Block Scale boreholes. All fracture orientations are in Äspö96 coordinates.*

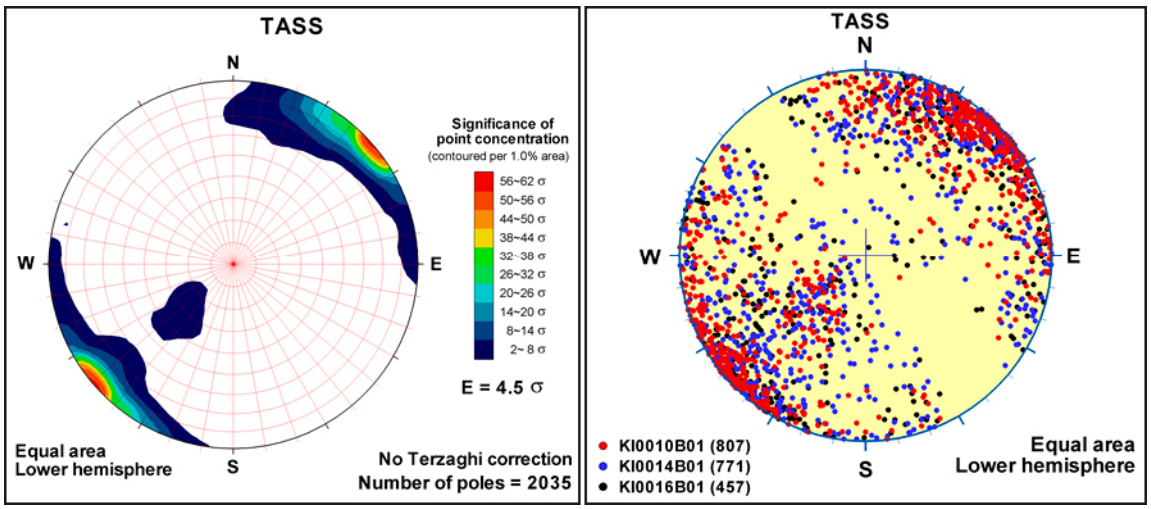

Figure 4-5. *Orientations of all fractures recorded in TASS pilot boreholes, presented as a Kamb-contoured stereonet (left) and a pole plot coloured by borehole name. All fracture orientations are in Äspö96 coordinates.*

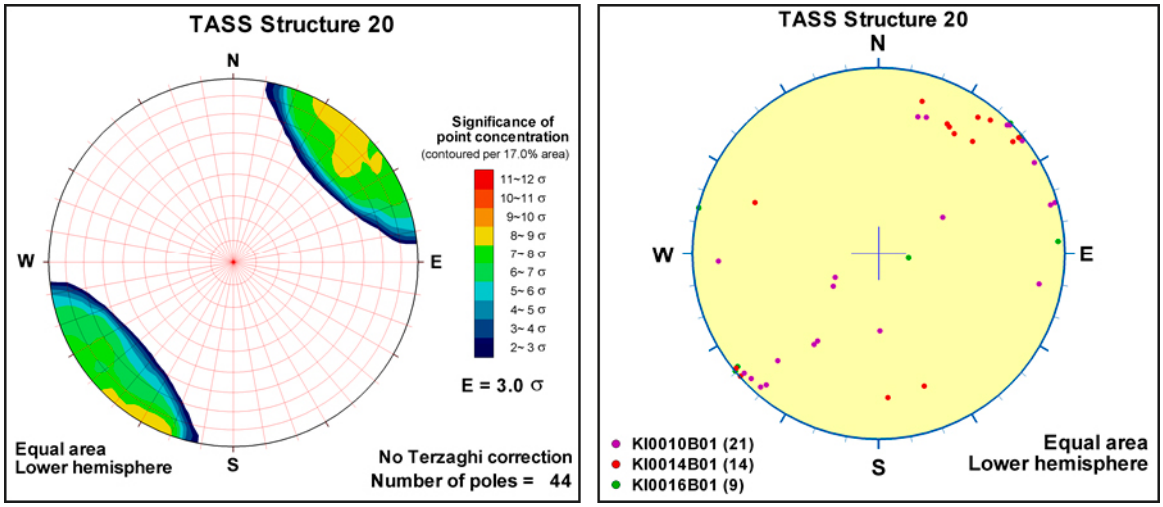

Figure 4-6. *Orientations of all fractures recorded in TASS pilot boreholes inside of or near (~ ± 2 m) the interpreted intercepts of Structure #20. All fracture orientations are in Äspö96 coordinates.*

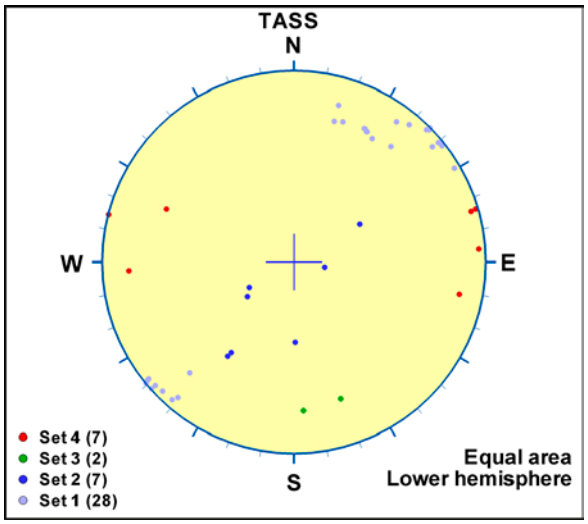

Figure 4-7. *ISIS analysis results for fractures inside of or near (~ ± 2 m) the intercepts of Structure #20 with the TASS tunnel pilot boreholes. All fracture orientations are in Äspö96 coordinates.*

In the case of data recorded in Sicada, fracture orientations recorded within ± 2 m of the Structure #20 intercept in the TRUE Block Scale boreholes (Figure 4-3) or the TASS Tunnel pilot bores (Figure 4-6) are not sufficient to conclusively identify the deformation zone without additional information. Orientations within the zone footprint are very similar to those recorded outside Structure #20 (Figure 4-2 and Figure 4-5); the only remotely visible trend is a slight decrease in the relative intensity of subhorizontal fractures within the assigned zone of influence of Structure #20. However, this result is neither conclusive nor useful, as limited studies of other sections of one of the pilot boreholes show a larger variability than that observed between the Structure #20 footprint and the rest of the pilot boreholes.

Two separate ISIS analyses (Table 4-4) were used to classify the fractures observed in the assigned zones of influence around Structure #20 into orientation sets. The first analysis, based on the TRUE Block Scale boreholes (Figure 4-4), divided the fractures into three sets, based largely on dip cut-offs. These fracture sets were then simplified into two orientation sets:

- A diffuse NW-striking steeply to moderately dipping set ("NW Set") that also encompassed the steeply-dipping east-west striking set ("EW Set);
- A gently- to subhorizontally-dipping, EW to WNW-striking set ("SH").

Two additional fracture sets were identified in the TASS pilot boreholes (Figure 4-6): a north-dipping and east-west striking set and a north-south striking nearly vertically dipping set. There are also significantly more fractures in the pilot borehole records than recorded in those from the TRUE Block Scale rock volume. The cause of the greater observed fracture intensity is not known, but is likely a mix of different core or image interpreters, advances in the understanding of fracture identification at Äspö and improvements in drilling and BIPS logging. Note that only two poles characterize the "EW set", making the location of its mean pole and dispersion exceptionally uncertain, and the resulting goodness of fit statistics for this set presented in Table 4-4 fairly useless.

Geologically, Structure #20 represents a pre-existing ductile shear zone re-activated at least once in the brittle regime. The orientations of the resulting fractures should represent a combination of the in situ stress at the time of deformation and the presence of existing discontinuities or rock fabric to control the orientations of the structures. Based on the analysis of recorded fracture orientations described, the patterns of fracture orientations in the damage zones surrounding Structure #20 appear to be controlled by larger-scale factors (in situ stress, foliation, past tectonics) rather than by local scale heterogeneity around the core of the deformation zone. It is difficult to identify any differences between fracture orientations inside of and outside of Structure #20. This implies that, for faults and deformation zones with a similar protolith and genesis as Structure #20, fracture orientation may not be a unique diagnostic characteristic. No evidence of secondary fracturing (Riedel shearing, tension fractures due to transpression) that could be mechanically- or genetically-linked to deformation along Structure #20 was noted at the scale of the drill core or image log.

4.3.2 Fracture intensity

Given that the orientation of fractures within the deformation zone boundary thresholds (Table 4-3) is not directly useful for identifying Structure #20, the next step is to determine fracture intensity characteristics. During the site descriptive modelling programs at Forsmark and Laxemar, both the single-hole interpretations and a data re-analysis in support of minor deformation zone (MDZ) identification efforts, Fox and Hermanson (2006) determined that changes in fracture intensity are a key discriminator in the identification of major and minor deformation zones (along with other morphological parameters). Consequently, understanding how the intensity of fracturing changes close to and within a deformation zone such as Structure #20 is a key to an integrated description. The tool for examining the intensity of fracturing in existing Sicada data is the cumulative fracture intensity (CFI) plot (La Pointe 2010).

Figure 4-8 shows an example of a CFI plot. In this plot, the Y-axis represents measured depth in units of feet. The X-axis is a cumulative intensity normalized to the interval 0.0 to 1.0. The value of normalized cumulative intensity is calculated by ordering all of the fractures according to their depth (or elevation, which allows for direct comparisons between boreholes for relatively flat-lying strata), from shallowest to deepest. If there are n fractures in the data set, then the shallowest fracture has the X-coordinate of $1/n$, since the probability of being at this depth or shallower is $1/n$. Similarly, the second shallowest point has the X-coordinate of $2/n$, and the deepest point has the X-coordinate of n/n or 1.0. The normalization from a cumulative number to a cumulative probability is advantageous because it allows the direct comparison of data sets that may have different amounts of data.

The CFI plot holds several advantages over more traditional moving-average fracture frequency plots. First, breaks in the CFI curve (sections without fractures) in the plot indicate completely unfractured intervals; the spacing of these intervals can be important in mechanically-stratified rock. Second, they are visually easier to interpret: steeper slopes (assuming elevation or distance is plotted along the Y-axis) represent zones of lesser fracture intensity, while shallower or flat slopes indicate spikes in fracture intensity, which can often be correlated to fractured intervals, i.e. deformation zones. Finally, it is possible to plot several different data sets. Note that all of these analyses can be performed on other types of graphs; the CFI plot facilitates simpler visualizations.

The CFI plots presented in this section contain not only a record of the total fracture intensity, but also cumulative fracture curves based on fracture mineralogy. A given fracture may have more than one mineral present as a coating or an infilling, so the only true metric of total intensity is the CFI curve for all fractures. However, using the fracture mineralization as a qualitative guide allows for

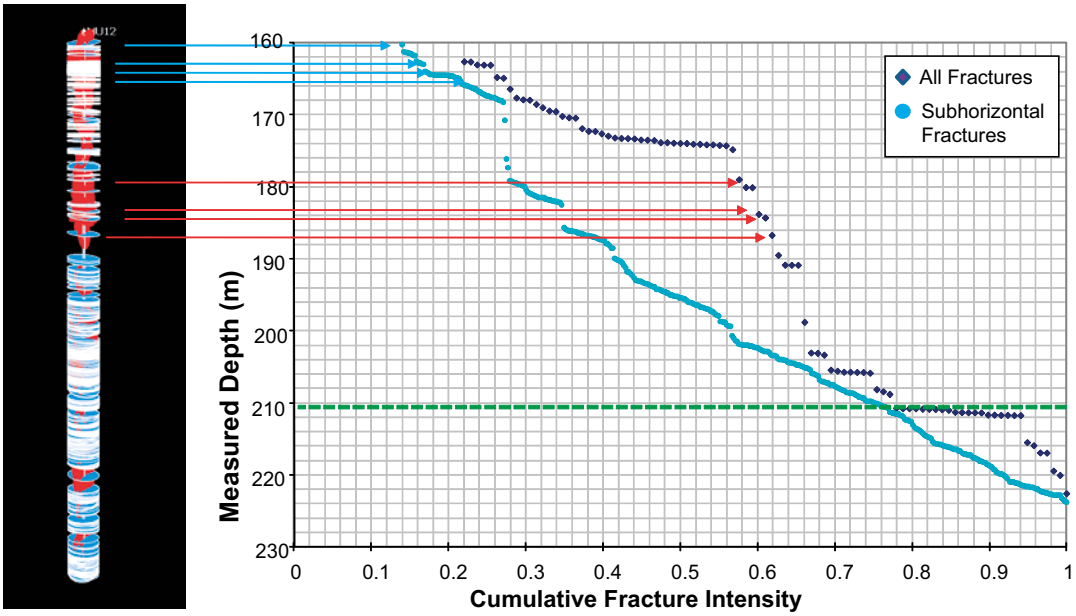

Figure 4-8. *Example of cumulative fracture intensity (CFI) plot.*

the testing of hypotheses regarding the presence or absence of certain minerals. Note that the mineral prehnite, was not used as a key mineral for addressing fracture intensity. The mineral was not identified at all in the TRUE Block Scale data taken from Sicada (only identified in the pilot boreholes), and was consequently left out of the intensity analysis. Key indicator minerals were assumed to be calcite, chlorite and epidote.

Several example CFI plots created from TRUE Block Scale boreholes and TASS pilot holes are presented as Figure 4-9 through Figure 4-14. It was not necessary to reproduce every CFI plot; only those illustrating some of the basic characteristics of fracture intensity surrounding Structure #20 were included in this report. The CFI plots are based solely on fractures recorded in Sicada table *p_fract_core*; they exclude data from *p_sealed_nw*.

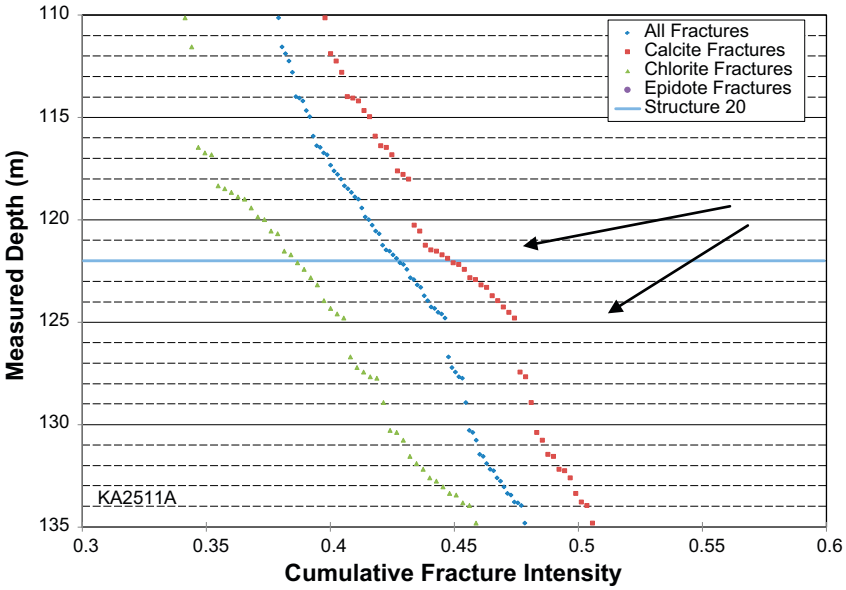

Figure 4-9. *CFI plot of fracture intensity in TRUE Block Scale borehole KA2511A, classified by fracture mineralogy. The horizontal line represents the approximate midpoint of Structure #20 in the borehole, as interpreted during the TRUE Block Scale project (Andersson et al. 2002a).*

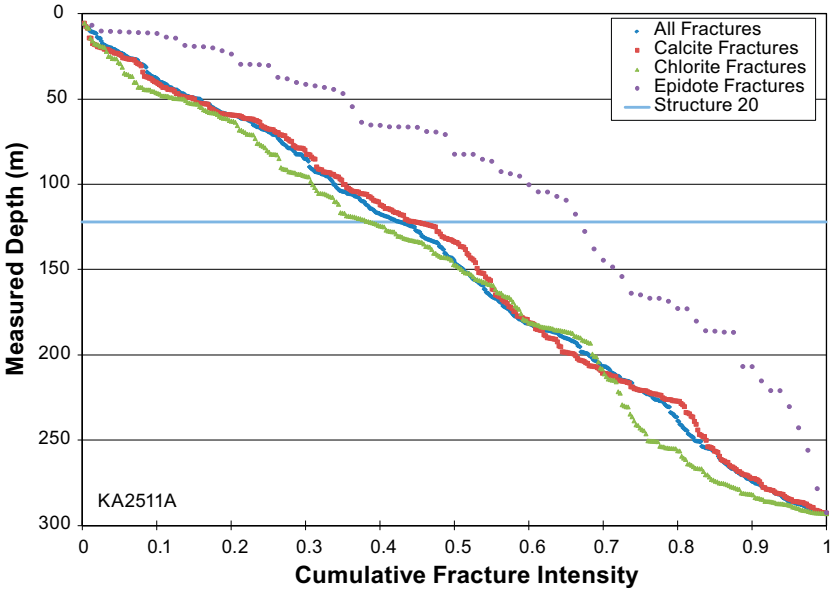

Figure 4-10. *Close up of the Structure #20 intercept with KA2511A. Note the spike (black arrows) in the All Fractures cumulative intensity, and in the intensity of calcite-mineralized fractures. No change in the intensity of chlorite-mineralized fractures is noted, suggesting a lack of association at this particular hole. There is also no association with epidote.*

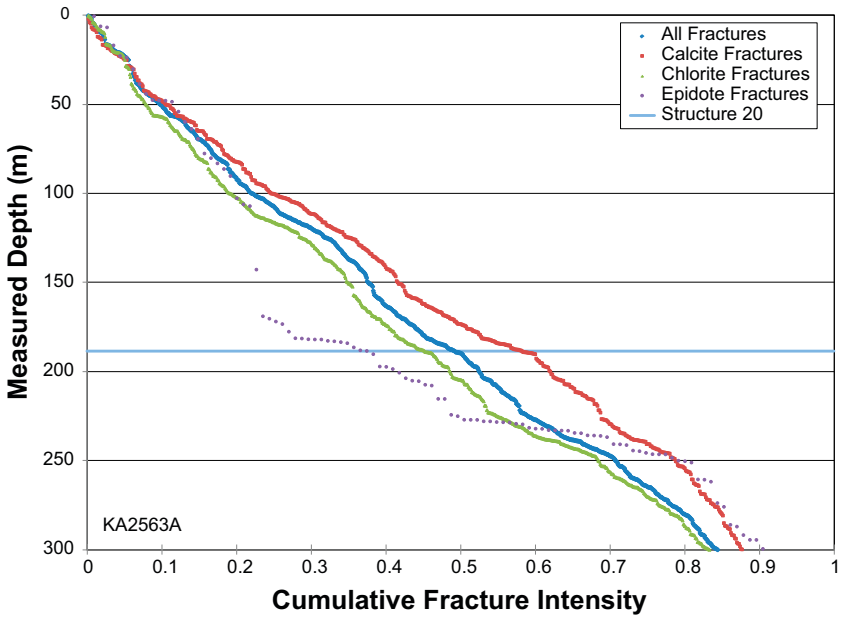

Figure 4-11. *CFI plot of fracture intensity in borehole KA2563A. The horizontal line represents the approximate midpoint of Structure #20 in the borehole, as interpreted during the TRUE Block Scale project (Andersson et al. 2002a). Note the strong association of an increase in fractures containing epidote with Structure #20.*

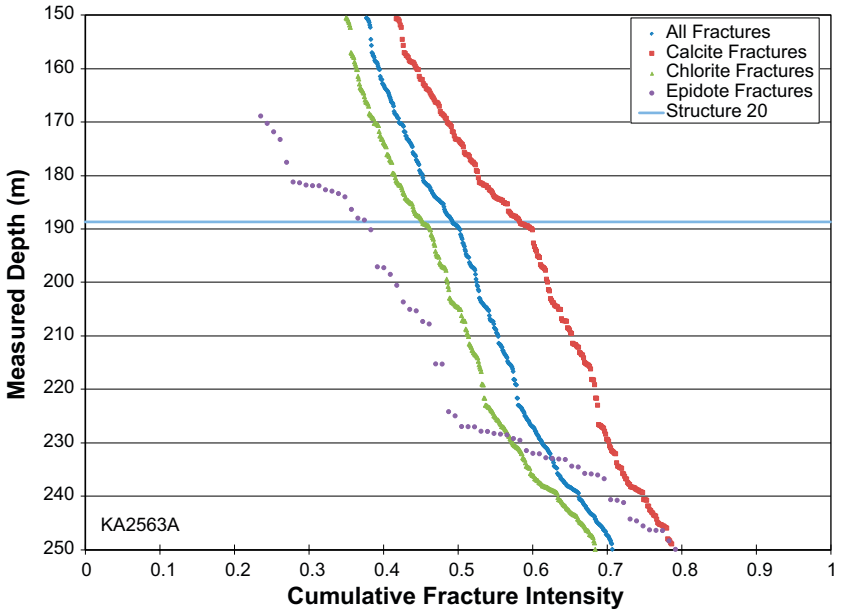

Figure 4-12. *Close up of the KA2563A intercept with Structure #20. The increase in epidote-filled fractures occur several metres away from the start of Structure #20. The same relationship (several subparallel epidote-filled fractures) is seen in the TASS tunnel (Chapter 5). Structure #20 sits near the 'base' of a wider interval (~ 10m thick in measure distance along the borehole) of more intense fracturing; whether this represents distal deformation effects from Structure #20, or the activity of some other process in the host rock is not known.*

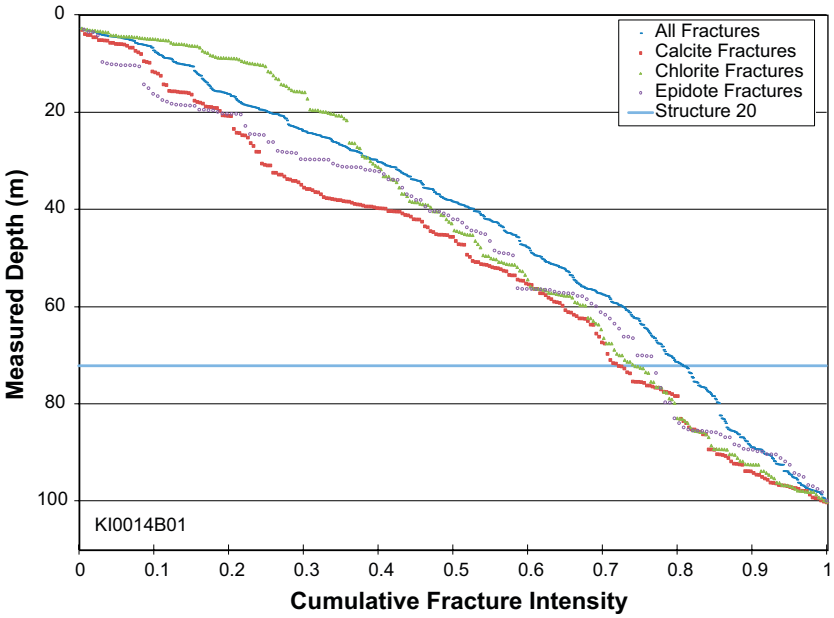

Figure 4-13. *CFI plot of fracture intensity in TASS pilot borehole KI0014B01. Any increase in total fracture intensity is undetectable in terms of total fracture intensity, but can be seen in terms of the intensity of calcite- and chlorite-filled fractures.*

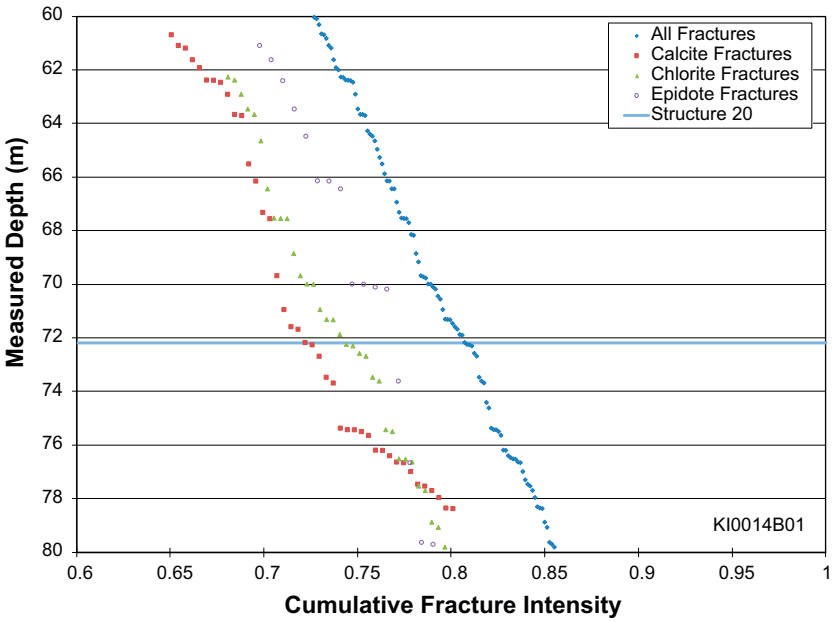

Figure 4-14. *Close up of the Structure #20 intersect with KI0014B01.There is a small spike in the intensity of both calcite- and chlorite-filled fractures near Structure #20, but neither is significant enough to be diagnostic. Note again the presence of the epidote-filled cluster of fractures close to Structure #20.*

The analysis of CFI plots from TRUE Block Scale and TASS pilot boreholes suggests that changes in fracture intensity are a useful diagnostic for identifying deformation zones with characteristics similar to Structure #20. Figure 4-10, Figure 4-12 and Figure 4-14 show distinct spikes in the intensity of fractures with calcite as an infilling mineral; this would be characteristic of a zone where flow of hydrothermal fluids have been significant in the past. The same figures also show spikes in the intensity of both total fracture intensity (both open and sealed) and of fractures containing chlorite as an infilling mineral. However, the spikes in the total and chlorite intensity curves are not particularly large, and are of a magnitude similar to the variability of fracture intensity along the length of the borehole. This suggests that using the intensity metric by itself, without additional information would not be conclusively diagnostic to the existence of a deformation zone.

The association of fractures containing epidote mineralization with deformation zones such as Structure #20 is a curious one. The CFI plots (Figure 4-9 through Figure 4-14) indicate that the deformation zone itself is not associated with increases in epidote infilling, at least not in the existing BIPS image log and Boremap core mapping results contained in Sicada. The only exception to this appears to be borehole KA2563A (Figure 4-11 and Figure 4-12), which shows a spike in the intensity of fractures containing epidote within the damage zone of Structure #20.

However, both drill core (Section 4.4.1) and tunnel (Section 5.3) mapping show a series of epidote-filled fractures and veins that apparently strike subparallel to Structure #20 and serve as a 'marker bed' of sorts for Structure #20 in both the TRUE Block Scale volume and the TASS tunnel. The orientation and persistence of these structures suggest that they may be genetically associated with Structure #20. It is possible they may represent the ductile equivalent of a 'splay fault' to Structure #20, or they may be the outer boundary of a much larger volume of rock, such that the true 'zone of influence' of Structure #20 is larger than the actual zone core and damage zones identified in drill core and image logs. The authors feel that, given the complicated history of deformation at Äspö, the former possibility is the most likely answer.

Linear fracture intensities for the TRUE Block Scale boreholes and TASS pilot boreholes are illustrated in Figure 4-15 and Figure 4-16. Similar patterns were noted as in the CFI plots; though fracture intensity tended to increase at the Structure #20 intercept, the magnitude of the increase was not large enough to make it stand out from some of the other intervals recorded in Sicada. Fracture intensity P_{10} was calculated over 4 m long intervals (Table 4-6) in the cored borehole array; the interval size is consistent with the ± 2 m length assigned to capture the fracturing surrounding Structure #20. Summary statistics are presented in Table 4-6. A box-and-whisker plot (Figure 4-17) is useful for summarizing P_{10} values and comparing the fracture intensity properties of the Structure #20 intercepts to the TRUE Block Scale rock volume (and the TASS rock mass) as a whole.

In general, the analysis of fracture intensity within the Structure #20 intercept from existing data sources suggests that, in the TRUE Block Scale Rock volume, the intercept has higher intensity than the mean value for the whole corresponding hole in the TRUE Block Scale rock volume (Figure 4-17). This relationship breaks down, however, for the TASS pilot boreholes, all of which have higher mean fracture intensities than the global mean value for the Structure #20 intercept. The cause of this observation is currently unknown; however, it likely reflects a mix of more highly-fractured intervals closer to the beginning of the TASS tunnel skewing the data and some level of censoring in previous or current mapping procedures.

Table 4-5. Zone of intervals used (~ ± 2 m) surrounding Structure #20.

Idcode	Secup (m)	Seclow (m)	Fracture count	P_{10} (m^{-1})
KA2511A	120.00	124.00	17	4.25
KA2563A	187.00	191.00	27	6.75
KI0025F	85.50	89.50	9	2.25
KI0023B	68.00	72.00	10	2.50
KI0025F02	73.50	77.50	12	3.00
KI0025F03	71.50	75.50	15	3.75
KI0010B01	73.50	77.50	30	7.50
KI0014B01	70.50	74.50	20	5.00
KI0016B01	69.00	73.00	11	2.75

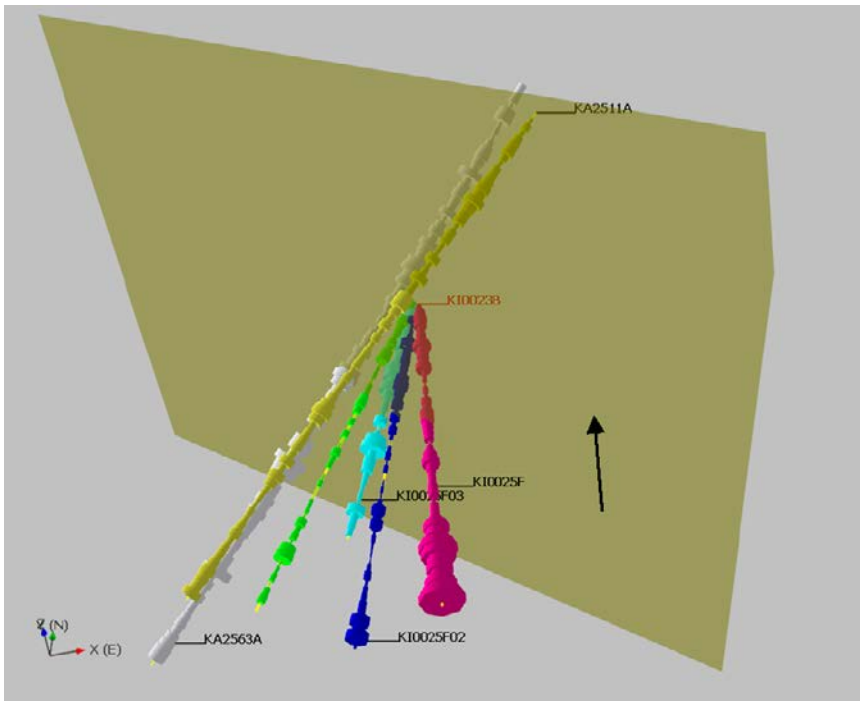

Figure 4-15. *Visualization of existing Structure #20 intercepts within TRUE Block Scale boreholes. Borehole radius is sized by total fracture linear intensity P_{10} (open and sealed combined).Transparent polygon (black arrow) is the interpreted Structure #20 from the TRUE Block Scale project (Andersson et al. 2002a). Note that though Structure #20 generally intersects zones of higher fracture intensity, they are not the highest recorded intensities in the hole.*

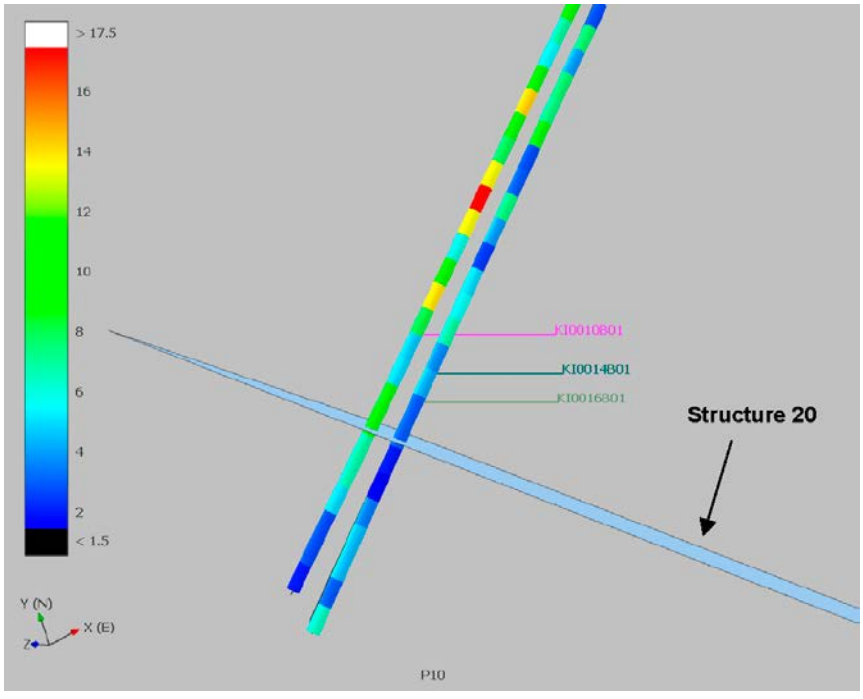

Figure 4-16. *Visualization of existing Structure #20 intercepts within the TASS pilot boreholes. Borehole radius is coloured by total fracture linear intensity P_{10} (open and sealed combined).*

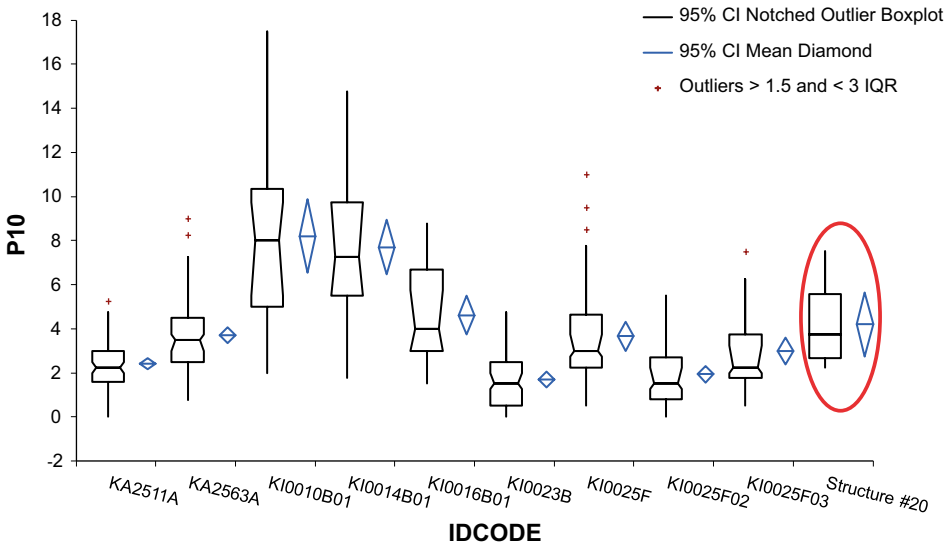

Figure 4-17. *Box and whisker plot of total linear fracture intensity P_{10} (m^{-1}) as a function of borehole. Note that, on average, the Structure #20 intercept (red circle) has higher fracture intensity than the mean fracture intensity in the TRUE Block Scale boreholes, but is below the average fracture intensity of the TASS pilot boreholes.*

Table 4-6. Linear fracture intensity P_{10} inside and outside of Structure #20 in TRUE Block Scale and TASS pilot boreholes within 4 m long intervals.

Borehole name Idcode	Total P_{10} (m^{-1}) Mean	Std. dev.	Min	Max
KA2511A	2.40	1.04	0.00	5.25
KA2563A	3.71	1.67	0.75	9.00
KI0010B01	8.20	4.03	2.00	17.50
KI0014B01	7.70	2.99	1.75	14.75
KI0016B01	4.62	2.10	1.50	8.75
KI0023B	1.69	1.23	0.00	4.75
KI0025F	3.66	2.29	0.50	11.00
KI0025F02	1.93	1.30	0.00	5.50
KI0025F03	2.99	1.78	0.50	7.50
Structure #20	4.19	1.89	2.25	7.50

It is likely that the difference in fracture intensities observed within the Structure #20 zone of influence between the TRUE Block Scale boreholes and the TASS pilot boreholes is not due to radical variation in the properties of the rock mass. The first of the TRUE Block Scale drillings were started in 1997; a significant amount of institutional knowledge of triple-tube core drilling, fractured core logging and BIPS image interpretation has been gained over the last 15 years. Rather, it is more likely that the TASS pilot boreholes have been logged at better resolution and with more detail than the TRUE Block Scale boreholes. Therefore, it is difficult to directly compare absolute fracture intensity values between the TRUE Block Scale boreholess and the TASS pilot boreholes.

Other metrics of fracture intensity have also been recorded in Sicada during the BIPS and Boremap mapping efforts. In particular, the results of queries *p_fract_crush*, *p_core_loss*, and *p_fract_sealed_nw* are all useful diagnostic indicators as to the presence or absence of a deformation zone or minor deformation zone within a cored borehole. Table 4-7 illustrates a quick look at these descriptors as they are currently recorded in Sicada. Even though the data coverage in the borehole array is erratic, both the presence of sealed networks and crushed rock are common at the Structure #20 intercepts. This finding is in line with the conclusions related to existing mapping of Structure #20 (Andersson et al. 2002a), as well as the results of the core analysis (Section 4.4.1) and the BIPS re-interpretation (Section 4.4.2) performed as part of this study.

Table 4-7. Presence or absence of potential diagnostic properties in Sicada for identification of deformation zones and minor deformation zones similar to Structure #20. "N/R" indicates that the Sicada query did not return any data at all for this particular borehole and property.

Idcode	Core loss?	Sealed network?	Crushed rock
KA2511A	N	N/R	Y
KA2563A	N	N/R	Y
KI0010B01	N	Y	N
KI0 014B01	N	Y	N
KI0016B01	N	Y	Y
KI0023B	N/R	N/R	N/R
KI0025F	N/R	N/R	N/R
KI0025F02	N/R	N/R	N/R
KI0025F03	N/R	N/R	N/R

4.3.3 Fracture morphology

In addition to an examination of fracture orientations and intensities from existing boreholes in Sicada, a brief analysis of other fracture morphological parameters was performed. The objective of this analysis was, as with the orientation and intensity analyses (Section 4.3.1 and Section 4.3.2, respectively), to see whether it is possible to identify a characteristic geologic signature of Structure #20. The parameters in Sicada used were:

- *fract_interpret*: Indicates whether a fracture is open (broken fractures), partly open (unbroken fractures), or sealed. A nominal metric of fracture aperture. In the summary charts, this parameter has been re-named "Aperture".
- *roughness*: In Sicada, this parameter is somewhat misnamed. It is in fact a description of the shape of the fracture; whether it is a planar break, an undulating (curved surface), a stepped appearance (characteristic of shear) or something else. In the summary charts, this parameter has been re-named "Shape".
- *surface*: An ordinal metric of the roughness of the fracture surface; generally a qualitative assessment based on the profile, regularity, and number of asperities along the fracture plane. Roughness can be an important factor in contaminant transport. In the summary charts, this parameter has been re-named "Roughness".
- *frac_alteration*: An ordinal metric of the degree of mineral and host-rock alteration (chemical weathering and hydrothermal alteration). In the summary charts, this parameter has been re-named "Alteration".

Fracture mineralogy was not explicitly used in this part of the analysis; the mineralogical characteristics of fractures within Structure #20 are discussed in Section 4.5. Note that if a parameter returned from Sicada was blank, it was assigned a null string value of "NDR". These null values have generally been removed from the summary tables, on the assumption that the proportions from records with data are an adequate sample from the population as a whole. The results of the analyses (Figure 4-18 through Figure 4-21) are presented as summary histograms created in Microsoft Excel from pivot tables. Note that in these histograms, the "Structure #20" data set contains data taken from all Structure #20 intercepts; effectively, it is a representative or average view of this particular deformation zone.

Overall, the pivot table analysis suggests that, outside of fracture aperture, the morphological properties collected in Sicada are not useful at uniquely identifying the Structure #20 intercept. There are significant differences in how fractures are mapped, both between the TASS pilot boreholes and the TRUE Block Scale boreholes. For example, in terms of fracture shape (Figure 4-19) there is a very clear difference in how the shape of the fractures was mapped in the TASS tunnel, versus in the TRUE Block Scale project. It is unlikely that fracture morphologies are that different over a relatively small distance (~ 200 m).

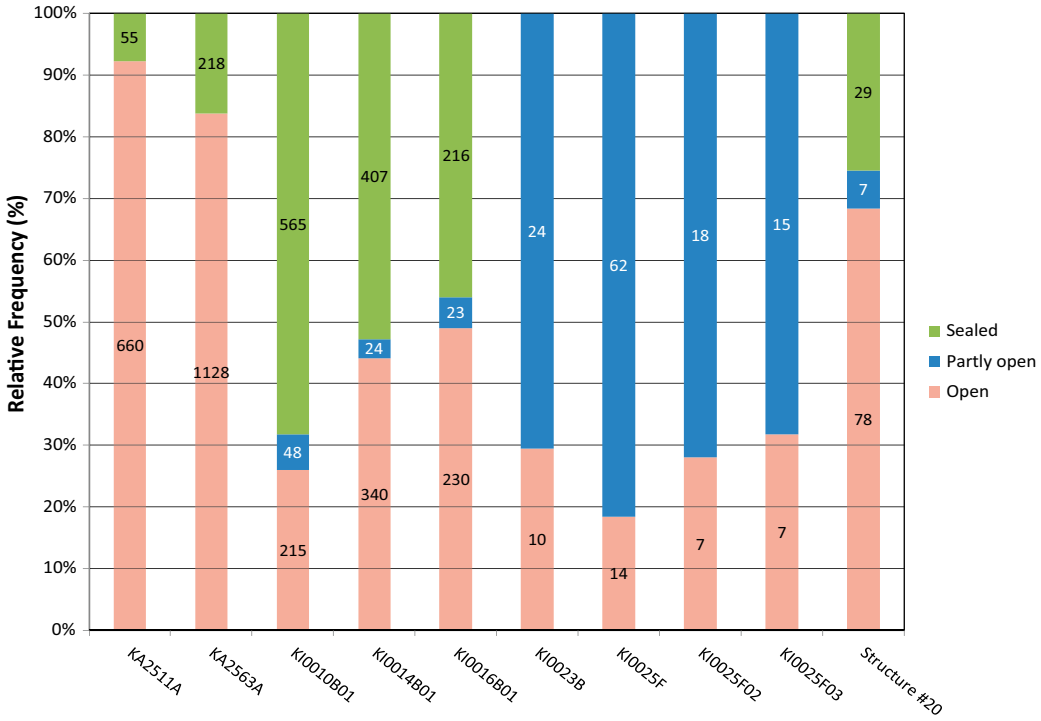

Figure 4-18. *Normalized frequency histogram of aperture measurements from TRUE Block Scale boreholes and TASS pilot boreholes. The measurements within Structure #20 intercepts are plotted as the rightmost column.*

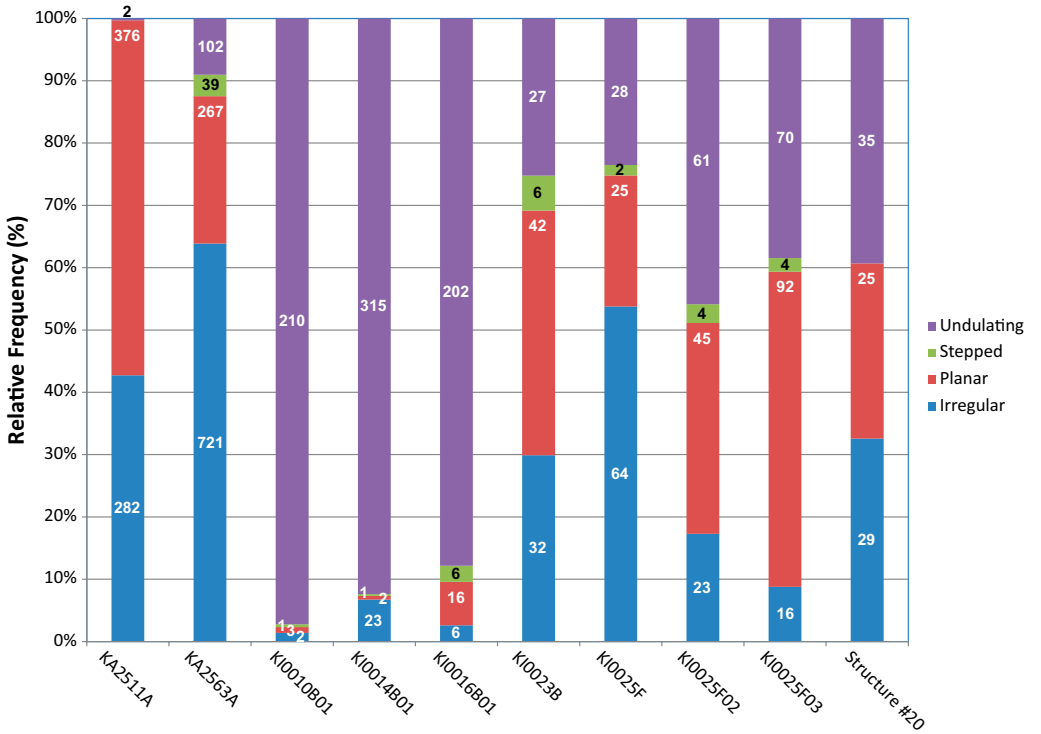

Figure 4-19. *Normalized frequency histogram of fracture shape measurements from TRUE Block Scale boreholes and TASS pilot boreholes.*

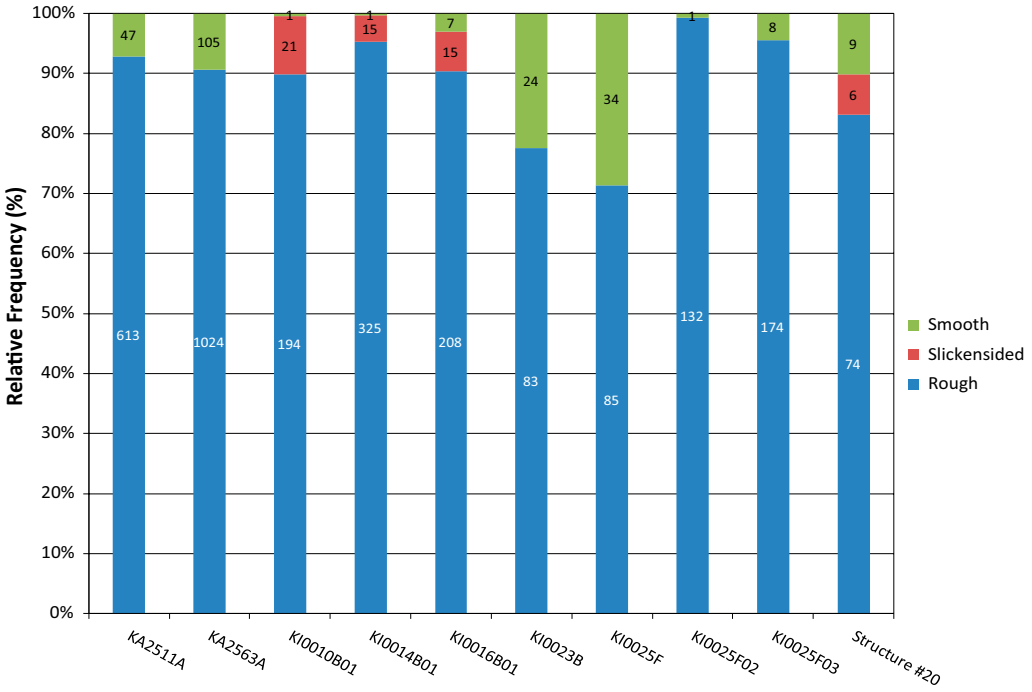

Figure 4-20. *Normalized frequency histogram of fracture roughness measurements from TRUE Block Scale boreholes and TASS pilot boreholes. Note that, with the exception of two TRUE Block boreholes, there is very little difference between the boreholes.*

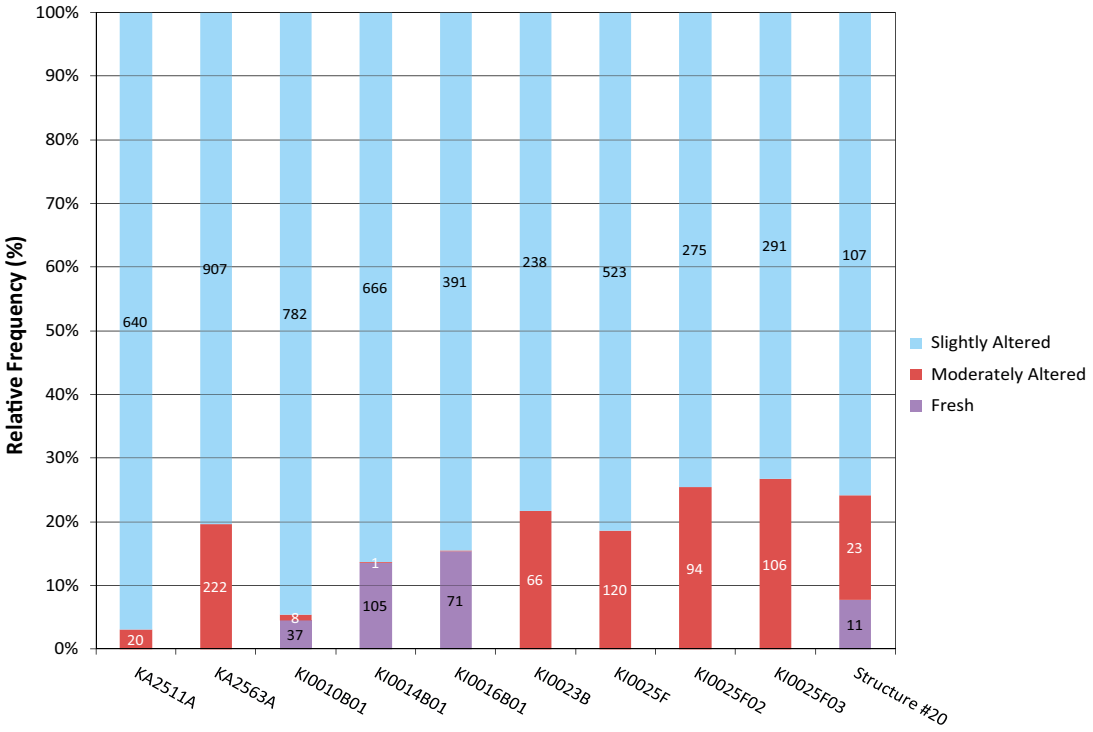

Figure 4-21. *Normalized frequency histogram of fracture alteration measurements from TRUE Block Scale boreholes and TASS pilot holes. Again, note the difference between the two datasets; it is clear that different mapping criteria have been used.*

4.4 Structural geology

4.4.1 Drill core analysis

The methodology behind the analysis of Structure #20 intercepts in drill cores is described in detail in Section 2.2. Drill cores were examined at the SKB's core logging facility at the Äspö Hard Rock Laboratory. Initial identification of the locations of the Structure #20 intercepts were first made using the results reported by the TRUE Block Scale project (Andersson et al. 2002a). Next, an extrapolation of Structure #20 to the TASS tunnel was made using the final TRUE Block Scale geometric model in RVS. Additional corroboration of the intercept was developed in the results from the TASS pilot borehole drilling (Hardenby et al. 2008), the structural projections of deformation zone characteristic features documented in the TASS tunnel geological mapping report (Hardenby and Sigurdsson 2010), and by a pressure response analysis of groundwatermonitoring borehole data during drilling (Chapter 3). A limited structural geological evaluation of the cores was performed, supplemented by extensive photographic documentation and fracture mineral sampling of the cores.

The results of the re-examination of the Structure #20 drill core sections are best summarized graphically, such that individual morphological, mineralogical, and structural trends can be highlighted and viewed directly rather than by reference in a table. Figure 4-22 through Figure 4-29 graphically illustrate the geology of the Structure #20 intercepts with both the TRUE Block Scale boreholes and the TASS pilot boreholes. Table 4-8 records the thicknesses of the Structure #20 core and damage zones, as interpreted from the performed new drill core analyses. Note that for many of the TRUE Block boreholes, whole-rock samples have previously been taken from the core, making assessment of the true size of deformation zone thickness impossible from core alone. For these holes, the interpreted zone thickness is based on the results of re-analysis of the BIPS images (Section 4.4.2).

Extensive work has already been done on the Structure #20 intercept within the TRUE Block Scale rock volume; these notes have already been summarized in Sections 1.6 and 4.1. The results of the re-evaluation of TRUE Block Scale drill cores are presented graphically later in this section. As the TASS pilot boreholes had not been subjected to the same level of scrutiny at the Structure #20 intercept, the majority of the description in this chapter revolves around the characterization of Structure #20 in pilot boreholes KI0010B01, KI0014B01, and KI0016B01.

TRUE Block Scale borehole KA2511A

The drill core record for the Structure #20 intercept in borehole KA2511A (Figure 4-22) is incomplete; much of the 'upper' damage zone and part of the deformation zone core has been taken for destructive testing during the TRUE Block Scale experiment.

The 'upper' damage zone of the Structure #20 intercept in KA2511A drill core is marked by a slight increase in sealed fracture intensity (~ 14 fractures in a 10 cm section) with abundant red staining and minor alteration rims around the larger feldspar phenocryst. There is no visible decrease in phenocryst or groundmass grain size as in other holes, nor is there the development of a pervasive ductile fabric.

The deformation zone core of Structure #20 in KA2511A drill core (Figure 4-22) is represented by an approximately 11 cm thick section of intensely-deformed Äspö diorite, consisting of alternating bands of chlorite-rich cataclasite, mylonite, and small amounts of brecciated rock. The mylonite bands have average thicknesses on the order of 5–6 mm. Two open fractures, with visible slickensides and a stepped morphology (suggesting stick-slip style brittle deformation) are likely the significant hydraulic conductors at this interval. Open fracture apertures range from 0.25 to 4.0 mm.

No lower damage zone was observed in KA2511A; Structure #20lower ends with a thin section (~ 1 cm) of bleached Äspö diorite, which gradually extends into reddish-stained altered Äspö diorite over a distance of approximately 3 cm. Previous work (Andersson et al. 2002a) suggested that the relatively simple nature of the KA2511A intercept might indicate that the maximum lateral extent of Structure #20 was nearby.

TRUE Block Scale borehole KA2563A

As in the KA2511A drill core, several sections of both the damage zone and deformation zone core of Structure #20 are missing from KA2563A; however sufficient drill core remains to make a detailed

assessment of the geological characteristics of the Structure #20 intercept. KA2563A has the thickest intercept of Structure #20 across all studied boreholes; the interpreted thickness of the deformation zone core plus 'upper' and 'lower' damage zones is almost two metres (Table 4-8). The core interpretation is significantly different than the BIPS image log reinterpretation (cf. Section 4.4.2); the authors chose to retain the thicker description of the intercept as seen in the core boxes, on the logic that simplifications (such as splitting the intercept into two different structures) could be performed later.

In KA2563A, Structure #20 manifests itself as a series of three distinct deformation zone cores, characterized by cataclasite and breccia, separated by damage zones with abundant red staining, sealed fractures, and weak to moderate foliation. The interpretation is that the third deformation zone core (~ 190.11 m borehole depth) is the primary Structure #20 intercept; the other two identified deformation zone cores represent splay faults, similar to those seen in KI0010B01. The three deformation zone cores are identified in the photographic record (Figure 4-23) with interpreted boundaries outlined by white dashed lines, and a white capital "C".

Damage zones within the interpreted Structure #20 intercepts are characterized by a weak foliation consisting of a preferred orientation of feldspar phenocrysts. In some locations, a decrease in average grain size of both phenocrysts and the groundmass is noted; however, unlike in other drill cores, this phenomena is not seen everywhere in the deformation zone intercept. Sealed fracture intensity is consistently higher (estimated P_{10} values of 80–144 fractures/meter) than in the rock mass outside of Structure #20. Minor amounts of very thin (< 1 cm thick) cataclasites are noted in the damage zones. The lower damage zone for Structure #20 in KA2563A is very thin (~ 5 cm), and is marked only by an increase in sealed fracture intensity and the gradual disappearance of the preferred alignment of feldspar phenocrysts.

The primary deformation zone core of Structure #20 in drillhole KA2563A is characterized by a combination of intense ductile and brittle deformation; the host rock has been largely altered to epidote-rich mylonite (with minor amounts of quartz) over approximately 20 cm length. The mylonite bands are subparallel to a large, rough open fracture. Sets of steeply-dipping veins filled with calcite, hematite, adularia, and chlorite crosscut the cataclasite while still showing evidence of shear offset, suggesting at least two phases of brittle deformation. Portions of the deformation zone core are also brecciated, though much of the pore space has been re-cemented by newer epidote and chlorite mineralization.

The deformation zone cores representing the splay faults and fractures are very similar to the primary core; they differ primarily in terms of the lack of open fractures and evidence for less-intense ductile deformation.

TRUE Block Scale borehole KI0025F

Most of the drill core containing the interpreted deformation zone core of Structure #20 in KI0025F is missing; the rock was taken for destructive testing during the TRUE Block Scale series of experiments. The drill core remaining is sufficient to characterize the lower damage zone of the Structure #20 intercept (Figure 4-24).

The remnants of the Structure #20 deformation zone core intercept with KI0025F is presumed to be marked by an open fracture at ~ 88.84 metres borehole depth. In comparison to other drillholes, there are no other features characteristic of the Structure #20 deformation zone core (breccia, fault gouge, mylonite or cataclasite) expressed in the drill core. The interpretation of this intercept as a deformation zone is made solely on the presence of a damage zone surrounding a single, open, transmissive feature. The fracture surface is undulating and exhibits chlorite, pyrite, and minor calcite mineralization. The upper half of the fracture is missing.

The Structure #20 damage zone in KI0025F is characterized by a well-developed bedrock foliation in the host Äspö diorite; the foliation is accompanied by an apparent slight increase in the proportion of mafic minerals in the groundmass. Unlike other drill core samples, there is no evidence of a grain-size change. The damage zone shows an increased frequency of sealed fractures (~ P_{10} of 10 fractures/meter), which is higher than rock outside of Structure #20, but less than in other drill core samples.

Note that the geological features of Structure #20 are very poorly-expressed in the BIPS imagery from KI0025F. In this borehole, the only indication of Structure #20 in BIPS is the presence of one single open fracture and a change in the size of the minerals in the rock groundmass. We hypothesize that this intercept is near the edge of the deformation zone, where it is thinnest.

TRUE Block Scale borehole KI0023B

Most of the drill core containing the interpreted deformation zone core of Structure #20 in KI0023B is missing; the only piece remaining is a 1.5 cm section of epidote-rich cataclasite at a borehole depth of 69.84 m (Figure 4-25); the actual thickness of the deformation zone core in this borehole is highly uncertain. drill coreStructure #20 in drill core KI0023B has been interpreted as consisting of two deformation zone cores: a splay fault at a borehole depth of 68.9 metres, and a master deformation zone core at a borehole depth of approximately 69.84 m (Figure 4-25). The thickness interpretation is based on the presence of damage zone features, including increased sealed fracture intensity, minor epidote cataclasite, and visible foliation.

Overall, the interpreted thickness of Structure #20 in drill core from KI0023B is the second largest. It is possible that the interpreted splay fault at 68.9 m is in fact a minor-deformation zone not genetically related to Structure #20. Given the similar nature of both deformation zone cores (ductile precursor, strong mylonitization, consistent damage zone properties), the authors believe that this possibility is unlikely.

The damage zones surrounding both the deformation zone core and the splay fault in the drill core show minor to moderate amounts of mylonitization, with a mix of epidote, chlorite, and quartz mineralization. No reduction in either groundmass or phenocryst grain size was observed. The damage zone is primarily delineated by a weak visible foliation, consisting of a preferred orientation of feldspar phenocrysts, and an increase in the average frequency of sealed fractures (P_{10} values of 60–140 fractures/meter).

The main deformation zone core of Structure #20 in KI0023B is missing. The core of the splay fault consists of strongly mylonitized hybrid rock, sandwiched between Äspö diorite and a thin lens of reddish fine-grained granite. The mylonite bands are mostly epidote-rich with thicknesses of 2–3 mm. The deformation zone core ends at a vuggy fracture filled with calcite, adularia, and chlorite.

TRUE Block Scale borehole KI0025F03

The interpreted thickness of Structure #20 in drill core in KI0025F03 is significantly smaller than in all other investigated drill cores observed; the total zone thickness is only ~ 0.21 m long. Part of this is due to the fact that most of the deformation zone core of Structure #20 is missing; it has been removed (presumably) for destructive testing during the TRUE Block Scale project. The remaining pieces of deformation zone core material show a mix of parallel mylonite and cataclastic bands of up to 3 mm thickness.

Damage zones are found on both the upper and lower of the Structure #20 intercept (Figure 4-26). The damage zones are characterized by a reduction in grain size of both feldspar phenocrysts and the diorite groundmass, an increase in the relative proportion of mafic minerals, and a moderate foliation (exhibited as rotation and stretching of feldspar phenocrysts). The ‘upper’ damage zone is characterized by a sealed fracture network (29 fractures within a 0.1 m interval) oriented subparallel to the rock foliation. The lower damage zone also hosts cataclasite lenses of up to 15 mm thickness, with the percentage of epidote-dominated cataclasite decreasing with increasing distance from the deformation zone core.

Pilot borehole KI0010B01

In KI0010B01 (Figure 4-27), Structure #20 is interpreted as a complex structure, with the deformation zone core represented by both a secondary splay fault and a master core of a deformation zone, separated by an approximately 20 cm thick damage zone between them. In addition, both the upper portion of the splay and the ‘lower’ portion of the master deformation zone core also possess damage zones. In this drill core, the Structure #20 consists of a double-fault, similar to borehole KI0025F02

in the TRUE Block. The host rock is Äspö diorite. The start of the 'upper' damage zone, which is the rock volume shallower than the secondary splay fault, is marked by an increase in the intensity of sealed fractures, an increase in the proportion of dark minerals in the host rock groundmass (possible recrystallization?), the development of a faint foliation characterized by preferential orientation of feldspar phenocrysts, and a reduction in phenocryst size. The secondary splay fault in KI0010B01 consists of a single open fracture, which is surrounded by a diffuse network of epidote veins that eventually merge into the open fracture. This network of epidote veins serves as a "marker bed" for Structure #20, especially in the TASS tunnel mapping (Chapter 5). The authors have interpreted this feature as being part of Structure #20; there is evidence for similar complex geometries in TRUE Block Scale drillhole KI0025F02 (Andersson et al. 2002a).

The splay fault and the deformation zone core of Structure #20 are separated by an additional damage zone, which is not seen in other cores. It was decided not to include this section of damaged rock as part of one large deformation zone core, which would have extended from the splay fault at 75.12 m to the start of the main core of the deformation zone at 75.34 m (cf. Figure 4-27). The rock in between these two structures, which consisted of a poorly-defined bedrock foliation and a clustered network of calcite- and/or quartz-filled fractures, is very similar to the damage zones seen around other Structure #20 intercepts. Sealed fracture intensity within the central damage zone is approximately 12–18 fractures per cm, corresponding to a P_{10} value of 120–180 1/m. Sections of drill core with sealed fracture intensities this high are normally mapped as "sealed fracture networks" in Sicada; the relevant query (*p_fract_sealed_nw*) does not exist in Sicada for any of the TRUE Block Scale boreholes except KA2563A; however, the variable returns no records (empty) in KA2563A.

The deformation zone core of Structure #20 in pilot borehole KI0010B01 consists of an approximately three cm thick zone containing three open fractures within a mylonitized groundmass. The open fractures have an estimated aperture of 0.25–0.75 mm. There are no visible kinematic indicators on the fracture surfaces. There appear to be at least two generations of fractures within the zone core. There is a sealed calcite-filled fracture that terminates at a steep angle at one of the open fractures in the deformation zone core. There are also numerous sealed fractures that appear to strike subparallel to the open fractures that offset or displace the mylonite bands within the zone core.

The extent of the 'lower' damage zone is much more ambiguous; the end of Structure #20 has been defined as the point where the visible foliation ends and the grain size of the quartz in the groundmass and the feldspar phenocrysts increases.

Pilot borehole KI0014B01

In KI0014B01 (Figure 4-28), Structure #20 presents a much less complicated geology than in either the TRUE Block Scale boreholes or in the other TASS pilot boreholes, The intercept consists of three subparallel steeply-dipping open fractures within an approximately 15 cm zone of mylonite. There appears to be less mylonite visible than in the other TASS pilot boreholes; it is possible (though impossible to prove) that this borehole is nearing the distal edge of brittle deformation for Structure #20. The network of sealed epidote veins that serves as a marker bed in other boreholes is not present in KI0014B10. The lower damage zone in KI0014B01 is marked by a gradual increase in the quartz and feldspar grain size and the decrease in the intensity of sealed fractures; the well-developed foliation is completely absent in therock in the 'lower' damage zone.

The core of Structure #20 in KI0014B01 is marked by a very well-developed foliation, leading to a schistose-like texture in the groundmass. The foliation eventually gives way to a well-developed epidote-rich mylonite. The sealed fracture intensity is very high (P_{10} of ~ 200–240 fractures/m) near the centre of the zone core, and a vuggy dissolution texture developed within epidote-rich mylonite bands.

There are at least two generations of brittle fractures within the zone core; an (interpreted) older set filled primarily with epidote and trending sub-parallel to the foliation, and a second younger set dipping at an approximately 70° angle to the first set. This second set of fractures is partially to mostly-filled with calcite, chlorite, and adularia. Open fractures in the zone core strike approximately northwest-southeast (130/81 in the Äspö96 system), and feature apertures ranging from 0.25 mm up to 3.5 mm, depending on where the aperture is measured. The mean fracture aperture is in the neighbourhood of 0.5 mm to 0.75 mm. Mineral lineations in the direction of the bedrock foliation are observed on two of the open fracture surfaces, though no slickensides are present.

Pilot borehole KI0016B01

In KI0016B01 (Figure 4-29), Structure #20 appears as a re-activated brittle-ductile shear zone that is localized against the contact between Äspö diorite and a fine-grained granite; technically, the entire intercept could be mapped as "hybrid rock". The start of the 'upper' damage zone in KI0016B01 is only approximately located, and is based on the presence of an increasing number of sealed fractures, the introduction of a visible foliation to the rock mass (subparallel alignment and elongation of feldspar phenocrysts), the start of a slight whole-rock alteration ("red staining"), and the beginning of a reduction in the grain size of the feldspar phenocrysts.

As in the other TASS pilot boreholes and several of the TRUE Block Scale boreholes, the core of Structure #20 in KI0016B01 is flanked by a network of persistent sealed epidote veins. These epidote veins serve as a sort of 'marker bed' for Structure #20 (cf. description for KI0010B01 above). The genetic relationship between this sealed network and Structure #20 is not known; the epidote fillings suggest that sealing occurred before brittle deformation along Structure #20 took place, and their persistence from the TRUE Block Scale borehole array into the area of the TASS tunnel suggests that they are genetically related to the ductile precursor in Structure #20.

The core of the Structure #20 intercept in KI0016B01 is marked by the development of a strong ductile fabric, leading to a schistose texture and a reduction in the average grain size of both the groundmass and the feldspar phenocrysts. The deformation zone core is also marked by the presence of cataclasite and a small amount of brecciated rock. The entire deformation zone core appears strongly sheared, with a visible schistose-like texture, segregation of the rock fabric into light-and dark mineral bands, and, in places, the development of a vuggy texture. The mineral banding appears to represent varying concentrations of epidote, quartz, and chlorite secondary mineralization.

Unlike the rest of the pilot boreholes, the zone core in KI0016B01 shows two generations of slickensides along the central water-bearing fracture. One set trends subparallel to the rock fabric, suggesting it represents the earliest phase of brittle deformation. The second set of slickensides is oriented at an approximately 23° angle in the clockwise direction to the first set in the plane of the fracture, suggesting a second phase of brittle deformation in response to different stress directions.

The lower damage zone around Structure #20 in KI0016B01 ends several centimetres inside the fine-grained granite; the termination is approximately mapped as the end of the network of very small calcite/quartz filled sealed fractures, as well as the presence of several cm-size chunks of fine-grained granite which have clearly been broken off the master dike.

Overall, Structure #20 in KI0016B01 is characterized principally by the rock fabrics and very high sealed fracture intensity (from 50–170 fractures/m). The entire intercept in KI0016B01 is mapped as lying inside a sealed fracture network, according to data in Sicada. Three open fractures with visible and measurable aperture were noted; open fracture apertures were in the range of 0.25 mm to 1.25 mm, depending on where along the fracture planes the aperture was measured.

The interpreted thicknesses of Structure #20 intercepts in the TASS pilot borehole and TRUE Block Scale borehole cores is summarized below in Table 4-8.

4.4.2 BIPS image interpretation of Structure #20 intercepts

The reinterpretation of borehole image logs was intended to be a complement to the detailed core analysis presented in the Section 4.4.1. The same methodologies and key structures were identified; this is important to allow for comparison of sections of the borehole where the drill core has been lost or removed for testing. Extensive image analysis was performed during the development of the TRUE Block hydrostructural modelling (Hermanson 2001a, b, Hermanson and Doe 2000, Andersson et al. 2002a). The BIPS re-interpretation introduces knowledge about deformation zone structure gained from the site descriptive modelling efforts at Forsmark and Laxemar; in particular, consideration of the increased thicknesses of damaged and altered rock surrounding the core of the deformation zone.

Table 4-8. Interpreted thicknesses of Structure #20 and its components as obtained from the review of drill cores.

Idcode	Zone start adjusted Secup (m)	Zone end adjusted Seclow (m)	Number of zone cores	Total thickness (m)	Damage zone thickness (m)	Zone core thickness (m)
KA2511A	Most of core missing		1	n/a	n/a	0.09
KA2563A	188.2	190.14	3	1.94	1.63	0.31
KI0023B	68.9	70.2	2	1.31	1.15	0.16
KI0025F	88.6	89.0	1	0.41	Missing	Missing
KI0025F02	No core reinterpretation			n/a	n/a	n/a
KI0025F03	DZ core incomplete*		1	> 0.21	0.16	> 0.5
KI0010B01	75.1	75.5	2	0.48	0.35	0.13
KI0014B01	72.0	72.4	1	0.39	0.25	0.14
KI0016B01	72.3	73.0	1	0.74	0.53	0.21

* Only 5 cm of deformation zone core is present; the rest was removed for destructive testing. Total deformation zone core thickness in drill core is unknown. Therefore, only minimum thickness values are given in the table.

BIPS image interpretation has both advantages and disadvantages when compared with the examination of drill core. The BIPS image is relatively straightforward to examine, and much easier to identify and reference to exact depths in the hole, and it is easier to get more accurate lengths of the zone core and damage zones. However, the limited resolution of the BIPS camera combined with dirty borehole walls make identifying small-scale structure (cataclasite, mylonite, and small open fractures) very difficult. A detailed structural analysis was really only possible in one image (KI0025F03). It is also difficult to resolve the changes in grain sizes and the weak foliation that characterizes the damage zones observed in drill core. Finally, the zone footprint (in terms of elevation or adjusted measured length) do not line up with the depths marked along the drill core. It is here assumed that the BIPS image results are the more accurate of the two data sources with respect to location of the Structure #20 intercepts along the borehole.

The results of the BIPS image re-mapping are presented in a graphical format in Figure 4-30 through Figure 4-38. The measured thicknesses of the zone core and damage zone are presented in Table 4-9. Overall, the BIPS remapping results are very similar to the drill core evaluations presented in Section 4.4.1. In comparison with the thicknesses of Structure #20 reported in the final TRUE Block hydrostructural model (Andersson et al. 2002a), the BIPS re-mapping produces slightly thicker zone core and damage zones.

Table 4-9. Interpreted thicknesses of Structure #20 intercept from review of BIPS images.

Borehole	ADJ_ SECUP (m)	ADJ_ SECLOW (m)	Number of DZ cores	Total thickness (m)	Damage zone thickness (m)	Core thickness (m)
KA2511A	121.99	122.10	1	0.12	0.05	0.07
KA2511A_Interp2	121.29	123.27	1	1.98	1.91	0.07
KA2563A	188.65	189.32	2	0.67	0.40	0.27
KI0025F	87.41	87.91	1	0.50	0.48	0.02
KI0023B	69.73	70.03	1	0.30	0.19	0.11
KI0025F02	74.64	75.58	2	0.94	0.59	0.35
KI0025F03	73.00	73.35	1	0.35	0.19	0.15
KI0010B01	74.60	75.52	1	0.92	0.68	0.25
KI0014B01	72.10	72.57	1	0.47	0.33	0.14
KI0016B01	70.35	71.10	1	0.75	0.57	0.18
Mean (all boreholes)			9	0.70	0.44	0.26
Standard Deviation (all boreholes)			9	0.53	0.54	0.22
95% confidence interval			9	0.32/1.07	0.05/0.83	0.10/0.42

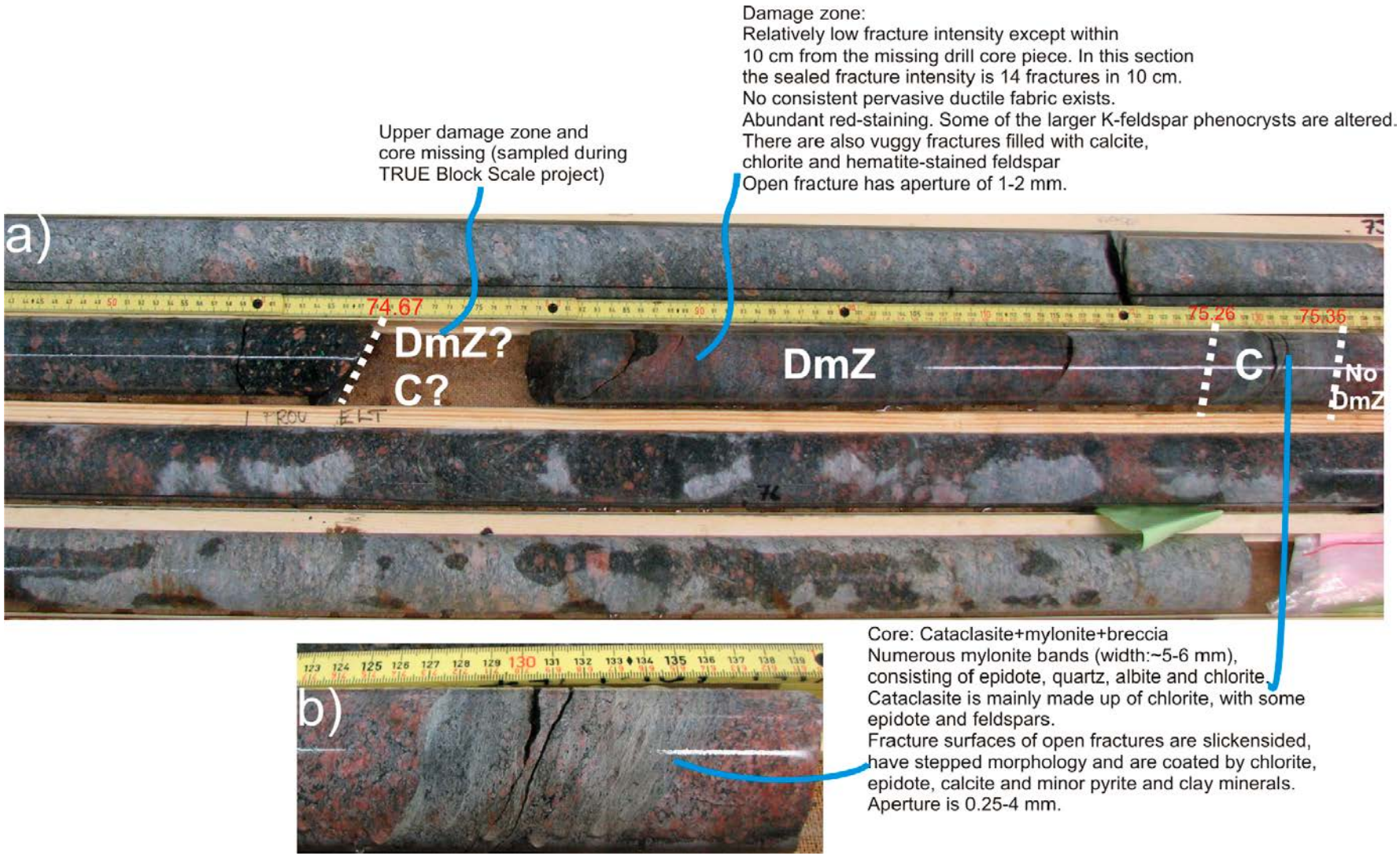

Figure 4-22. *Description of Structure #20 intercept with TRUE Block Scale borehole KA2511A.*

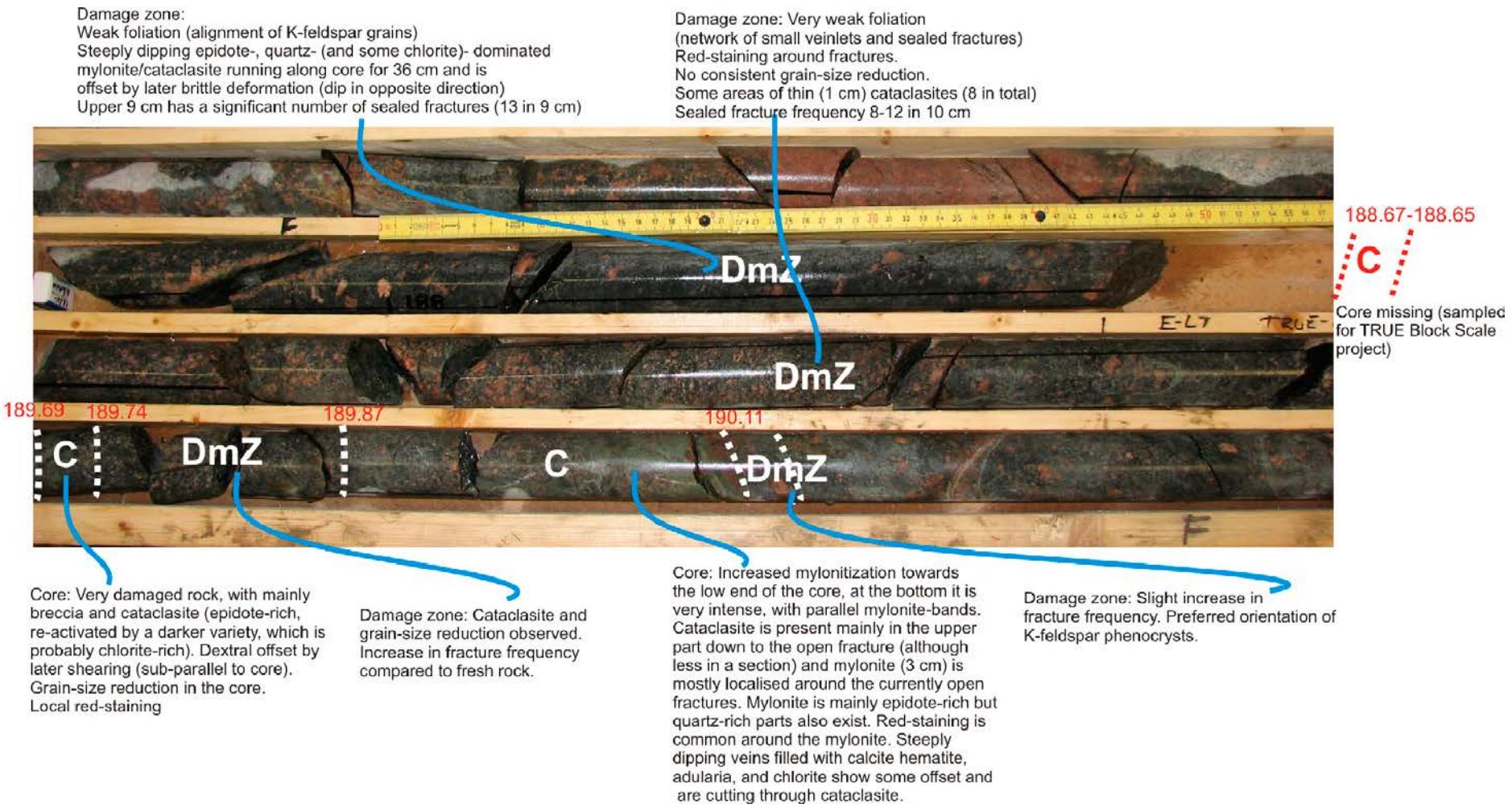

Figure 4-23. *Description of Structure #20 intercept with TRUE Block Scale borehole KA2563A.*

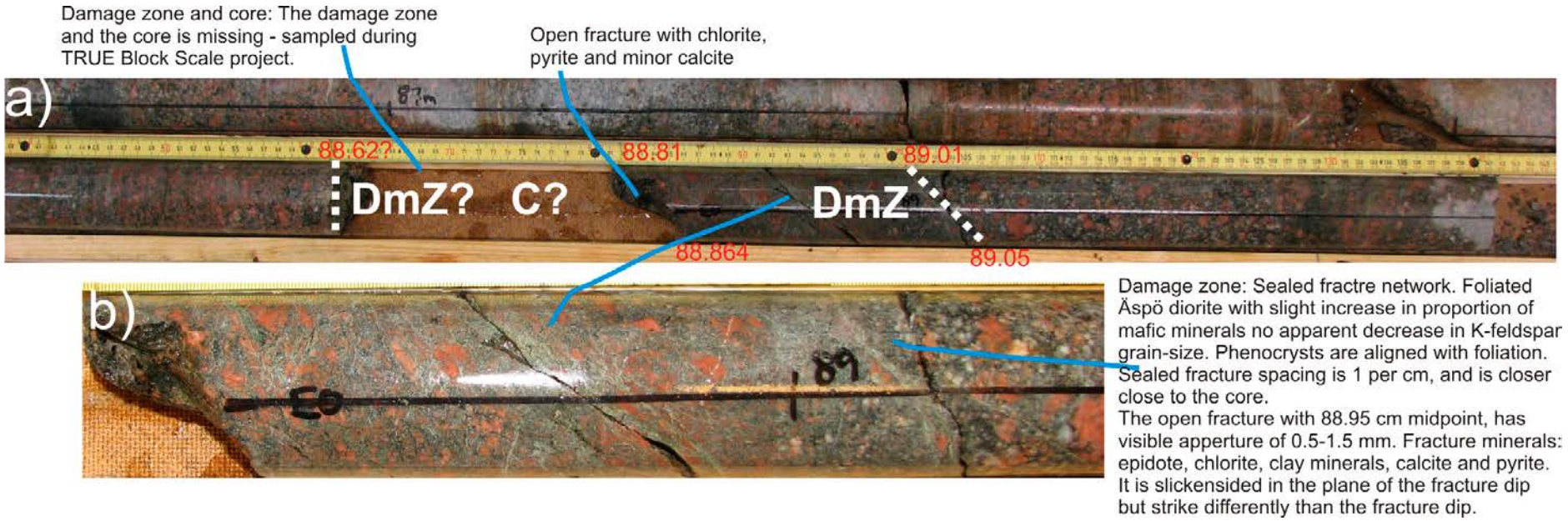

Figure 4-24. *Description of Structure #20 intercept with TRUE Block Scale borehole KI0025F.*

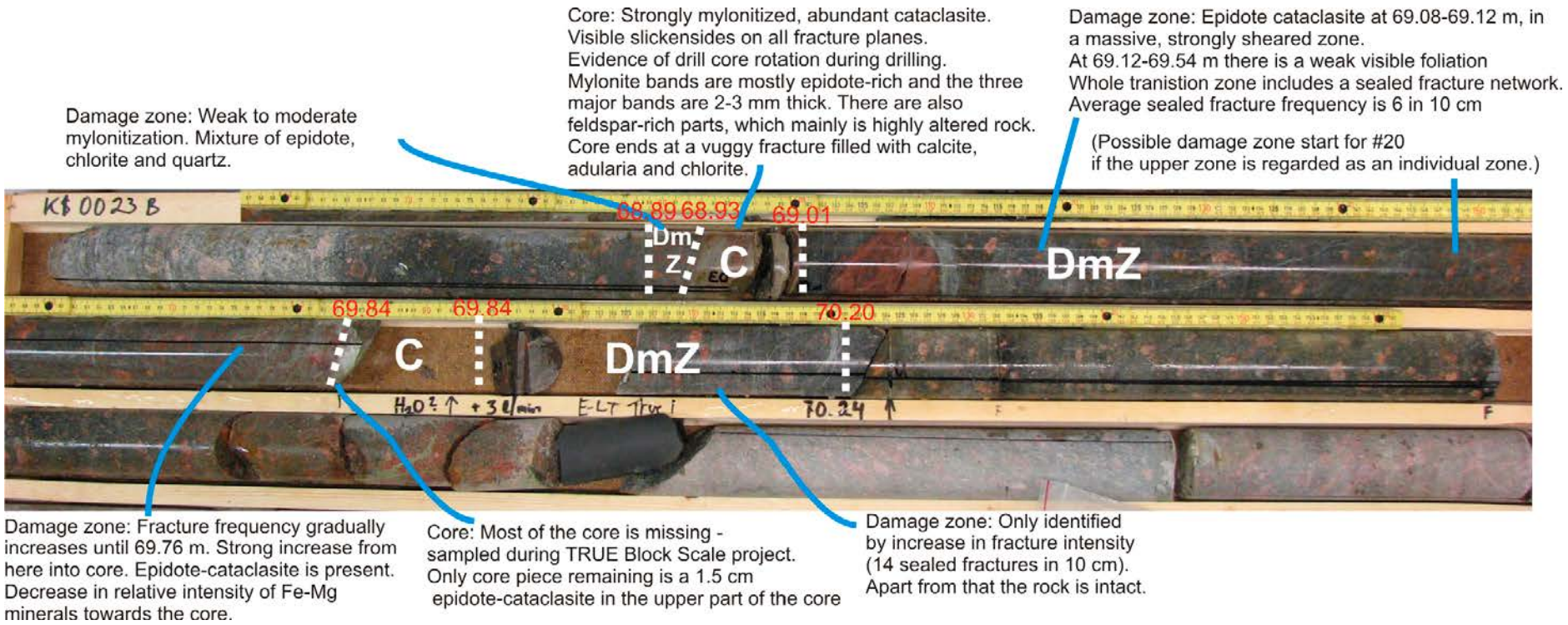

Figure 4-25. *Description of Structure #20 intercept with TRUE Block Scale borehole KI0023B.*

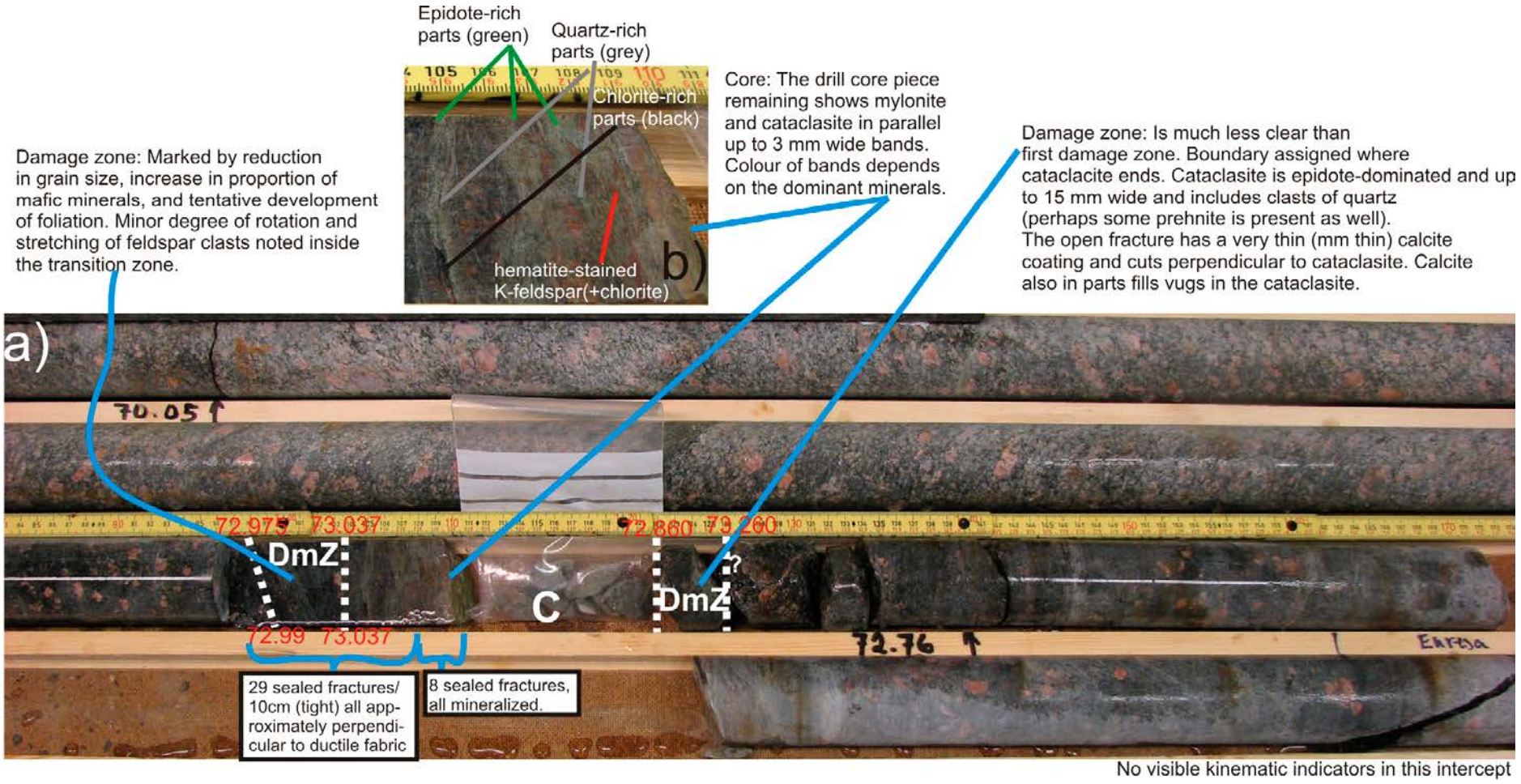

Figure 4-26. *Description of Structure #20 intercept with TRUE Block Scale borehole KI0025F03.*

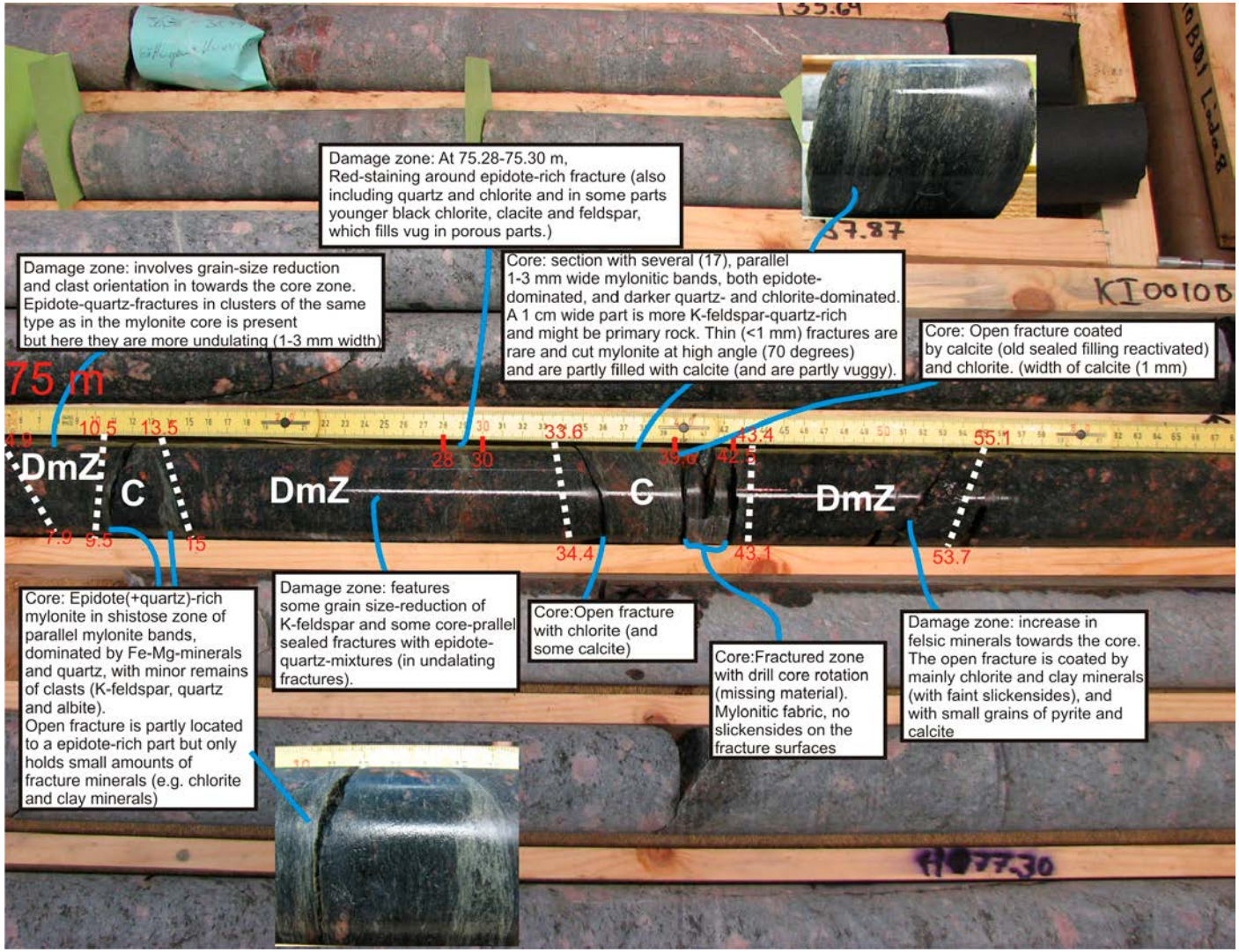

Figure 4-27. *Description of Structure #20 intercept with TASS pilot borehole KI0010B01.*

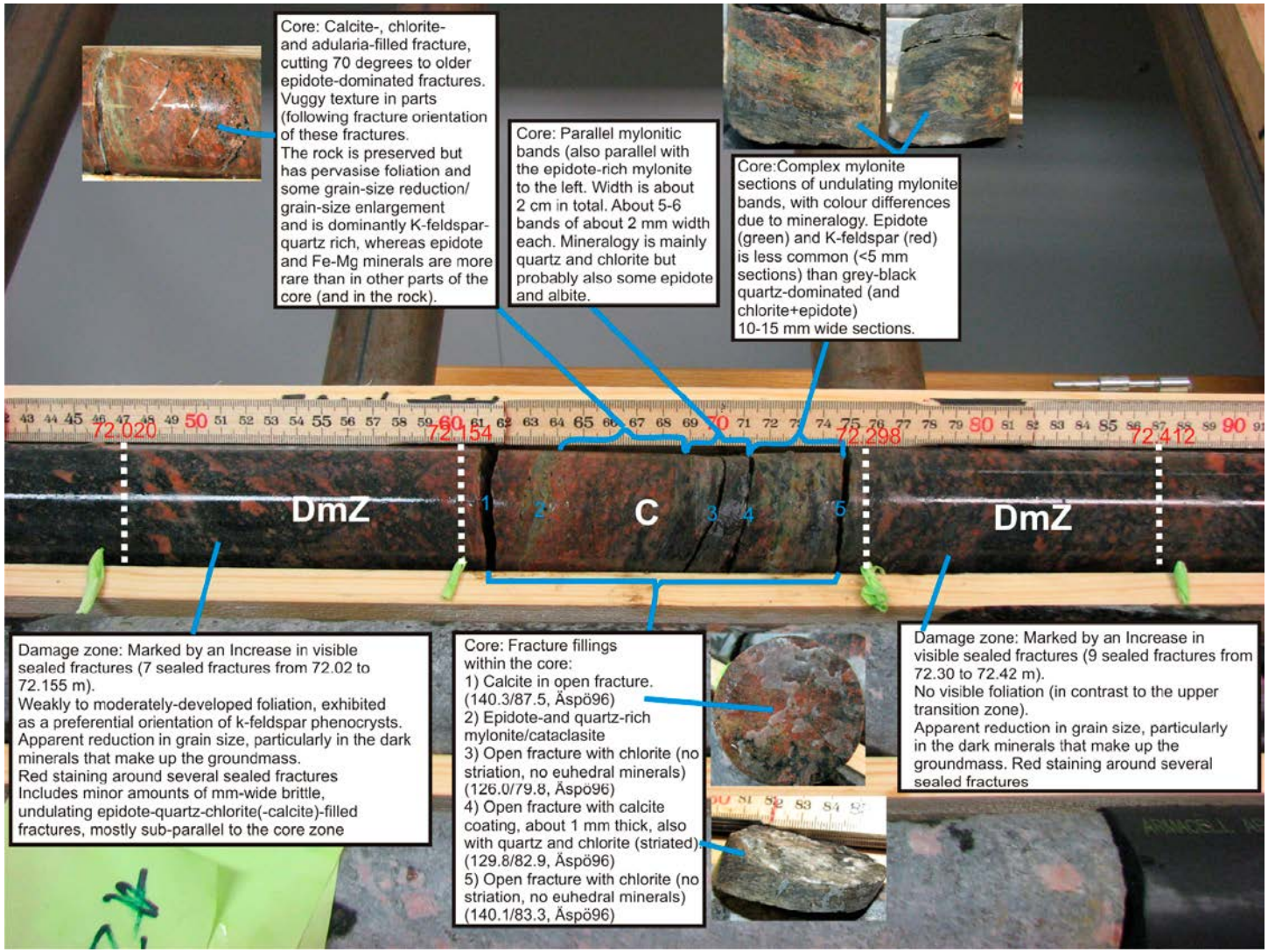

Figure 4-28. *Description of Structure #20 intercept with TASS pilot borehole KI0014B01.*

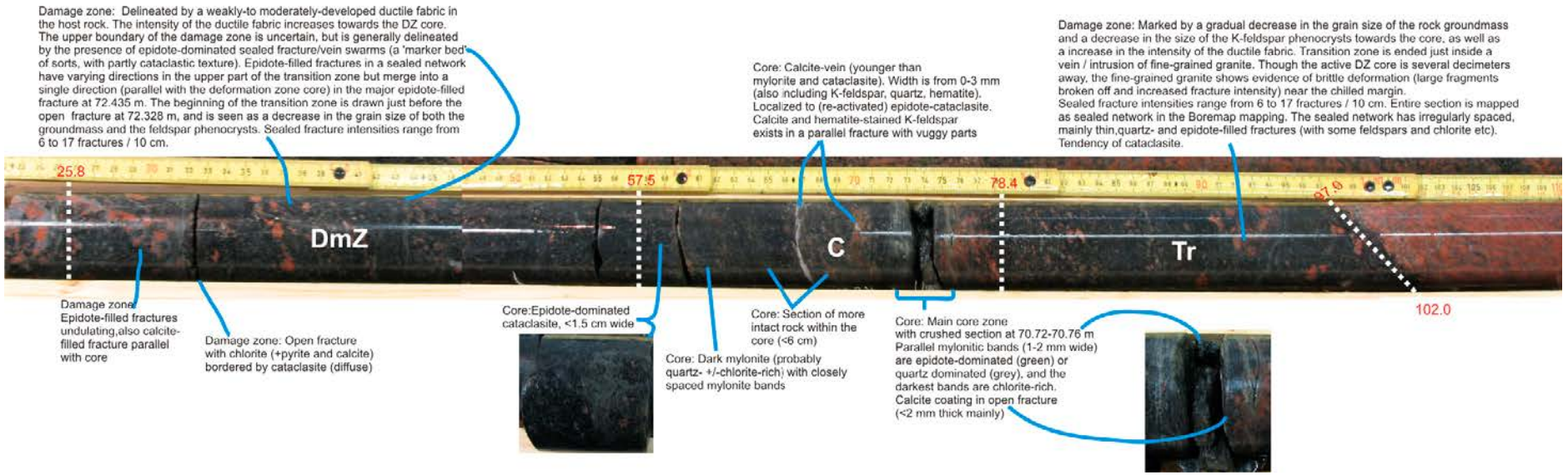

Figure 4-29. *Description of Structure #20 intercept with TASS pilot borehole KI0016B01.*

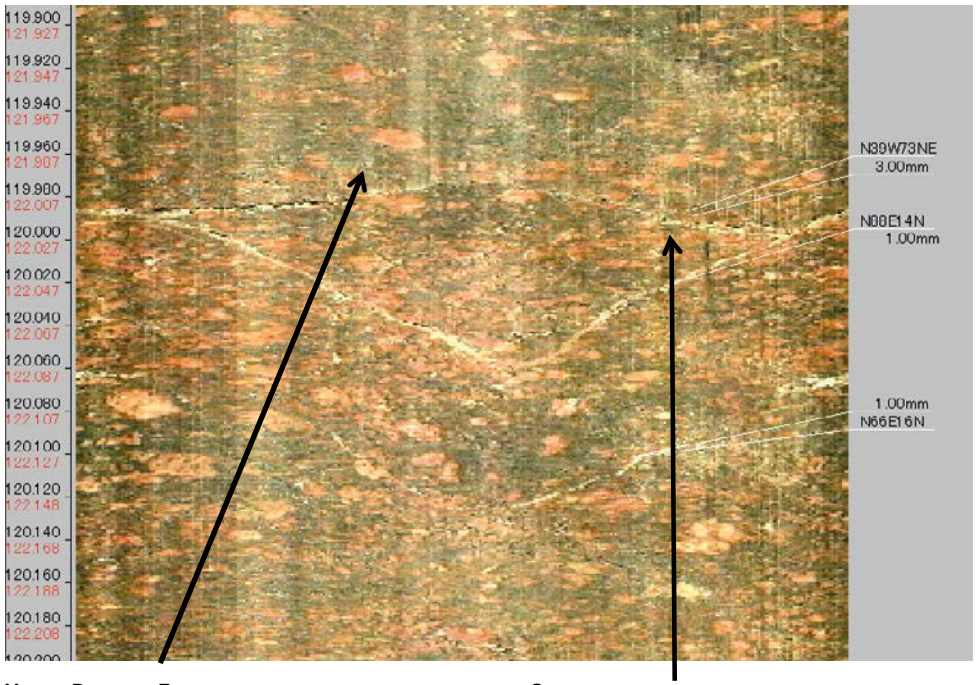

Upper Damage Zone

No well-defined upper TZ in this intercept; transition zone defined by increase in red staining around open fracture.
MD(Adjusted): 121.987–122.004 m

Lower Damage Zone

No real significant thickness; tentative identification made based on slight increase in grain size and a decrease in the intensity of pervasive bedrock alteration ('red staining').
MD(Adjusted): 122.07–122.102 m

Core

Two open to partially-mineralized fractures. No visible cataclasite or mylonite, though host rock shows development of foliation (preferred orientations of feldspar phenocrysts. Mineral infilling looks to be mix of calcite and possibly epidote, or prehnite?
MD (Adjusted): 122.004–122.07 m

K2511A Interpretation 1
Total Zone Thickness: 0.115 m

Figure 4-30. *BIPS image re-interpretation for borehole KA2511A, interpretation 1.*

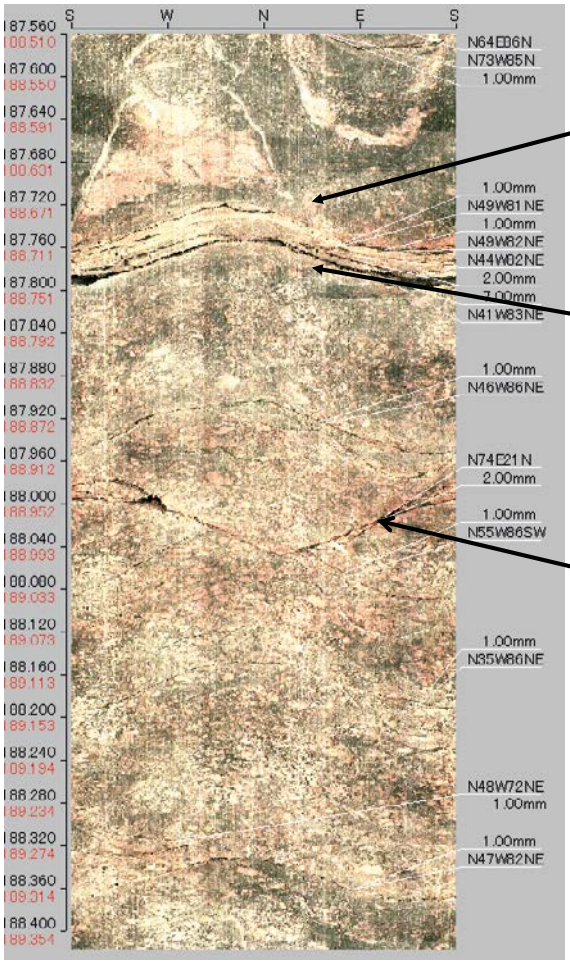

KA2563A
Total Zone Thickness: 0.67 m

Upper Damage Zone
Very thin upper damage zone, marked by decrease in grain size, host rock alteration, and start of mylonitization. It is possible that the open fracture at ~ 188.450 m is part of this zone; very similar orientations.
MD (Adjusted): 188.651–188.671 m

Core1
Brecciated zone with visible fault gouge between 2-3 open fractures. Fractures appear to follow mylonitic fabric. Core is fairly tight and distinct.
MD (Adjusted): 188.671–188.762 m

Core2 (Splay)
Network of 3 open fractures interpreted to represents play from master Structure 20 fault. Two of three fractures have strike/dip nearly identical to those in Core1. Visible aperture and 'open' (plucked) holes.
MD (Adjusted): 188.862–189.043 m

Lower Damage Zone
Marked by increased intensity of sealed fractured, altered wall rock, decrease in grain size of host rock and development of ductile fabric (foliation). Lower boundary set at open fracture, beneath which rock texture becomes less weathered and coarser-grained.
MD (Adjusted): 189.043–189.32 m

Figure 4-31. *BIPS image re-interpretation for borehole KA2563A.*

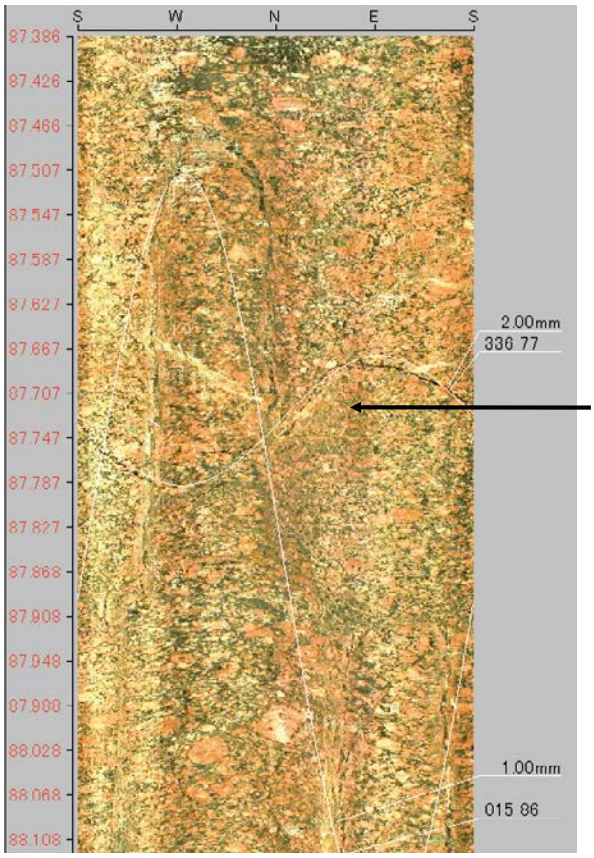

KI0025F
Total Zone Thickness: 0.502 m

Upper Damage Zone
Defined by the start of intense red staining within the rock mass and the development of a very weak bedrock foliation. The foliation is visible in terms of preferential orientation of k-spar phenocrysts. No visible grain size reduction, and no increase in fracture intensity observed.
ADJ_SECUP (m): 87.406–87.717 m

Core
DZ core marked by single open (2 mm aperture) fracture. No visible cataclasite, gouge, or breccia, and only a slight intensification of the ductile fabric. It is possible that this intercept represents the edge of the DZ, where it has exited older ductile structures and propagated out into relatively massive host rock. Very different DZ characteristics than other sections. Arbitrary 2 cm thickness applied around fracture as "core".
ADJ_SECUP (m): 87.717–87.737

Lower Damage Zone
Marked by red staining, weak ductile fabric, and a small decrease in the size of k-spar phenocrysts. End of DZ (lower damage zone end) is defined by the MD at which the ductile fabric dies out.
ADJ_SECUP (m): 87.737–87.908

Figure 4-32. *BIPS image re-interpretation for borehole KI0025F. Structure #20 is not well-visualized in this image log; the drill core (Figure 4-24) provides a much better view of the ductile structures surrounding the deformation zone core.*

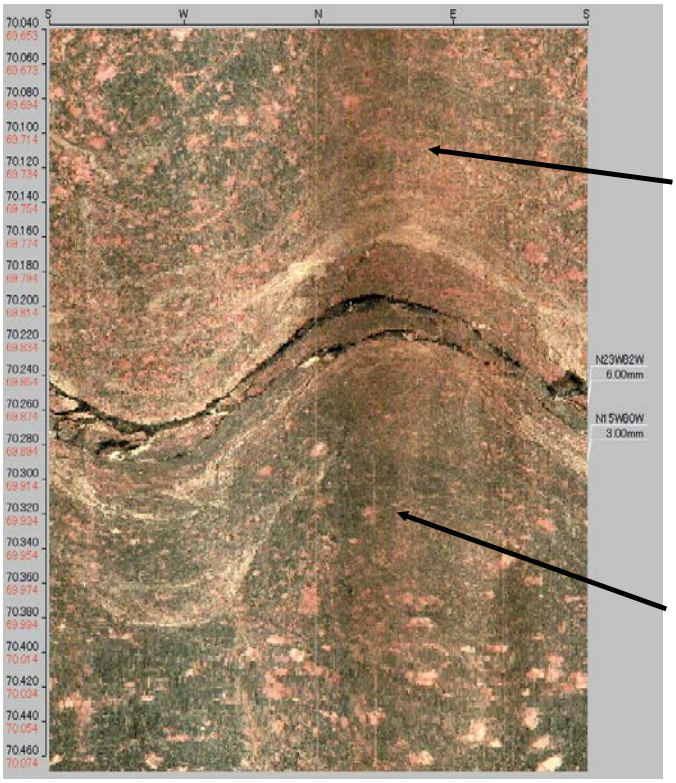

KI0023B

Total Zone Thickness: 0.3 m

Upper Damage Zone

Start of DZ marked by apparent decrease in grain size, start of a visible foliation/ductile fabric, grading into very thin layers of mylonite. Looks to be increased degree of host rock alteration, but VERY difficult to see from BIPS images.
MD (Adjusted): 69.734–69.804 m

Core

Marked by open fractures with significant aperture, partial brecciation, and minor amounts of fault gouge. No visible cataclasite in the BIPS images, though.
MD (Adjusted): 69.804–69.91

Lower Damage Zone

End of DZ marked by increase in grain size, decrease in degree of alteration of host rock, decrease in frequency of sealed fractures and veins (epidote-filled?).
MD (Adjusted): 69.91–70.034 m

Figure 4-33. *BIPS image re-interpretation for borehole KI0023B.*

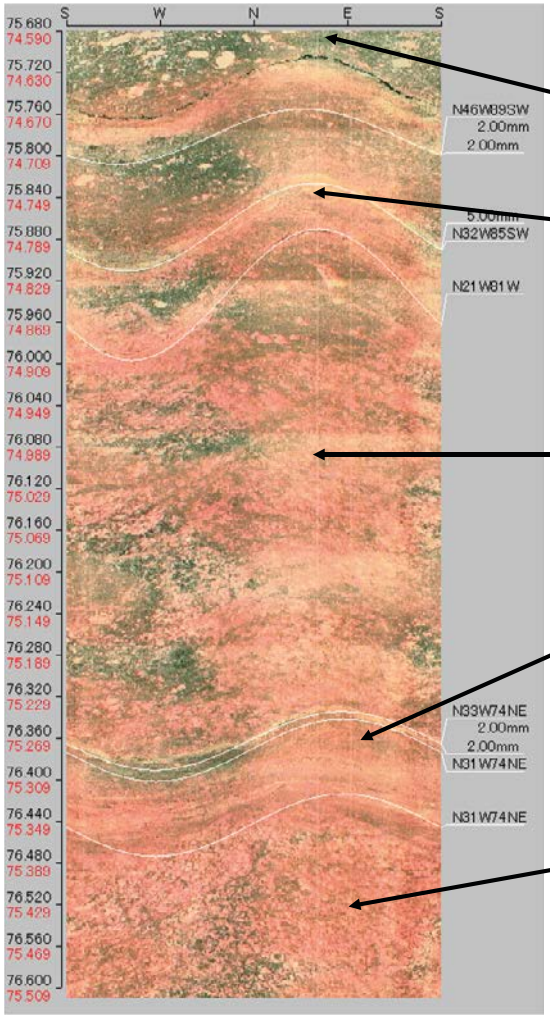

KI0025F02

Total Zone Thickness: 0.94 m

Upper Damage Zone

Marked by faint red staining on top of open fracture.
MD (Adjusted): 74.64 –74.66 m

Core1 (Structure 20 has two splays in KI0025F02)

Open fracture (chlorite + Illite), cataclasite, mylonite with significant host rock grain size reduction. This is interpreted as the main intercept of Structure 20.
MD (Adjusted): 74.66–74.92

Middle Damage Zone

Altered rock, reduced grain size, visible foliation with minor mylonitization. Difficult to see on BIPS images, but there may be some brecciationin the core in this interval.
MD (Adjusted): 74.92–75.269 m

Core2

Strongly mylonitized and altered host rock. Zone boundary appears marked by either sealed fracture or cataclasite (difficult to see in image). This is interpreted as a splay of Structure 20.
MD (Adjusted): 75.269–75.359 m

Lower Damage Zone

End of damage zone marked by increase in host rock grain size, reduction in intensity of ductile fabric, reduction in red staining (alteration).
MD (Adjusted): 75.359 –75.58m

Figure 4-34. *BIPS image re-interpretation for borehole KI0025F02.*

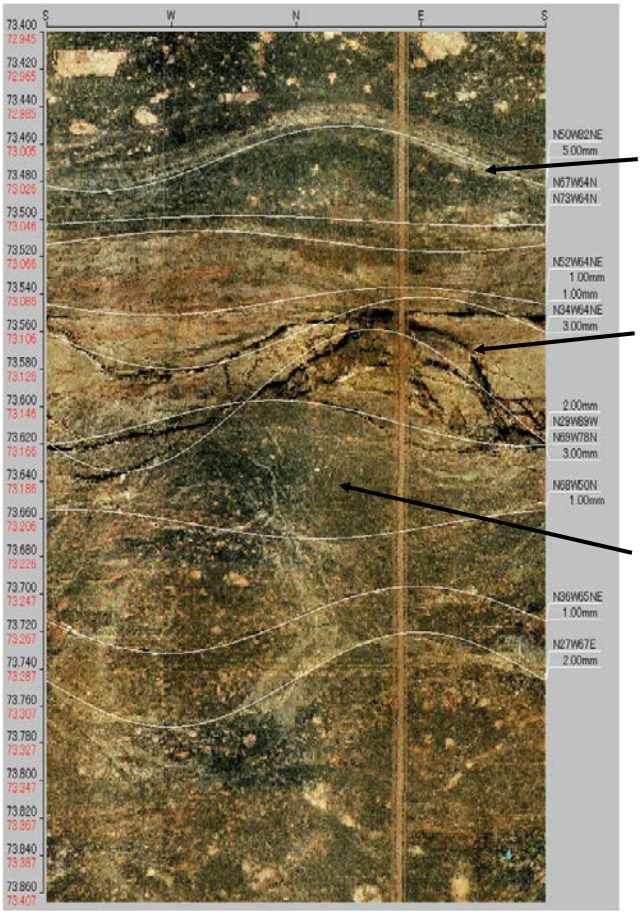

KI0025F03

Total Zone Thickness: 0.345 m

Upper Damage Zone

Marked by reduction in grain size of host rock, development of a ductile fabric, minor mylonitization, faint degree of alteration.
MD (Adjusted): 73.0025 -73.0425 m

Core

Marked by significant open fracturing, partial brecciation, thick layers of mylonitizedrock. TR-02-13 suggests presence of fault gouge of 2 mm–5 mm thickness; not visible on BIPS images. Bottom of DZ core difficult to identify in BIPS, so assigned to sealed fracture NOT mapped in BDT file.
MD (Adjusted): 73.0425–73.196 m

Lower Damage Zone

Lower damage difficult to identify. 15-20 cm of altered rock beneath the core. Faint mylonitization and weak ductile fabric. Appears to be numerous hydrothermal veins (epidote?). Lower boundary indistinct with no real grain size contrast; boundary pinned on sealed fracture.
MD (Adjusted): 73.196–73.347 m

Figure 4-35. *BIPS image re-interpretation for borehole KI0025F03.*

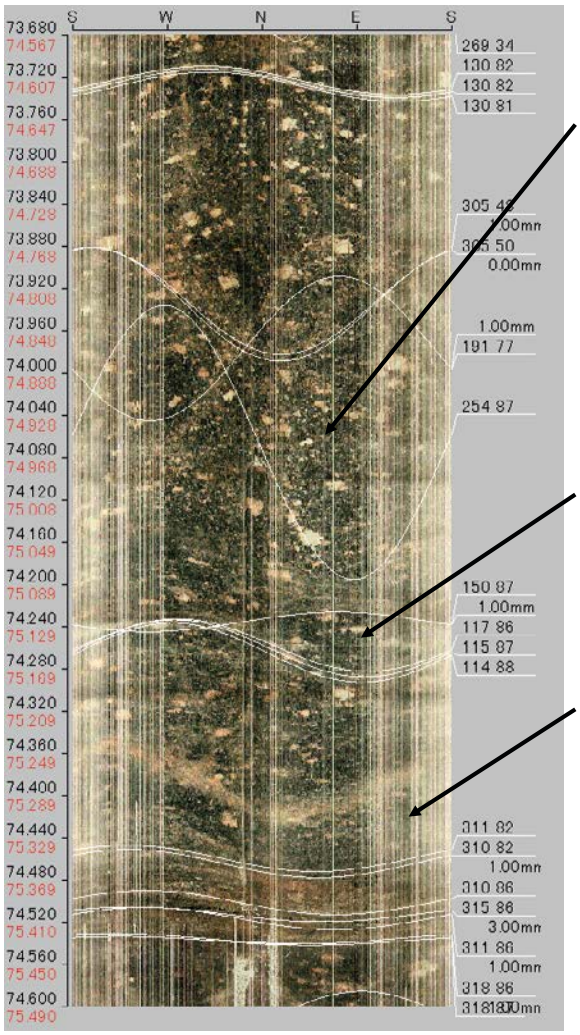

KI0010B01

Total Zone Thickness: 0.677 m

Upper Damage Zone

The upper damage zone is defined by the occurrence of three closely-spaced epidote-filled fractures. This is based largely on relationships seen in the TASS tunnel mapping. As one proceeds through the damage, an increase in the intensity of a pervasive bedrock foliation is noted, a gradual decrease in the grain size of both the groundmass and the feldspar phenocrysts, and a minor degree of alteration (as red staining).
ADJ_SECUP (m): 74.597–75.049 m

Core1

DZ core is marked by dramatic increase in intensity of ductile fabric, the presence of moderate amounts of cataclasite, and the presence of three closely-spaced partly-open epidote/chlorite filled fractures. Feldspar phenocrysts show evidence of flattening and rotation parallel to foliation.
ADJ_SECUP (m): 75.049–75.189 m

Core2

DZ core is marked by another increase in the intensity of the bedrock foliation, even finer-grained host rock groundmass, moderate amounts of cataclasite, and three open fractures with apertures in the 1–3 mm range. Intense red staining around open fractures. This is likely the master slip plane for #20.
ADJ_SECUP (m): 75.319–75.425 m

Lower Damage Zone

Marked by red staining, weak ductile fabric, and a small decrease in the size of k-spar phenocrysts. End of DZ (lower TZ end) is defined by the MD at which the ductile fabric dies out. Also marked by changes in fracture orientations. Very abrupt transition.
ADJ_SECUP (m): 75.425–75.52

Figure 4-36. *BIPS image re-interpretation for TASS pilot borehole KI0010B01.*

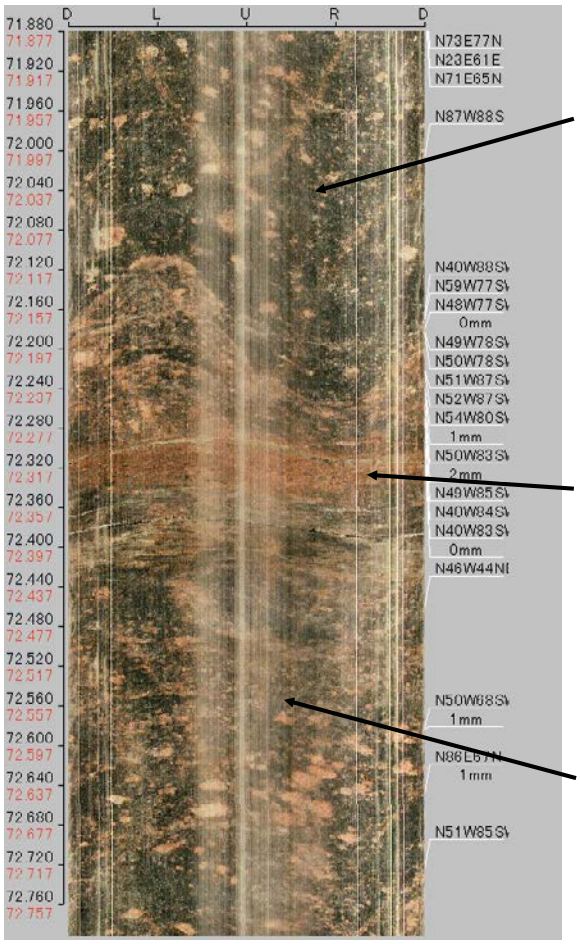

KI0014B01

Total Zone Thickness: 0.47 m

Upper Damage Zone

The onset of the Structure #20 damage zone is indicated by a change in the grain size of the host rock (decrease in feldspar phenocryst size along with a corresponding decrease in the visible groundmass size) along with a weak bedrock foliation. This is very visible in core, but difficult to see in BIPS images. Near the bottom of the damage zone a number of very steeply-dipping NW-striking sealed fractures are present; however, the fracture intensity increase does not appear to extend into the DZ core.
ADJ_SECUP (m): 72.1–72.279 m

Core

The start of the Structure 20 DZ core is marked by an epidote-filled sealed fracture, visible reddish staining, and the development of a strong bedrock foliation with a series of parallel mylonite bands. Just below this sealed fracture appears to be a partially-open fracture within a zone of intense mylonitization, but it is difficult to fit a full sinusoid to the contact. There also appears to be the development of small zones of cataclastic texture, but it is difficult to resolve cataclasite versus mylonite in this image. One visibly open fracture with significant aperture and a mix of epidote and quartz infilling. A second open fracture occurs just outside the most intense band of mylonitization.
ADJ_SECUP (m): 72.279–72.417 m

Lower Damage Zone

The end of the core is just below the last major visible partly-open fracture, and is just outside the zone of mylonitization. The lower damage zone is marked by a gradual decrease in the intensity of the ductile fabric, accompanied by a gradual increase in the groundmass grain size.
ADJ_SECUP(m): 72.417–72.57 m

Figure 4-37. *BIPS image re-interpretation for TASS pilot borehole KI0014B01.*

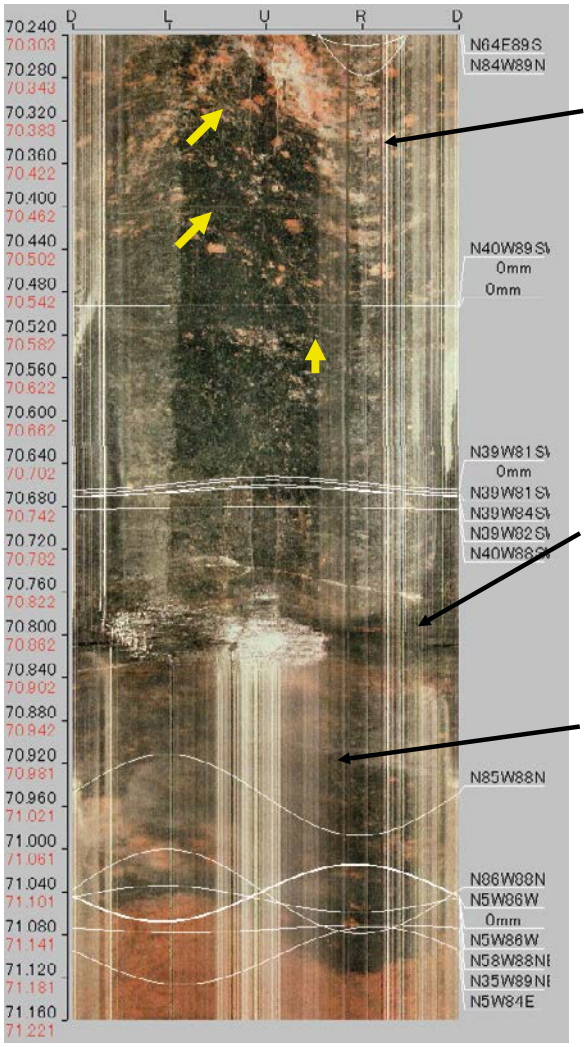

KI0016B01

Total Zone Thickness: 0.747 m

Upper Damage Zone

The onset of the Structure #20 damage zone is not quite as clear in this BIPS image as in other holes due to image smearing and the presence of quartz-rich coarse-grained inclusions of host rock. As in several other wells, an increase in the intensity of epidote-filled fractures (clearly olive green color in the BIPS images, note yellow arrows in image), accompanied by a decrease in both phenocryst and groundmass grain size. Overall, there is a increase in sealed fracturing as one moves from the edge of the zone to the DZ core. Strangely enough, many visible open and sealed fractures are NOT recorded in the BIPS data file.
ADJ_SECUP (m): 70.354–70.732 m

Core

In the BIPS imagery, most of the Structure #20 core is obscured by smearing on the camera mirrors, possibly due to the influx of water and Silica Sol grout. The start of the core is interpreted as occurring just after a large calcite-filled fractures, and is characterized by a well-developed rock foliation and a ductile fabric consisting of bands of cataclastic material, grading towards mylonite as one approaches the center of the DZ core. Only one large open visible open fracture is visible in BIPS.
ADJ_SECUP (m): 70.732–70.912 m

Lower Damage Zone

The lower damage zone is extremely difficult to see in BIPS due to smearing and poor image quality, but appears to be marked by decreasing amounts of cataclasite, a few partially-visible sealed fractures, and a continued reduced grain size and lack of large feldspar phenocrysts. The DZ appears to terminate at or within the fine-grained granite dyke visible from 71.101 m to 73.7 m. We have interpreted the end of the zone at the start of the fine-grained granite, but it is possible that the damage zone extends inside the dyke.
ADJ_SECUP (m): 70.912–71.101 m

Figure 4-38. *BIPS image re-interpretation for TASS pilot borehole KI0016B01.*

The image log for one borehole (KI0025F03) was of high-enough quality to attempt quantification of the microstructure of the core of the Structure #20 intercept. During the TRUE Block Scale project, significant importance was placed on understanding the relative proportions of fault rock (clayey fault gouge, cataclasite, breccia, and altered rock) due to its potential profound influence on tracer transport. TRUE Block Scale borehole KI0025F03 combined both a very high quality BIPS image with a relatively complicated and thick Structure #20 intercept; this enabled estimation of the relative abundance of each type of fault rock within the intercept.

A high-resolution screen capture was made of the entire length of the Structure #20 core and damage zones. The image was loaded into the GNU Image Manipulation Program (Win-GIMP), where the image colour levels, brightness, and sharpness were enhanced using a variety of built-in filters. Next, the type of rock represented was classified on a pixel-by-pixel basis, and assigned a certain colour (Figure 4-39). Automatic attempts to identify structural edges or volumes through image transforms (Laplace, Sobel, and Hough) were unsuccessful, largely due to the lack of contrast between pixels in the BIPS image. The results of the image analysis suggest that both fault gouge (yellow) and open fracture area (black) were a relatively small (4% and 7%, respectively) fraction of the total deformation zone area. It was not possible to easily distinguish between mylonite and cataclasite inside the core of the deformation zone; the classification is made primarily based on the relative light colours of the quartz and epidote-rich layers, which in drill core appear to be characteristic of the cataclastic texture within Structure #20 intercepts. Approximately 54% of the total deformation zone area can be classified as either open-fracture or fault rock perimeter.

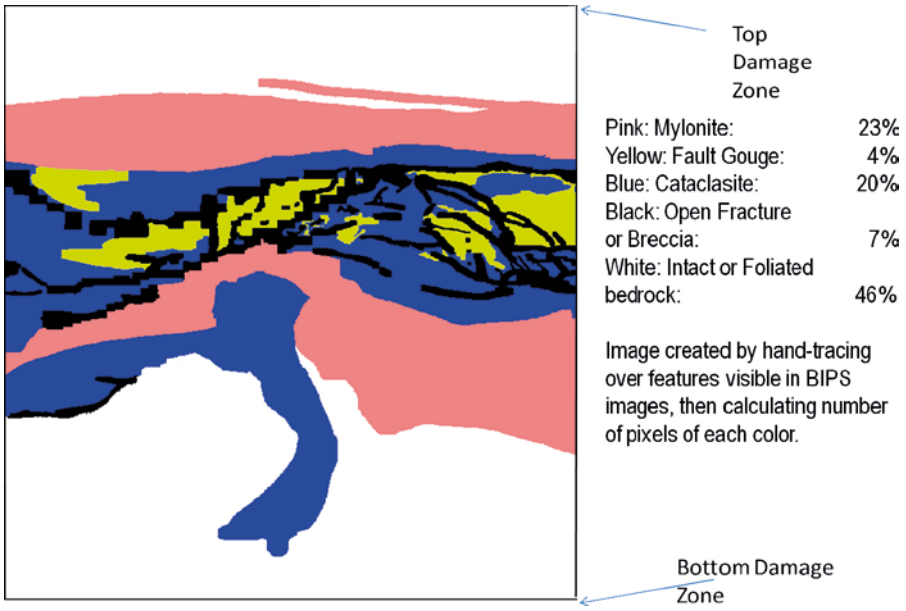

Figure 4-39. *Relative abundance of fault rock types within Structure #20. This example is taken from TRUE Block Scale borehole KI0025F03.*

4.4.3 Summary of Structure #20 characteristics in borehole data

While the relative abundance of certain features (amount of fault gouge, presence of open fractures and breccia) varies significantly along strike, as seen in cored holes and TASS pilot boreholes, the geological character of Structure #20 is fairly well-understood. It represents a deformation zone that resulted from multiple events of reactivation of a ductile precursor in the brittle regime.

The total measured thickness of Structure #20 (Figure 4-40) is highly variable, with significant differences between drill core and BIPS image logs, even in the same borehole. Although the geological characteristics of the intercepts remain very similar, total zone thickness (core + damage zone) ranges from a little more than 2 decimetres to almost 2 metres (KA2511A alternative model in BIPS). This suggests that a conservative approach should be used to assign zone thicknesses during detailed site investigations, given the potential effects on seismic and buffer stability cases that zones in the Structure #20 size range may have in safety assessments. Structure #20 damage zone thicknesses are generally 0.2–0.4 m thicker than previously mapped. This is most likely due to the evolution of the definition of "damage zone" that occurred during site descriptive modelling efforts at Forsmark and Laxemar.

However, the limits and mean thickness (Figure 4-41 and Table 4-10) of the zone core of Structure #20 are fairly well-constrained, with little overall change compared with the descriptions assigned during the TRUE Block Scale project. The highly deformed core of Structure #20 is 0.2 to 0.3 m in thickness, with much of the associated rock volume occupied by mylonite and cataclasite. The correlation between zone core thickness and zone damage zone thickness is analyzed in Figure 4-42. The shown trend line regression illustrates quantitatively what the graph illustrates qualitatively; there is no relationship between the thickness of the zone core and the damage zone thickness for Structure #20, at least not within the area covered by the TRUE Block Scale and the TASS borehole arrays.

Table 4-10. Descriptive statistics of the distribution of deformation zone core thicknesses (m) for Structure #20 based on BIPS image log, drill core inspection and tunnel mapping.

Data source	Zone core thickness (m) Mean	Median	Std. dev.	Max	Min
TASS tunnel mapping	0.17	0.15	0.06	0.27	0.09
BIPS remapping	0.26	0.21	0.22	0.68	0.02
Core remapping	0.17	0.15	0.08	0.31	0.09

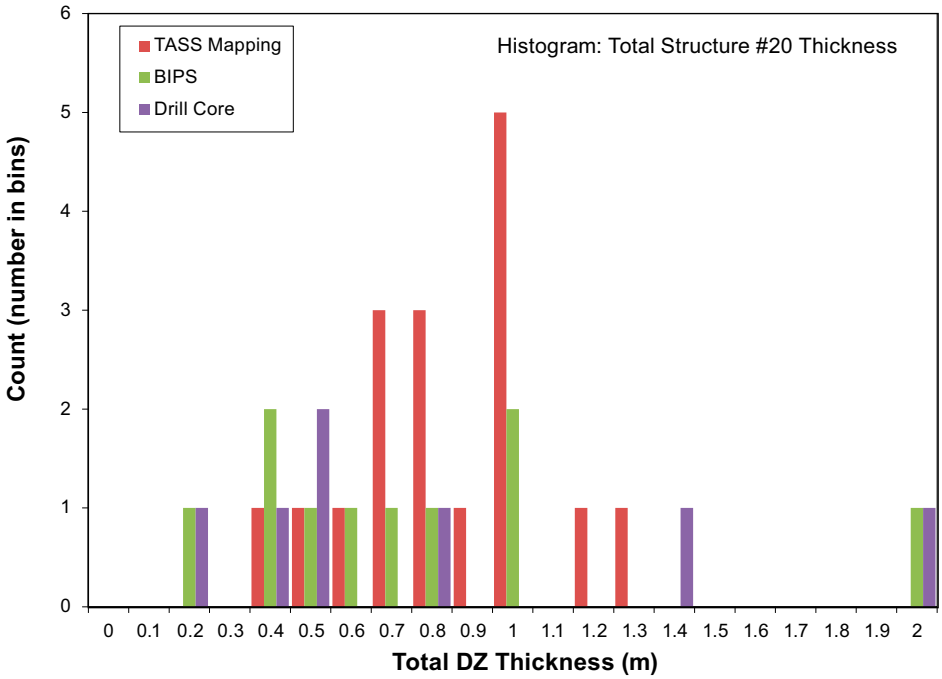

Figure 4-40. *Measured total thickness of Structure #20 as a function of sampling type. This figure illustrates the difficulty in measuring the true thickness of a deformation zone, even with access to a large-diameter underground opening (TASS mapping).*

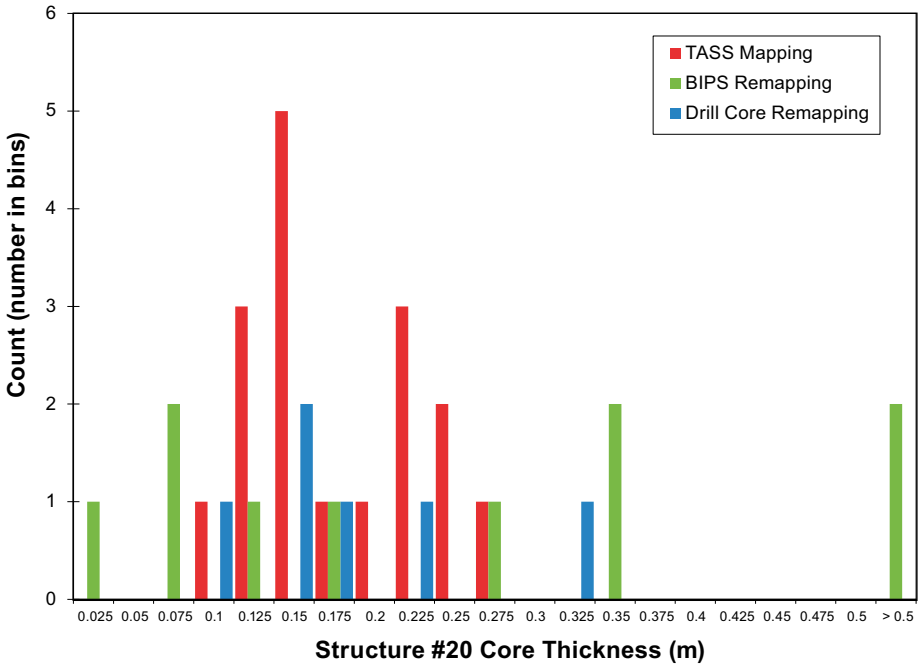

Figure 4-41. *Measured thickness of the zone core of Structure #20 as a function of sampling type. The identification of the zone core has much less spread (most values are from 0.1 m to 0.3 m) than the total zone thickness.*

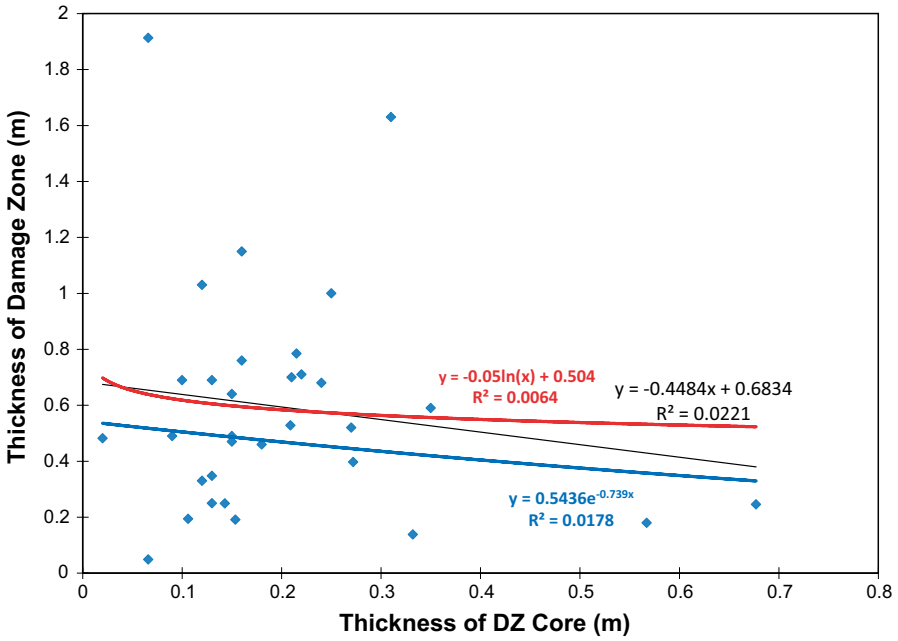

Figure 4-42. *Scatterplot of zone core thickness versus damage zone thickness with correlation functions (exponential, logarithmic, and linear) fit to the data. Notice that the correlation coefficient (R^2) is poor for all fits.*

Structure #20 damage zone characteristics

In general, in both drill core and BIPS images, the damage (transition) zone around Structure #20 is associated with the following characteristics:

- Decrease in average grain size of groundmass of Äspö diorite;
- Decrease in the average size of feldspar phenocrysts within Äspö diorite. In many cases, the phenocrysts serve as strain indicators, with evidence of foliation/ductile fabric parallel stretching;
- Significant increase in the visible sealed fracture intensity (P_{10} values of greater than 200 fractures per metre) beginning in the damage zone and extending up to and occasionally including the zone core. Many of these fractures are difficult, if not impossible, to see in BIPS images, such that their presence could only be noticed by a detailed examination of the drill core. This was frequently missed in the TRUE Block Scale boreholes, but was well-accounted for in Boremap results for the TASS pilot bores (Sicada query *p_fract_sealed_nw*); and
- In several boreholes, a sealed network/swarm of epidote-filled fractures serves as a marker bed for Structure #20. It is hypothesized that they represent a vein network emplaced in the same stress field as the ductile precursor for Structure #20.

The deformation zone core of Structure #20, as seen in drill core and BIPS image logs, is characterized by:

- An intense mix of cataclasite and mylonite, with a significant reduction in host rock grain size;
- Several (2–3) open fractures with apertures in the 0.5 to 2.0 mm range. Though not visible in the BIPS images or in drill core, this structure still produces water in the TASS tunnel even after grouting;
- An irregular development of a vuggy dissolution texture within epidote-rich cataclastic layers and along epidote-filled fracture planes;
- A relative lack of clay-rich fault gouge. In BIPS images, it is difficult to visually separate clay-rich fault gouge from cataclasite, since they exhibit very similar colours. For TRUE Block Scale drill cores, many of the Structure #20 core intercepts with clay gouge have been removed for destructive testing. In the TASS pilot bores, there is relatively little clay gouge observed. Whether this is due to relatively high temperatures during deformation events or high historical water flows is unknown;
- Two sets of sealed to partly-open fractures, representing at least two periods of brittle deformation.

One consistent feature of Structure #20 is the relationship between brittle deformation, pre-existing ductile fabrics, and the occurrence of dikes of fine-grained granite. This relationship is discussed in more detail in the description of mapping in the TASS tunnel (Section 5.3) but is also visible in pilot borehole KI0016B01. Both brittle and ductile deformation have been localized along the boundary between the Äspö diorite and the fine-grained granite in KI0016B01, resulting in a 'thinner' but more geologically complex intercept. However, at the same time, the fine-grained granite dike exhibits signs of deflection, suggesting that its propogation path was altered by ductile shearing during its emplacement or early cooling history. Even though the total thickness of Structure #20 becomes thinner at this interface, most of the significant post-grout inflow to the TASS tunnel occurs at this contact.

It is recognized that grain size reduction is a common characteristic of the Structure #20 intercept, though it is difficult to see in BIPS images (Section 4.4.2). The reduction in grain size of the feldspar phenocrysts suggests one of several evolutionary options for Structure #20:

- Ductile shearing was initiated during initial emplacement and cooling, suggesting that these features are extremely old; or
- Grain-size reduction by strain energy drive grain-boundary migration (ρGBM), which tends to occur at high rock stresses but at relatively low temperatures (Platt and Behr 2011); or
- Grain-size reduction through a combination of cataclasis and dynamic recrystallization (Handy et al. 2007).

Whatever the likely process is, zones of brittle deformation within re-activated ductile deformation zones in rocks similar to those encountered at Äspö, changes in both rock texture and grain size are important potential indicators to be looked for during core logging and/or image interpretation.

A limited number of potential kinematic indicators were visible in the drill cores. These included slickensides along fractured mylonitic features in the core of Structure #20 and mineral lineations within the rock mass, being subparallel to the rock fabric ("foliation"). A formal kinematic study was outside of the scope of this project; however, some indications of the sense of shear along Structure #20 can be seen in the mineralogical analysis of thin-section samples as described in Section 4.5.

4.5 Mineralogy/fracture mineralogy in cored boreholes

4.5.1 Description of fracture mineralogy in samples from the TASS pilot boreholes

For the cored boreholes, the thin sections are not oriented and consequently sense of shear is apparent (in contrast to the thin sections from the tunnel samples), but facilitates a thorough description of zone deformation and shear sense elements (important for comparison with tunnel samples).

Drill core sample KI0010B01: 75.35–75.42 m

From this sample one thin section and two fracture surface samples were analysed (Figure 4-43). Detailed images of these samples are shown in Figure 4-47 through Figure 4-50.

Thin section

General feature: Mylonite exists in the core of the deformation zone; this very fine-grained mylonite consists of numerous parallel shear bands. The main kinematic indicator suggests sinistral motion, shown by C-S fabric with more epidote-rich S-bands in the quartz-rich matrix and by σ-type porphyroblasts/mantled porphyroclasts of K-feldspar and quartz, also with stair-stepping. C-S fabric is a micro-fabric developed in shear zones: S surfaces are generally defined by a planar fabric caused by the alignment of micas or platy minerals, C surfaces are formed parallel to the shear zone boundary: the orientation of the S surfaces in relation to the C surfaces indicates the shear sense [the C-S fabric]). The mylonite is totally dominated by epidote and quartz. Minor minerals are muscovite, biotite, plagioclase, K-feldspar, pyrite, magnetite, titanite. Especially quartz and feldspar show signs of dynamic re-crystallisation, such as sub-grain formation and sub-grain rotation re-crystallisation.

Figure 4-43. *Top: Photograph showing the sample KI0010B01: 75.35–75.42 m. Bottom left: Scanned thin section, with crossed polars. Bottom right: Photographs of the fracture surface samples from KI0010B01 (1, left; 2, right).*

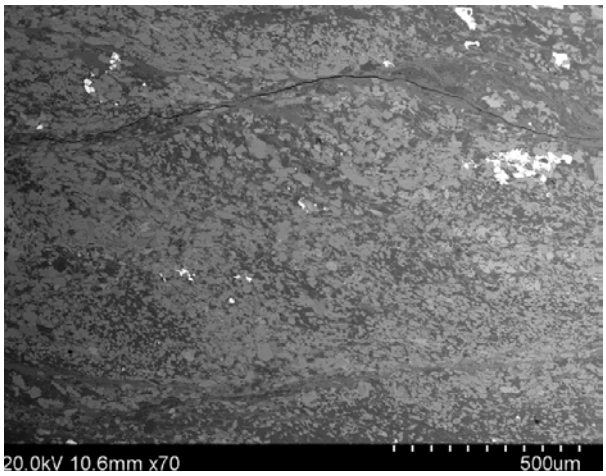

Figure 4-44. *Back-scattered SEM image of epidote-rich part of mylonite. Sample KI0010B01: 75.35–75.42 m.*

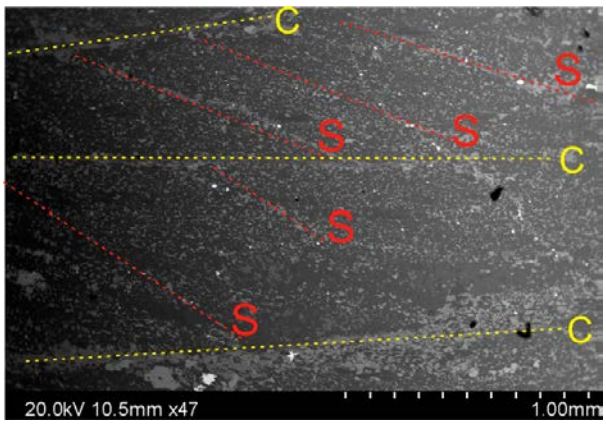

Figure 4-45. *Back-scattered SEM image of C-S mylonite fabric (defined by epidote-rich bands in a fine-grained matrix dominated by quartz), and oblique foliation indicating apparent sinistral shear sense. Sample KI0010B01: 75.35–75.42 m.*

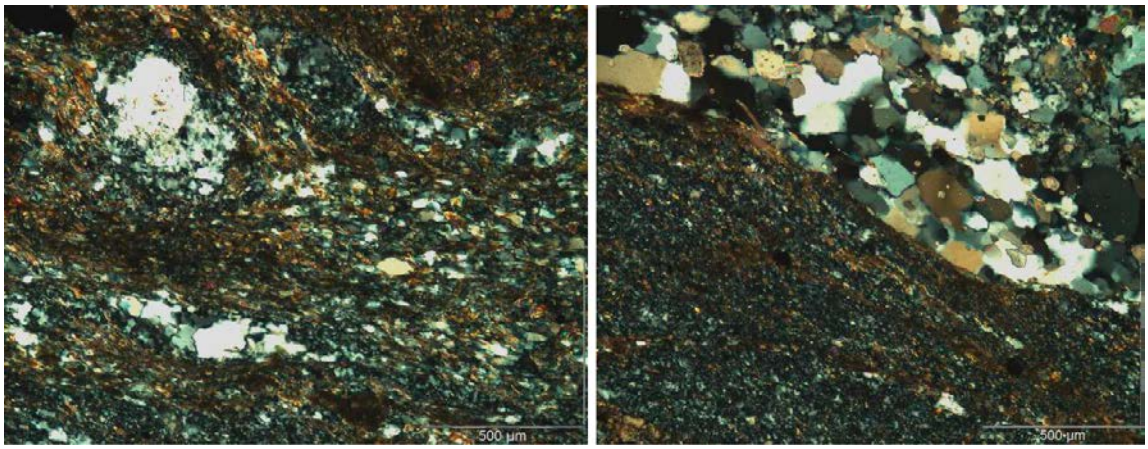

Figure 4-46. *Left: Photomicrograph of σ-type porphyroblasts, with related stair-stepping indicating apparent sinistral shear. Right: Photomicrograph of re-crystallised (dynamic) quartz in mylonite (top, with scattered secondary calcite crystals) and very fine-grained mylonite (bottom), dominated by quartz, epidote and K-feldspar. Sample KI0010B01: 75.35–75.42 m.*

Fracture surface sample #1

Minerals on fracture surface: Calcite, fluorite, chlorite, quartz, pyrite, (Fe-oxides)

Calcite is present in one part as a layer, which is a remnant of a sealed fracture filling, also including abundant cubic fluorite. Chlorite/clay minerals cover the outermost part of this layer. The clay mineral content is indicated by Ca and K contents in the EDS-analyses (indicating e.g. in-mixed smectite [e.g. saponite which holds Ca], or corrensite which holds both Ca and K). When calcite is the uppermost surface, it shows highly dissolved texture. Pyrite and quartz are also observed (as well as some Fe-oxides). The layer underneath the calcite-fluorite-layer is mainly dominated by chlorite (possibly including clay minerals), and shows striations and abundant pyrite crystals.

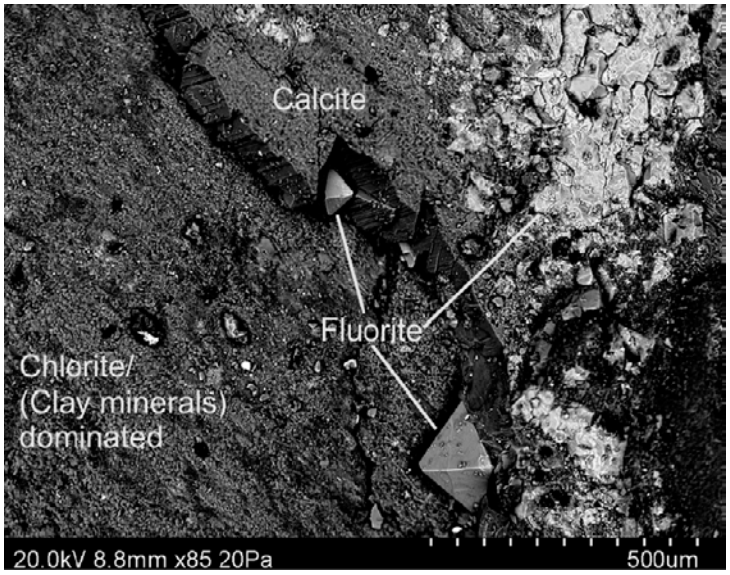

Figure 4-47. *Back-scattered SEM-image of chlorite/clay minerals covered by a younger calcite-fluorite coating. Sample KI0010B01: 75.35–75.42 m.*

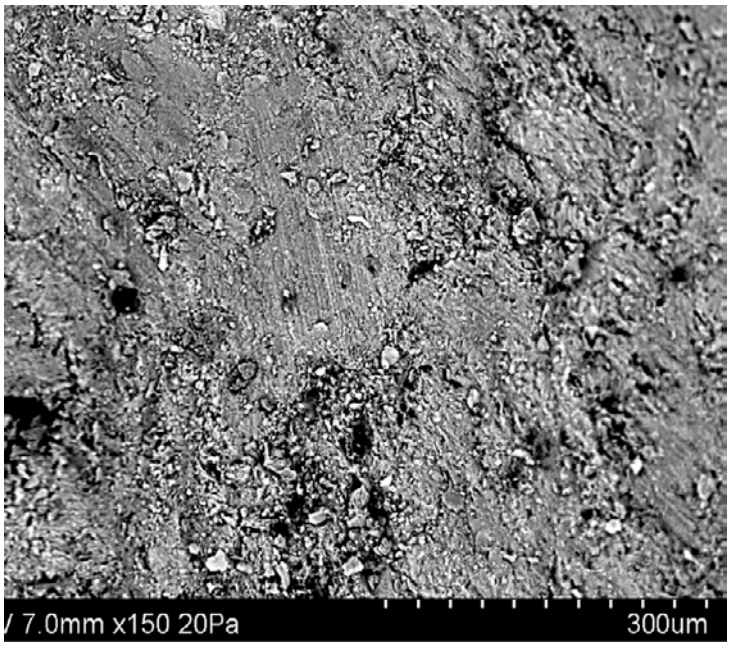

Figure 4-48. *Back-scattered SEM-image of striated chlorite/clay minerals on the fracture surface. Sample KI0010B01: 75.35–75.42 m.*

Fracture surface sample #2

Minerals on fracture surface: Chlorite, clay minerals, fluorite, epidote, pyrite and apatite.

Mostly smooth surface, which is green-coloured and chlorite-dominated. Clay minerals are probably also present in-mixed with chlorite, based on the Na-, K-, and Ca-contents in the EDS-analyses (indicating e.g. in-mixed smectite [e.g. saponite which holds Ca], or corrensite which holds both Ca and K). Both Mg-rich and more Fe-rich varieties exist. Some parts are more rough with visible individual clay mineral crystals, e.g. of corrensite, in gauge with wall rock fragments (of e.g. biotite). Epidote is present in clusters in some minor parts of the coating, along with occasional apatite. In the very smooth chlorite/clay mineral dominated parts, cubic fluorite is present on top of chlorite (which is striated). The wall rock is visible in minor parts (e.g. plagioclase and titanite). Pyrite crystals are also present.

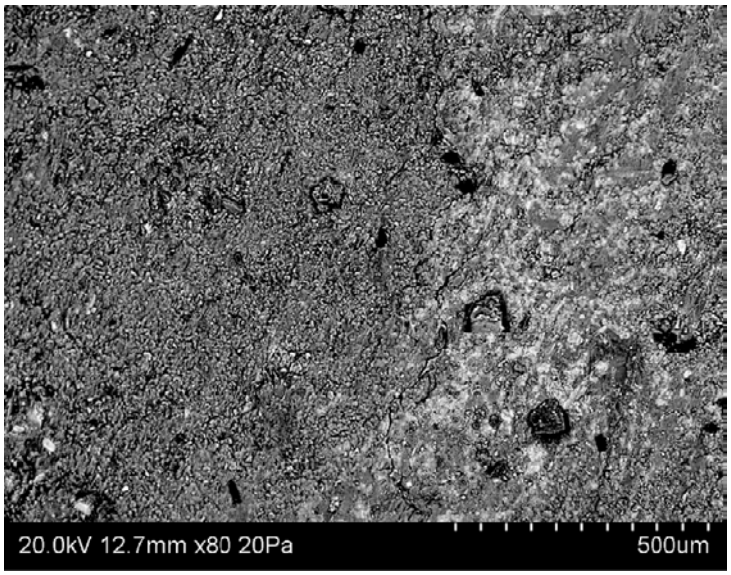

Figure 4-49. *Back-scattered SEM-image of chlorite/clay minerals, bright parts are Fe-rich and darker parts are more Mg-rich. Sample KI0010B01: 75.35–75.42 m.*

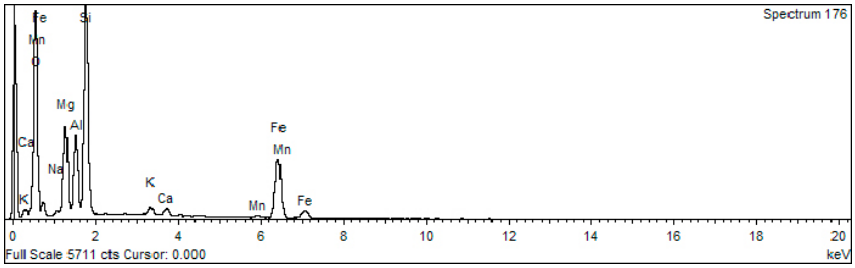

Figure 4-50. *EDS spectrum of chlorite/clay minerals. Sample KI0010B01: 75.35–75.42 m.*

Drill core sample KI0014B01: 72.16–72.28 m

From this sample, two thin sections and two fracture surface samples were analysed (Figure 4-51). Detailed images of this sample are shown in Figure 4-52 through Figure 4-59.

Thin section #1

General feature: Mylonite in core of deformation zone. Very fine-grained mylonite consisting of numerous parallel shear bands either dominated by quartz (and minor feldspar), epidote or mica (mainly muscovite). Quartz shows signs of dynamic re-crystallisation, such as sub-grain formation and sub-grain rotation re-crystallisation, and less pronounced grain boundary migration re-crystallisation. Main kinematic indicator is sinistral, shown by σ-type porphyroblasts, diffuse oblique foliation of re-crystallised quartz, and mantled porphyroclasts of K-feldspar and quartz, although porphyroclasts are not so common and those present are K-feldspar or plagioclase with deformation twins and synthetic micro-faults and are often mantled with re-crystallised K-feldspar, or they are made up of quartz which is completely re-crystallised (dynamic). Brittle veins filled with euhedral epidote, quartz, hematite-stained K-feldspar, fluorite, pyrite and possibly prehnite cut the mylonite perpendicular or run parallel with mylonite foliation. Veins running perpendicular to foliation are youngest. Wall rock is highly altered and fragmented, with increasing intensity towards the mylonite, and primary quartz is completely re-crystallised in a dynamic manner and surrounds fragments of primary feldspars which have rotated slightly and are to a large degree replaced by secondary minerals (mainly adularia and albite, sericite and saussuritization assemblages). Parts of the wall rock show proto-mylonite texture.

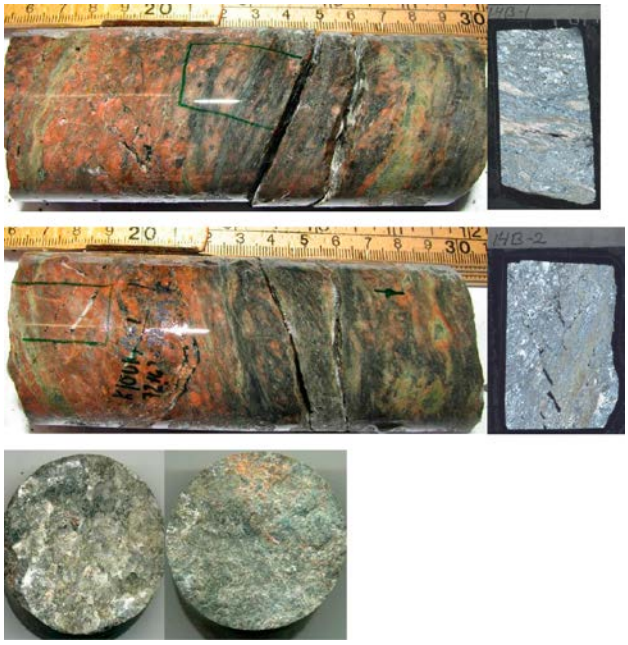

Figure 4-51. *Top: Photographs showing the sample KI0014B01: 72.16–72.28 m from two angles, the top with thin section 1 indicated, the bottom with thin section 2 indicated, also included next to each photograph are scanned thin section 1 and 2, with crossed polars. Bottom: Photographs of fracture surfaces 1 and 2.*

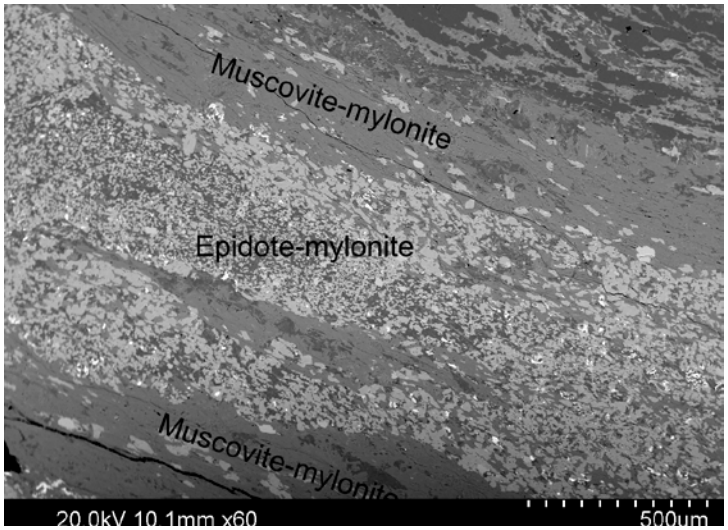

Figure 4-52. *Back-scattered SEM-image showing parallel mylonite-bands either dominated by epidote or by muscovite. Uppermost part is quartz-dominated (darker mineral). Sample KI0014B01: 72.16–72.28 m.*

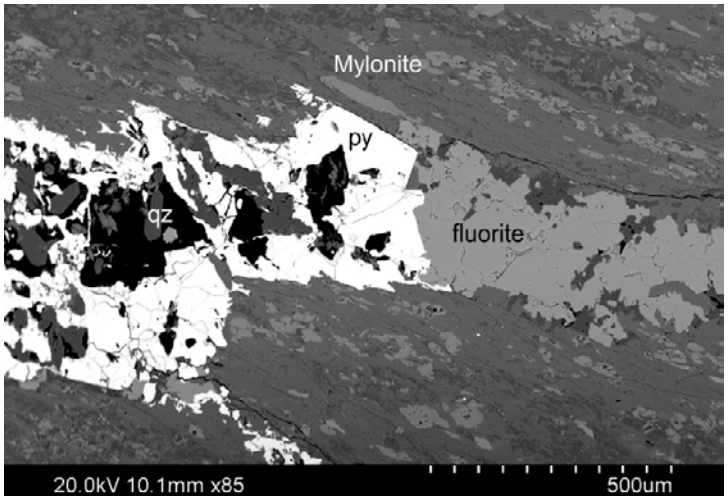

Figure 4-53. *Back-scattered SEM-image of fluorite, pyrite (denoted "py" in image) and quartz (qz) in a brittle fracture cutting through fine-grained mylonite. Sample KI0014B01: 72.16–72.28 m.*

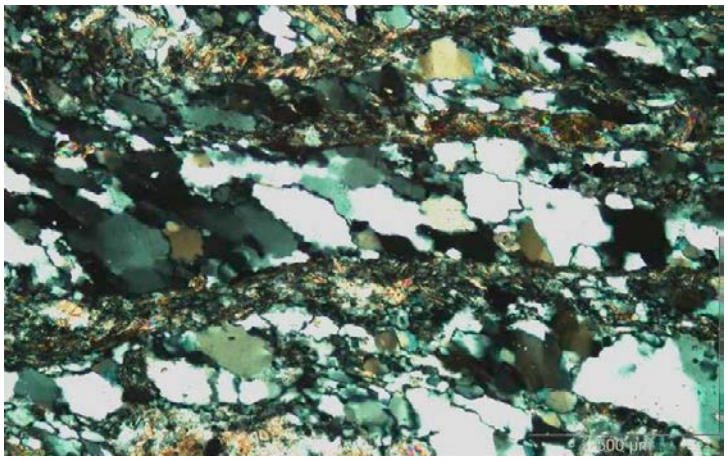

Figure 4-54. *Photomicrograph showing dynamic re-crystallisation textures of quartz (e.g. sub-grain rotation re-crystallisation) in mylonite, which also includes high amounts of epidote and muscovite. Sample KI0014B01: 72.16–72.28 m.*

Thin section #2

The mylonite is very fine-grained and consists of numerous parallel shear bands either dominated by quartz (and K-feldspar), epidote or mica (mainly muscovite, not as common as epidote). Quartz shows signs of dynamic re-crystallisation, such as sub-grain formation and sub-grain rotation re-crystallisation, and grain boundary migration re-crystallisation. Main kinematic indicator indicates sinistral displacement, shown by a few σ-type mantled porphyroclasts of K-feldspar and quartz.

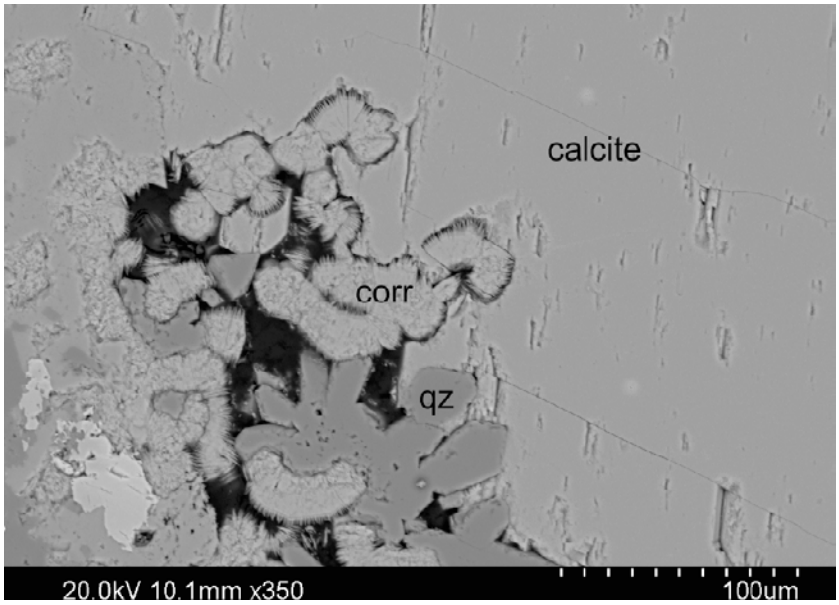

Figure 4-55. *Back-scattered SEM-image showing a close up of a void in a calcite-filled fracture, where euhedral quartz (denoted "qz" in image) and corrensite ("corr") have precipitated. Sample KI0014B01: 72.16–72.28 m.*

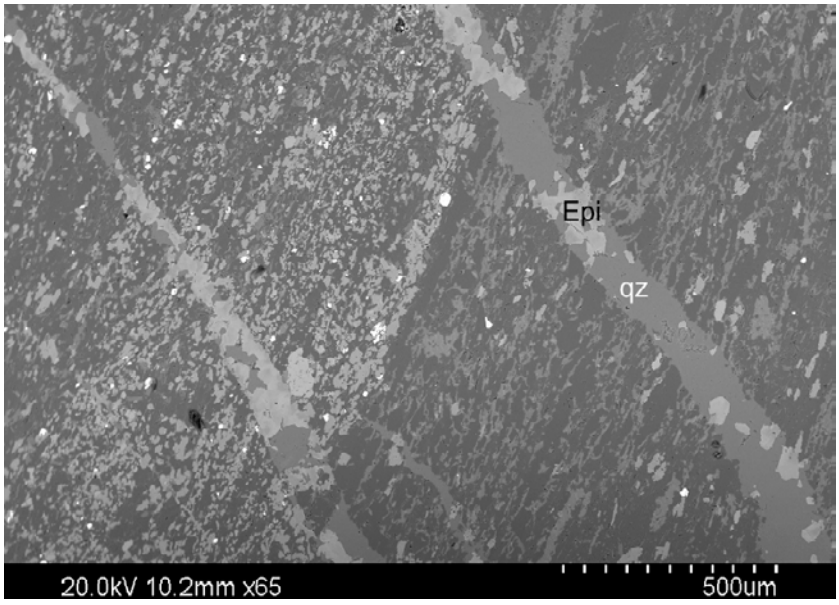

Figure 4-56. *Back-scattered SEM-image of two fractures filled with euhedral epidote (denoted "Epi" in image) and quartz (denote "qz") cutting through mylonite which is either dominated by epidote (left, bright intensity – also including some darker quartz and mica) or quartz (right, dark intensity, also including some brighter K-feldspar). Sample KI0014B01: 72.16–72.28 m.*

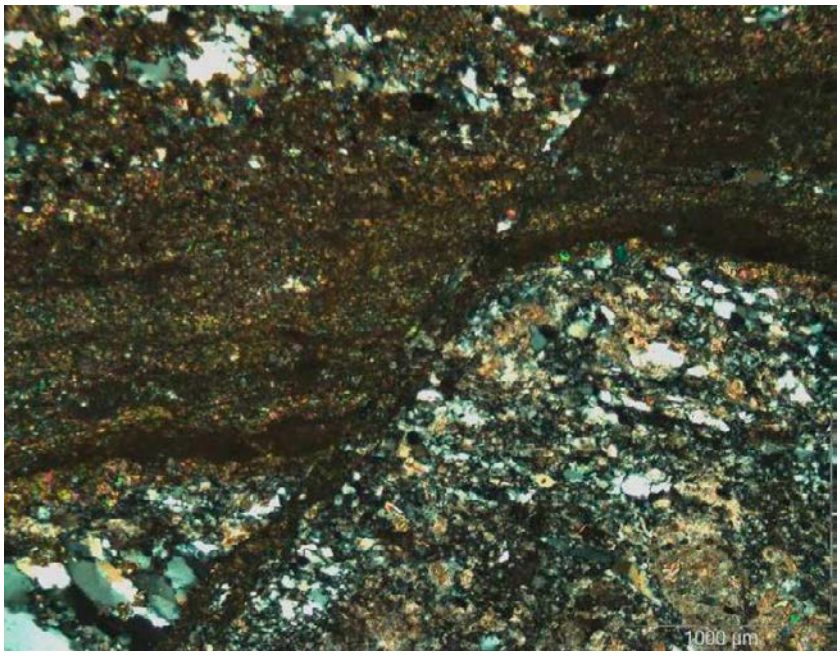

Figure 4-57. *Photomicrograph showing a cataclasite cutting and off-setting mylonite through apparent sinistral movement. The individual mylonite bands are either epidote-rich (dark) or quartz-rich (bright). Cataclasite is mainly epidote-dominated. Sample KI0014B01: 72.16–72.28 m.*

Mylonite and wall rock are cut by several brittle veins, with vuggy texture. Veins are coated by euhedral epidote, and on top of epidote are euhedral quartz and K-feldspar and chlorite (which also partly fill the centre of the fracture). The central part of the fracture is either filled with calcite (rather fresh with only minor amounts of deformation twins), fluorite (?) or are barren. These fractures show indication of displacement by brittle faulting which has offset the veins by up to 2 mm, so movement has probably occurred in this zone after calcite-formation. A set of fractures running sub-parallel with the calcite-filled (or barren) fractures are filled with epidote, quartz and K-feldspar. These are thinner than the calcite-filled fractures. It is indicated that the epidote-fractures have been reactivated and that calcite and fluorite were formed in these fractures at a later event than epidote, quartz etc. The epidote fractures partly run along older epidote-rich cataclasite which off-set the mylonite in a sinistral way by up to 1 mm. Therefore we can distinguish five events: 1) mylonite formation (sinistral sense of shear), 2) formation of epidote-rich cataclasite with related sinistral offset of mylonite, 3) epidote-formation in veins (along with quartz and K-feldspar) re-activating the cataclasite, 4) Re-activation of epidote-fractures and partial filling by calcite, corrensite, and fluorite (and minor pyrite), and 5) dextral displacement of calcite-veins by up to 2 mm.

Fracture surface sample #1

Minerals on fracture surface: Calcite, chlorite, clay minerals, fluorite, epidote, pyrite, quartz, illite and adularia.

Most of the fracture surface is covered by calcite, both as a striated coating and as younger euhedral freely growing crystals (equant). The latter are found on top of the older calcite, along with chlorite and clay minerals, cubic fluorite, pyrite, and quartz are also found on top of the older calcite. There are also gauge-like (thin on the surface) clusters with e.g. quartz, biotite, chlorite, epidote etc (mainly wall rock fragments). Also K-feldspar, illite and chlorite/clay minerals area present on top of old calcite in a fine-grained mixture.

The fracture coating underneath the old calcite coating is dominated by chlorite, but the wall rock is exposed in some parts as well (e.g. amphibole, feldspars and quartz).

Fracture surface sample #2

Minerals on fracture surface: Chlorite, clay minerals (e.g. illite), fluorite, epidote, plagioclase, quartz, albite, calcite, pyrite and hematite.

The main part of the coating is chlorite/clay mineral-dominated (mixed-layer clay and illite) and shows a smooth striated and stepped surface, with occasional minerals on the surfaces (e.g. quartz, fluorite, calcite and pyrite). A cluster of fluorite crystals is present (together with e.g. some quartz) in the coating, and is surrounded by chlorite and clay minerals mainly (underlying wall rock minerals are also visible). One part of the coating hosts abundant epidote and plagioclase with some hematite. A sealed fracture with a different orientation than the studied fracture "crops out" at the fracture surface of the studied fracture, and this sealed fracture is filled with fluorite and quartz.

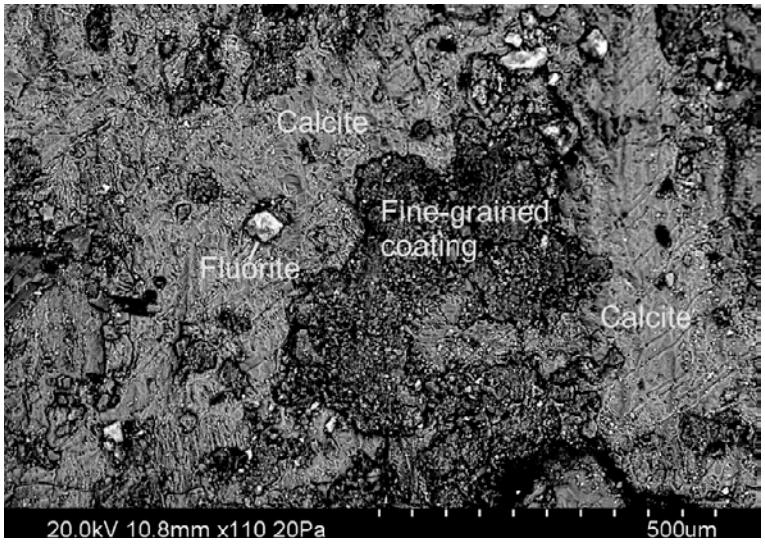

Figure 4-58. *Back-scattered SEM-image of calcite coating with a fine-grained, gauge-like coating as well as younger fluorite crystals on the surface. Sample KI0014B01: 72.16–72.28 m.*

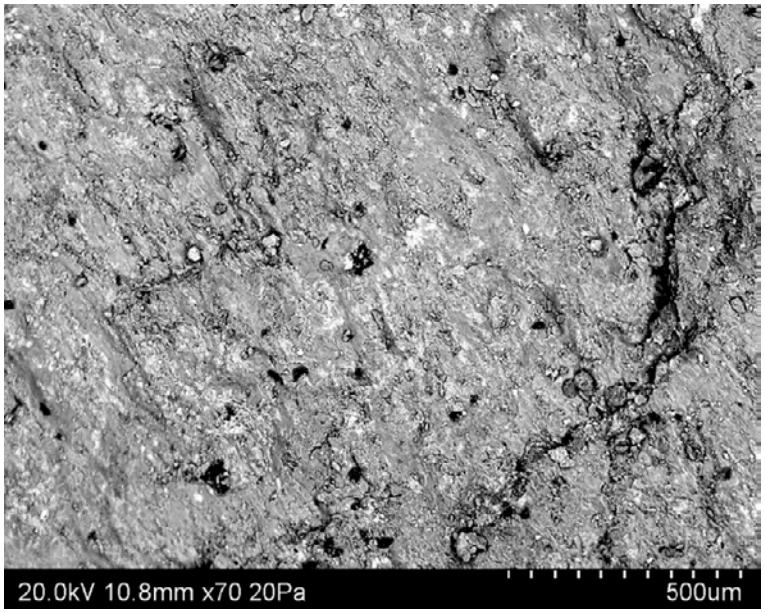

Figure 4-59. *Back-scattered SEM-image of striated and stepped fracture surface with dominantly chlorite/ clay minerals. Bright euhedral crystals on the surface are fluorite. Sample KI0014B01: 72.16–72.28 m.*

Drill core sample KI0016B01: 70.32–70.83 m

From this sample three thin sections and two fracture surface samples were analysed (Figure 4-60). Detailed images of this sample are shown in Figure 4-61 through Figure 4-66.

Thin section #1

General feature: The thin section covers the core section next to the main open fracture of the Structure #20 intercept. The two centimetres closest to the fracture is made up of numerous mm-thick parallel mylonite bands, dominated by epidote, quartz, with smaller amounts of biotite, plagioclase, K-feldspar and chlorite, and probably muscovite/sericite. Bands are alternately epidote-(green) or quartz-dominated (grey), and some bright bands are sericite-rich. Quartz-rich parts show signs of dynamic re-crystallisation, e.g. sub-grain rotation re-crystallisation and grain boundary migration re-crystallisation and sub-grain formation along with undulose extinction. Clasts of primary minerals such as plagioclase and Fe-oxides exist but are highly altered, and chlorite and muscovite have grown in the pressure-shadow around the blasts. Some kinking of muscovite-chlorite crystals exist in the mylonite. Sinistral shear-sense is indicated. The more remote part of the thin-section, from the fracture, contains cataclasite of wall rock fragments and fine-grained quartz, epidote etc. Fragments of primary plagioclase remains but are altered to secondary minerals, which are red-stained due to minute secondary hematite-grains. Larger quartz-fragments are completely re-crystallised to poly-crystalline aggregates, with grain-boundaries showing pressure solution texture. Undulose extinction is abundant. 80–90% of the wall rock minerals are re-crystallised or fragmented into fine-grained minerals.

Thin section #2

General feature: The thin section covers the damage zone of the Structure #20 intercept in this core. The thin section is dominated by a thin mylonite with related sealed fracture network and cataclasite. The wall rock has maintained its primary texture, although the minerals are altered and abundant secondary minerals are present between the grains (quartz, K-feldspar, biotite), through fluid penetration/alteration along grain-boundaries, and cataclastic texture is observed in places.

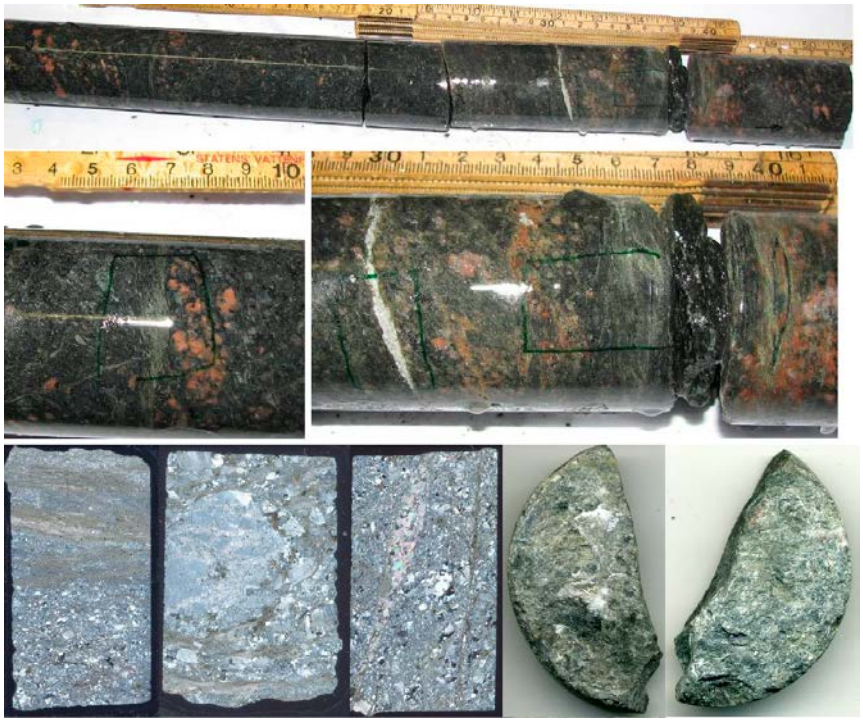

Figure 4-60. *Top: Photographs showing the sample KI0016B01: 70.32–70.83 m, with the three thin section locations indicated on the photographs on the second row. Bottom row: Scanned thin sections 1, 2 and 3, with crossed polars and photographs of fracture surfaces 1 and 2.*

The quartz and feldspars in between primary minerals show signs of dynamic re-crystallisation, e.g. sub-grain formation, grain-boundary migration re-crystallisation etc. Primary plagioclase is sericitized/saussurritized (incl. calcite) and replacement by albite and K-feldspar is evidenced. Primary quartz is re-crystallised to poly-crystalline quartz aggregates, primary microcline augens (perthite) have secondary minerals such as calcite in their lattice. Aggregates of biotite also exist and the biotite is rather fine-grained and may therefore have been re-crystallised. Chlorite is present in the biotite aggregates as well. The main fracture-filling/mylonite is dominated by epidote and muscovite, with some quartz, albite, K-feldspar and biotite as well. There are very clear dextral kinematic indicators (indicated e.g. by σ-type porphyroclasts and synthetic microfaults in clasts). Clasts of feldspars show deformation twinning.

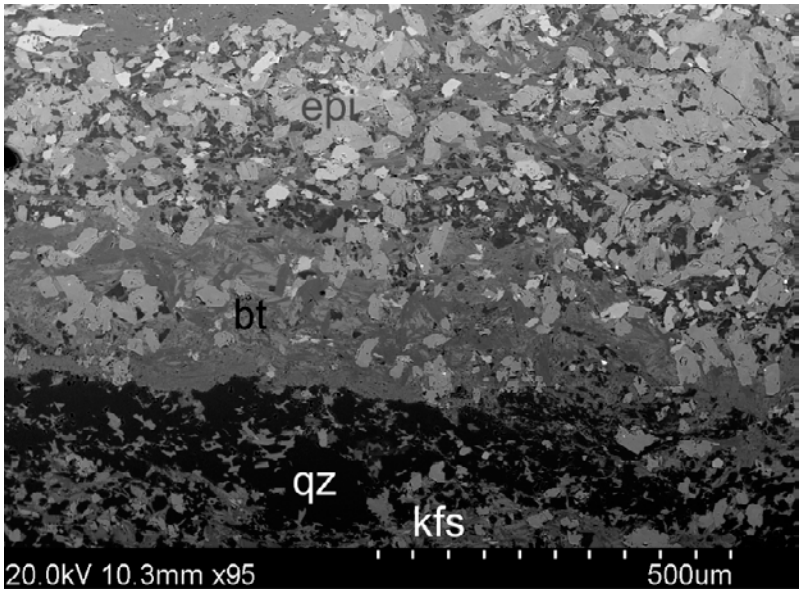

Figure 4-61. *Back-scattered SEM image of mylonite bands dominated by from top to bottom, epidote (epi), biotite (bt), quartz (qz), and K-feldspar (kfs). Sample KI0016B01: 70.32–70.83 m.*

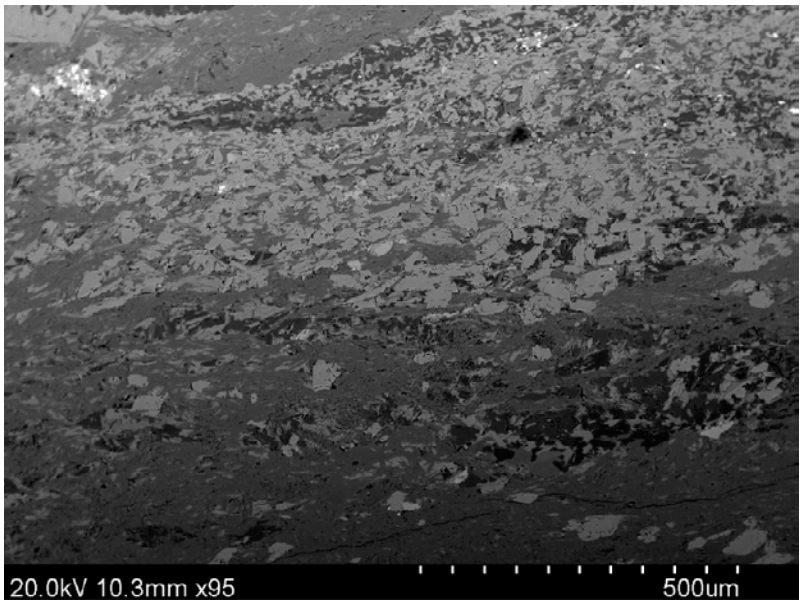

Figure 4-62. *Back-scattered SEM-image of mylonite dominated by epidote (bright), muscovite (medium grey) and quartz (very dark grey). Sample KI0016B01: 70.32–70.83 m.*

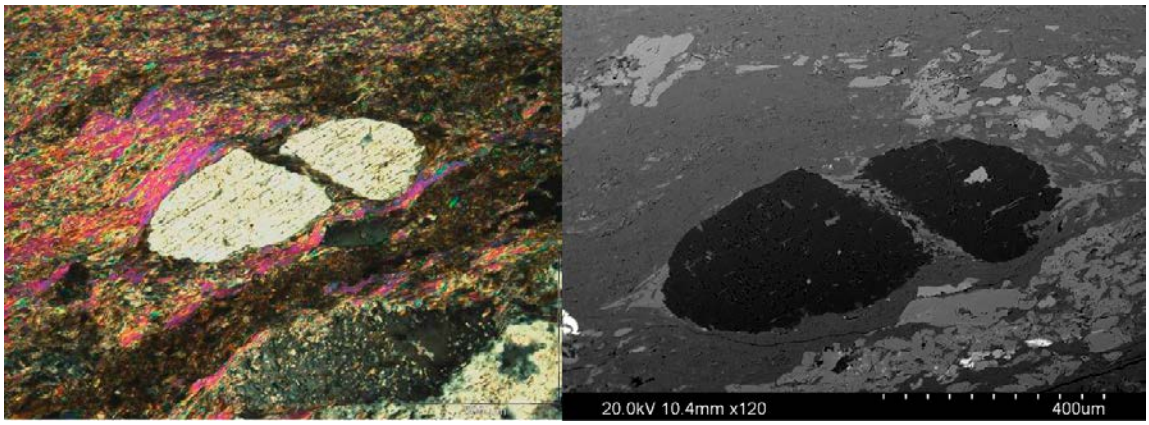

Figure 4-63. *Photomicrograph (left) and back-scattered SEM-image (right) of mantled plagioclase porphyroclast in muscovite-rich mylonite. The porphyroclast shows synthetic microfaulting. Sample KI0016B01: 70.32–70.83 m.*

Thin section #3

General feature: Calcite-vein in core.

The calcite vein is made up of a single generation of calcite (+minor pyrite, quartz, biotite, K-feldspar) with blocky crystals, occasionally with thick twin-lamellae. The wall rock is highly altered and 60–70% has been re-crystallised/fragmented to a fine-grained matrix (epidote- and quartz-rich) with primary coarser-grained minerals remnant as fragments (e.g. plagioclase, larger aggregates of dynamically re-crystallised quartz, and microcline). The wall rock is sometimes locally highly-foliated in a mylonitic manner, and one of these mylonitic parts is cut by the calcite-vein. A thin vein of epidote, biotite, muscovite, quartz runs sub-parallel with the calcite-fracture at a distance of c. 1 cm.

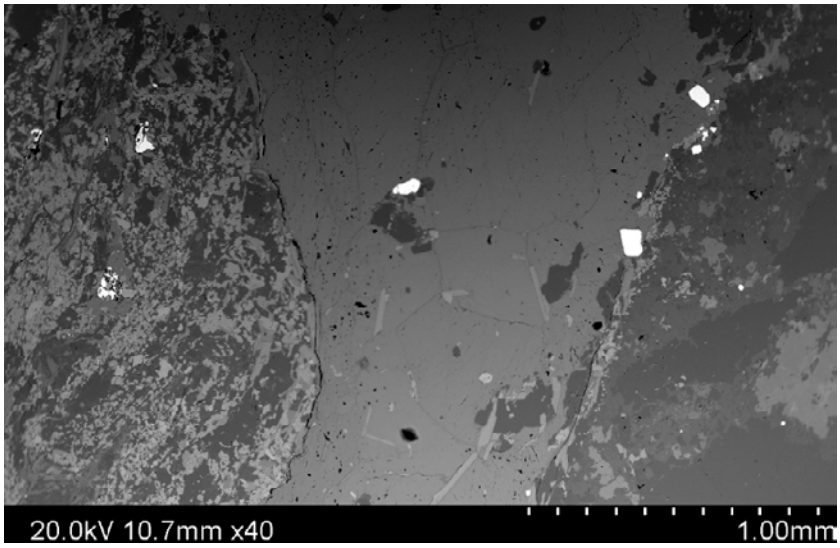

Figure 4-64. *Back-scattered SEM-image of a fracture filled with calcite, pyrite, quartz and biotite cutting through mylonite. Sample KI0016B01: 70.32–70.83 m.*

Fracture surface sample#1

Minerals on fracture surface: Chlorite, calcite, clay minerals, illite, fluorite, quartz and epidote.

A large part of the fracture surface is covered by calcite (massive), which is present on top of an older chlorite- and illite-coating. The illite-chlorite-dominated fracture is very smooth with occasional fine-grained fracture minerals on the surface. Younger chlorite and clay minerals (especially illite), in turn, partly cover the outermost part of the calcite coating (and is striated). Young euhedral calcite (equant) also covers parts of the lowermost chlorite-coating where it is not covered by the massive calcite. Quartz and fluorite is also present together with calcite (fluorite can be coarse-grained and massive). Young calcite (scalenohedral-equant) is found on top of older calcite together with fluorite. A part of the filling also holds large amounts of euhedral epidote.

Fracture surface sample #2

Minerals on fracture surface: Chlorite, clay minerals, illite, fluorite, quartz and epidote.

Quite smooth fracture surface totally dominated by chlorite (and clay minerals; mixed-layer clay and illite). The surface is striated. Other minerals in-mixed with (or on the surface of) chlorite are e.g. quartz, fluorite, illite, epidote, some apatite, titanite, and biotite, of which at least the latter two probably are wall rock fragments. Fault gouge-like sections (clusters of very fine-grained minerals) exist in minor amounts and consist mainly of quartz, illite, biotite and chlorite.

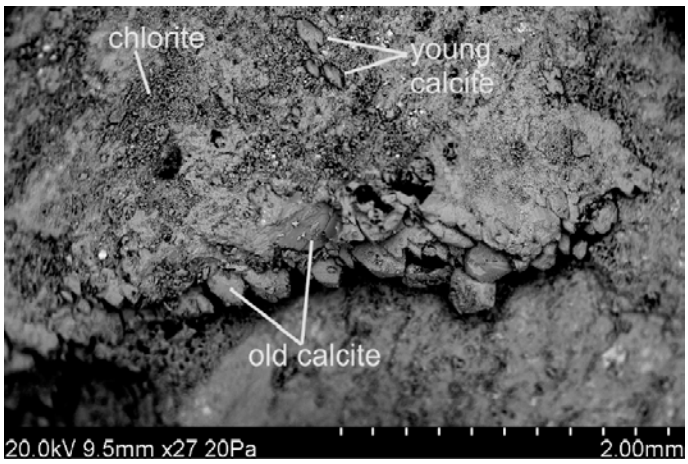

Figure 4-65. *Back-scattered SEM-image of old calcite coating partly coated by younger euhedral calcite crystals and chlorite. Sample KI0016B01: 70.32–70.83 m.*

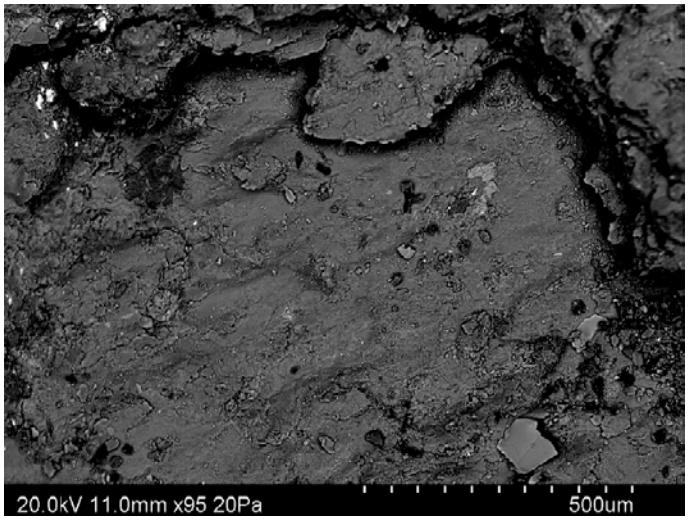

Figure 4-66. *Back-scattered SEM-image of dominantly chlorite/clay minerals. Sample KI0016B01: 70.32–70.83 m.*

4.5.2 Description of fracture mineralogy in samples from the TRUE Block Scale boreholes

Scanned thin sections from the TRUE Block Scale boreholes are shown in Figure 4-67. Detailed images of these samples are shown in Figure 4-68 through Figure 4-75.

KA2563A: 188.74 m

This thin section consists of numerous mylonite and cataclasite bands (sub-parallel). Cataclasite has reactivated the mylonite. The wall rock minerals in between these bands are highly fragmented and fractured. There are also fractures filled with adularia cutting through mylonite. Mylonite consists of epidote, quartz, chlorite, muscovite and albite. Quartz shows signs of sub-grain formation, e.g. grain-boundary migration re-crystallisation. Dextral shear is indicated by oblique foliation of re-crystallised quartz crystals, stair-stepping and diffuse C-S fabric. Clasts of plagioclase/quartz/K-feldspar exist and around them are muscovite and chlorite etc in strain shadows, mantling the porphyroclasts. Some cataclasite parts have very epidote-rich matrix. Other minerals in cataclasite are e.g. albite, quartz and muscovite. Fractures, filled with euhedral epidote, K-feldspar, quartz and pyrite have re-activated the cataclasite/mylonite.

Figure 4-67. *Scanned thin sections from TRUE Block Scale boreholes. From left to right: KA2563A: 188.74 m, KI0023B: 85.6 m, KI0023F: 69.9 m, KI0025F02: 74.6 m (two thin sections), KI0025F03: 73.2 m. Scanned with crossed polars (except KI0025F02: 74.6 m – plane polarised light).*

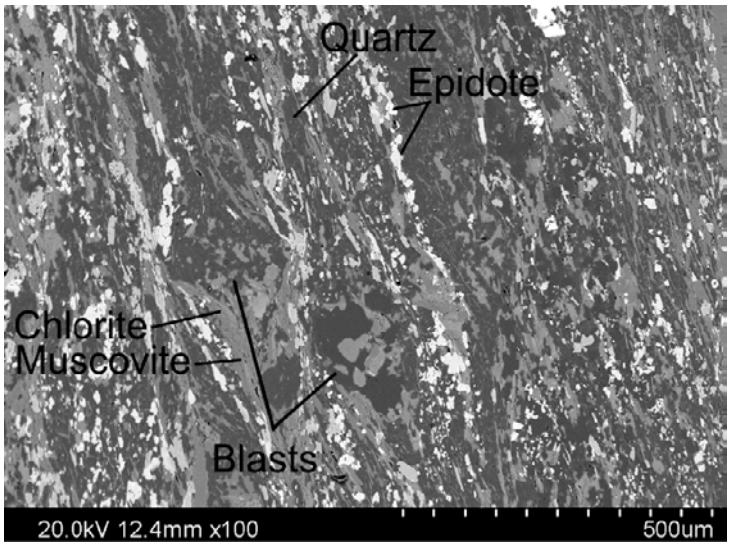

Figure 4-68. *Back-scattered SEM-image of mylonite rich in epidote, chlorite, quartz, albite, muscovite etc, also including porphyroblasts of plagioclase, with mainly chlorite and mylonite grown around it. Sample KA2563A: 188.74 m.*

KI0023B: 85.6 m

Highly-fractured rock with numerous sub-parallel mylonite and cataclasite bands. One part of the mylonite is dominated by bands rich in epidote, whereas others are rich in quartz and K-feldspar. Chlorite exists in both of these types. Clasts of primary quartz and feldspars exist. Quartz in these clasts are re-crystallised, to poly-crystalline aggregates and grain-boundary migration re-crystallisation is indicated. Dextral shear-sense is indicated by oblique foliation and stair-stepping. C'-fabric is indicated in the mylonite. C'-fabric is a late-stage shear indicator which overpints earlier formed C-S fabric. Some muscovite is also present in the mylonite. A fracture filled with adularia is cutting through the mylonite. Cataclasite is rich in epidote, quartz, K-feldspar, chlorite, albite and some mica. Fragments of the wall rock are abundant within the cataclasite. The cataclasite is cut by numerous K-feldspar dominated fractures which mainly run perpendicular to the cataclasite/ mylonite. A fracture filled with adularia and fluorite has reactivated the cataclasite.

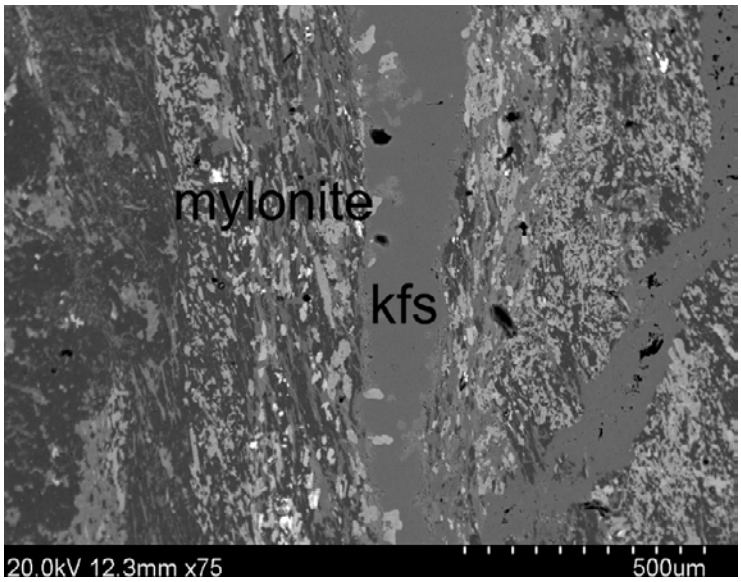

Figure 4-69. *Back-scattered SEM-image of mylonite cut by a K-feldspar (Kfs)-filled fracture. Sample KA2563A: 188.74 m.*

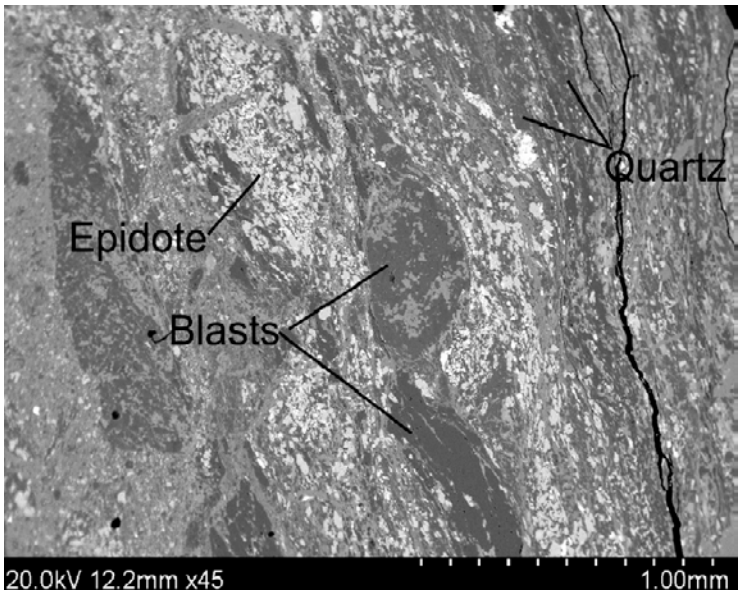

Figure 4-70. *Back-scattered SEM-image of mylonite rich in e.g. epidote and quartz, including porphyroclasts of quartz. Sample KI0023B: 85.6 m.*

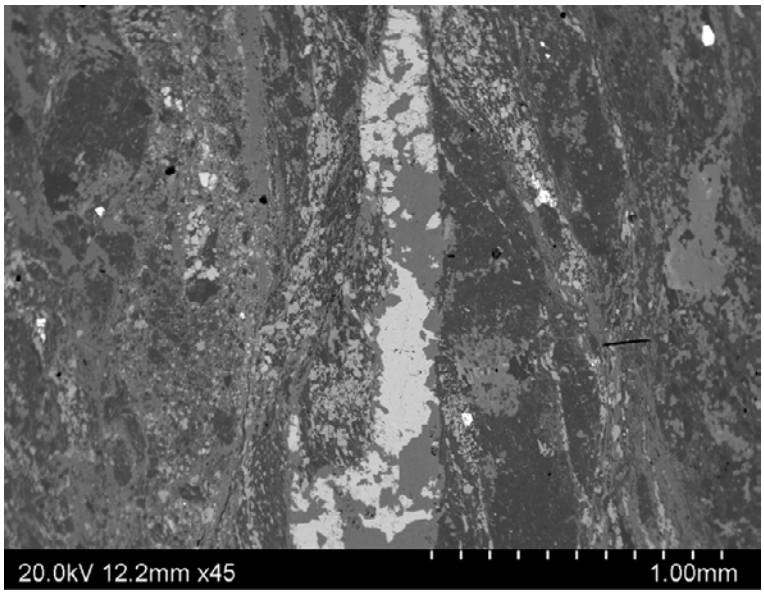

Figure 4-71. *Back-scattered SEM-image of K-feldspar (dark) and fluorite (bright)-filled fractures cutting through mylonite/(cataclasite). Sample KI0023B: 85.6 m.*

KI0023F: 69.9 m

There are several parallel bands (at most 1–2 mm thick) of cataclasite/mylonite made up of epidote, chlorite, quartz, K-feldspar, albite, also with some muscovite/sericite, and some titanite. Clasts of magnetite, titanite and quartz+feldspars exist. Epidote is the most common mineral in the more coarse-grained bands. In the very fine-grained mylonite, epidote and quartz dominate. Quartz shows dynamic re-crystallisation features, sub-grain formation, undulose extinction, grain boundary migration re-crystallisation and oblique foliation (indicating dextral shear). In pressure shadows around clasts e.g. chlorite and K-feldspar have grown. Very high fracture frequency. The wall rock minerals are micro-fractured and/or fragmented. In the right side of the thin section, the primary plagioclase and quartz of the wall rock are still of original grain-size. In the left side of the thin section, cataclasite dominates (and also some mylonite) in sub-parallel bands and the wall rock minerals show pronounced grain-size reduction (some primary minerals are still intact though, like titanite).

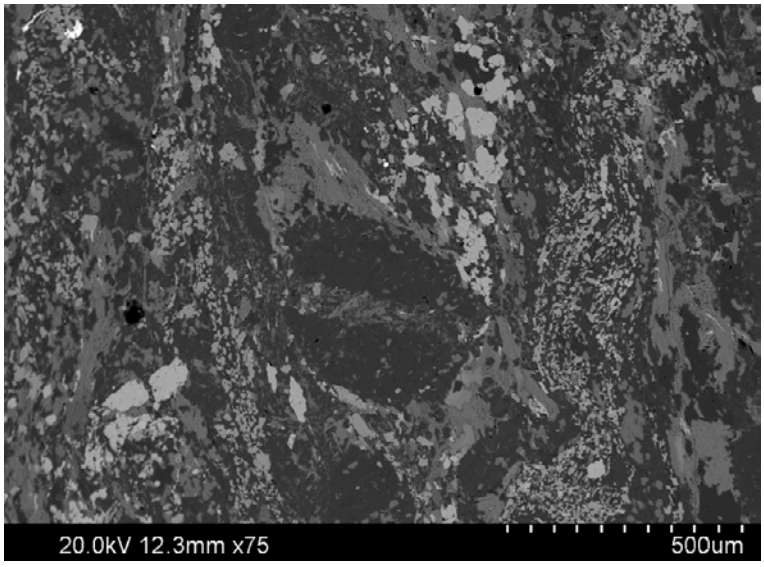

Figure 4-72. *Back-scattered SEM-image of mylonite a plagioclase porphyroblast mantled by K-feldspar and chlorite. Sample KI0023F: 69.9 m.*

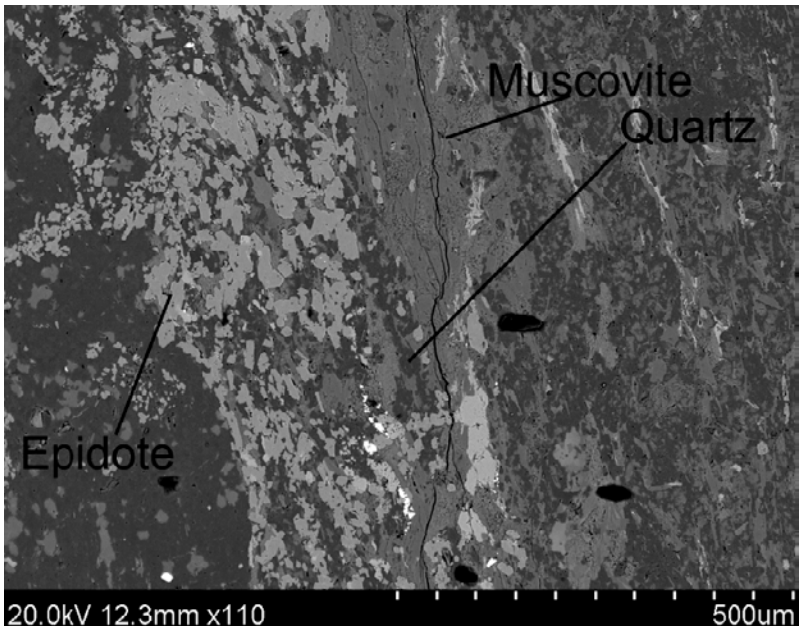

Figure 4-73. *Back-scattered SEM-image of mylonite rich in epidote, muscovite and quartz. Sample KI0023F: 69.9 m.*

KI0025F02: 74.6 m (two thin sections)

Thin section #1

Closest to the fracture is a couple of millimetre thick cataclasite/mylonite. Mylonite is oldest and has been re-activated by at least two events of cataclasite formation, of which the youngest is the most fine-grained, and both are epidote-dominated. Brittle micro-fractures run as Riedel shears from the fracture surface into the mylonite-cataclasite and indicate dextral movement. Shear sense of ductile deformation is also dextral, shown by σ–shaped quartz porphyroblasts. Parallel cataclasite bands are present at greater distance into the wall rock (essentially with the same mineralogy as in the thick mylonite/cataclasite, but perhaps even more dominated by epidote and quartz), which is highly fractured. Wall rock minerals are highly fractured and fragmented. Mylonite and cataclasite is made up of epidote, quartz, chlorite and K-feldspar. Clasts of quartz and other wall rock minerals are present in the thick mylonite. There are fractures filled with quartz (re-crystallised to polycrystalline aggregates), K-feldspar and calcite, which are younger than the mylonite and the cataclasite.

Thin section #2

Closest to the fracture is a couple of mm thick mylonite. Parallel cataclasite bands are also present and have re-activated the mylonite and run parallel with the mylonite. Cataclasite is also present in the highly fractured and fragmented wall rock. Wall rock minerals are highly fractured and fragmented. Clasts of plagioclase and quartz and other wall rock minerals are present in the mylonite. Mylonite is made up of epidote, quartz, muscovite, chlorite and K-feldspar. Mylonite bands are either dominated by quartz, epidote or muscovite and consist of very much K-feldspar as well.

Quartz shows dynamic re-crystallisation texture (poly-crystalline aggregates with sings of grain boundary migration re-crystallisation). Shear sense of the mylonite is sinistral as shown by stair-stepping muscovite bands (with oblique foliation). There is also a fracture filled with quartz and K-feldspar which is younger than the mylonite/cataclasite. At the very edge of the fracture surface is a thin calcite coating as well.

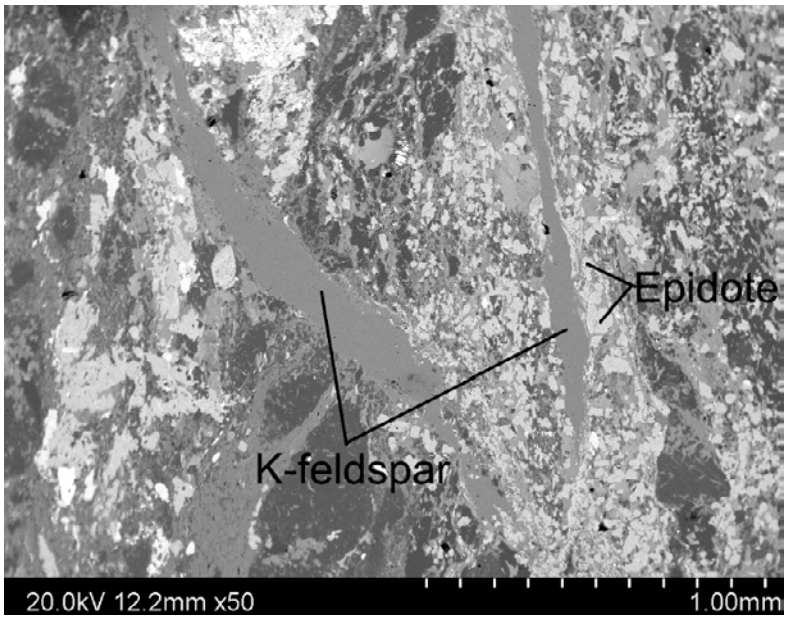

Figure 4-74. *Back-scattered SEM-image of K-feldspar-filled fractures cutting through cataclasite/mylonite with abundant epidote. Sample KI0025F02: 74.6 m.*

KI0025F03: 73.2 m

The whole thin section is dominated by fine-grained mylonite, with some minor fractures filled with quartz and muscovite and another generation with quartz, K-feldspar and calcite. Mylonite is of two types. The first is very fine-grained and epidote and quartz-dominated and quite homogeneous. There is not much wall rock fragments. Some K-feldspar and plagioclase also exist and there is quite high amount of fine-grained Fe-oxides in the mylonite. Some titanite is present as well. The other mylonite type is more coarse-grained and highly epidote-dominated. Quartz is the second most abundant mineral. Quartz exists as occasional clasts as well. K-feldspar, Fe-oxide and titanite exist in the mylonite.

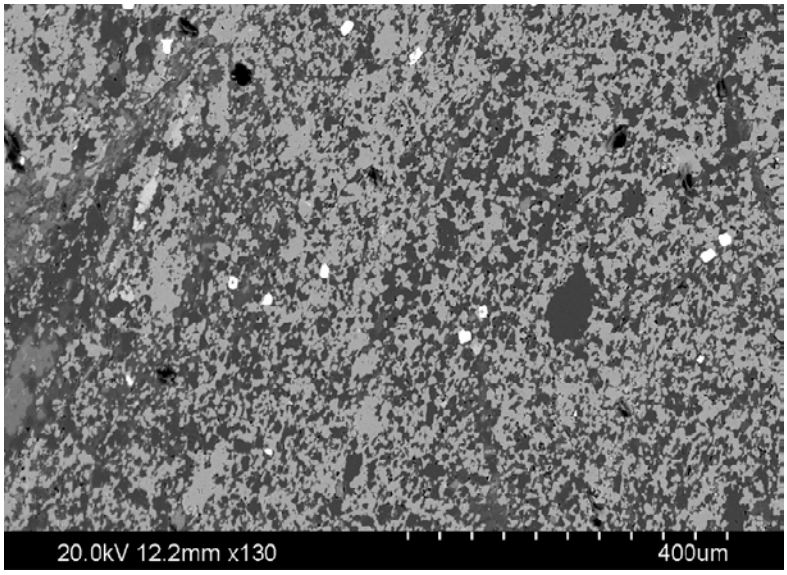

Figure 4-75. *Back-scattered SEM-image of very fine-grained mylonite, dominated by epidote (bright) and quartz (dark). Very bright spots are Fe-oxides. Sample KI0025F03: 73.2 m.*

4.5.3 Chemical analysis

Mylonite, including variable amounts of proto-mylonite has been analysed for whole rock chemical composition. The major and minor element composition of minerals in thin sections from the cored boreholes has been obtained with EDS analyses.

Whole rock chemistry

Three mylonite samples from the pilot boreholes have been analysed for major, minor and trace elements (cf. Table 2-1). The results are shown in Table 4-11. Reference rock analyses of Äspö diorite, the dominant rock type on Äspö, used for comparisons in figures were taken from Landström et al. (2001) (samples A8, A10, A13, B1–B4, B6 and B8).

Table 4-11. Whole rock chemistry of mylonite samples from cored boreholes.

Element		KI0010B01	KI0014B01	KI0016B01
SiO_2	%	60.9	66.8	68.7
Al_2O_3	%	17.7	16.6	14.6
CaO	%	6.70	3.15	4.10
Fe_2O_3	%	5.67	3.48	4.58
K_2O	%	1.93	4.64	2.65
MgO	%	1.58	1.16	1.72
MnO	%	0.08	0.05	0.07
Na_2O	%	4.72	3.21	3.42
P_2O_5	%	0.35	0.25	0.21
TiO_2	%	0.79	0.63	0.53
Total	%	100.4	100	100.6
LOI	%	1.2	1.3	1.1
Ba	mg/kg	826	2,930	1,310
Be	mg/kg	2.29	2.67	2.28
Co	mg/kg	8.52	< 6	13
Cr	mg/kg	144	182	123
Cs	mg/kg	1.73	0.78	1.88
Ga	mg/kg	22.4	21.6	21.4
Hf	mg/kg	550	542	596
Mo	mg/kg	6.46	< 2	< 2
Nb	mg/kg	12.7	11.7	6.68
Ni	mg/kg	24.6	21.5	24.7
Rb	mg/kg	80.9	143	107
Sc	mg/kg	9.18	6.13	5.57
Sr	mg/kg	2,100	838	1,080
Ta	mg/kg	1.34	1.43	1.50
Th	mg/kg	10.5	12.3	13.6
U	mg/kg	3.95	2.72	4.83
V	mg/kg	92.4	60.8	73.6
W	mg/kg	0.71	1.38	0.73
Y	mg/kg	27.2	26.4	22.5
Zr	mg/kg	269	257	268
La	mg/kg	61.5	61.7	78.2
Ce	mg/kg	138	130	146
Pr	mg/kg	15.9	14.7	16.0
Nd	mg/kg	58.2	52.0	56.6
Sm	mg/kg	9.5	8.82	9.41
Eu	mg/kg	1.99	1.20	1.68
Gd	mg/kg	7.20	6.84	6.84
Tb	mg/kg	1.00	0.98	0.86
Dy	mg/kg	5.25	5.54	4.23
Ho	mg/kg	1.02	1.08	0.836
Er	mg/kg	2.67	2.83	2.24
Tm	mg/kg	0.41	0.45	0.33
Yb	mg/kg	2.46	2.48	2.10
Lu	mg/kg	0.37	0.34	0.33

Mylonite chemistry in the drill core samples show that the sample from KI0010B01 has lower concentrations of e.g. SiO_2 (Figure 4-76,), K_2O, Ba and higher Al_2O_3, CaO, Fe_2O_3, Na_2O, MnO, TiO_2 and Sr (Figure 4-77, Figure 4-78) compared to the samples from KI0014B01 and KI0016B01, which are more similar in composition, compared to the KI0010B01 sample. MgO is however lowest in the KI0014B01 sample. The chemical difference between the samples is related to the difference in mineralogy, with e.g. lower amounts of quartz, K-feldspar and mica and higher amounts of e.g. epidote and chlorite in the KI0010B01 sample. The samples show, for example, generally higher SiO_2, CaO and MgO, lower Al_2O_3, TiO_2 compared to the wall rock, mainly reflecting leaching of SiO_2, CaO and MgO during alteration of the wall rock (plagioclase and biotite dominantly) and formation of epidote, quartz and mica in the mylonite, whereas Al_2O_3, TiO_2, as expected have been less mobile. Differences in REE-concentrations are very small (Figure 4-79).

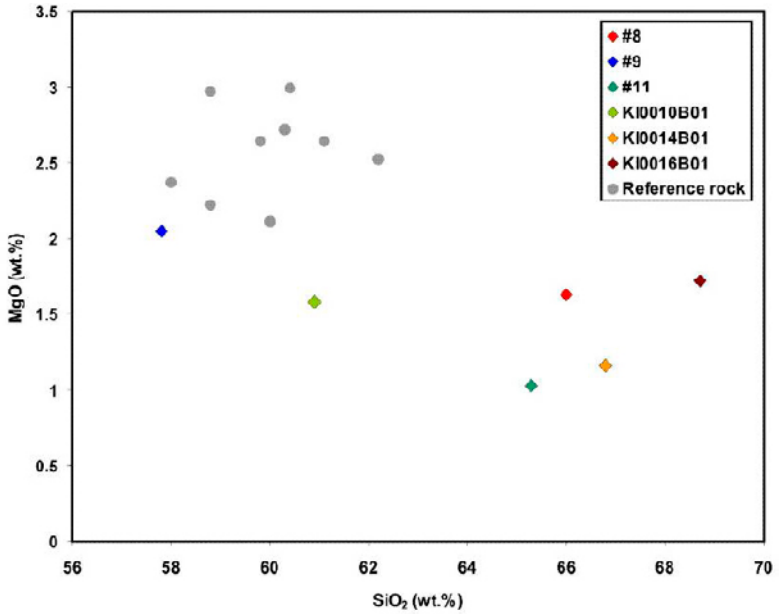

Figure 4-76. *MgO vs. SiO_2 for mylonite and reference rock.Samples #8, #9, #11 represent analyses from the TASS tunnel (see Section 5.5.2).*

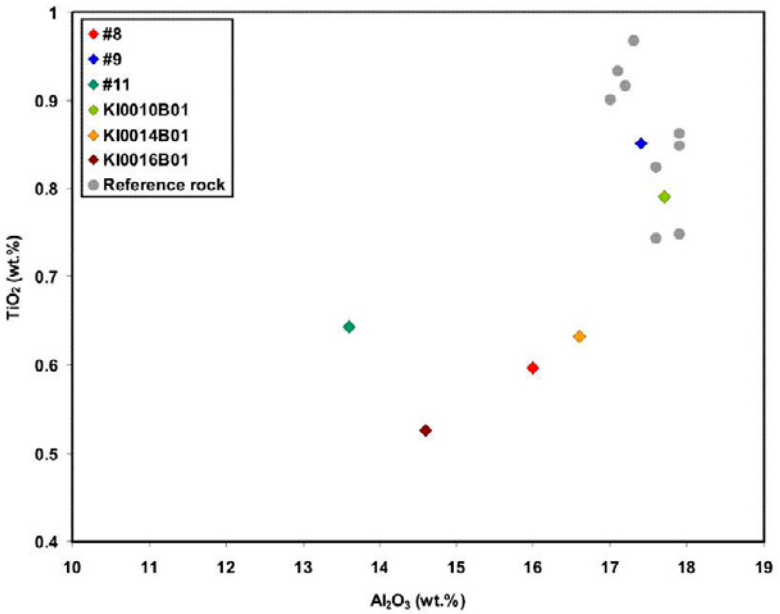

Figure 4-77. *TiO_2 vs. Al_2O_3 for mylonite and reference rock.Samples #8, #9, #11 represent analyses from the TASS tunnel (see Section 5.5.2).*

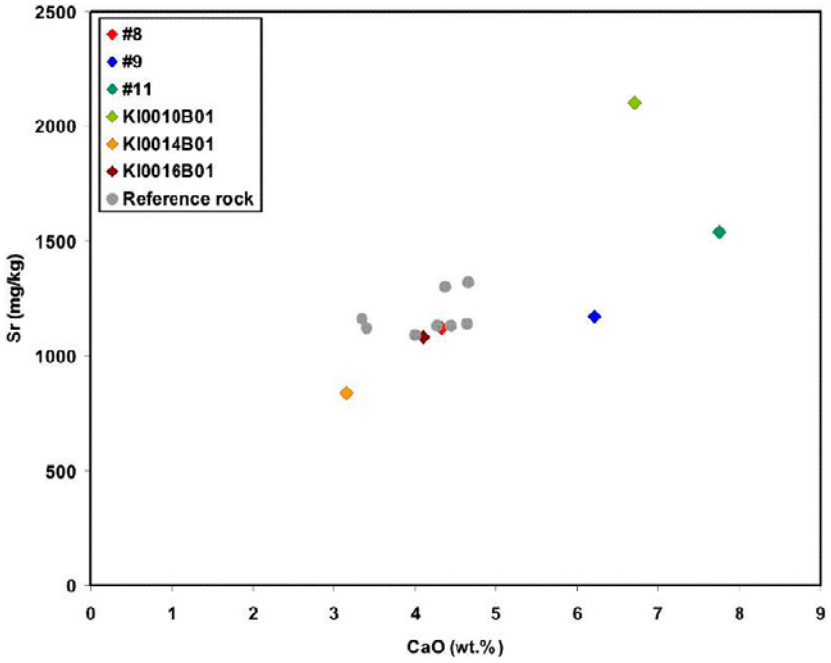

Figure 4-78. *Sr vs. CaO for mylonite and reference rock.Samples #8, #9, #11 represent analyses from the TASS tunnel (see Section 5.5.2).*

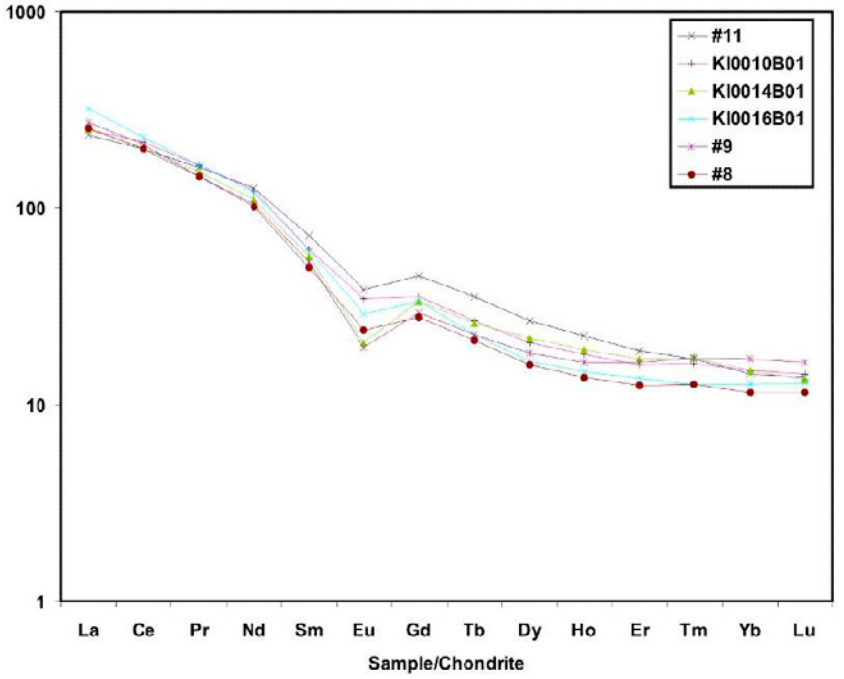

Figure 4-79. *Chondrite-normalized REE-patterns for mylonite samples.Samples #8, #9, #11 represent analyses from the TASS tunnel (see Section 5.5.2).*

Mineral chemistry

SEM-EDS analysis was carried out on minerals in thin sections. Results are shown in Table 4-12.

Epidote in veins has lower Al_2O_3 (21.1%) and higher FeO (16.0%) concentration than epidote in mylonite (mainly > 23.3% and < 13.3%, respectively; both in core and damage zone) (Figure 4-80). Calcite has up to 0.84 wt.% MnO. Muscovite and biotite show no unexpected concentrations for any element and the variation in muscovite chemistry is very small.

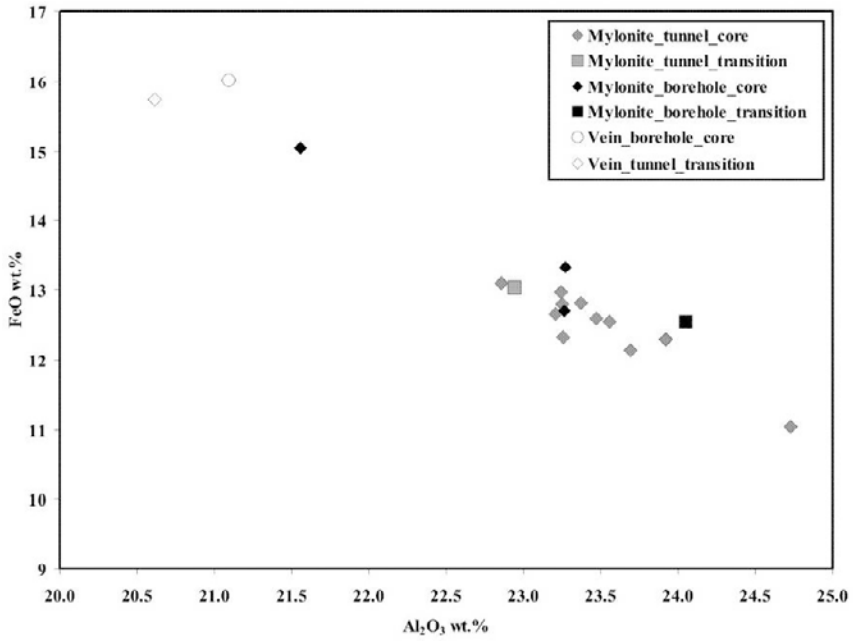

Figure 4-80. *FeO vs. Al_2O_3 in epidote.*

Table 4-12. SEM-EDS analyses of minerals in thin sections. n.d. = not detected.

Epidote in mylonite	**Na_2O**	**MgO**	**Al_2O_3**	**SiO_2**	**K_2O**	**CaO**	**TiO_2**	**MnO**	**FeO**	**SrO**	**BaO**
KI0010B01	n.d.	n.d.	23.3	37.9	n.d.	23.1	n.d.	n.d.	13.3	n.d.	n.d.
KI0014B01-2	n.d.	n.d.	21.6	37.1	n.d.	22.8	n.d.	n.d.	15.0	1.5	n.d.
KI0016B01-1	n.d.	n.d.	23.3	37.7	n.d.	22.9	n.d.	n.d.	12.7	1.11	n.d.
KI0016B01-2	n.d.	n.d.	24.1	37.5	n.d.	23.4	n.d.	n.d.	12.5	n.d.	n.d.
Epidote in veins	**Na_2O**	**MgO**	**Al_2O_3**	**SiO_2**	**K_2O**	**CaO**	**TiO_2**	**MnO**	**FeO**	**SrO**	**BaO**
KI0014B01-2	n.d.	n.d.	21.1	37.7	n.d.	23.6	n.d.	n.d.	16.0	0.8	n.d.
Muscovite in mylonite	**Na_2O**	**MgO**	**Al_2O_3**	**SiO_2**	**K_2O**	**CaO**	**TiO_2**	**MnO**	**FeO**	**SrO**	**BaO**
KI0014B01-1	n.d.	1.8	30.4	45.7	10.1	n.d.	0.4	n.d.	3.8	n.d.	1.2
KI0014B01-2	n.d.	1.4	30.5	46.6	10.5	n.d.	1.0	n.d.	4.4	n.d.	n.d.
KI0016B01-2	n.d.	1.7	30.4	46.4	10.9	n.d.	0.73	n.d.	4.24	n.d.	n.d.
Calcite in veins	**Na_2O**	**MgO**	**Al_2O_3**	**SiO_2**	**K_2O**	**CaO**	**TiO_2**	**MnO**	**FeO**	**SrO**	**BaO**
KI0014B01-2	n.d.	n.d.	n.d.	n.d.	n.d.	55.3	n.d.	n.d.	n.d.	n.d.	n.d.
KI0016B01-3	n.d.	n.d.	n.d.	n.d.	n.d.	54.9	n.d.	0.6	n.d.	n.d.	n.d.
KI0016B01-3	n.d.	n.d.	n.d.	n.d.	n.d.	54.9	n.d.	0.8	n.d.	n.d.	n.d.
Corrensite in vein	**Na_2O**	**MgO**	**Al_2O_3**	**SiO_2**	**K_2O**	**CaO**	**TiO_2**	**MnO**	**FeO**	**SrO**	**BaO**
KI0014B01-2	n.d.	19.3	17.5	29.5	n.d.	0.17	n.d.	0.5	24.3	n.d.	n.d.
Biotite in mylonite	**Na_2O**	**MgO**	**Al_2O_3**	**SiO_2**	**K_2O**	**CaO**	**TiO_2**	**MnO**	**FeO**	**SrO**	**BaO**
KI0016B01-1	n.d.	12.4	15.2	34.6	9.1	n.d.	2.0	0.3	17.6	n.d.	n.d.

4.5.4 Stable isotopes

Stable isotopes ($\delta^{13}C$ and $\delta^{18}O$) were analysed for four calcite samples from the cored boreholes (Table 4-13).

The results from the borehole samples are compared with stable isotope composition of calcite from the TASS tunnel as well as from structure #20 in the TRUE Block Scale boreholes (Andersson et al. 2002a) in Figure 4-81.

Calcite from the cored boreholes and tunnel shows calcite of two populations; 1) made up of three samples, KI0010B01-75.35–75.42 m, KI0014B01-72.16–72.28 m and KI0016B01-70.32–70.83 m-2 with a relatively small (1.4‰) variation in $\delta^{13}C$ (–11.7 to –10.3‰) and 3.4‰ variation for $\delta^{18}O$ (–16.0 to –12.6‰), and 2) made up of just sample KI0016B01-70.32–70.83 m-1 which has much lower $\delta^{18}O$ and higher $\delta^{13}C$ than the other samples. The similarity of the first group of samples suggests formation at similar conditions for the samples in this group and thus probably formation at the same event. The relatively depleted $\delta^{13}C$ values suggest influence of organic matter, and the combination of $\delta^{13}C$ and $\delta^{18}O$ values indicates formation during the Paleozoic (~ 440–400 Ma), from brine fluids at 80–145°C, based on earlier studies in this area (cf. e.g. Drake and Tullborg 2009, Drake et al. 2009). The stable isotope signature of sample KI0016B01-70.32–70.83 m-1, on the other hand, indicate formation at hydrothermal conditions (> 200°C) with no organic influence, probably in the Proterozoic, based on the information gathered in the earlier extensive fracture mineralogical studies in this area (cf. Drake and Tullborg 2009, Drake et al. 2009).

Table 4-13. Stable isotopes in calcite.

Sample	Weight (mg)	$\delta^{13}C$VPDB	$\delta^{18}O$VPDB
KI0010B01-75.35–75.42 m	15.9	–11.7	–13.4
KI0014B01-72.16–72.28 m	7.7	–10.3	–12.6
KI0016B01-70.32–70.83 m(1)	6.1	–3.5	–23.7
KI0016B01-70.32–70.83 m(2)	4.4	–11.4	–16.0

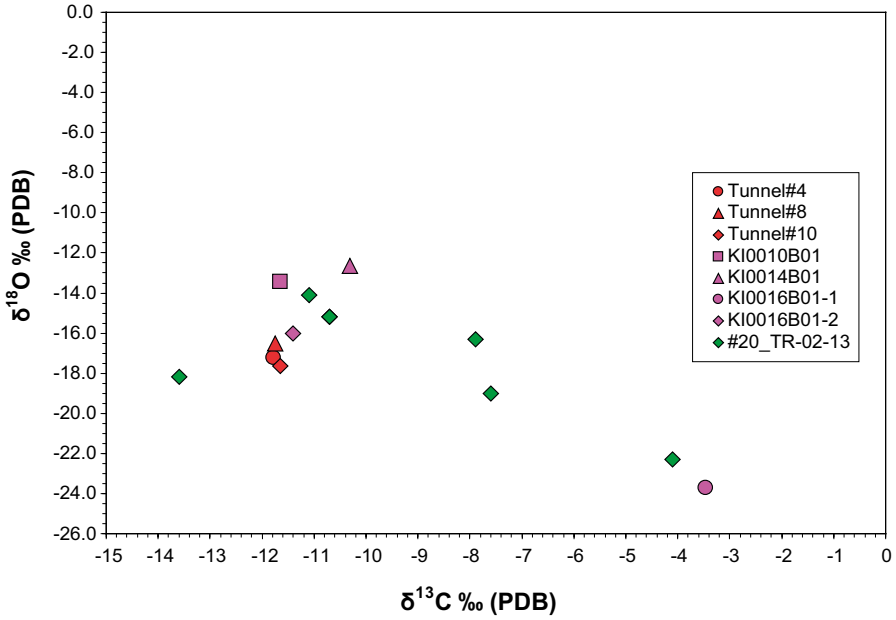

Figure 4-81. *$\delta^{18}O$ vs. $\delta^{13}C$ in calcite from Structure #20 in the TASS tunnel and TASS pilot boreholes shown together with calcite from Structure #20 from the TRUE Block Scale boreholes (in green).*

4.6 Integrated description of Structure #20 from borehole information

The planar geometry of Structure #20 inferred by the TRUE Block Scale Project, as extrapolated from the interior of the TRUE Block Scale volume to intercept the TASS tunnel, is comparable with the intercept interpreted by the TASS project. The location of geometrically inferred intercept is further sustained by pressure responses in the TRUE Block Scale array during drilling of the TASS tunnel pilot borehole KI0010B01. The collective evidence supports Structure #20 being across its known extent.

From a structural geology standpoint, Structure #20 exhibits a wide variety of morphologies across the array of structures studied. Structure #20 clearly represents a brittle shear zone developed from a ductile deformation zone pre-cursor that has been re-activated several times.. Well-developed foliations and changes in mineral size and proportions suggest that initial shearing may have started soon after crystallization of the parent rock. As observed during the TRUE Block Scale project (Andersson et al. 2002a), the current morphology of Structure #20 is a brittle fault within a previous ductile shear zone. Secondary splay fractures related to the core of the fault are common but appear to be confined to central parts of the structure (if one assumes that borehole KI0025F is intersecting near the margin of the structure.

Structure #20 is characterized by damage zones featuring increased frequency of sealed fractures, reductions in grain size of both phenocrysts and the groundmass of the Äspö diorite, the development of a weak foliation primarily expressed through preferred alignment of potassium feldspar phenocrysts, the presence of occasional thin layers or lenses of cataclasite, and the presence of swarms of fractures sealed with epidote. The deformation zone core typically consists of one to three open and flowing fractures within a larger zone of previous moderate to intense ductile deformation, which in turn is marked by alternating bands of mylonite and cataclasite. Occasionally, brecciation and re-mineralization are noted, as well as minor amounts of clay-rich fault gouge. There are few obvious kinematic indicators, but those available appear to indicate oblique slip with a relatively subordinate dip-slip component.

As Structure #20 was a key target of the TRUE Block Scale tracer experiment, significant work has been completed previously, with a focus on defining mass transport parameters along the deformation zone. The results of this body of work is contained in the TRUE Block Scale summary reports (Andersson et al. 2002a, Poteri et al. 2002, Winberg et al. 2003), which in turn reference earlier works conducted as a part of the TRUE-1 experiments (Winberg et al. 2000). For key conductors such as Structure #20, a detailed conceptualization of the volume (in terms of area of coverage and porosity) and type of geological material within the deformation zone pore space was presented. This conceptualization is summarized below in Figure 4-82. Of particular importance to radionuclide transport are the following lithologies (after Andersson et al. 2002a and Poteri et al. 2002):

- *Fine-grained fault gouge including clay minerals*. Fracture porosities are estimated to be greater than or equal to 10%. Fault gouge is important because of its relatively high porosity, combined with the presence of materials likely to retard radionuclides through sorption and diffusion.
- *Mylonite.* Fracture porosities are estimated to be approximately 0.3 to 0.6%. Typically, the mylonites are enriched in epidote, which possesses different retention properties than unaltered Äspö diorite. Previous work (de la Cruz et al. 2000) suggested that mylonites in Structure #20 consist of alternating bands of fine-grained epidote-rich bands alternating with coarse-grained quartz and plagioclase-rich bands. Mylonite is assumed to be part of the “altered wall rock” group of materials.
- *Altered wall rock/cataclasite*. Porosities of this material are estimated to be 0.5%–2%. Cataclasite is assumed to be in contact with mineral coatings on the open fracture walls which are the conductive features in Structure #20. Conceptually, cataclasites and mylonites are similar in their mineralogical characteristics, but form from fundamentally different processes. Mylonites signify conditions where deformation is almost exclusively ductile, while cataclasite is a cohesive fault rock formed in the brittle regime mainly by frictional flow. The end result is that while mineralogically similar, the surface area available for sorption and diffusion is likely to be different than that for mylonite.

Later works such as the Site-Scale modelling completed during Task 6C (Dershowitz et al. 2003) further conceptualized structural intercepts from a transport perspective as either Fault or Non Fault. An example of the simplified Fault cross-section is presented in Figure 4-83. Note the lack of mylonite as a distinct material phase; proto-mylonites are largely assumed to have transformed completely to cataclasite during brittle re-activation. Structure #20 is treated as if it was a Type 1 (Fault) feature.

BIPS image logs from one borehole, KI0025F03, were used to make quantitative estimates of the percentage of fault-rock materials with likely differing retention properties (Figure 4-39). Using image analysis techniques, the ratios of cataclasite, fault gouge, mylonite, and fault breccia were calculated. The results are presented in Section 4.4.2. As no similar study was done during TRUE Block Scale activities, it is impossible to make direct comparisons to previous studies. However, qualitative conclusions based not only on the KI0025F03 interpretation, but on the core and BIPS imagery analysis discussed earlier in this report include:

- Significantly less breccia and fault gouge than anticipated. Sampling conducted during the various TRUE Block Scale experiments showed significant amounts of clay-rich fault gouge in Structure #20 intercepts (Andersson et al. 2002a, Winberg et al. 2003). Some minor amounts of fault gouge were noted in the TASS pilot boreholes, but not nearly the same amount as was previously identified. Whether this is due to long-term erosion from experimental activities within the TRUE Block or as a result of washout during drilling is not known.
- Complex geometric relationship between mylonite and cataclasite in Structure #20 deformation zone cores. During the TRUE Block Scale tracer-transport tests, cataclasite and mylonite were assumed to be separate rock types, in contact with each other, but treated as separate immobile zones for transport calculations. This is not, however, the case. The mylonitic ductile shear zone may be the protolith, but there is likely significantly more interbreeding of cataclasite and mylonite, especially in the damage zones surrounding the fault cores. This has the effect of producing a 'hybrid rock' immobile zone, which is likely to have diffusion and sorption coefficients different than the parent materials.

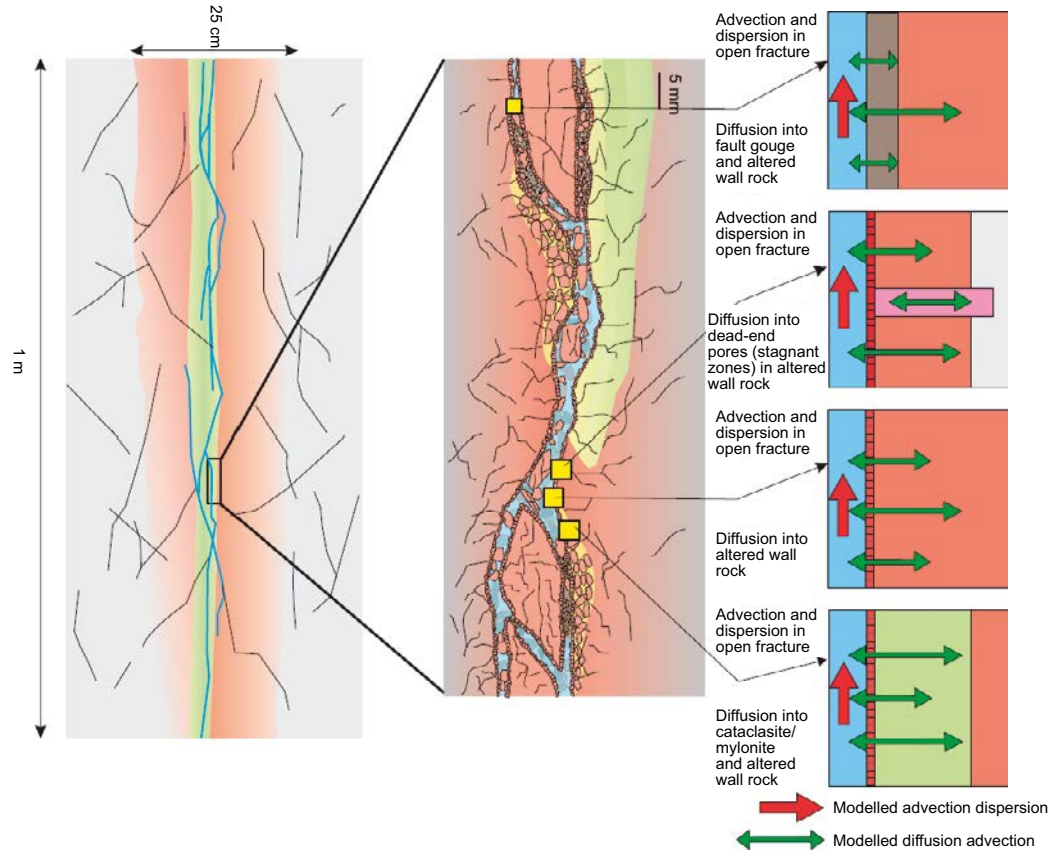

Figure 4-82. *Illustration of conceptual models for pore space inside significant structures within the TRUE Block Scale volume (from Poteri et al. 2002).*

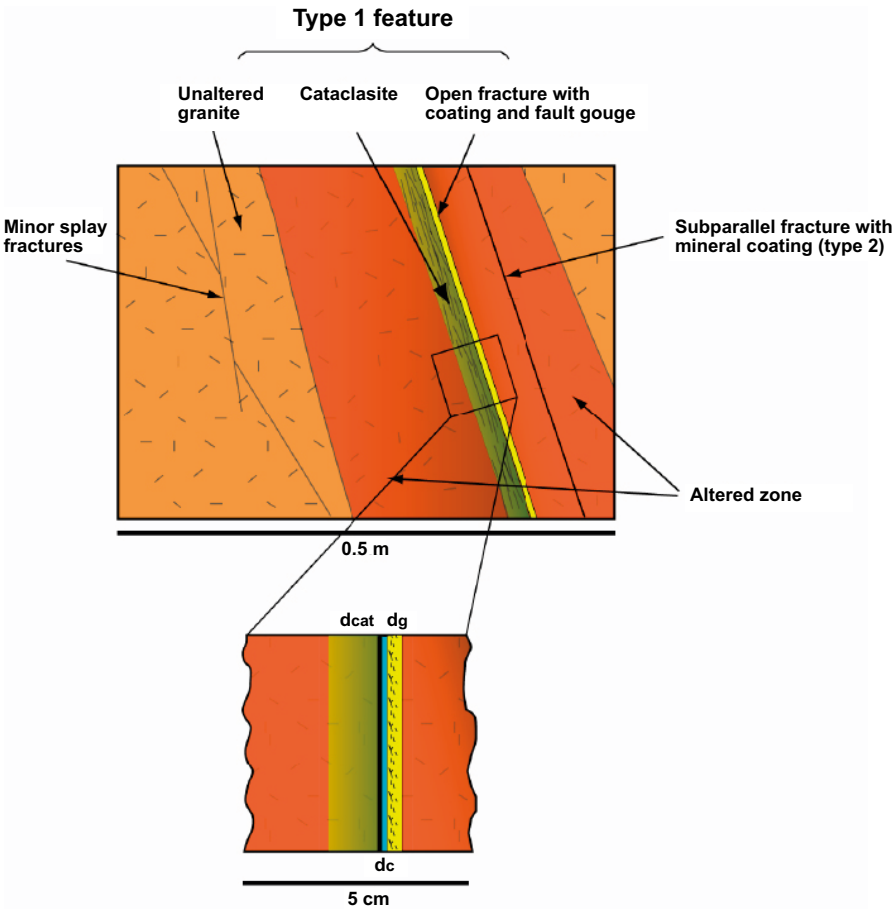

Figure 4-83. *Illustration of Geological Structure Type 1 (Fault). This schematic representation is taken from the TRUE Block Scale Task 6C summary report (Dershowitz et al. 2003).*

Overall, the general features of Structure #20 were similar for most intercepts. Whole rock chemistry of the core of the deformation zone showed only small variations, mainly related to the proportion of the dominant minerals and wall rock alteration and mineralogical assemblages showed similar features although with some variation. The general features were (in order of formation):

- Ductile origin; abundant mylonite (epidote- and quartz-dominated occasionally with abundant mica) was as a rule present in the core of the deformation zone and kinematic indicators were observed (e.g. C-S fabric, σ-type porphyroblasts/mantled porphyroclasts, oblique foliation and occasional C´surfaces).
- Cataclasite, often epidote-rich, with related offset of mylonite indicated. At least two generations of cataclasite were observed.
- Sealed fractures with Proterozoic massive calcite (based on stable isotopes) with thick twin-lamellae, euhedral epidote, quartz, hematite-stained adularia (K-feldspar), fluorite, pyrite (and prehnite) cut the mylonite and cataclasite.
- Brittle fractures, sealed, open or partly open, filled by (mainly) Paleozoic calcite (based on stable isotopes), fluorite, chlorite, clay minerals, adularia and pyrite.
- On the mostly smooth fracture surfaces of the presently open fractures, calcite was observed (partly euhedral, several generations observed) as well as abundant chlorite and clay minerals (illite or mixed-layer clay) and scattered occurrences of cubic fluorite and pyrite. Chlorite and clay minerals were mostly present in a thin smooth cover on the fracture surface, although euhedral individual crystals were observed as well. Striations were observed on chlorite and clay minerals (also on calcite). Quartz and Fe-oxides were found in minor amounts on the fracture surfaces. Wall rock minerals and epidote existed in minor clay mineral-rich (gouge) parts (not as frequently found as reported in Andersson et al. (2002a).

However, it should be noted that the features observed in the Structure #20 intercepts showed a slight variation between the different boreholes, such as varying thickness of mylonite, cataclasite, calcite fillings/coatings, amount of chlorite and clay minerals on the fracture surfaces, as well as in the frequency of epidote-sealed fractures, sealed networks and open and sealed calcite-filled fractures. Compiled point-wise borehole transmissivity data attributed to Structure #20 shows a variability between 2.5×10^{-8} and 7.1×10^{-6} m^2/s, i.e. variation over more than two orders of magnitude, cf. Table 3-2. Statistical analysis shows that the geometric mean and variance of the transmissivity of Structure #20 based on the TASS pilot and probe boreholes (N=6) differ within 45% of the "global mean" established based on all available data related to the structure (N=21), cf. Table 3-3. This finding suggests that the statistical sample for Structure #20 from the TASS pilot boreholes (representing a length scale of metres) may be regarded as representative of the "global statistical properties" of the structure (over length scale of several decametres).

5 Geological information from tunnel mapping

5.1 Objectives and scope

The TASS tunnel at Äspö, which was originally designed to evaluate hypotheses regarding excavation damage zones and grouting of faults and fractures, provides a very useful testing ground for further studies of deformation zone and MDZ-size features projected from the TRUE Block Scale volume. Extensive fracture mapping work was performed after the construction of the tunnel (Hardenby and Sigurdsson 2010); however, the mapping scope was not specifically focused on investigation fault rocks associated with specific deformation zone structures and characteristics. Therefore, a portion of this project was dedicated to the geometrical, geological, geological/structural and mineralogical analysis of Structure #20 in the TASS tunnel, with the aim to describe in detail its geological and hydraulic heterogeneity. The tunnel mapping occurred as an important complement to original TRUE Block Scale analysis, entirely based on borehole data, and to the re-analysis and mineral sampling of drill core and BIPS images from the TRUE Block Scale project and the TASS tunnel pilot boreholes made as part of this project.

The scope of the tunnel mapping efforts includes:

- Experimentation with high-resolution digital photography in the TASS tunnel, including HDR and UV fluorescence imaging;
- Structural geological mapping of the intercept of Structure #20 with the TASS tunnel, with a focus on the morphological characteristics of the intercept in terms of fracturing and fault rock types;
- Mineralogical sampling and chemical analysis of material from the Structure #20 intercept at the TASS tunnel. Samples of cataclasite, mylonite, breccia, altered wall rock, and fracture surface minerals were taken; and
- An initial attempt was made to digitize fracture trace maps using very-high resolution (~ 1 mm per pixel resolution) normal-light, UV-light and HDR photographic images. The goal was to show that, with the use of more advanced digital photography techniques, significant increases in data resolution (in terms of fracture patterns) could be realized.

The methodologies behind each of the tasks identified above are described in detail in Chapter 2 of this report (“Methods”).

5.2 Tunnel image acquisition and initial processing

Digital images of the TASS tunnel were acquired over a three-day period during December 2010. Normally, the photographic process should proceed very quickly. However, given that the photography efforts were an experiment, a significant amount of time was spent testing different combinations of lighting, camera positioning, image resolutions, and photographic methodologies. In particular, experimenting with the best way to illuminate the rock surface using the available small ultraviolet light provided by SKB took some time. However, the lessons learned during the photographic effort should pave the way for a smoother process during tunnel mapping in the future. The lighting systems used, and the tunnel geometries studied, are illustrated below in Figure 5-1.

The Nikon digital camera was placed on a tripod with a universal stage mount allowing for 360° of rotation; the camera and tripod were positioned along the tunnel centreline using surveyed painted markers scribed on the tunnel walls and tunnel pavement. The tripod was then ratcheted to its maximum elevation, so as to get the camera lens as close to the true centre of the tunnel as possible. This step was necessary in order to minimize the differences in image coverage from shot to shot, and to limit distortion due to multiple focal lengths. Both of these factors have the potential of inducing scale effects and artefacts when mosaics of the RAW images are constructed.

Figure 5-1. *Wide-angle photograph of the TASS tunnel, illustrating portable construction lights used for site illumination. Note the lighted section near the end of the tunnel; this is the location of the Structure #20 intersection with the TASS tunnel. The elongated rectangular slot along right side of the tunnel wall is the excavation from the Excavation Damage Zone project (Olsson et al. 2009).*

Digital images of Structures #20 were captured by rotating the camera around nodal point of the setup with the lens facing the tunnel wall. It is crucial that the camera and tripod are not moved laterally from their starting position during photography, and only rotated around the nodal point of the camera (in the vertical plane, perpendicular to the tunnel wall). The use of a geared universal stage (similar devices are used on astronomical telescopes and in optical mineralogy) allows for specific arc paths to be traversed extremely precisely, which minimizes distortion and makes the process of producing image mosaics much easier.

The image acquisition process consisted of several passes along predefined arcs along the tunnel wall. Each pass was sized such that the entire visible width of Structure #20, including damage zones, would be visible in the final results. For each section of the photographic arc, five images were captured, with a single f-stop change from image to image. “F-stop” is a dimensionless number describing the diameter of the entrance pupil (the hole in the shitter which allows light to reach the imaging sensor) in terms of the focal length (the distance at which the light passing through the camera lens narrows down to a point). The F-stop quantifies the speed of the camera lens and represents the amount of light the lens lets through. Each F-stop represents a 50% reduction in the amount of light getting through the lens to the imaging sensor. Taking different images at different exposures (F-stops) captures different aspects of the scene, and is the key to generating HDR (High Dynamic Range) images.

After the completion of the first (regular light and HDR) imaging run, a second run of capture was performed using the UV light for illumination. It was necessary to perform the UV illumination at the same time and position of the visible light images so as to produce a perfect alignment between the two image sets.

After all images had been captured, the resulting RAW files were downloaded to a laptop running LightRoom 3 and PTGui. The images were converted from NEF format to TIFF and/or JPEG. The images where stitched together using PTGui to generate a panorama that covers the fractured segment of the tunnel. The resulting images have a resolution of approximately 2 mm per pixel. The HDR images were generated in the same fashion, but required significantly more processing, as a total of five images were necessary in order to create each section of the tunnel panorama.

5.2.1 Photography at ordinary light (including HDR)

The first rounds of photographs of Structures #20 in the TASS tunnel were made using a single exposure in visible light, so as to provide a base set of images for tuning the alignment of the lights, the alignment of the camera, and for making the decision on the number of images necessary to produce a successful panoramic image. An example of the final work product for visible light is presented below as Figure 5-2. After a successful pass and mosaicking using single visible light imagery, a longer series of photographs designed to be used as input to HDR reprocessing were shot.

Given the relative novelty of the High Dynamic Range (HDR) image post-processing technique it is reviewed and discussed here in more detail. HDR post-processing is designed to increase the dynamic range captured in photographic images (High-dynamic-range imaging, n d). The "dynamic range" refers to the limits of luminance, which is a photometric measure of the intensity per unit area of light travelling in a given direction and falls within a given solid angle (Dynamic range, n d). The human eye has a maximum dynamic range of about 20 f-stops (contrast ratio of ~ 1,000,000:1), though on average the useful range of the human eye is 10–14 f-stops (contrast ratio of ~ 1024:1 to 16384:1). Within a single image, the contrast ratio for a high-end digital single-lens reflex camera (DSLR) is approximately 8–14 f-stops, depending on the model of the camera.

HDR imaging works by taking several images of the same scene, in series. Each image has a different shutter speed and lens aperture setting, which controls the amount of light entering the camera sensor. This allows for the imaging of sections of the rock mass cast in shadow (such as steeply-dipping fracture planes where a rock block has fallen out) while not over-correcting for well-exposed and well-lit sections of the scene.

The total dynamic range within the TASS tunnel image, calculated using software and the initial single visible-light, was 11 EVs (Exposure Value). 1 EV is equivalent to a single f-stop. The digital camera used in this project, a Nikon D200, has a theoretical dynamic range of 12 EV at its base speed of 100 ISO[1]. This implies that a single image is enough to capture the entire dynamic range available in the TASS tunnel. However, experience has shown that it is still useful to capture additional images, as it is common to lose information in a single exposure due to noise in the shadow areas and by possible "blown highlights" (the bright areas of an image where all detail has been lost).

Figure 5-2. *Visible light image of a portion of the Structure #20 intercept within the TASS tunnel. This image has been extensively re-sized using Photoshop so as to fit into the report. The processed image on which this photography is based is 26,040×5,149 pixels, with a total file size (JPG) of 88.8 MB. The non-lossy TIFF version is 1.03 GB in size. The photograph is oriented such that the left edge of the photo represents the left wall of the TASS tunnel if you are facing the far end (SW) of the tunnel.*

[1] ISO is a concept descended from film photography, and is a measure of the film's sensitivity to light. Low ISO slow film (such as the classic Kodachrome, with speeds of ISO 24/40/64), requires much more exposure to light than does a high ISO fast film (ISO film of 400–800 are commonly used by sports photographers). The higher the ISO number, the lower the quality of the resulting film image; fast film, while useful in catching objects in motion, often appears very grainy. For digital cameras, the ISO value is effectively the relationship between the signal gain of the imaging sensor and the "lightness" of the finished image when it is interpolated into an image colour space (such as sRGB).

A process known as exposure bracketing, in which images are taken at greater and lesser exposure values (EVs) than the starting image, was used during image acquisition to provide enough information to create HDR renditions of the Structure #20 intercept. In the imaging of Structures #20 in the TASS tunnel, exposures were bracketed by ± 2 F-stops, resulting in a series of five images for each scene. However, after processing the test run, it was found that, in a well-illuminated rock tunnel such as TASS, it was only necessary to take a total of 3 images, one master image and two bracketing (+1 and –1 EV) to capture the available dynamic range of the rock surface.

HDR is very similar in technique to the multispectral imaging techniques used by remote sensing analysts to capture more information by broadening the spectrum of light sampled. However, the HDR image is not really a format that a human can easily view. It is a wide spectrum representation of light. Only parts of the whole dynamic range can be presented on a normal screen or in photographic prints; they have a significantly smaller dynamic range (a typical LCD screen has a contrast ratio of 700–1,000:1, up to about 9.5 f-stops) than either the image sensor or the human eye.

In order to print a HDR image it needs to be processed to fit within the dynamic range of the printer. This can be done by compressing the dynamic range or by applying selective exposure to select the part of the dynamic range that shows the most detail for that area. This latter technique, known as tone mapping, reduces the total dynamic range of the image (removing the very light and very dark sections) while retaining and enhancing local contrast between individual pixels. Tone mapping has been used extensively in recent years as an art form, with over-compressed images (Figure 5-3) taking on a surreal quality. Tone mapping allows for the use of different exposures in the shadows created by rock fractures from those on the well-exposed rock surface.

An example of the resulting tone-mapped image of Structure #20 in the TASS tunnel is presented as Figure 5-4. It is difficult to see a difference in the printed photograph, but the HDR image is overall lighter, with fracture traces standing out better, as if a sharpen filter had been run on the image. A comparison of a single-exposure to an HDR exposure is presented below as Figure 5-5. The best use of the HDR imagery is as an overlay in the GIS interpretation process (Section 5.4.2), or in collaborative interpretations of images where extracting detail from shadows is important.

Figure 5-3. *Example of a highly contrast-compressed tone mapped image. Notice the surreal, almost neon appearance of the photograph. Image courtesy Pedro Szekely, and is used in accordance with the Creative Commons 2.0 license.*

Figure 5-4. *HDR image, after of a portion of the Structure #20 intercept within the TASS tunnel. This image has been extensively re-sized using Photoshop so as to fit into the report.*

Figure 5-5. *Side-by-side comparison of a close-up section of the visible light (left) and HDR (right) image. Notice the significant enhancement of detail in the shadowed areas.*

5.2.2 Photography in UV light

Fluorescence is the emission of light by a substance that has absorbed light, or any other electromagnetic radiation of a different wavelength. Typically, the emitted light has a longer wavelength (and a corresponding lower energy) than the absorbed radiation. In minerals, fluorescence is often observed when rocks are illuminated with shortwave or long wave ultraviolet light (UV). The most common minerals to exhibit fluorescence are fluorite (blue to violet) and calcite (just about any colour, depending on the contaminant contained in the crystal structure).

The goal of the UV photography was twofold:

- Increase the ability to detect thin calcite-sealed fractures, in the hope of better constraining the total fracture intensity within the damage zones of Structures #20; and
- Better pinpoint the locations of inflow into the TASS tunnel. Groundwater typically contains minor to moderate amounts of dissolved calcite, which will precipitate and stain at open fractures.

Initially, the project setup was intended to use two 35-watt UV lights as illumination sources. However, availability of such lights was limited, and, combined with access and health/safety considerations, only a single handheld UV light was used for illumination. This light source, however, was sufficient to demonstrate the feasibility of UV imaging in the TASS tunnel. An example of the output of the UV fluorescence photography is presented as Figure 5-6.

Because of the need to have a totally dark environment in order to see and take photos of the fluorescing minerals, the digital camera required the use of focus assist lights in order to allow for properly-focused photos. This was accomplished by attaching a flashgun with built-in focus assist lamps to the camera, but turning off the flash strobe light. The focus assist on flashguns usually consists of an illumination grid pattern from lasers or LEDs in the infrared light range projected on to the surface that will be photographed. The focus assist measures the distance to the objects in the photograph scene, and, in combination with the autofocus functionality of the digital single-lens reflex (DSLR) camera, automatically selects the correct focal length. This method works much better than having to turn on and off the UV and white lights when taking photos.

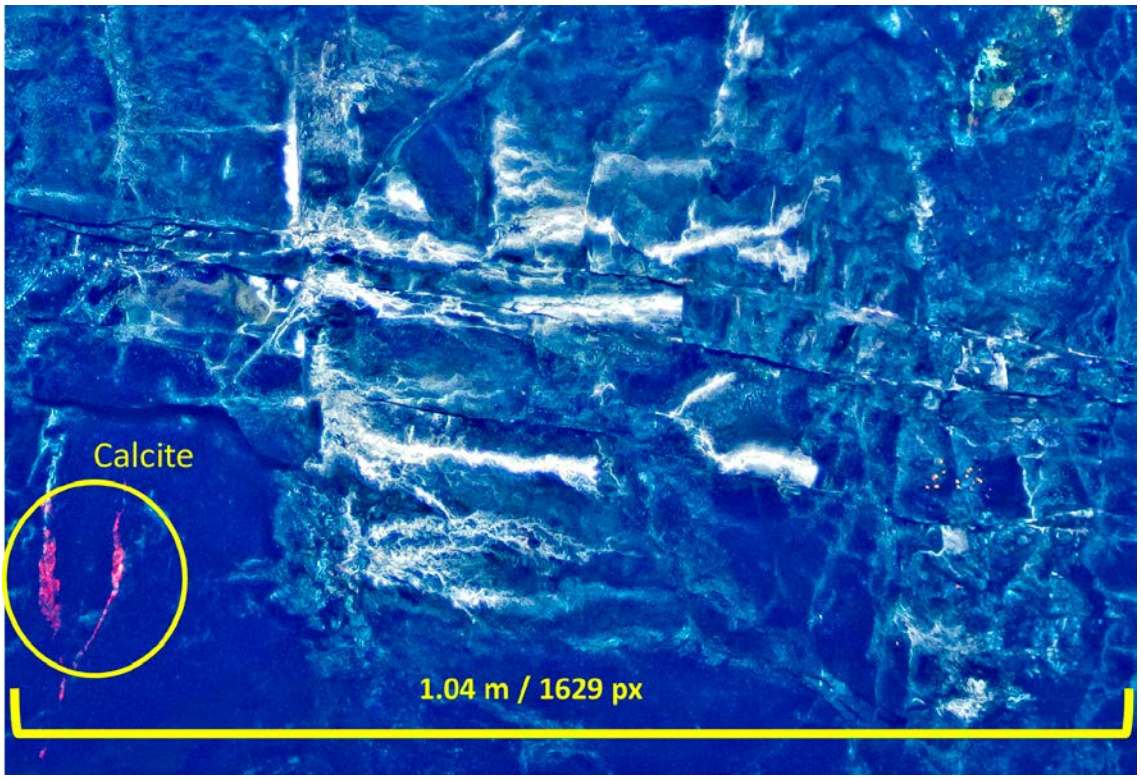

Figure 5-6. *Close-up section of the UV fluorescence image. White colour is mostly silica sol grout leaking from flowing fractures. Note that it is slightly easier to see some fractures due to calcite filling, but overall the image quality is much poorer than the HDR and visible-light imagery. Yellow bar indicates approximate image scale.*

This project only captured visible light images due to UV-induced fluorescence. In order to capture images directly in the UV spectra, a specially-built camera is needed. Modern digital cameras have an extremely efficient UV filter in front of the image sensor, to prevent the degradation of visible light images. In addition, the camera autofocus system needs to be recalibrated to compensate for the different path the UV radiation takes through the lens; otherwise the image will be out of focus. Thankfully, direct UV emission is neither particularly common nor useful in fracture or mineral analysis.

The best use of the UV fluorescence photography is as a transparent overlay on top of visible-light or HDR imagery. Photographic prints of the UV images themselves are not particularly useful. To properly benefit from the resolution enhancement an interactive medium, image editing software such as (Photoshop, the GIMP) or image interpretation software such as (ArcGIS, IDRISI, or any other commonly-used remote sensing software) is needed in order to pan, zoom, and turn image transparency on and off. The difference in appearance between the UV florescent light image and the visible light image makes it very hard to find the same spot on both images. This implies that careful georegistration should be done for all three types of images before mapping is performed.

All three types of images (visible light, HDR, and UV fluorescence) are used in the tunnel fracture trace mapping (Section 5.4). The visible light image is used as the base image for mapping, given its minimal number of processing artefacts and high resolution. The HDR images are used to visualize portions of the fractures that are in shadow, such as those hidden by overhangs. The HDR images are also very useful for distinguishing between fracture faces formed by blasting (wedge failures) and for locating the edges of fine-grained granite dikes and epidote veins. The UV fluorescence images are primarily used to confirm the presence or absence of calcite, to pinpoint leaky fractures from both silica sol grout influx and from calcite precipitated on the tunnel walls.

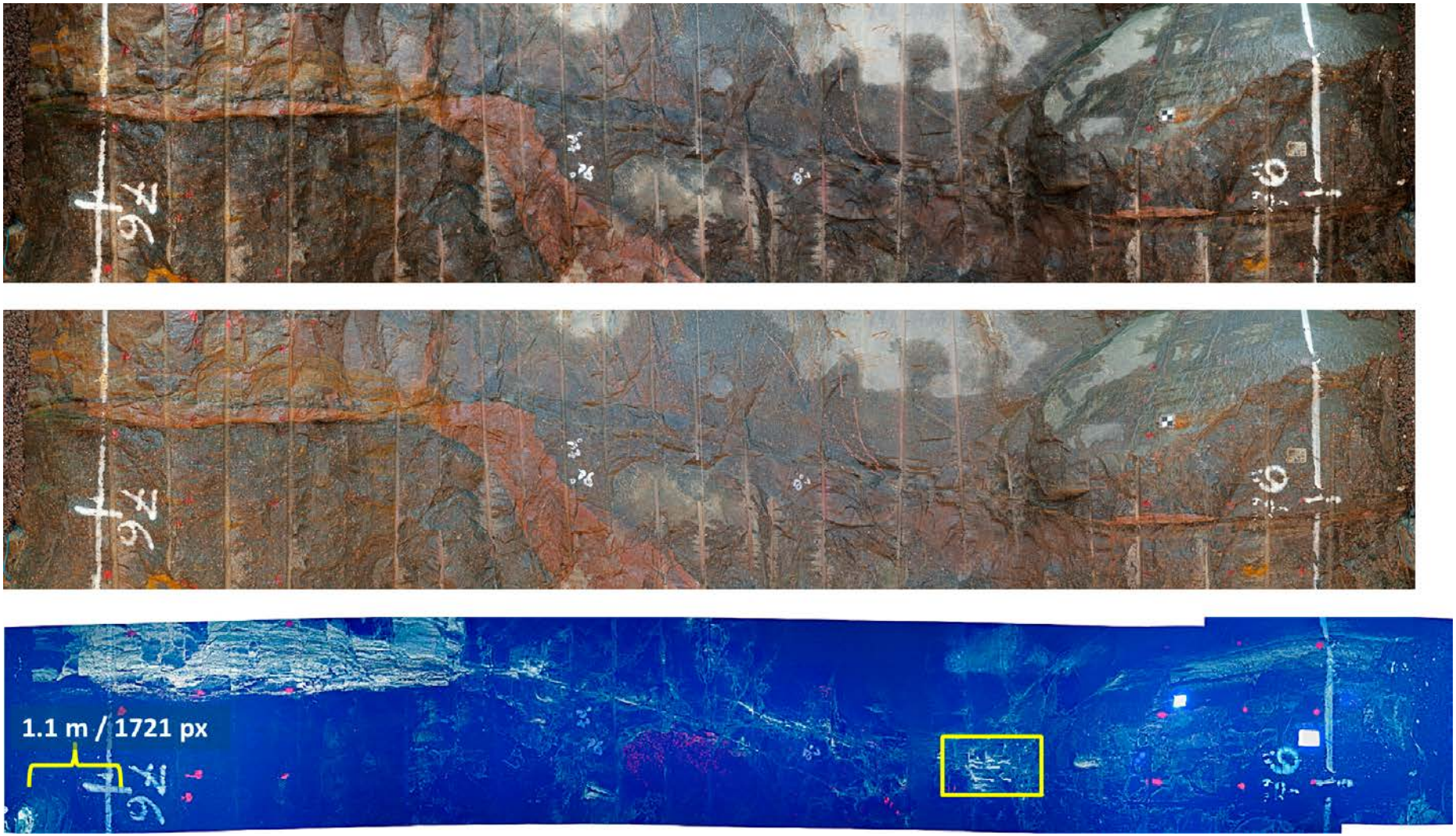

Figure 5-7. *Structure #20 full-perimeter photomosaic in visible light (top), after HDR reprocessing (middle), and using UV fluorescence (lower). The yellow box on the UV image illustrates the location of the close-up section presented in Figure 5-6. The A wall (left, if you are facing the end of the TASS tunnel, which points southwest) is on the left side of the images. The deflection of the fine-grained granite dyke (upper two images) may indicate that the dike was emplaced syn- to late-ductile shearing.*

5.2.3 Lessons learned from tunnel imagery

The use of UV fluorescence and HDR photography as part of the TASS tunnel mapping in this study should be regarded as an experiment designed to add additional value to the existing tunnel mapping protocol (including use of RoCS) with a minimum amount of additional work. In terms of producing high-quality images for digital mapping, the project was successful. The key lessons learned while working on this aspect of the BS-TASS project were:

- In order to successfully capture HDR images a large number of stationary high-intensity lights are required. Portable flashguns do not have significant power to over-expose the scene, especially when attempting to image the tunnel roof. The portable high-intensity LED lights provided by SKB were excellent for the task. It is recommended to use at least six different lights for illuminating features of the size of Structure #20. It is important to move the lights as little as possible. Every movement will change the image shadows and make the images harder or impossible to stitch together automatically. One flash, mounted on the camera, should be used to minimize the shadows cast by the lights illuminating the tunnel by firing directly at the features in the same angle as the camera lens points.
- The handheld UV light used during this work was adequate for its intended purpose, but was not ideal for geoscientific use. For future work, two 35-watt UV lights, with an illumination circle large enough to cover the entire photographic scene (for a single image), would be ideal for taking UV fluorescence images in a more controlled fashion. Also, a very fast (*f*2 to *f*2.5) lens is highly recommended; this will allow for the use of reasonable shutter speeds with minimal image noise or distortion.
- The UV light photography effort was not as successful as hoped for. The silica sol grout, which is a colloidal version of silica (SiO_2) that was used to pre-seal the tunnel before excavation, is often mixed with an optical brightener that fluoresces in UV light. Significant grout leakage from fractures around Structure #20 made it difficult to pick up individual small sealed fractures in UV.

A HDR image is best viewed on a computer screen using software that provides the ability to zoom, pan, turn on and off image overlays, and to interactively change the visible dynamic range by tone-mapping from the image stack. This allows for the interpreter to compensate for "blown highlights" (assuming the camera has recorded sufficient information in the RAW data file) or to dynamically lighten shadows. The creation of adequate and useful HDR images is very much an art form, and it is highly recommended that an experienced photo interpreter/artist be included during the image processing.

5.3 Geological mapping of Structure #20 in the TASS tunnel

5.3.1 Analysis of fracture data from TMS

Geological mapping during the construction of the TASS tunnel (Hardenby and Sigurdsson 2010) indicated the presence of two primary fracture sets: a roughly east-west striking, steeply-dipping set and a subhorizontal to gently, predominantly north-dipping set with poorly-constrained strikes. A third subvertical set of lesser intensity striking roughly north-south was also recorded. The most common fracture mineral appears to be chlorite, followed by calcite, epidote, and prehnite in order of decreasing abundance. An orientation dependence on fracture mineral infilling was noted; gently-dipping fractures were dominated by chlorite and prehnite infilling, while steeply-dipping features predominantly hosted calcite and epidote. Planar features (suggestive of jointing, rather than shear fracturing) with rough surface morphologies dominate the fracture database from the mapping during the construction of the TASS tunnel. A relatively small (0.57%) amount of all fractures exhibited direct evidence of shear motion (slickensides). Observations of displacement and shear offset are uncommon, but present; most displacements, including the largest ones (0.8–1.2 m of offset) occur along the subhorizontal to gently-dipping features.

Several deformation zones were mapped within the TASS tunnel. The zones have been classified into two categories:

- Deformation zones with increased fracture intensity, with thicknesses ranging from 0.5 m to 8 m. Observations of these zones are confined largely to the floor of the tunnel; and
- Deformation zones represented by tunnel-cutting steeply- to moderately-dipping brittle/ductile zones, with zone core thicknesses in the order of 0.1 to 0.3 m.

In the vicinity of the Structure #20 intercept, Hardenby and Sigurdsson (2010) report that the TASS tunnel is dominated by fresh, unaltered Äspö diorite. Areas of chemical alteration and oxidization/ red-staining are included in the TMS maps as "hybrid rock". However, it is noted that beyond chainage ~ 73.00 m, the distribution of rock types becomes more irregular. This area happens to also coincide with the interpreted location of the Structure #20 intersection (~ 75.00 m). Stereonets of fracturing within this block of the tunnel are dominated by subhorizontal to gently-dipping features; this was readily apparent on the tunnel walls, and is discussed briefly in the 2D fracture trace map (Section 5.4.1).

5.3.2 Mapping of Structure #20 in the TASS tunnel

The methodology employed in the mapping of the intercept of Structure #20 with the TASS tunnel is described in detail in Section 5.2. The description of Structure #20 takes advantage of the "half-pipes" of blast holes remaining from tunnel excavation. These features are roughly uniformly distributed along the tunnel wall, and possess finite start and endpoints that could be easily surveyed in using an electronic total station.

Structural geological mapping was performed at 23 different blast holes, beginning at blast hole 1 (located ~ 1 m elevation above the tunnel floor on the TASS "A" wall, northern wall) and ending at blast hole 23 (~ 0.9 m elevation above the tunnel floor on the TASS "B" wall, southern wall). The coordinates of the intersection of the blast holes with the chainage 76+00 m arc along the tunnel ceiling and walls are presented in Table 5-1; each mapped section is approximately 2 m long, extending from chainage 74.00 to 76.00 m for the A wall and from chainage 75.00 to 77.00 m for the B wall. No magnetic declination was set on the compasses used to map fracture orientation; all orientations are with respect to magnetic north. The right-hand-rule method was applied when measuring orientations. The geometry, geology, and mineralogy of the Structure #20 intercept are described blast-hole by blast-hole in the following section, rather than in tabular form. A complete continuous photographic depiction of the intercept is shown in Section 5.2, while preliminary fracture trace maps are shown in Section 5.4.1. A summary of the observed Structure #20 damage zone and core thicknesses is presented in Table 5-2.

Table 5-1. Coordinates of intersection of blast holes used in Structure #20 mapping with the tunnel perimeter arc at the 76 m chainage. All coordinates are according to the Äspö 96 system.

Blast hole number	X (m)	Y (m)	Z (m)	Height above tunnel floor	Horizontal distance from centre line	Distance recorded at section
1	7,201.888	1,899.816	–446.681	1.100	–2.164	76
2	7,201.963	1,899.753	–446.297	1.484	–2.067	76
3	7,201.899	1,899.806	–445.919	1.862	–2.150	76
4	7,201.885	1,899.819	–445.487	2.294	–2.169	76
5	7,201.830	1,899.865	–444.821	2.960	–2.240	76
6	7,201.743	1,899.938	–444.484	3.297	–2.354	76
7	7,201.841	1,899.855	–444.086	3.695	–2.226	76
8	7,201.967	1,899.750	–443.569	4.212	–2.062	76
9	7,202.184	1,899.568	–443.362	4.419	–1.778	76
10	7,202.454	1,899.341	–443.091	4.690	–1.426	76
11	7,202.768	1,899.077	–442.980	4.801	–1.015	76
12	7,203.109	1,898.791	–442.818	4.963	–0.57	76
13	7,203.447	1,898.508	–442.746	5.035	–0.129	76
14	7,203.843	1,898.176	–442.637	5.144	0.387	76
15	7,204.438	1,897.676	–442.848	4.933	1.164	76
16	7,204.989	1,897.214	–443.192	4.589	1.884	76
17	7,205.375	1,896.890	–443.622	4.159	2.387	76
18	7,205.513	1,896.775	–444.141	3.64	2.567	76
19	7,205.323	1,896.934	–445.093	2.688	2.319	76
20	7,205.258	1,896.988	–445.5	2.281	2.235	76
21	7,205.256	1,896.990	–445.987	1.794	2.232	76
22	7,205.363	1,896.900	–446.418	1.363	2.372	76
23	7,205.337	1,896.922	–446.909	0.872	2.338	76

Blast Hole 1:

The ‘upper’ damage zone extends from 74.54 m to 75.18 m (64 cm), the zone core extends from 75.18 m to 75.40 m (22 cm), and the ‘lower’ damage zone extends from 75.40 m to 75.47 m (7 cm). Structure #20 intersects and localizes against a dike of fine-grained granite from 75.23 m to 75.35 m. At this blast hole, the Structure #20 deformation zone core contains of a single open, water-conducting fracture inside a zone of highly mylonitized rock; this fracture has the orientation 127/85. The damage zone is defined in terms of increased amount of parallel-striking sealed fractures (sealed fracture network). No grain size reduction was observed in the damage zones. A sealed fracture in the damage zone has the orientation 136/89. One sealed fracture is cataclastic with red-staining around it.

Blast Hole 2:

The ‘upper’ damage zone extends from 74.48 m to 75.185 m (70.5 cm), and is characterized primarily by the increase in sealed fracture intensity. No foliation or ductile fabric is visible until the zone core is reached. However, there is evidence of a grain size reduction, increasing with decreasing distance from the fault core. The epidote-filled sealed fracture network (“marker bed”) extends from 74.94 m to 75.07 m, and consists of five closely-spaced, subparallel, steeply-dipping epidote-filled veins/fractures.

Structure #20 intersects and localizes against a dike of fine-grained granite from 75.22 m to 75.38 m. The deformation zone core of Structure #20 at Blast Hole 2 extends from 75.185 m to 75.40 m (21.5 cm), and is characterized by a single steeply-dipping open fracture with significant (~ 2 mm aperture and visibile water flow inside a zone of strongly mylonitized rock. The surface morphology of the open fracture is rougher and less planar than the intercept in Blast Hole 1. The open fracture appears to be partially filled by a mix of calcite, quartz, and adularia.

The ‘lower’ damage zone extends from 75.40 m to 75.48 m (8 cm) and is much narrower than the ‘upper’ damage zone, with no ductile fabric or grain size reduction, and can only be roughly identified by the increased intensity of sealed fractures.

Blast Hole 3:

The ‘upper’ damage zone extends from 74.56 m to 75.16 m (60 cm), the zone core extends from 75.16 m to 75.40 m (24 cm), and the footwall damage zone extends from 75.40 m to 75.48 m (8 cm). The ‘upper’ damage zone is marked by a network of five sealed epidote-filled fractures from 74.92 m to 75.02 m. The zone core is well-delineated in this blast hole, with distinct cataclastic zones and well-defined mylonite bands with an orientation of 135/84. The lower part of the zone core is made up of approximately 25% cataclasite, with a high intensity (9 fractures in 5 cm) of sealed fractures. The upper part of the zone core has less than 5% cataclasite, and is predominantly a well-banded mylonite. Structure #20 extends into the fine-grained granite from 75.25 m to 75.35 m; the primary expression of the zone core is in the fine-grained granite and is represented by an open fracture with an orientation of (139°, 86°) and a visible 2 cm step-over. Mineral coatings inside the open fracture consist of calcite, quartz, and potassium feldspar. The ‘lower’ damage zone is very similar to what was observed in Blast Hole 2; no reduction in groundmass or phenocryst size and a transition to a lower intensity of sealed fractures. A very weak foliation of subparallel alignment of feldspar phenocrysts is noted.

Map Section 1:

Map Section 1 represents a panel of the A-wall mapped in more detail than the blast holes; a screenshot is shown below as Figure 5-8. The map section extends from chainage 74.00 to 76.00 m, and is located approximately 2 m above the tunnel floor, just below Blast Hole 4. Map sections were logged in higher detail than regular blast holes, with photographs taken to document the logging.

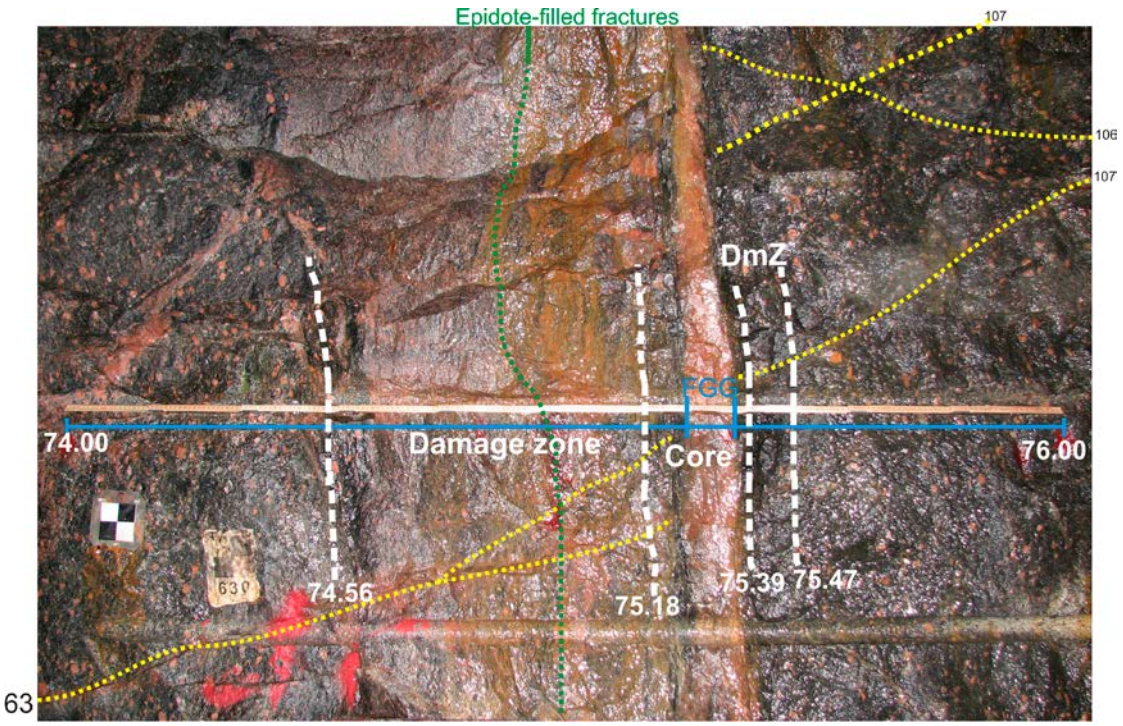

Figure 5-8. *Photograph of Map Section 1 with wooden marker ruler and epidote-filled fractures (yellow dashed lines).*

Upper damage zone: 74.56–75.18 m

A very strong contrast to the host rock is noted at the start of the damage zone. The damage zone is characterized by a change in the grain-size of K-feldspar phenocrysts and the beginning of a foliation. The foliation is oriented roughly vertical, and is characterized by a weak banding of light and dark minerals and a preferred orientation of feldspar phenocrysts. A swarm of sealed epidote-filled fractures is present from 74.88 m to 74.92 m; all of the fractures/veinlets are less than 1 mm thick and have an approximate orientation of 87/85. Sealed fracture intensity peaks from 75.00 m through the zone core. The damage zone foliation increases towards the zone core and eventually transforms into mylonite. The rock surface is coated with a mix of silica sol and grout that has exuded from open fractures, as well as a reddish-orange iron oxide coating; this makes it difficult to estimate fracture frequency.

Zone core: 75.18–75.39 m

The core of Structure #20 at Map Section 1 is characterized by the presence of hybrid rock (a mixture of Äspö diorite, fine-grained granite, and strongly-sheared rock). The fine-grained granite actually divides Structure #20 into two distinct zones. On the 'upper' side of the granite dike, the wall rock is strongly mylonitized, with seven visible alternating light/dark bands of approximately 1–6 mm thickness. The lighter bands appear to be quartz-rich. Within the 'upper' portion of the Structure #20 core, the mylonitized part of the zone core features no to only a few wall-rock fragments and little or no cataclasite. The zone core contains four open fractures within a 6 cm thick band. The orientations of the two measurable open fractures are 104/83 and 108/87. The open fractures appear to represent pre-existing planes of weakness in the mylonite (possibly contacts between mica-rich layers) opened along the pre-existing mylonite fabric.

Inside the fine-grained granite (75.26 m to 75.35 m), a very weak mylonitic fabric (much weaker than the ductile fabric expressed in the surrounding Äspö diorite) is present. The main evidence of brittle deformation within the fine-grained granite is the presence of a high intensity (17 fractures in 9.5 cm) of sealed fractures oriented subparallel to both Structure #20 and the fine-grained granite dike. The fractures are filled with calcite, feldspar, and chlorite.

The ‘lower’ side of the Structure #20 core is strongly mylonitized, with roughly the same spacing and size of mylonitic bands as at the other side of the fine-grained granite. The number of mylonitic bands is fewer (5) than on the other side. The mylonitic bands are grey in colour and are probably quartz-rich. Small amounts of epidote-rich cataclasite are also present. Seven sealed fractures exist within 2.5 cm, and strike sub-parallel to each other and to the mylonite fabric. The intensity of sealed fracturing drops very quickly with increasing distance from the fine-grained granite dike; this appears to be a characteristic of the Structure #20 ‘lower’ damage zone. One partially open fracture is present at 75.36 m. This fracture has an orientation of 134/84 and is coated with calcite, feldspar and chlorite.

Lower damage zone: 75.39–75.47 m

The ‘lower’ damage zone consists of a slight reduction in the grain size of K-feldspar phenocrysts and a gradual elimination of the pervasive rock foliation. Sealed fracture frequency is approximately 4 sealed fractures over a roughly 9 cm span.

Blast Hole 5

At Blast Hole 5, the interpreted ‘upper’ damage zone of Structure #20 extends from 74.48 m to 75.19 m (71 cm), the zone core extends from 75.19 m to 75.35 m (16 cm), and the ‘lower’ damage zone extends from 75.35 m to 75.40 m (5 cm). A set of three epidote-filled sealed fractures are found between 74.84 and 74.89 m; these epidote fractures serve as a “marker bed” locally indicating the start of the damage zone around Structure #20. The rock within the ‘upper’ damage zone begins with a weak foliation which increases to moderate intensity before grading into mylonite at the damage zone/zone core boundary. As in other blast holes, the foliation consists principally of a preferential orientation and stretching of feldspar phenocrysts. A gradual reduction in the size of the feldspar phenocrysts is also noted.

The zone core is characterized by intense mylonitization and the presence of cataclasite; approximately 15% of the zone core is epidote-rich cataclasite. The mylonite bands are approximately 2 to 4 mm thick. A sealed fracture parallel to the mylonitic bands has an orientation of 133/88. The deformation zone core is again bisected by a fine-grained granite dike; as previously mentioned, it seems likely that Structure #20 is localizing along the Äspö diorite/fine-grained granite contact. The ‘upper’ side of the deformation zone core has six sealed and one open fracture. The fine-grained granite dike is again observed between tunnel length 75.25 to 75.31 m. There is an open fracture at 75.33 m, within the fine grained granite. At the boundary between the fine-grained granite and the surrounding mylonite, an open fracture with orientation 131/85 is coated by both calcite and earlier-formed epidote; this suggests it has been re-activated in the brittle regime at least twice. The ‘lower’ side of the DZ core has one partially open fracture coated in calcite; approximately 10% of the core is cataclasite. As seen in Map Section 1 above, the ‘lower’ side of the zone core is much thinner than the ‘upper’ side.

The ‘lower’ damage zone is defined solely in terms of the intensity of parallel-striking sealed fractures (i.e. a sealed fracture network). No grain size reduction is observed and only a very weak foliation exists.

Blast Hole 7:

At Blast Hole 7, the ‘upper’ damage zone begins at 74.26 m along the tunnel, and extends to 75.05 m. The upper damage zone is characterized by a spike in sealed fracture intensity (nine sealed fractures within a ~ 20 cm thickness), which increases towards the deformation zone core, a decrease in the average phenocryst grain size, and the development of a weak foliation.

The transition from damage zone to deformation zone core (75.05–75.17 m) occurs at the start of mylonitization of the host rock. Within the Structure #20 core, there are two open, currently seeping fractures approximately 2 cm apart. The fractures are partially filled/coated with epidote, quartz, and a minor amount of calcite. In addition, it appears that minor amounts of both conventional grout and silica sol are present at points along the open fractures. Both mylonite banding and a

boudinage texture in feldspar phenocrysts is present, but is difficult to see everywhere due to iron oxide precipitation. In between the open fractures, there are bands of epidote-rich cataclasite. The deformation zone core is terminated at the contact between the host rock (Äspö diorite) and a fine-grained granite dike.

The 'lower' damage zone (75.17–75.41 m) is entirely within the fine-grained granite dike, and is marked by a subparallel sealed fracture network (11 fractures within a 20 cm length). No foliation or grain-size reduction is observed, though the latter is likely due to the largely aphanitic texture of the fine-grained granite.

Blast Hole 9:

The start of the upper damage zone in Blast Hole 9 (74.94–75.01 m) is based on the development of a foliation, which is expressed through a preferred sub-parallel alignment of feldspar phenocrysts. There is no observable grain-size reduction in the phenocryst fraction in this blast hole. Near the start of the deformation zone core, an increase in sealed fracture intensity (nine fractures over a 20 cm length) is noted; these fractures are filled with a mixture of quartz and epidote.

The deformation zone core of Structure #20 (75.01 m to 75.16 m) starts at a thick epidote-filled fracture; the same fracture is also noted at blast holes 11, 13, 15, 18, and 20, in Map Sections 2 and 3, and in several of the cored drillholes in the TRUE Block. Colloquially, the authors have referred to this fracture as a "marker bed" for Structure #20. In reality, however, it is likely that this structure is one of a swarm of veins that have been re-activated in the brittle regime. The epidote-filled fracture is 5 mm thick and partially cataclastic.

Towards the centre of Structure #20, the deformation zone core becomes mylonite-dominated; it is dark in colour, suggesting the mylonitic bands are rich in chlorite and quartz. There are 2–4 mm thick cataclastic bands within the mylonite. A large partially-open fracture within the core shows at least two generations of fracture mineralization: an original epidote filling, followed by a brittle re-activation during which (or after which) calcite and pyrite were deposited in the new void space. The deformation zone core is intensely fractured, with 16 sealed fractures and two open fractures within a 15 cm length. Open fracture apertures are in the range of 0.5–1.5 mm. As in Blast Hole 7, the deformation zone core terminates at the boundary between the fine-grained granite and the host Äspö diorite.

The lower damage zone (75.16–75.58 m) is contained entirely within the fine-grained granite dike, and is marked by the presence of an increased intensity of sealed fractures. Sealed fracture P_{10} values in the damage zone range from 50–110 1/m (5 to 11 sealed fractures within 10 cm lengths). No foliation or grain-size reduction is observed in the fine-grained granite.

Blast Hole 11:

The start of the upper damage zone (75.04–75.26 m) is recorded by a network of epidote-filled sealed fractures between 75.04 m and 75.06 m. The sealed fracture network (re-activated veins) has the orientation 128/82. The rock volume between the epidote fracture network and the Structure #20 core is marked by an increase in sealed fracture intensity and a weak foliation visible as a preferred alignment of feldspar phenocrysts.

The deformation zone core (75.26–75.35 m) of Structure #20 is thinner at Blast Hole 11 than elsewhere in the TASS tunnel. However, it is very strongly mylonitized, with numerous parallel bands approximately 2 mm thick. The deformation footprint is strong enough that the rock within the deformation zone core appears laminated, with planes of weakness at the contacts of light and dark minerals in the mylonite. No open, leaking fractures were noted in the deformation zone core at Blast Hole 11; only one partially-open fracture with calcite filling was noted. This fracture was oriented subparallel to Structure #20.

The lower damage zone of Structure #20 (75.35–75.62 m) at Blast Hole 11 is defined in terms of an observed increase in sealed fracture intensity; the fractures are mineralized shut with quartz cement. The damage zone has a fracture intensity of 7 fractures within a 27 cm length.

Blast Hole 13:

The start of the upper damage zone (75.32–75.54 m) in Blast Hole 13 occurs at an epidote-filled fracture; this is the 'marker bed' referred to in previous blast holes. The epidote-filled fracture thickness is approximately 7 mm, and is partially mylonitized. The upper damage zone is characterized by a reduction in the grain size of potassium feldspar phenocrysts and increased sealed fracture intensity. There are six sealed (calcite infilling) fractures striking parallel to the orientation of Structure #20 within the damage zone (22 cm); the wall rock along two of these sealed fractures exhibit red staining.

The deformation zone core (75.54–75.81 m) in Blast Hole 13 shows the weak foliation characteristic of the damage zone at other locations; some evidence of pinch-and-swell structures (boudinage) can be seen in the potassium feldspar phenocrysts. Only a minor amount (< 10% of the deformation zone core by area) of cataclasite is observed, though as in other sections the core is moderately to intensely mylonitized. The mylonite bands are quartz-dominated, but the mineralogical composition varies along strike to either side of the blast hole, from quartz-dominated to epidote-dominated, within an interval of 20 cm.

Due to rock fall-out probably induced during post-blast scaling, determining the end of the lower damage zone at Blast Hole 13 is difficult. Structure #20 is terminated at 76.11 m against a calcite- and quartz-filled sealed fracture; this is a very uncertain value.

Blast Hole 15:

In Blast Hole 15, the epidote-filled fracture/fracture swarm that has served as a marker bed for Structure #20 begins to diverge from Structure #20; it is encountered at 75.06 m, whereas the actual upper damage zone does not begin until 75.57 m. The fracture is thick (~ 1 cm) and offsets a vein of fine-grained granite; this implies formation as a brittle fracture rather than re-activation of a filled vein. In addition to the thick epidote-filled fracture, a partially-open calcite-filled fracture runs from the outside of the damage zone through the Structure #20 core. A closer examination of open sections of this fracture shows some euhedral pyrite crystallized along the (calcite-mineralized) fracture faces.

In Blast Hole 15, the start of the upper damage zone (75.57–75.69 m) is denoted by the presence of a single partly-open fracture with a visible aperture of approximately 1 mm. The foliation noted at other intercepts with Structure #20 is not seen, but there is an increase in sealed fracture intensity.

The deformation zone core (75.69–75.79 m) is strongly mylonitized, with very thick light (up to 4 mm thick) and dark (up to 5 mm thick) bands. Minor amounts of cataclasite are present, but there are no visible seeping open fractures. The deformation zone core contains a sealed fracture network, with 9 subparallel fractures within a 10 cm length.

The lower damage zone (75.79–76.36 m) in Blast Hole 15 is defined in terms of a faint foliation and increased sealed fracture intensity. The authors have assigned the end of the lower damage zone to the contact with an epidote-filled fracture at 76.36 m; however, this is an uncertain assignment, as it was difficult to determine where the foliation actually ended. This fracture was chosen as the endpoint for the Structure #20 damage zone based on the presence of a small amount of visible cataclasite.

Map Section 2:

Map Section 2 represents a panel of the B-wall mapped in more detail than the blast holes; a screenshot is shown below as Figure 5-9. The map section extends from chainage 74.00 to 76.00 m, and is located approximately 4.5 m above the tunnel floor along the tunnel roof, between blast holes 16 and 17. This map section features the longest mapped thickness (1.25 m) of the Structure #20 intercept with the TASS Tunnel.

Map section 2 features the best exposure of the so-called "marker bed" of epidote-filled vein fractures; they exist in a 3 cm thick zone of numerous sealed fractures from 75.21 m to 75.24 m. These epidote-filled fractures are outside of the damage zone for Structure #20, which starts at 75.52 m.

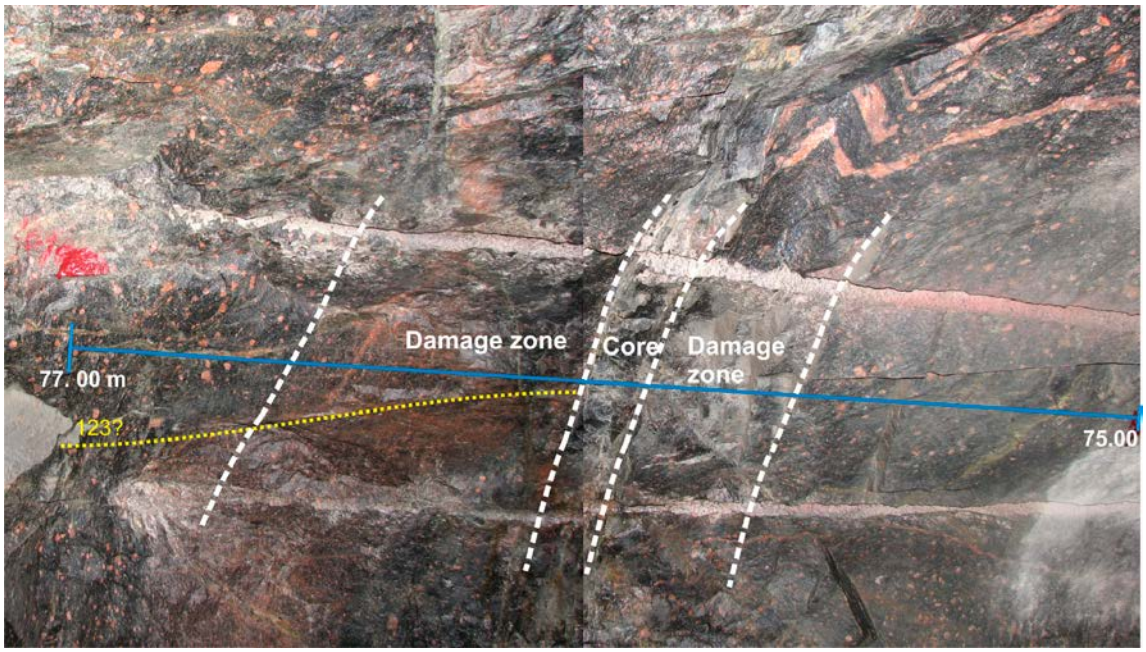

Figure 5-9. *Photograph of Map Section 2 illustrating the core and damage zone contacts, as well as the large calcite-filled fracture (dashed yellow line) described previously.*

The upper damage zone starts at a large sealed fracture filled with a complex mix of calcite, epidote, and chlorite. The upper damage zone features a weak foliation, but there is no visible grain-size reduction. The lower half of the upper damage zone, beginning at 75.74 m, features a gradual increase of sealed fracture intensity towards the Structure #20 core. Fracture frequency is 11 sealed fractures in a 12 cm length. These fractures are filled with epidote, quartz, and minor amounts of potassium feldspar and calcite. No reddish-brown staining of the wall rock is noted. The upper damage zone hosts one open fracture, with apertures ranging from 0.5 to 3 mm, but generally less than 1 mm.

In Map Section 2, the deformation zone core (75.86 m to 76.11 m) is characterized by strong mylonitization, with mylonite band thicknesses ranging from 1–5 mm. Feldspar phenocrysts show a strong preferred alignment parallel to the direction of mylonitization. The colours of the mylonite bands reflect the dominant mineralogy:

- Light red bands: Hematite-stained feldspar.
- Light green bands: Epidote-dominated.
- Light gray to white bands: quartz-dominated.
- Darker bands: A mix of chlorite, quartz, and mafic minerals.

The Structure #20 core at Map Section 2 shows numerous sealed fractures, with at least two different orientation sets. The dominant fracture set is parallel to the deformation zone core orientation (121/85), while the other strikes perpendicular and dips towards the TASS tunnel floor (209/56). When broken open, the sealed fractures show slickensides with a rake of 46° from vertical, suggesting oblique slip. The sealed fractures are filled by epidote, chlorite, pyrite, and minor amounts of quartz. There are 14 sealed fractures within the length of the deformation zone core (25 cm).

The lower damage zone (76.11–76.77 m) is determined by the presence of a grain-size reduction in the potassium feldspar phenocrysts and a continued increased frequency of sealed fractures. A weak to moderate foliation, consisting of a preferred phenocryst orientation, is also observed. Minor amounts of epidote alteration and red staining are observed around sealed fractures in the damage zone.

Blast Hole 18:

In Blast Hole 18, the upper damage zone (75.46–75.98 m) begins at a thick (6 mm) epidote-filled fracture that also hosts minor amounts of chlorite. A weak foliation, consisting of a preferred alignment of potassium feldspar phenocrysts, begins at 75.76 m. There is a fairly dramatic increase in sealed fracture intensity from 75.75 m to the start of the deformation zone core; 12 sealed fractures were logged over a 13 cm length. No grain-size reduction was visible in the upper damage zone.

The deformation zone core (75.98–76.13 m) in Blast Hole 18 is strongly mylonitized. At the centre of Structure #20 a 3 cm thick, cigar-shaped cataclastic band was observed. In contrast to other mapped intercepts of Structure #20 in the TASS tunnel, there were only four visible sealed fractures in the deformation zone core and no obvious open fractures. The four sealed fractures are filled with calcite.

The extent of the lower damage zone (76.13–76.25 m) of Structure #20 at Blast Hole 18 is highly uncertain. The epidote-filled fracture used as the lower boundary of the damage zone in Map Section 2 and Blast Hole 15 has terminated against the deformation zone core. The only evidence of ductile or brittle deformation in the lower damage zone is a very weak foliation.

Map Section 3:

Map Section 3 represents a panel of the B-wall mapped in more detail than the blast holes. The map section extends from chainage 75.00 to 77.00 m, and is located approximately 2.53 m above the tunnel floor along the tunnel roof, between blast holes 19 and 20. The map section is illustrated in Figure 5-10.

The upper damage zone at Map Section 3 starts at a 4 mm thick epidote-filled sealed fracture. Some parts of the filling are dark green with more coarse-grained epidote. The light-green parts of the fracture infilling are made up of fine-grained epidote and quartz (with far more epidote than quartz). The fracture is segmented and is sometimes divided into two separate splays, with a maximum spacing of 1.4 cm between the fracture segments. This “marker bed” becomes thicker towards the tunnel floor. A second epidote-filled fracture is at 75.91 m (sampled at the following coordinates: X = 75.89 m along the tunnel centreline, and Y = 2.36 m from the tunnel floor, and has an orientation of 96/88. The thickness of this second sealed fracture ranges from 2 mm to 7 mm.

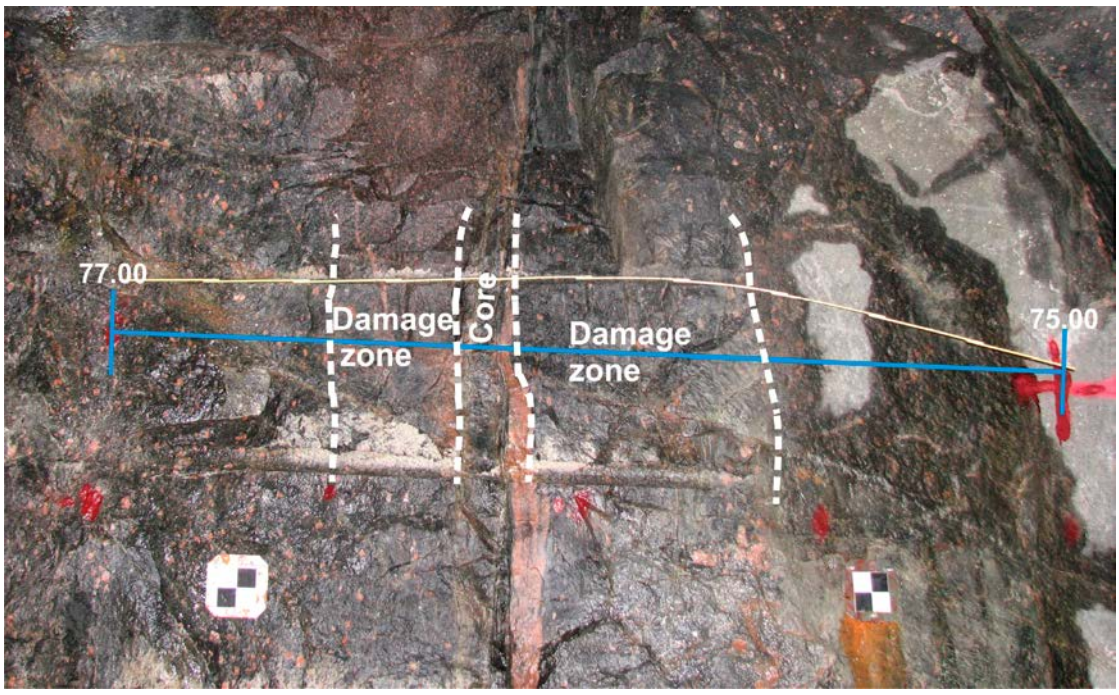

Figure 5-10. *Photograph of Map Section 3 with wooden marker ruler and epidote-filled fractures (yellow dashed lines).*

The upper damage zone is weakly to moderately foliated, with the degree of foliation increasing towards the deformation zone core. The rock mass between the second observed epidote-filled fracture and the deformation zone core features an increase in the intensity of sealed fractures (9 fractures within a 20 cm length). This area of Structure #20 also shows a significant decrease in the size of feldspar phenocrysts, the development of a foliation, and evidence of near-vertical shear offset (up to 1 cm of displacement) where sealed fractures cross large feldspar phenocrysts.

The deformation zone core (76.12–76.27 m) of Structure #20 at Map Section 3 is strongly mylonitized, with alternating mylonite separating two zones of cataclastic banding (7 mm and 1.5 cm thick in the first set of bands, and 2–3 mm thick in the second). The spacing between the two bands in the first zone is 2.6 cm, while the second zone of cataclastic banding (76.12 m), the spacing between bands is approximately 1 cm. The cataclasite appears to be epidote-dominated, with minor amounts of quartz. The deformation zone core is intensely fractured (15 sealed fractures within 10 cm); numerous sub-horizontally dipping sealed fractures cut across the Structure #20 core. Many of these fractures show evidence of silica sol, implying that they were previously open and/or flowing before grouting.

One large partially-open fracture is present near the centre of Structure #20. This fracture shows abundant vugs inside fracture infill dominated by calcite, with minor amounts of quartz and adularia. The aperture of this fracture ranges from 0.5 to 2 mm, and it is oriented 109/88. A fine-grained granite dike occurs between 76.145 and 76.17 m; the thickness of the dike increases towards the tunnel floor.

The lower damage zone (76.27–76.55 m) is defined in terms of a moderate to weak foliation, expressed primarily as a weak banding of dark-coloured minerals. The lower damage zone also features a reduction in the grain size of potassium feldspar phenocrysts, and a slightly increased fracture frequency (0–4 sealed fractures per 10 cm length).

Blast Hole 20:

The upper damage zone for Structure #20 in blast hole 20 (75.76–76.07 m) starts at a cluster of two epidote-filled fractures; the fractures have thicknesses of 6 mm (chainage 75.76 m) and 8 mm (chainage 75.81 m). The damage zone consists of a weak to moderate foliation (visible as banding in dark minerals in the Äspö diorite and a preferred orientation to potassium feldspar phenocrysts, the intensity of which increases closer to the deformation zone core. There is also an increase in the intensity of sealed fractures, with intensities ranging from 5 to 8 sealed fractures within 10 cm lengths. Finally, there is a decrease in the grain size of potassium feldspar phenocrysts.

The deformation zone core (76.07 m to 76.25 m) in blast hole 20 is marked by a dike of fine-grained granite that is strongly sheared and has developed a banded appearance. The bands take the form of alternating layers of dark mafic-rich (0.6–1.0 cm thick) and felsic (1.5–2.0 cm), feldspar-rich layers, similar to gneissic banding. The fine-grained granite dike extends from 76.08 m to 76.13 m. The remainder of the deformation zone core is also strongly mylonitized and intensely fractured. Two distinct bands of cataclasite are present; they have thicknesses of 4 mm and 1.2 cm, respectively, and are spaced 2 cm apart. A single, large open flowing fracture is visible at the contact between the mylonite and the fine-grained granite (76.08 m). This fracture has an orientation of 110/87 and a visible aperture of 1–2 mm. The open fracture has calcite and clay minerals visible on the fracture surface, as well as near-horizontal slickenlines.

The lower damage zone (76.25–76.40 m) is difficult to identify in blast hole 20. The only visible indicator is the presence of a weak foliation expressed as a preferred orientation of potassium feldspar phenocrysts. There is no increase in fracture intensity, and the reduction in grain size is significantly less than in the upper damage zone.

Blast Hole 21:

The upper damage zone (75.86–76.12 m) in blast hole 21 begins at a 2 cm thick epidote-filled fracture, the walls of which appear to be partially mylonitized. This epidote filled fracture is also seen in blast hole 20; however, in that blast hole, it is expressed as two parallel fractures instead of a single fracture. The upper damage zone also features a foliation of weak to moderate intensity, a reduction

in the potassium feldspar phenocryst grain size, and a preferred orientation (subparallel to foliation) of potassium feldspar phenocrysts. There is a slight increase in the intensity (4 fractures per 10 cm length) of sealed fractures; these discontinuities are largely calcite-filled.

The deformation zone core consists largely of mylonite, with cataclastic features and mixed cataclasite/mylonite. Boudinage texture can be seen in the darker mylonitic layers (~ 4 cm thick), which are chlorite- and mafic mineral-rich. The lighter-coloured cataclasite bands and pods are on average thicker (8 cm) than the darker bands, and are dominated by epidote and altered host-rock fragments. The grain size is too small to be considered a breccia. The thickest mylonite band is ~ 5 mm, but the majority of bands are significantly thinner than this, such that measuring spacings is extremely difficult. As in blast hole 20, a small dike of fine-grained granite (76.12 m to 76.14 m) is included inside the deformation zone core.

As in blast hole 20, the extend of the lower damage zone is somewhat ambiguous. It is defined in the TASS tunnel in terms of a very weak foliation, a slight decrease in the grain size of both the groundmass and phenocrystsin the Äspö diorite, and a slight increase in sealed fracture intensity (2–4 fractures per 10 cm length) relative to the intact host rock outside Structure #20.

Blast Hole 22:

In blast hole 22, the Structure #20 upper damage zone (75.91 m to 76.13 m) begins at a 2 cm thick epidote-filled fracture around which the host rock has been partially mylonitized. Sealed fracture intensity increases towards the deformation zone core (approximately 6 fractures in a 10 cm length). There is a weak foliation developed, but no evidence of a grain-size reduction.

The deformation zone core (76.13–76.25 m) is segmented into two sections: a 3 cm thick dark-coloured (chlorite-rich) mylonite and a bright-coloured 3.5 cm thick mylonite-cataclasite mix. Individual mylonitic bands are on the order of 2 cm thick. The remainder of the deformation zone core consists of strongly foliated Äspö diorite, with a slight increase in sealed fracture intensity (ten sealed fractures over a 12 cm length). There is one open, seeping fracture at the centre of the deformation zone core.

The lower damage zone (76.25–76.36 m) is defined in terms of a weak foliation that decreases rapidly in intensity away from the deformation zone core. There is also a slight reduction in the size of the potassium feldspar phenocrysts, but no observable change in the groundmass. No sealed fractures are visible in the lower damage zone in blast hole #20.

Blast Hole 23:

At blast hole 23, the upper damage zone (75.94–76.11 m) begins at a thick (19 mm) series of epidote-filled veinlets/parallel sealed fractures. While this structure may have started as a complex series of veinlets, the presence of cataclastic texture along the walls of some of the structures suggests that the epidote-filled veinlets/sealed fractures post-dates the formation of the cataclasite. Mineral infillings are dominated by epidote, quartz, and minor amounts of chlorite. Only a weak foliation is present, and the potassium feldspar phenocrysts are smaller than in other damage zone sections. There is an increased intensity of sealed fractures in the upper damage zone (~ 10 fractures in a 10 cm length), but the intensity does not change towards the deformation zone core.

The deformation zone core (76.11–76.24 m) in blast hole 23 consists of dark-coloured strongly mylonitized rock sandwiched between two fine-grained granite dikes (76.12 to 76.13 m and 76.17 to 76.20 m, respectively). The fine-grained granite is intensely fractured, with a total of 16 fractures over a 5 cm length (the combined thickness of both fine-grained granite dikes). The fractures in the fine-grained granite are sealed and filled with calcite. The majority of the fractures in the fine-grained granite are parallel to the orientation of Structure #20. Where broken open, the fractures in the fine-grained granite show slickensided surfaces, with dominant orientations nearly horizontal (parallel to strike direction of Structure #20).

In the inner mylonite portion of the deformation zone core, potassium feldspar blasts (fragmented phenocrysts) are deformed and aligned parallel to the mylonite fabric orientation. The core of Structure #20 in blast hole 23 contains four open fractures. The largest fracture has an aperture that varies from 1–3 mm along its exposed length in the TASS tunnel.

Table 5-2. Summary of Structure #20 dimensions from TASS tunnel mapping. MD = measured distance.

Blast hole number	MD (along TASS centre line), in m				Zone thicknesses (m)			
	Upper damage zone Start	DZ core Start	DZ core End	Lower damage zone End	Upper damage zone	Core	Lower damage zone	Total
1	74.54	75.18	75.4	75.47	0.64	0.22	0.07	0.93
2	74.48	75.18	75.4	75.48	0.705	0.215	0.08	1
3	74.56	75.16	75.4	75.48	0.6	0.24	0.08	0.92
Map Section 1	74.56	75.18	75.39	75.47	0.62	0.21	0.08	0.91
5	74.48	75.19	75.35	75.4	0.71	0.16	0.05	0.92
7	74.26	75.05	75.17	75.41	0.79	0.12	0.24	1.15
9	74.94	75.01	75.16	75.58	0.07	0.15	0.42	0.64
11	75.04	75.26	75.35	75.62	0.22	0.09	0.27	0.58
13	75.32	75.54	75.81	76.11	0.22	0.27	0.3	0.79
15	75.57	75.69	75.79	76.36	0.12	0.1	0.57	0.79
Map Section 2	75.52	75.86	76.11	76.77	0.34	0.25	0.66	1.25
18	75.46	75.98	76.13	76.25	0.52	0.15	0.12	0.79
Map Section 3	75.73	76.12	76.27	76.55	0.39	0.15	0.28	0.82
20	75.76	76.07	76.25	76.4	0.31	0.18	0.15	0.64
21	75.86	76.12	76.27	76.48	0.26	0.15	0.21	0.62
22	75.91	76.13	76.25	76.36	0.22	0.12	0.11	0.45
23	75.94	76.11	76.24	76.32	0.17	0.13	0.08	0.38

The three other open fractures generally have apertures that are 0.5 mm or less. Inside the central mylonite, and in the mylonitic core rock outside the lower fine-grained granite dike (76.20–76.24 m), the mylonite bands are approximately 1.0 mm to 1.5 mm thick. Minor pods and thin bands of epidote-rich cataclasite are also observed.

As in other blast holes on the left wall (facing away from the Äspö TASS True Block Scale investigation niche), the lower damage zone is somewhat ambiguous in scope. The end of the damage zone is difficult to determine, and is estimated as the point at which there is not a visible potassium feldspar phenocryst size reduction (76.25–76.32 m). There is only a slight increase in sealed fracture intensity (~ 5 cm in the 7 cm length of the lower damage zone). There is no visible foliation.

5.4 Tunnel maps from high-resolution photography

5.4.1 Methodology for using high-resolution images to map fracture traces

This section documents the attempt made to map bedrock fractures (both natural and blast-induced) along the Structure #20 intercept using the high-resolution multi-spectral digital imagery discussed previously in Section 5.2. The goal of the project was to demonstrate that, in addition to automated methods of fracture mapping from laser swath maps or photogrammetric surveys such as are included in SKB's RoCS system (Magnor et al. 2006), the use of very high resolution digital imagery taken with off-the-shelf hardware could also be used for geoscientific applications. Standard desktop GIS or CAD mapping software can be used to generate fracture trace maps, rather than expensive single-seat custom packages such as SIROVision, Split-FX, 3DM Analyst, or JointMetriX-3D.

This task utilized the high-resolution (12 megapixel) visible light images, the tone-mapped HDR post-processed images, and UV fluorescent light images previously discussed in Section 5.2. All three data sources were useful in identifying fracture geometries: HDR images brought fracture faces out of shadow and enhanced detail at contacts, while the UV fluorescence images allowed for a more precise indication of calcite-filled fractures and open flowing fractures.

All mapping was done as a desktop study using ArcGIS 10. Image post-processing, re-sizing and rotation were done in Gnu Image Manipulation Program (GIMP). Primary data and mapping results were

stored in a file geodatabase and in ESRI-format shapefiles, respectively. One key factor to remember is that all mapping is done in an unregistered coordinate system, with measured lengths and distances a function of pixel count and image resolution. This means that, while the relative positions of each fracture trace, relative to the images and to each other, are fixed, the data itself does not live in real-world coordinates. To be useful in the construction of 3D models in software such as FracMan or RVS, it is necessary to scale and project the images and the fracture traces. This can be done in SKB's RoCS software package, using the digital terrain model constructed from laser swath mapping.

The workflow to open the high-resolution images and map fractures inside ArcGIS is as follows:

1. A file geodatabase is created using ArcCatalog. Uncompressed images (TIFF file format) are loaded into the geodatabase and pyramids are built to allow for easier zooming during mapping efforts.
2. As each TIFF image file of the full length of Structure #20 around the perimeter of the TASS tunnel is larger than a gigabyte in size, it is desirable to break the images into smaller tiles for using in mapping. This allows portions of the image not currently being used for mapping to be turned off or unloaded. The ArcToolbox "Mosaic Dataset" function (Data Management Tools > Raster) is used to break each TIFF file into a three by nine gridded image mosaic. Each image type (white light, HDR, UV) is mosaicked.
3. The mosaicked images are loaded into a blank ArcMap document.
4. A blank polyline shapefile (*76m_TunnelArc*) is created in ArcCatalog and loaded into ArcMap. A straight polyline is digitized across the entire image, such as to connect the chainage 76+00 markers on the A- and B-walls of the tunnel. This line will be used as the reference point when re-scaling and georegistering the image.
5. A blank point shapefile (*76m_BorepipeNumbers*) is created in ArcCatalog and opened in ArcMap. This file is used to contain the intersection between the "borepipe" (the semi-circular remnants of the tunnel blasting holes) and the 76+00 chainage arc. This is for use in referencing the Structure #20 blast hole descriptions presented in Section 5.3.
6. A blank polyline shapefile (*St20_FractureTraces*) is created in ArcCatalog and opened in ArcMap. Fracture traces along the walls of the TASS tunnel are digitized and created inside this layer. The Attribute Table of this feature is customized to include the following fields:
   - **Ap_Vz**: Is the aperture of the fracture making the trace on the tunnel wall visible?
   - **Aperture**: Open, Partly Open, or Sealed. The intention of this field was to indicate which features were open, such that additional ground-truthing could be performed in the field. Partly Open fractures are largely those features where the actual aperture was ambiguous; it may have been re-opened by blasting, by scaling, or by unloading after tunnel construction. Most have obvious signs of blast damage (wedge fall-out)_ or very fresh faces.
   - **Interpreter**: The person logging the fracture traces.
   - **Comments**: Text field used to contain notes about individual fractures, questions, observations of mineral infillings, termination type and style, and observations of blast damage. Many of the comments could theoretically be placed into separate attributes, similar to the RoCS mapping system.
7. **Struct_ID**: Used to determine the type and orientation of fracture traces. Values are "Wall Perpendicular", "Wall Subparallel", and "Blast Structure".Fracture traces are manually digitized from the high-resolution tunnel imagery inside ArcGIS. The analyst switches between HDR, UV, and white light as needed to best determine the geometry of a given fracture trace.

The criteria for determining whether a fracture was open, partly open, or sealed, is as follows:

- Open fractures have clearly visible water inflow, open void space between fracture walls, or silica sol staining on UV images.
- Partly open fractures are those that may have been re-opened by tunnel excavation. There must be signs of blast damage (clear rock wedges, fresh fracture faces with plumose structure or fracture hackles), lack of mineral infillings or coatings on fracture surfaces, and there must be visible fracture pore volume.
- Sealed fractures are those in which there is no visible pore space in any images, clear calcite/quartz/epidote infilling, and a lack of evidence of water or silica sol flow.

Table 5-3. Example of data about fracture traces recorded in GIS.

Table

St20_FractureTraces

FID	Shape *	Id	Ap_Viz	Aperture	Comments	Interprete	Struct_ID
0	Polyline	0	Yes	Open	Possibly open due to blast damage. Fracture surface is fresh.	ALF	Wall Perpendicular
1	Polyline	0	Yes	Open	Possibly open due to blast damage. Fracture surface is fresh.	ALF	Wall Perpendicular
2	Polyline	0	No	-999.25		ALF	Wall Perpendicular
3	Polyline	0	No	-999.25	Rock wedge face from blasting.	ALF	Blast Structure
4	Polyline	0	No	-999.25	Rock wedge face from blasting.	ALF	Blast Structure
5	Polyline	0	Yes	Partly Open	Sealed fracture (calcite?) in part of of scene, re-opened by blasting / excavation, forms rock block f	ALF	Wall Perpendicular
6	Polyline	0	No	-999.25	Rock wedge face from blasting.	ALF	Blast Structure
7	Polyline	0	No	-999.25	Rock wedge face from blasting.	ALF	Blast Structure
8	Polyline	0	Yes	Partly Open	Sealed over ~ 1/2 of length, leftmost portion (towards portal) opened by blasting.	ALF	Wall Perpendicular
9	Polyline	0	Yes	Partly Open	Sealed over ~ 1/2 of length, leftmost portion (towards portal) opened by blasting.	ALF	Wall Perpendicular
10	Polyline	0	No	-999.25	Rock wedge face from blasting.	ALF	Blast Structure
11	Polyline	0	Yes	Sealed		ALF	Wall Perpendicular
12	Polyline	0	Yes	Partly Open	Wedge face from blasting. Majority of fracture is epidote filled.	ALF	Wall Subparallel
13	Polyline	0	Yes	Sealed		ALF	Wall Perpendicular
14	Polyline	0	Yes	Sealed		ALF	Wall Perpendicular
15	Polyline	0	Yes	Sealed	Epidote-filled?	ALF	Wall Perpendicular
16	Polyline	0	Yes	Sealed		ALF	Wall Perpendicular
17	Polyline	0	No	-999.25		ALF	Wall Perpendicular
18	Polyline	0	No	-999.25		ALF	Wall Perpendicular
19	Polyline	0	Yes	Partly Open	Opened by blasting. Image suggests Qz or Calcite filling.	ALF	Wall Perpendicular
20	Polyline	0	No	-999.25	Pre-existing near-vertical fracture, connects to blast hole (EDZ feature)	ALF	Wall Perpendicular
21	Polyline	0	Yes	Sealed	Looks to be sealed with greenish mineral; unable to determine if chlorite, epidote, or other.	ALF	Wall Perpendicular
22	Polyline	0	Yes	Sealed		ALF	Wall Perpendicular
23	Polyline	0	Yes	Sealed	Epidote-filled. Cuts across DZ without offset, so younger than Structure #20	ALF	Wall Subparallel
24	Polyline	0	Yes	Sealed	Terminates against long fracture trace. Possibly epidote-filled.	ALF	Wall Perpendicular

1 (0 out of 295 Selected)

St20_FractureTraces

Fracture traces were digitized such as to avoid the inclusion of digitized perimeters of clear open faces where rock wedges had fallen out or of circular "fallouts" in the tunnel ceiling (Figure 5-11). The assumption is that we are digitizing a fracture trace map, which is a network of two-dimensional lines that represent the intersection of two planes. This assumption is necessary for computing fracture statistics (P_{21}, P_{32}), in that the calculations assume that the fracture trace represents a random chord through a circular disk fracture. Inclusion of the perimeters of wedge or slab failures violates the assumption of a 2D trace and so were not included in the mapping. Previous tunnel maps at Äspö (Hardenby and Sigurdsson 2010) and Olkiluoto (Fox et al. 2012) have included oval-shaped traces on the roof of the tunnel maps, which have caused problems for DFN modelling efforts in the past.

The GIS mapping was intended as a test of whether the combination of UV, HDR, and high-resolution digital imagery would prove useful for fracture mapping; it was not intended as a formal SKB activity. As such, no official Activity Code is available for the effort, and the fracture attribute tables do not correspond to any official SKB method description. In addition, due to time and personnel constraints, the fracture digitization effort was not completed to 100%; only about 40% of the fracture traces visible in the high-resolution imagery were digitized, with a bias towards longer traces. The authors suggest that the primary use of this analysis should be as a demonstration of potential techniques, with the goal of offering feedback to the RoCS project. It is not designed to replace the existing TMS maps of the TASS tunnel.

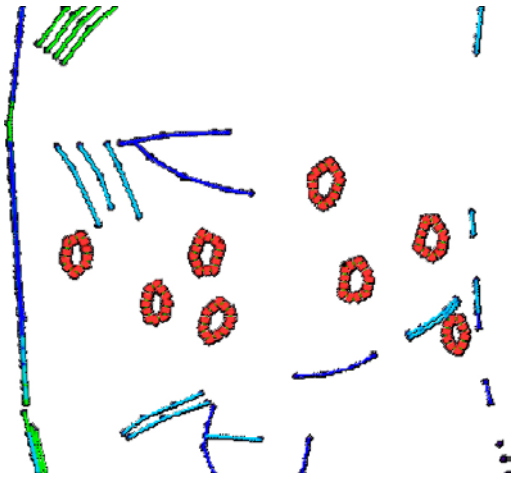

Figure 5-11: Example of circular trace windows and wedge failure blocks in trace data. *This particular example is from the ONKALO tunnel mapping data set at Olkiluoto, and was used in the version 2.0 Olkiluoto GeoDFN (Fox et al. 2012). NB. This figure is not present in that report.*

5.4.2 2D fracture trace maps

The results of the fracture trace mapping from high-resolution digital imagery are presented below as Figure 5-12 and Figure 5-13. Note that these images are only approximately to scale; to get accurate lengths and angles it will be necessary to georeference and then drape the image across the DTM of the TASS tunnel created from laser swath mapping. After that, the polyline shapefiles can then also be draped over the same image, resulting in a 3D trace map in Äspö96 coordinates, rather than a 2D trace map in image (pixel) coordinates. These steps were not taken during this project due to time limitations.

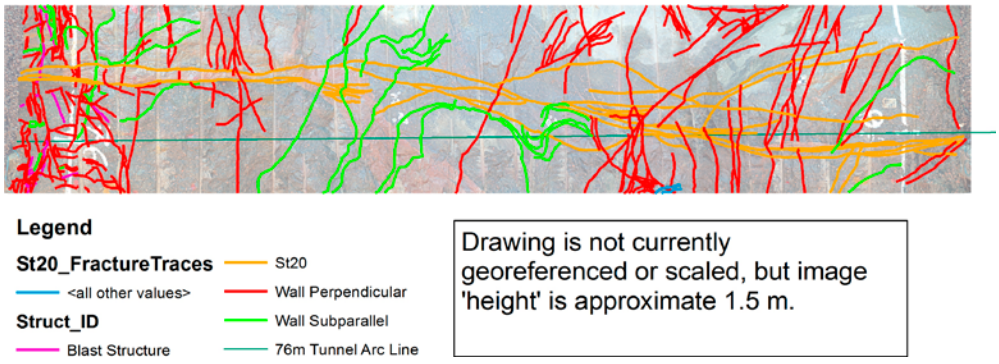

Figure 5-12. *Incomplete fracture trace map of Structure #20 based on high-resolution digital images. Fractures are coloured by their type, which distinguishes between those subparallel to the tunnel walls, those that cut across the tunnel, and those fractures that are likely blast-induced. The teal line in the image represents the chainage 76+00 m tunnel arc; the A-wall (left if one is facing the completed end of the TASS tunnel).*

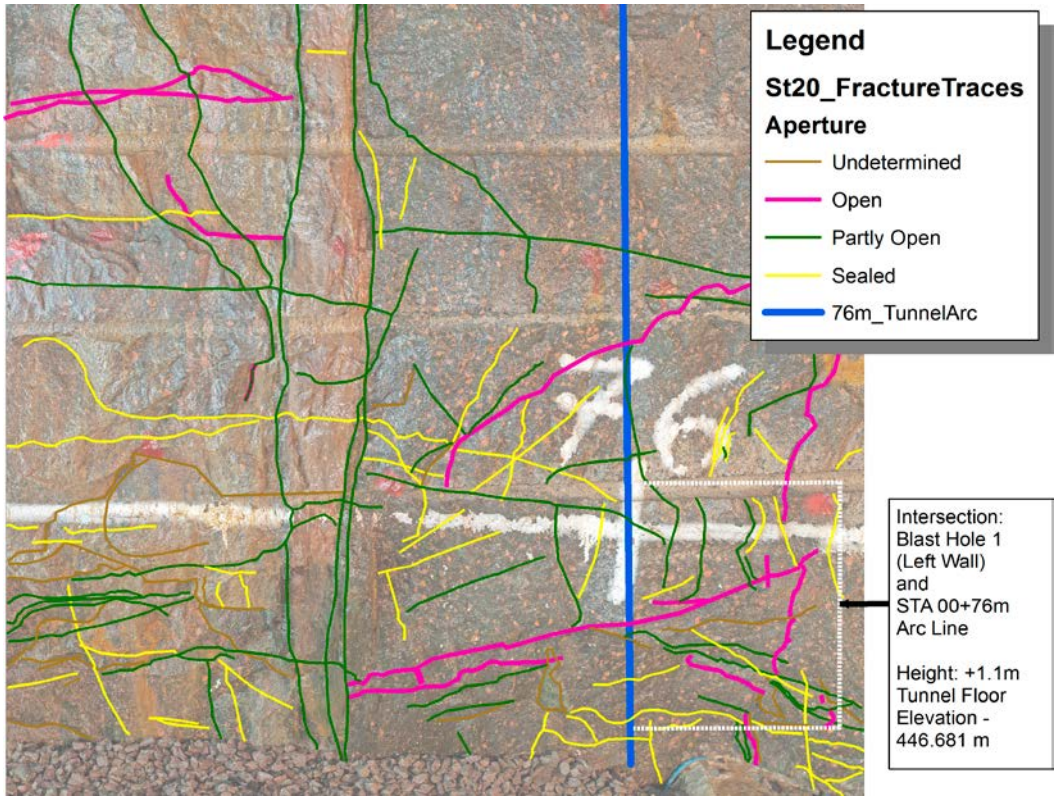

Figure 5-13. *Close up of A-wall (left wall) of the TASS tunnel at the Structure #20 intercept. Fractures are coloured by their visible aperture. The white brackets on the rightside of the image indicate the height (1.1 m) of the first blast hole above the tunnel floor, and are an indication of scale, since the image is not georeferenced.*

5.4.3 Limitations and lessons learned

The most significant limitation of the tunnel mapping from high-resolution imagery is that it is difficult to nearly impossible to work with a single mosaicked image showing the entire tunnel perimeter inside ArcGIS. Due to overlapping horizontal and vertical coordinates, it is also not possible to georegister images in anything other than an image-local coordinate system. Finally, even if images are broken up into tunnel walls and tunnel ceilings and "unfolded" in a fashion similar to TMS maps produced in Microstation, reconstructing and re-projecting the fracture traces back to 3D is not possible in ArcGIS. It is simply the wrong tool for the job.

A better workflow in the future would be to utilize lower-resolution images draped atop a DTM of the tunnel in native 3D software such as Sirovision, side-by-side with the 2D image suite. Mapping can be done in 3D, while the 2D high-resolution images can provide additional insight not easily distinguished in the 3D mesh. It may even be possible to use the high-resolution images in Sirovision directly, though the large file sizes may make mapping large sections of the tunnel at once unwieldy.

The use of multispectral methods (HDR + visible + UV light) proved very useful in identifying fracture apertures and in confirming trace geometries. The very high resolution (approximately 1 mm per pixel) allowed for very precise digitization of fracture trace geometry and preservation of some fracture morphological features such as twist hackles and plume structures, which were used to distinguish between natural fractures and blast-induced structures. Significant knowledge as to fracture geometries, apertures, morphology, and termination relationships can be garnered from high-resolution imagery, without adversely affecting the rate of tunnel advancement. Provided the tunnel is unlined, ground truthing can be done at a later date directly on printed versions of the high-resolution imagery, or inside a tablet GIS application.

5.5 Fracture mineralogy of Structure #20

Samples for mineralogical investigations were collected from the tunnel walls using a rock saw. Analytical methods used are the same as described above for the drill core investigations. Sampling strategy was focused on covering all materials present in the shear zone; mylonite (fine-grained epidote-dominated, quartz-dominated and protomylonite), cataclasite, epidote-rich splay, sealed and open fractures filled and coated by e.g. calcite.

5.5.1 Samples from the TASS tunnel

All thin sections were oriented, along strike or dip.

Tunnel sample #1

Orientation of thin section was aligned with Structure #20, vertical, looking from the A-wall towards the B-wall, to the WNW, i.e. ~ 297° with respect to magnetic north. The shear sense indicators observed in the thin section reveal dip slip along Structure #20 at the sampling point, with the inner part of the TASS tunnel (SW part) moved downwards Images are shown in Figure 5-14 through Figure 5-16.

General features: The sample is dominated by several parallel mylonite bands. The mylonite is generally very fine-grained, with light bands of quartz and mica (sericite and partly chloritized biotite) and also darker bands of fine-grained epidote and plagioclase. Quartz-dominated bands show re-crystallised quartz (dynamic re-crystallisation, e.g. sub-grain rotation re-crystallisation and grain boundary migration re-crystallisation). Fine-grained K-feldspar dominated bands are also present in some parts of the thin section. Diffuse C-S fabric, mantled porphyroclasts (of re-crystallised quartz surrounded by mica) and oblique foliation of re-crystallised quartz indicate dip slip with SW part of zone moved downwards. Mica-rich bands show overprinting, indicating refolding on at least one occasion (a secondary foliation – S2, parallel with quartz- and feldspar-dominated bands described above), or may alternatively be C'-fabric formed at progressed shear All ductile deformation phases in this area have been interpreted to be Proterozoic, indicatively pre 1.76 Ga (Wahlgren et al. 2008). Epidote is present, preferentially in the mica-rich bands but is not as abundant as mica. Wall rock fragments are very rare, only represented by magnetite and re-crystallised quartz fragments.

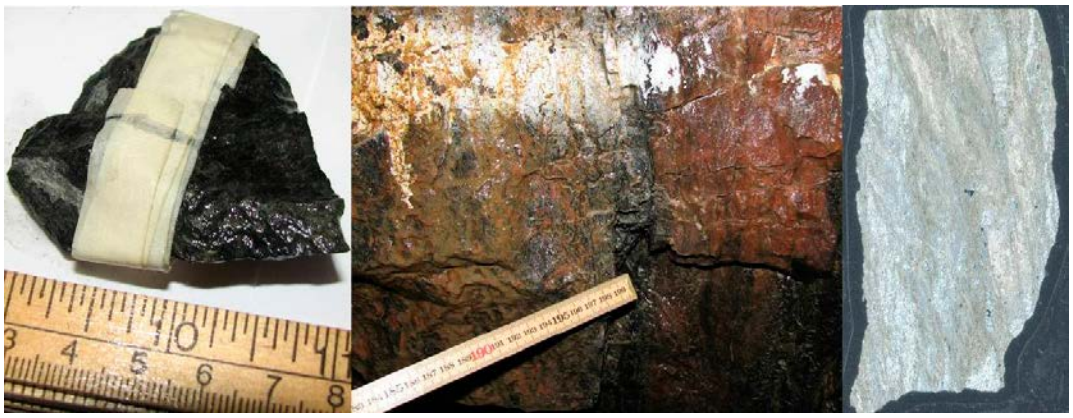

Figure 5-14. *Photograph of sample (left), photograph of sample location (middle) and scanned thin section, with crossed polars (right). Tunnel sample #1.*

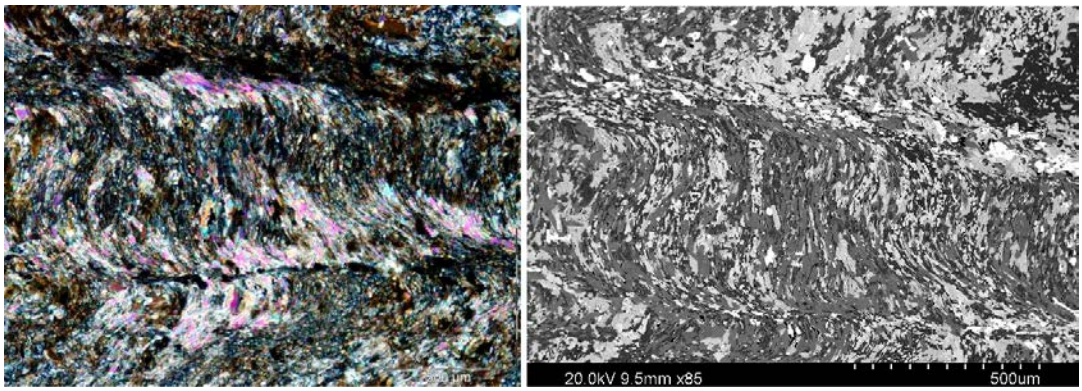

Figure 5-15. *Photomicrograph (top) and back-scattered SEM-image (bottom, same view) refolded mica (muscovite and biotite) in mylonite. S2 foliation runs horizontally (dark bands) in the image. Epidote and quartz are also present. Tunnel sample #1.*

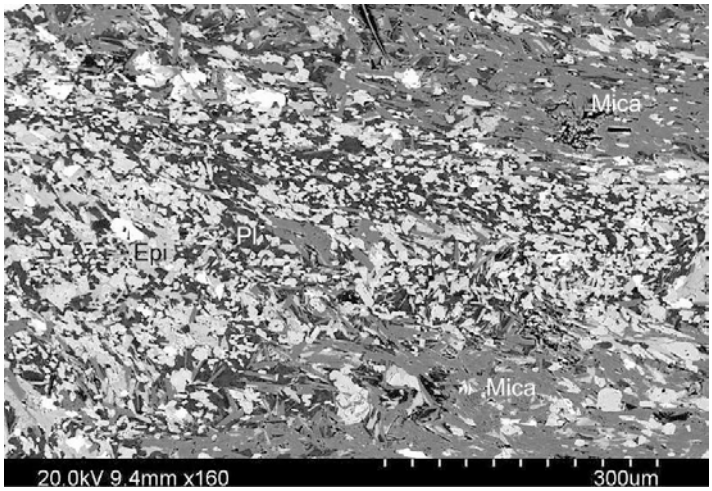

Figure 5-16. *Back-scattered SEM-image of slightly re-folded mylonite with bands rich in mica or epidote and plagioclase (Epi, Pl). Tunnel sample #1.*

Tunnel sample #2

This sample is made up of fine-grained granite but no thin section was prepared for it and therefore it is not described in detail.

Tunnel sample #3

Orientation of thin section is aligned with Structure #20 looking into the B-wall, with a strike of 297/90. The shear sense indicators observed in the thin section reveal dip slip along Structure #20 at the sampling point, with the inner part of the TASS tunnel (SW part) moved downwards. Images are shown in Figure 5-17 through Figure 5-19. This sample consists of highly altered wall rock, which is mylonitized (i.e. protomylonite); towards the left edge of the thin section the mylonite becomes more intense and wall rock fragments are not abundant in the matrix. The mylonite in the left edge of the thin section has been re-activated in the brittle regime, first by cataclasis and later by a brittle fracture coated by euhedral epidote, quartz and K-feldspar and filled with euhedral to subhedral fluorite and anhedral calcite.

The mylonite is dominated by epidote, which is fine-grained and mainly aligned with the mylonite foliation. Smaller amounts of fine-grained mica, quartz and feldspars are also present in the mylonite. The shape of the porphyroclasts indicates dip-slip with SW side moved downwards, along Structure #20 locally. The cataclasite has re-activated the mylonite and is mainly made up of epidote and quartz, with minor K-feldspar and titanite. The wall rock fragments are highly altered, with primary feldspars (plagioclase and microcline) showing intense sericitization. Primary quartz is completely re-crystallised (e.g. by grain-boundary migration, re-crystallisation and sub-grain formation). Biotite and other Fe-Mg minerals are re-crystallised to more fine-grained micas and chlorite.

Figure 5-17. *Photograph of sample (left), photograph of sample location (middle) and scanned thin section, with crossed polars (right). Tunnel sample #3.*

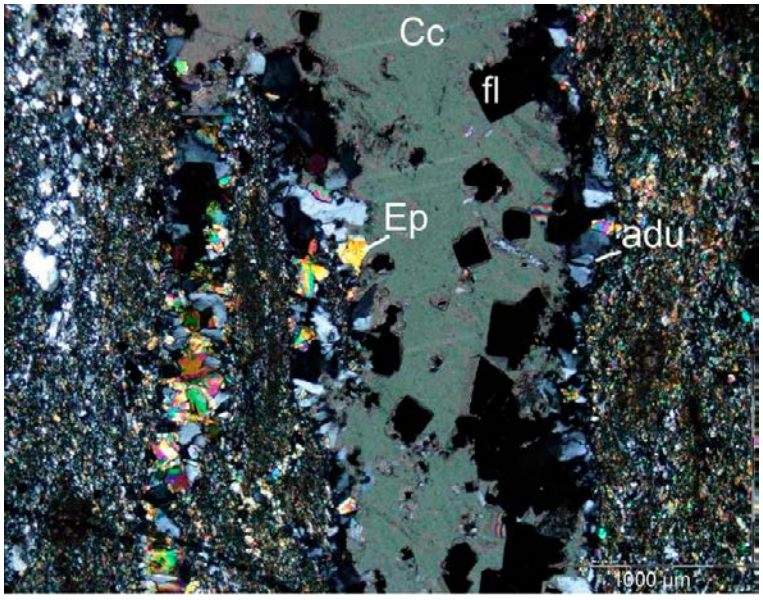

Figure 5-18. *Photomicrograph of a fracture filled with epidote (Ep), adularia (adu), fluorite (fl) and calcite (Cc), cutting through mylonite. Tunnel sample #3.*

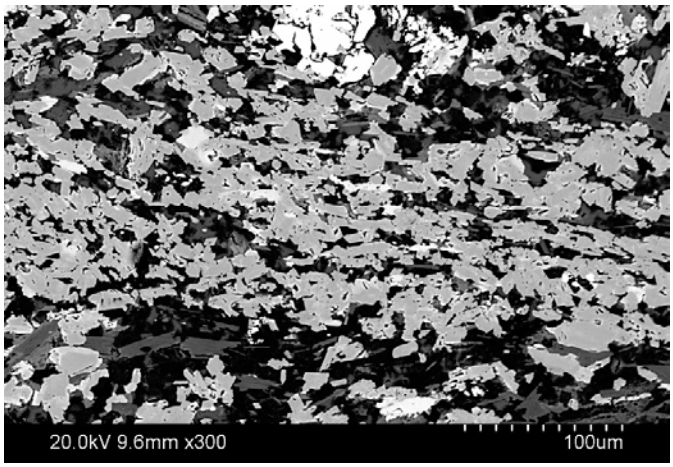

Figure 5-19. *Back-scatter image of epidote-rich mylonite. Tunnel sample #3.*

Tunnel sample #4

Tunnel sample #4 is aligned with Structure #20, looking into the B-wall at a vertical angle (WNW). Images of the sample are shown in Figure 5-20 through Figure 5-22. This sample consists of a sealed fracture with at least two generations of mineralization; the oldest is a epidote-muscovite-quartz-plagioclase cataclasite/mylonite mixture, and the younger is a brittle fracture coated by euhedral (cubic) fluorite and filled with calcite and a mixture of very fine-grained K-feldspar, quartz and chlorite, which indicates that it is Palaeozoic (Drake and Tullborg 2004, Drake et al. 2009).

Figure 5-20. *Photograph of sample (left), photograph of sample location (middle) and scanned thin section, with crossed polars (right). Tunnel sample #4.*

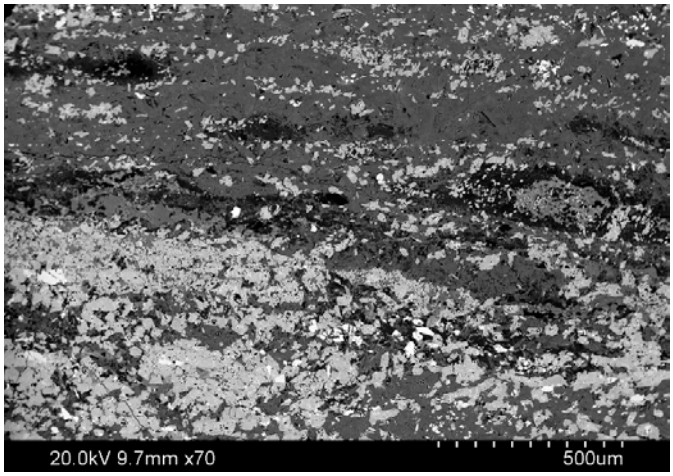

Figure 5-21. *Back-scattered SEM-image of muscovite-rich mylonite (dark, top) and epidote-rich mylonite (bright, bottom). Tunnel sample #4.*

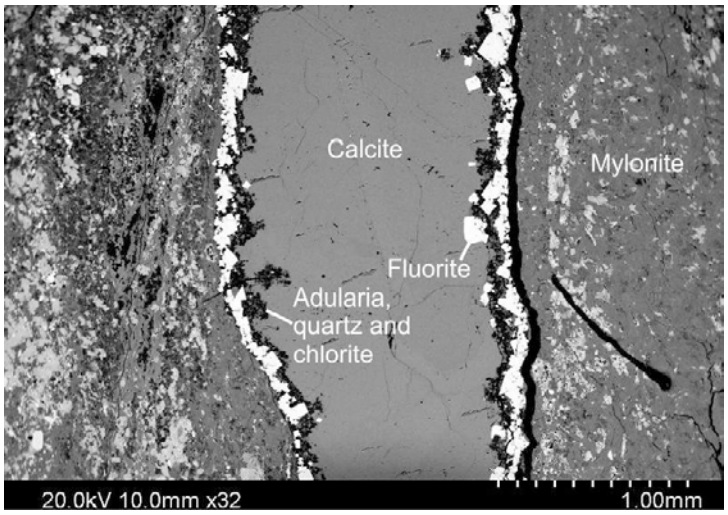

Figure 5-22. *Back-scattered SEM-image of a fracture filled with fluorite, chlorite, adularia, and quartz (fine-grained assemblage) and calcite cutting through mylonite/cataclasite. Tunnel sample #4.*

The calcite-fracture cuts through the cataclasite but the orientation is roughly the same as the cataclasite, which implies it is following the same brittle-ductile fabric. The wall rock is altered, especially close to the cataclasite, where quartz is completely re-crystallised, with abundant sub-grain formation. Primary feldspars in the wall rock (plagioclase and microcline) show sericitization and primary quartz is re-crystallised. Biotite and other Fe-Mg minerals are rare.

Tunnel sample #5

This sample is made up of epidote-rich fractures and mylonite in a splay to Structure #20 but no thin section was prepared for the sample and therefore it is not described in detail.

Tunnel sample #6

This sample is made up of mylonite in the core of Structure #20 but no thin section was prepared for the sample and therefore it is not described in detail.

Tunnel sample #7

Images of this sample are shown in Figure 5-23 through Figure 5-29.

Thin section

The orientation of the thin section take from Sample #7 is vertical and aligned along strike with Structure #20, looking from the B-wall towards the A-wall (mirrored in the thin section). The shear sense observed in the thin section indicates dip-slip with inner part of the tunnel (SE part) moved downwards.

General features of the thin section: Mylonite with several parallel very fine-grained bands. Mylonite bands are either quartz-and feldspar-dominated (very fine-grained and completely re-crystallised through dynamic re-crystallisation, e.g. sub-grain rotation and grain boundary migration), with epidote or are (in lower part of thin section) dominated by epidote-and mica (mostly biotite, +chlorite). Primary rock fragments exist but are highly altered, e.g. K-feldspar, plagioclase and magnetite. The feldspars show undulose extinction and limited sub-grain formation as well as deformation twinning. Secondary calcite has formed from altered plagioclase. Very diffuse C-S fabric and mantled porphyroclasts (of re-crystallised quartz surrounded by mica) indicate dip-slip with SE wall moved downwards. Thin layers and lenses of epidote-cataclasite are present and have been reactivated by brittle fractures filled with euhedral quartz, K-feldspar, epidote, fluorite, chlorite and mica.

Figure 5-23. *Photograph of sample location (left) photograph of fracture surface (middle), sample from the side (right). Tunnel sample #7.*

Figure 5-24. *Scanned thin section. Crossed polars. Tunnel sample #7.*

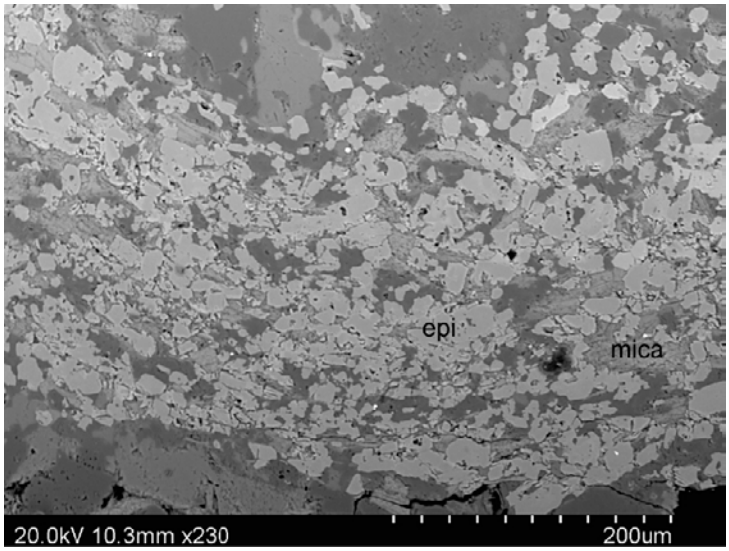

Figure 5-25. *Back-scattered SEM-image of mylonite rich in epidote (epi) and mica. Tunnel sample #7.*

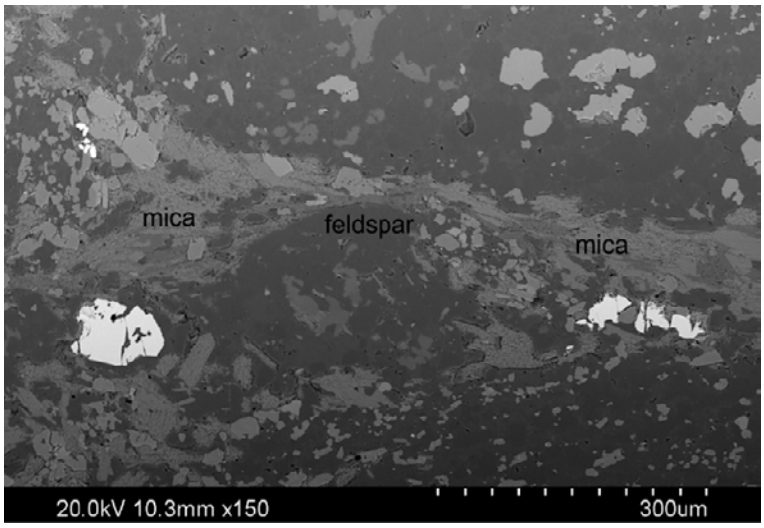

Figure 5-26. *Back-scattered SEM-image of mylonite with a feldspar porphyroclast mantled with mica. Tunnel sample #7.*

Fracture surface sample

The minerals found on the fracture surface include chlorite (and clay minerals), epidote, apatite, quartz and fluorite.

The fracture exposed in Tunnel Sample #7 has a smooth surface with some striated chlorite-rich parts (perhaps with some mixed-layer clay as indicated by occasional elevated Ca contents, indicating e.g. smectite). Epidote is very common (often together with chlorite) and some parts contain secondary apatite. Illite is also present and also some cubic fluorite. In places, both Fe-rich chlorite (also incorporating Mn, Ca, K and Na – perhaps clay mineral in-mixed) on top of Mg-rich chlorite is present and the Mg-rich chlorite has some K incorporated and has gradually replaced wall rock biotite, as shown by remnants of biotite being still present within chlorite. Wall rock is exposed in some parts of the fracture surface, and show e.g. plagioclase and titanite. There are a few minor occurrences of fine-grained mineral clusters with gauge-like appearance. These contain crushed wall rock material (e.g. biotite, plagioclase and titanite), epidote and chlorite/clay minerals.

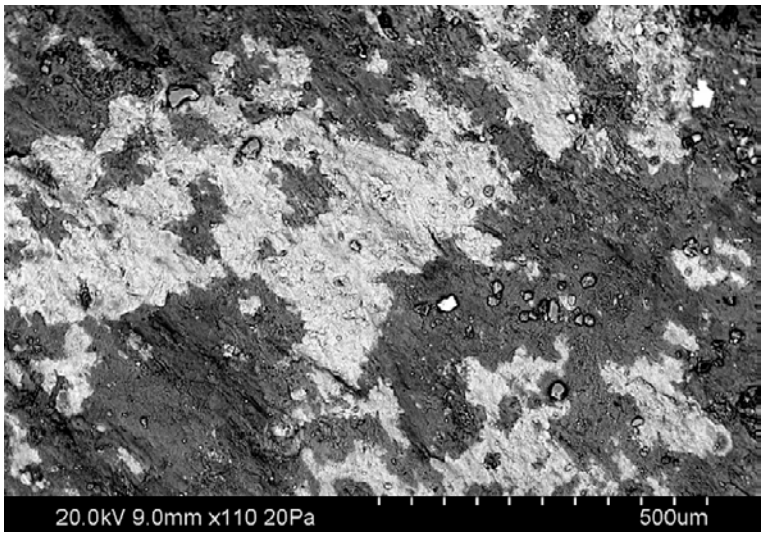

Figure 5-27. *Back-scattered SEM-image of dominantly chlorite (bright = Fe-rich, dark = Mg-rich + additional biotite). On top of chlorite are fine-grained fluorite crystals. Tunnel sample #7.*

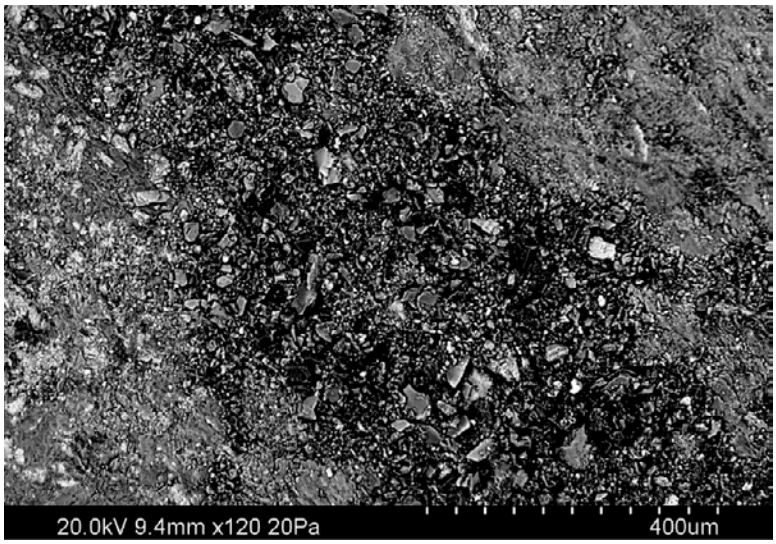

Figure 5-28. *Back-scattered SEM-image of a fine-grained mineral cluster with gauge-like appearance. Tunnel sample #7.*

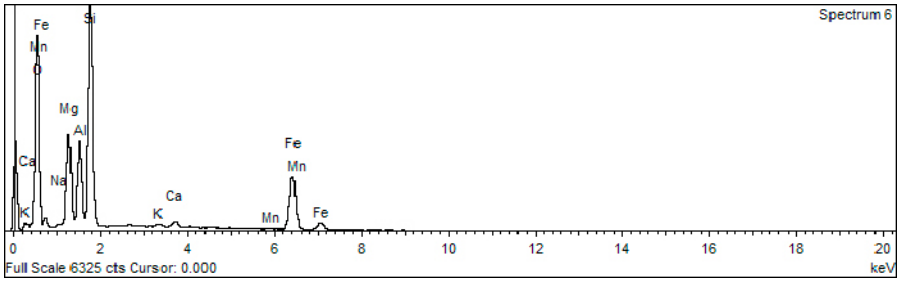

Figure 5-29. *EDS spectrum of chlorite/clay minerals. Tunnel sample #7.*

Tunnel sample #8

The orientation of the thin section is horizontal, looking from the floor to the roof of the tunnel, and aligned along strike with Structure #20. A sinistral sense of shear suggests strike-slip to oblique-slip movement of Structure #20 with the SW wall moving towards the NW. However, younger brittle dextral indicators indicate reverse-slip movements. Images are shown in Figure 5-30 through Figure 5-32.

Figure 5-30. *Photograph of sample (left), photograph of sample location (middle) and scanned thin section, with crossed polars (right). Tunnel sample #7.*

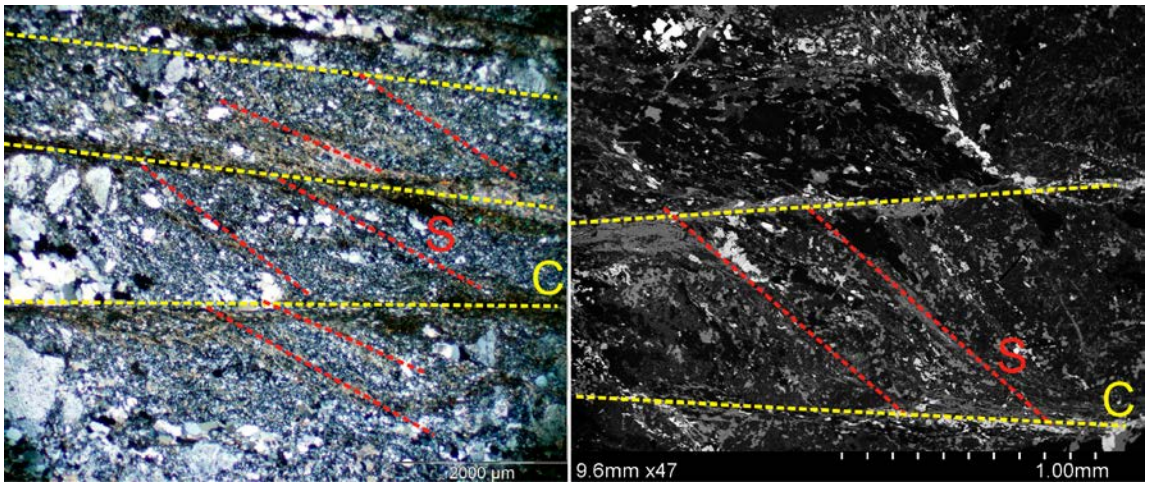

Figure 5-31. *Photomicrograph (left) and back-scattered SEM-image of fine-grained mylonite showing C-S fabric, defined by epidote-rich and mica-rich bands (C-bands running horizontally in image and S-bands running between the C-bands from upper left to lower right), indicating sinistral shear (oriented thin section). Tunnel sample #7.*

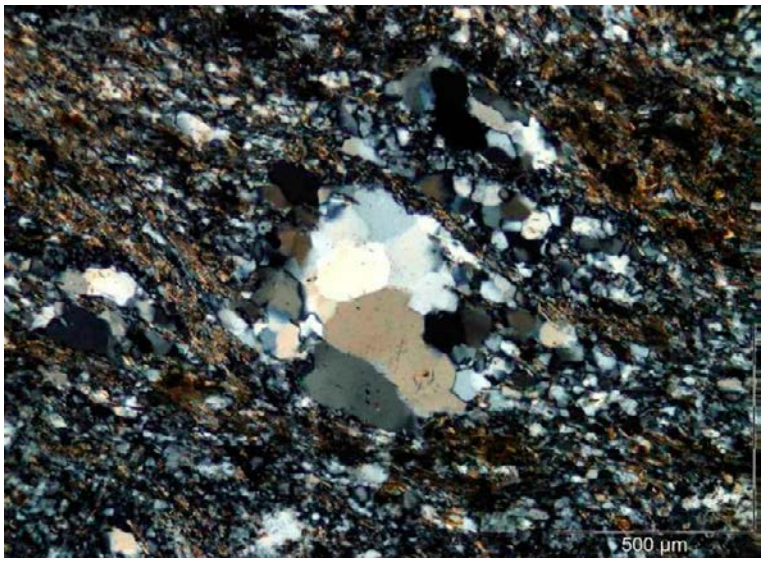

Figure 5-32. *Photomicrograph of one of many mantled quartz porphyroclast indicating sinistral shear (oriented thin section). Tunnel sample #7.*

Mylonite (sinistral), very thin parallel bands of epidote-rich mylonite is characteristic in between thicker bands of very fine-grained quartz. Epidote rich bands occasionally show C-S fabric and the re-crystallised quartz crystals in the mylonite show oblique foliation indicating sinistral sense of shear. Furthermore, mantled porphyroclasts of quartz also indicate sinistral shear sense. Quartz crystals show signs of dynamic re-crystallisation, such as grain-boundary migration re-crystallisation and sub-grain rotation re-crystallisation. Mica-rich mylonite exists in some parts of the thin section and the mica crystals are either aligned with the mylonite bands or show oblique foliation indicating sinistral shear. Cataclasite is epidote-rich and Riedel shears indicating dextral movement in the brittle regime. Wall rock fragments exist as porphyroclasts or in minor proto-mylonite parts of the thin section. The fragments are mainly feldspars which are altered and fractured. Quartz-fragments are completely re-crystallized to polycrystalline aggregates, through dynamic re-crystallisation.

Tunnel sample #9

Images of this sample are shown in Figure 5-33 through Figure 5-36.

Thin section

The orientation of the thin section is vertical, looking at the A-wall (orientation of 297°) and aligned along strike with Structure #20. Both sinistral and dextral shear sense indicators are found; the sample indicates dip-slip with the SW side moving both up and down, respectively, depending on the portion of the sample examined.

The mylonite is very fine-grained and dominated by quartz-rich bands, epidote-rich bands and mica-rich bands (mostly muscovite). Minor brittle quartz-veins and calcite-veins are present. Both dextral and sinistral shear is indicated, mainly by mantled porphyroclasts (and diffuse C-S fabric), which do not always render straightforward indications, and may thus be the reason why there is both dextral and sisitral shear indicated (i.e. uncertain observations). Quartz shows grain-boundary migration re-crystallisation and sub-grain rotation re-crystallisation. Wall rock fragments are rare, but exist, e.g. plagioclase which shows deformation twinning and are mantled indicating sinistral as well as dextral movement in different parts of the thin section.

Figure 5-33. *Photograph of sample location (left) photograph of fracture surface (middle), sample from the side (right). Tunnel sample #9.*

Figure 5-34. *Scanned thin section: Crossed polars. Tunnel sample #9.*

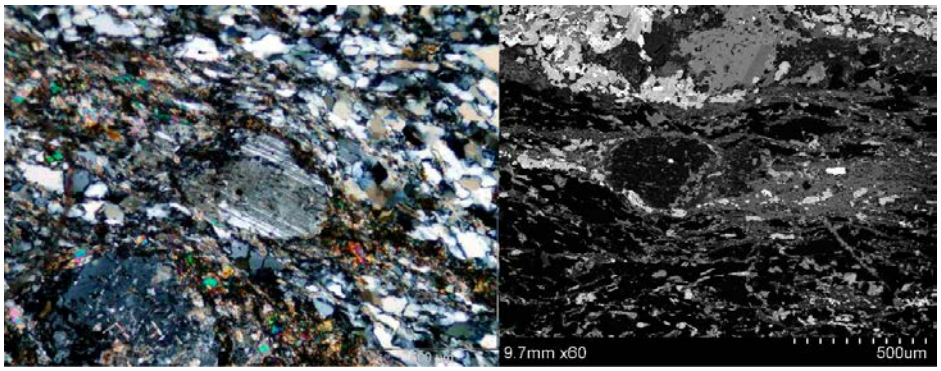

Figure 5-35. *Photomicrograph (left) and back-scattered SEM-image (right) of mylonite with a plagioclase porphyroclast (centre of image) showing deformation twinning and mantling indicating sinistral shear (oriented thin section). Tunnel sample #9.*

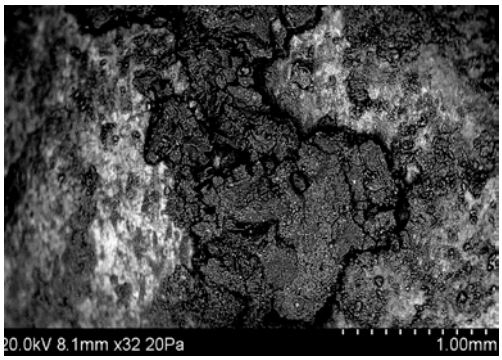

Figure 5-36. *Back-scattered SEM-image of dominantly calcite and quartz (dark) on top of an older chlorite-dominated coating (bright). Tunnel sample #9.*

Fracture surface sample

Minerals on the fracture surface include calcite, chlorite, quartz, (and small amounts of pyrite). Calcite is abundant, both as striated thin coatings (with quartz) and as euhedral crystals. Large parts of the surface are covered with smooth (sometimes striated) chlorite/clay minerals. Often fine-grained calcite and quartz (both as crystals and as fragments in fine-grained mixtures) are observed on top of this surface. Chlorite contains abundant Ca, but this is probably mainly due to in-mixed calcite. However, clay mineral incorporation cannot be ruled out. Very small crystals of pyrite are also observed.

Tunnel sample #10

This sample was only analysed for stable isotopes in calcite.

Figure 5-37. *Photograph of sample (left) and sample location (right). Tunnel sample #10.*

Tunnel sample #11

The orientation of the thin section taken from Tunnel Sample #11 is vertical, looking from the B-wall towards the A wall, and aligned along strike with Structure #20. Shear sense indicates dip-slip, where SW wall has moved up relative to the NE wall. Images of this sample are shown in Figure 5-38 through Figure 5-39.

General characteristics of Tunnel sample #11: Mylonite with several parallel bands, which are generally very fine-grained, except for some quartz-bands which have slightly larger grain-size. Bands are either quartz-dominated (with abundant re-crystallised feldspars) or dominated by epidote-mica (+chlorite) and calcite (with minor pyrite). The quartz bands show abundant signs of dynamic re-crystallisation, including sub-grain formation, sub-grain rotation re-crystallisation and grain-boundary migration re-crystallisation. Occasional porphyroclasts of K-feldspar and plagioclase show deformation twinning. Very diffuse C-S fabric indicates dip-slip (SW-wall moved upwards) movement but apart from that there are no shear-sense indicators. Two generations of calcite-filled fractures exist. One is parallel to the mylonite foliation and one cuts the mylonite at approximately 45º; both sets have minor amounts of pyrite.

Figure 5-38. *Photograph of sample (left), photograph of sample location (middle) and scanned thin section, with crossed polars (right). Tunnel sample #11.*

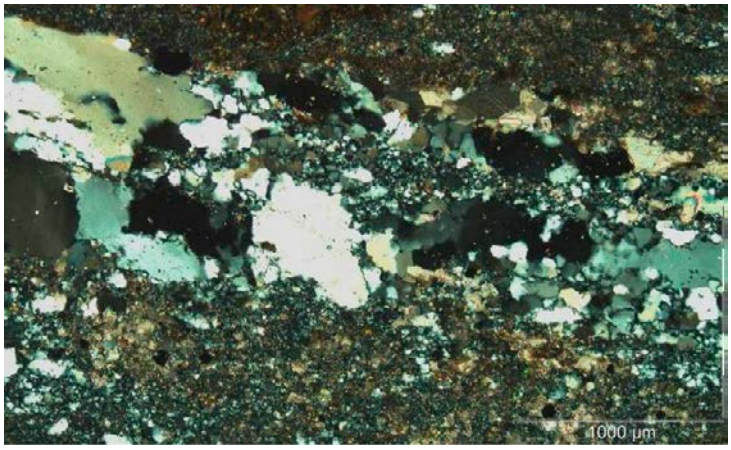

Figure 5-39. *Photomicrograph of quartz-rich mylonite. Tunnel sample #11.*

5.5.2 Chemistry

Mylonite, including variable amounts of proto-mylonite has been analysed for whole rock chemical composition. The major and minor element composition of minerals in thin sections from the TASS tunnel and from the TASS-tunnel pilot boreholes has been obtained with EDS analyses.

Whole rock chemistry

Three mylonite samples from the tunnel have been identified for major, minor and trace elements (Table 2-1). The results are shown in Table 5-4. Reference rock analyses of Äspö diorite, the dominant rock on Äspö, used for comparisons in figures were taken from Landström et al. (2001) (samples A8, A10, A13, B1–B4, B6 and B8).

Table 5-4. Whole rock chemistry of mylonite samples from the TASS-tunnel.

Element		Tunnel#8	Tunnel#9	Tunnel#11
SiO_2	%	66.00	57.80	65.30
Al_2O_3	%	16.00	17.40	13.60
CaO	%	4.32	6.21	7.75
Fe_2O_3	%	4.60	6.17	4.27
K_2O	%	3.33	4.58	1.14
MgO	%	1.63	2.05	1.03
MnO	%	0.07	0.10	0.09
Na_2O	%	3.33	2.21	4.31
P_2O_5	%	0.27	0.41	0.29
TiO_2	%	0.60	0.85	0.64
Total	%	100.10	97.80	98.40
LOI	%	1.20	2.50	3.00
Ba	mg/kg	2,120	2,570	376
Be	mg/kg	2.84	3.23	1.48
Co	mg/kg	8.04	7.43	< 6.00
Cr	mg/kg	130.00	314.00	197.00
Cs	mg/kg	2.09	1.31	1.12
Ga	mg/kg	22.50	27.50	23.00
Hf	mg/kg	402.00	579.00	435.00
Mo	mg/kg	< 2	< 2	< 2
Nb	mg/kg	11.20	16.80	9.28
Ni	mg/kg	26.50	31.60	21.40
Rb	mg/kg	119.00	159.00	52
Sc	mg/kg	6.80	7.57	25.5
Sr	mg/kg	1,120	1,170	1,540
Ta	mg/kg	1.32	1.36	1.14
Th	mg/kg	13.60	11.80	7.42
U	mg/kg	3.34	8.03	4.50
V	mg/kg	74.4	99.70	104
W	mg/kg	0.91	1.52	0.623
Y	mg/kg	20.40	24.80	31.20
Zr	mg/kg	214.00	277.00	225.00
La	mg/kg	62.40	67.10	57.40
Ce	mg/kg	128.00	134.00	128.00
Pr	mg/kg	13.90	14.0	15.60
Nd	mg/kg	48.50	49.70	60.20
Sm	mg/kg	7.70	8.18	11.20
Eu	mg/kg	1.40	1.14	2.23
Gd	mg/kg	5.71	6.00	9.23
Tb	mg/kg	0.79	0.85	1.32
Dy	mg/kg	4.06	4.67	6.80
Ho	mg/kg	0.77	0.94	1.27
Er	mg/kg	2.07	2.73	3.10
Tm	mg/kg	0.33	0.45	0.44
Yb	mg/kg	1.92	2.82	2.36
Lu	mg/kg	0.29	0.41	0.35

Mylonite chemistry in the tunnel samples shows that Sample #9 has lower concentrations of e.g. SiO_2, Na_2O (Figure 4-76,), and higher Al_2O_3, Fe_2O_3, MgO, MnO and TiO_2 (Figure 4-77, Figure 4-78) compared to the samples #8 and #11, which are more similar in composition, compared to Sample #9. However, #11 has significantly lower concentrations of K_2O, Al_2O_3, Rb and Ba, and higher CaO concentrations than the other samples. The chemical difference between the samples is related to the difference in mineralogy; with e.g. highest mica and chlorite contents of Sample #9 and highest epidote, quartz and albite contents in Samples #7 and #11 (the latter seems to be the richest in epidote and the poorest in mica and/or K-feldspar). The samples show, for example, generally higher SiO_2, and MgO, lower Al_2O_3, TiO_2 compared to the wall rock, mainly reflecting leaching of SiO2, and MgO during alteration of the wall rock (e.g. plagioclase and biotite) and formation of epidote, quartz and mica in the mylonite, whereas Al_2O_3, TiO_2, as expected have been less mobile. Differences in REE-concentrations are very small (Figure 4-79).

Mineral chemistry

SEM-EDS analysis was carried out on minerals in thin sections. Results are shown in Table 5-5.

Epidote in veins has lower Al_2O_3 (20.6%) and higher FeO (15.7%) concentration than epidote in mylonite (mainly > 23% and < 13%, respectively; both in core and damage zone) (Figure 4-80). The variation in muscovite chemistry is small.

Table 5-5. SEM-EDS analyses of minerals in thin sections. n.d. = not detected.

Epidote in mylonite	Na_2O	MgO	Al_2O_3	SiO_2	K_2O	CaO	TiO_2	MnO	FeO	SrO	BaO
Tunnel #1	n.d.	n.d.	23.9	37.1	n.d.	23.2	n.d.	n.d.	12.3	1.16	n.d.
Tunnel #1	n.d.	n.d.	23.9	37.1	n.d.	23.2	n.d.	n.d.	12.3	1.16	n.d.
Tunnel #1	n.d.	n.d.	23.2	36.5	n.d.	23.2	n.d.	0.20	12.7	0.85	n.d.
Tunnel #3	n.d.	n.d.	22.9	37.1	n.d.	23.3	n.d.	0.28	13.0	0.93	n.d.
Tunnel #4	n.d.	n.d.	24.7	37.3	0.16	23.2	n.d.	0.27	11.0	n.d.	n.d.
Tunnel #7	n.d.	n.d.	23.6	37.4	n.d.	23.2	n.d.	0.22	12.5	1.35	n.d.
Tunnel#7	n.d.	n.d.	23.3	37.8	n.d.	23.1	n.d.	n.d.	12.8	0.68	n.d.
Tunnel #8	n.d.	n.d.	23.4	37.7	n.d.	23.5	n.d.	0.29	12.8	n.d.	n.d.
Tunnel #8	n.d.	n.d.	23.2	37.4	n.d.	23.6	n.d.	0.21	13.0	0.86	n.d.
Tunnel #9	n.d.	n.d.	22.9	36.7	n.d.	23.0	n.d.	0.22	13.1	1.01	n.d.
Tunnel #9	n.d.	n.d.	23.7	37.3	n.d.	23.6	n.d.	0.24	12.1	n.d.	n.d.
Tunnel #11	n.d.	n.d.	23.3	37.4	n.d.	23.5	n.d.	0.20	12.3	n.d.	n.d.
Tunnel #11	n.d.	n.d.	23.5	37.7	n.d.	23.2	n.d.	0.30	12.6	0.82	n.d.
Epidote in veins	**Na_2O**	**MgO**	**Al_2O_3**	**SiO_2**	**K_2O**	**CaO**	**TiO_2**	**MnO**	**FeO**	**SrO**	**BaO**
Tunnel #3	n.d.	n.d.	20.6	36.2	n.d.	20.9	n.d.	n.d.	15.7	3.79	n.d.
Muscovite in mylonite	**Na_2O**	**MgO**	**Al_2O_3**	**SiO_2**	**K_2O**	**CaO**	**TiO_2**	**MnO**	**FeO**	**SrO**	**BaO**
Tunnel #1	0.25	1.62	30.0	45.2	10.3	n.d.	0.50	n.d.	4.63	n.d.	0.85
Tunnel #4	n.d.	1.41	31.7	45.6	10.8	n.d.	1.1	n.d.	4.66	n.d.	n.d.
Tunnel #8	0.24	1.86	30.4	44.8	10.7	n.d.	0.42	n.d.	5.85	n.d.	n.d.
Tunnel #8	n.d.	1.58	30.0	45.6	11.0	n.d.	0.65	n.d.	5.44	n.d.	n.d.
Chlorite in mylonite	**Na_2O**	**MgO**	**Al_2O_3**	**SiO_2**	**K_2O**	**CaO**	**TiO_2**	**MnO**	**FeO**	**SrO**	**BaO**
Tunnel #9	n.d.	17.6	16.8	27.4	n.d.	n.d.	n.d.	0.45	25.0	n.d.	n.d.

5.5.3 Stable isotopes

Stable isotopes ($\delta^{13}C$ and $\delta^{18}O$) were analysed for three calcite samples from the tunnel (Table 5-6).

Table 5-6. Stable isotopes in calcite.

Sample	Weight (mg)	$\delta^{13}C$VPDB	$\delta^{18}O$VPDB
Tunnel sample #4	14.8	–11.8	–17.2
Tunnel sample #8	12.6	–11.8	–16.5
Tunnel sample #10	8.3	–11.7	–17.7

The results from the borehole samples are compared with stable isotope composition of calcite from the TASS-tunnel as well as from structure #20 in the TRUE Block Scale boreholes (Andersson et al. 2002a) in Figure 4-81.

Calcite from the TASS tunnel shows very similar stable isotope values with only 0.1‰ variation for $\delta^{13}C$ (–11.8 to –11.7‰) and 1.2‰ variation for $\delta^{18}O$ (–17.7 to –16.5‰), suggesting formation at similar conditions and thus probably at the same event. The relatively depleted $\delta^{13}C$ values suggest influence of organic matter, and the combination of $\delta^{13}C$ and $\delta^{18}O$ values indicates formation during the Paleozoic (~ 440–400 Ma), from brine fluids at 80–145°C, based on earlier studies in this area (cf. Drake and Tullborg 2009, Drake et al. 2009).

5.6 Integrated description of Structure #20 based on TASS tunnel data

Overall, the integrated description of Structure #20 developed from a review of cored borehole data and image logs (Section 4.6) is also consistent with the intercept mapped along the TASS tunnel. From a structural geology standpoint, Structure #20 is a brittle-ductile shear zone that has been re-activated several times in both the ductile and brittle regime. Key features observed in the cored borehole data (weak to strong ductile fabrics, the presence of both mylonite and cataclasite in the deformation zone core, and the association of the deformation zone with epidote-filled fracture swarms) are also seen in the TASS tunnel. The relative dominance of mylonite over other types of fault rock, the relative lack of visible fault gouge or breccia, and the complex interbedding of mylonite and cataclasite noted in drill core are also seen along and across the TASS tunnel intercept.

Structure #20 is characterized by damage zones featuring increased frequency of sealed fractures, reductions in grain size of both phenocrysts and the groundmass of the Äspö diorite, the development of a weak foliation primarily expressed through preferred alignment of potassium feldspar phenocrysts, the presence of occasional thin layers or lenses of cataclasite, and the presence of swarms of vein fractures sealed with epidote. The deformation zone core typically consists of one to three open and flowing fractures within a larger zone of previous moderate to intense ductile deformation, which in turn is marked by alternating bands of mylonite and cataclasite. Only a few kinematic indicators were observed during this study, but those visible at the microscopic scale suggest an oblique-slip environment.

Where the tunnel mapping provides significant insight is to the amount of variability in the thicknesses of the damage zone surrounding the core of Structure #20 over very short distances. The relict blast holes in the TASS tunnel are spaced approximately 2–3 m apart, which is a much closer spacing than boreholes in the TRUE Block Scale volume. The resulting information provides a very detailed look at the in-plane "roughness" of Structure #20, albeit within a very limited window (the approximately 5m width of the TASS tunnel). In addition, the combined TASS tunnel and

pilot borehole database allows for a 'calibration' of what is important to look for in the drill cores. Studying Structure #20 on the walls of the TASS tunnel provides significant insight into the relationship of the deformation zone to other structures (fine-grained granite, epidote-filled fractures and rock fabric) that would be more difficult to observe in drill core. This in turn results in a better interpretation of BIPS images and core data, because the interpreter has an understanding of the 'larger picture' of the structure.

Geologically, the thickness of the deformation zone core is fairly consistent; it ranges between 1.0 to 2.2 decimetres in total thickness across its TASS tunnel intercept. The thickest sections of deformation zone core tend to occur where Structure #20 encounters dikes of fine grained granite. Statistically, there is no difference in terms of the mean deformation zone core thicknesses (Figure 5-40) from either data source. A Wilcoxon signed rank test (Wilcoxon 1945) was run to confirm this, by determining whether the mean ranks of the two samples (BIPS and tunnel maps) are statistically different. The Wilcoxon test was chosen because it does not require the probability distribution of the samples to be normal.

At a significance level of 5%, the samples showed no difference (Figure 5-41). Results of Wilcoxon signed-rank test of the mean deformation zone core thickness of Structure #20 from the TASS tunnel mapping (variable "DZ Core thickness – 1") and from BIPS borehole observations (variable "DZ Core thickness – 2").

This suggests that for deformation zones similar to Structure #20, the estimate of the mean deformation zone core thickness from a widely-spread array of boreholes can be as good as that derived from a detailed study such as the one described here, provided the key geologic indicators (i.e. a deformation zone 'signature') are known before mapping is begun.

The variance in total deformation zone thickness is quite a bit larger than the thickness of the deformation zone core (Figure 5-42). The overlapping mean and median confidence intervals indicate that, even though there is an observable difference between total thickness established from the TASS tunnel and from boreholes, it is not significant enough to suggest that the data are from separate populations. The same Wilcoxon test was completed on the total deformation zone thickness data set from tunnel and BIPS images, and failed to reject the null hypothesis of no difference.

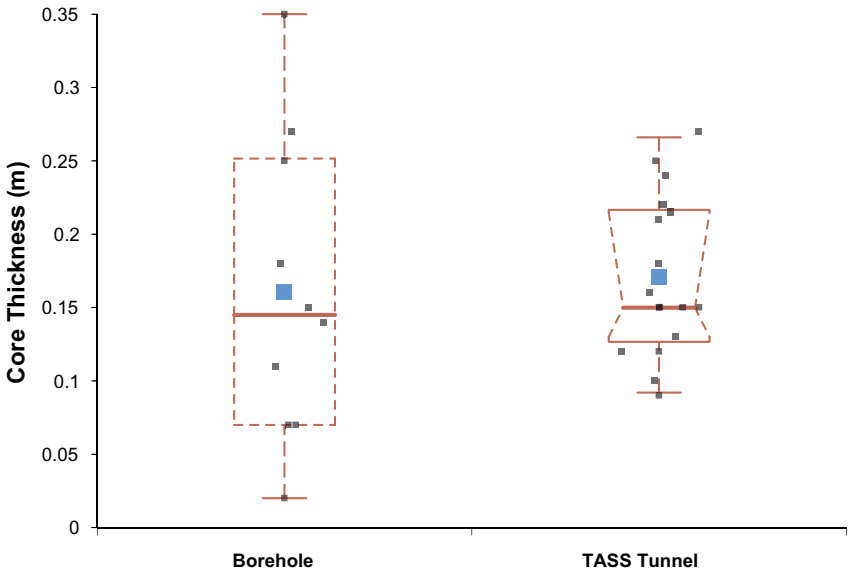

Figure 5-40. *Box-and-whisker plot illustrating thickness of the Structure #20 deformation zone core, as a function of data source (tunnel or cored borehole). The teal dot represents the mean value for each sample, and the red line the median value.*

Descriptives

N	10

DZ Core Thickness	Minimum	1st Quartile	Median	3rd Quartile	Maximum	Inter-quartile range
DZ Core Thickness - 1	0.0900	0.11833	0.18500	0.22167	0.2700	0.10333
DZ Core Thickness - 2	0.0200	0.06600	0.21275	0.36808	0.6770	0.30208

Location

Hodges-Lehmann shift	0.03800
95.12% CI	-0.10150 to 0.26650

$F(_{DZ\ Core\ Thickness\ -\ 2}) = F(_{DZ\ Core\ Thickness\ -\ 1} + \Delta)$

Wilcoxon test

Hypothesized difference	0

Sign	n	Rank sum	Mean rank
Positive	6	34.0	5.67
Negative	4	21.0	5.25
Zero			

T statistic	34.00
Exact p-value	0.5566 [1]

H0: $\Delta = 0$
The shift in location between the distributions of the populations is equal to 0.
H1: $\Delta \neq 0$
The shift in location between the distributions of the populations is not equal to 0.
[1] Do not reject the null hypothesis at the 5% significance level.

Figure 5-41. *Results of Wilcoxon signed-rank test of the mean deformation zone core thickness of Structure #20 from the TASS tunnel mapping (variable "DZ Core thickness – 1") and from BIPS borehole observations (variable "DZ Core thickness – 2").*

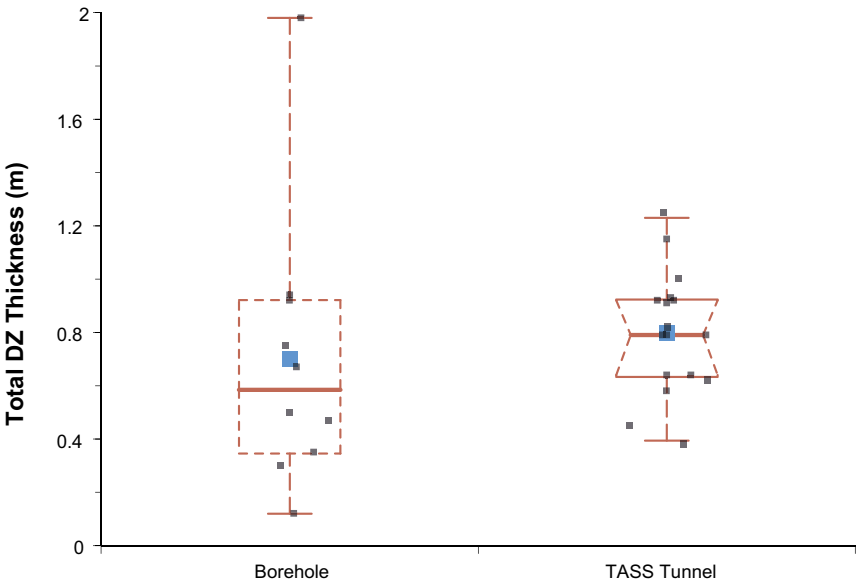

Figure 5-42. *Box-and-whisker plot illustrating total deformation zone thickness of Structure #20 as a function of data source (tunnel or cored borehole). The teal dot represents the mean value for each sample, and the red line the median value.*

Descriptives

N	10

	Minimum	1st Quartile	Median	3rd Quartile	Maximum	Inter-quartile range
TT_Tunnel	0.5800	0.77750	0.91500	0.93583	1.1500	0.15833
TT_BIPS	0.1150	0.34079	0.58550	0.92442	1.9790	0.58363

Location

Hodges-Lehmann shift	-0.25100
95.12% CI	-0.51250 to 0.28550

$F(_{TT\_BIPS})=F(_{TT\_Tunnel}+\Delta)$

Wilcoxon test

Hypothesized difference	0

Sign	n	Rank sum	Mean rank
Positive	2	16.0	8.00
Negative	8	39.0	4.88
Zero			

T statistic	16.00
Exact p-value	0.2754 [1]

H0: Δ = 0
The shift in location between the distributions of the populations is equal to 0.
H1: Δ ≠ 0
The shift in location between the distributions of the populations is not equal to 0.
[1] Do not reject the null hypothesis at the 5% significance level.

Figure 5-43. *Results of Wilcoxon signed-rank test of total thickness (TT) of Structure #20 from the TASS tunnel mapping data set and the reinterpretation of BIPS images.*

The wide spread in the values of total deformation zone thickness, when compared to the (relatively) consistent deformation zone core thicknesses, highlights the uncertainty inherent in attempting to define where the damage zones begin and end. In Structure #20, no single property is suitable for delineating whether a given rock volume is inside the damage zone or not. It is frequently an assemblage of characteristics (foliation, grain size, sealed fracture intensity, and presence of epidote 'marker beds'), of which not every characteristic is present in every cored borehole or tunnel section. It is important to note, however, that the TASS tunnel is only sampling a spatial subset of Structure #20; the borehole array, which covers a larger volume of rock, is still the 'best' estimator for the potential maximum thickness of Structure #20.

One of the key results from the cored borehole data re-analysis (Chapter 4) was that the distribution of thicknesses in the damage zone is highly anisotropic. The upper side of structure #20 (the so-called 'upper' damage zone in Section 5.3.2) appears to be consistently and significantly thicker in both cored boreholes and in the TASS tunnel (Figure 5-41, Figure 5-43). This is not an uncommon finding in the literature (Aarland and Skjerven 1998, Bradbury et al. 2002), though it is somewhat difficult to explain why this would be so for massive igneous/metamorphic rocks. However, a statistical analysis (ANOVA and Kruskal-Wallis) suggests that even though there is an apparent difference in thickness between the upper and lower damage zones (Figure 5-44), the two samples cannot be said to come from different populations at the 5% significance level (Figure 5-45). This indicates that, at least in terms of Structure #20, modelling the deformation zone as symmetric around a central core may be a reasonable approximation.

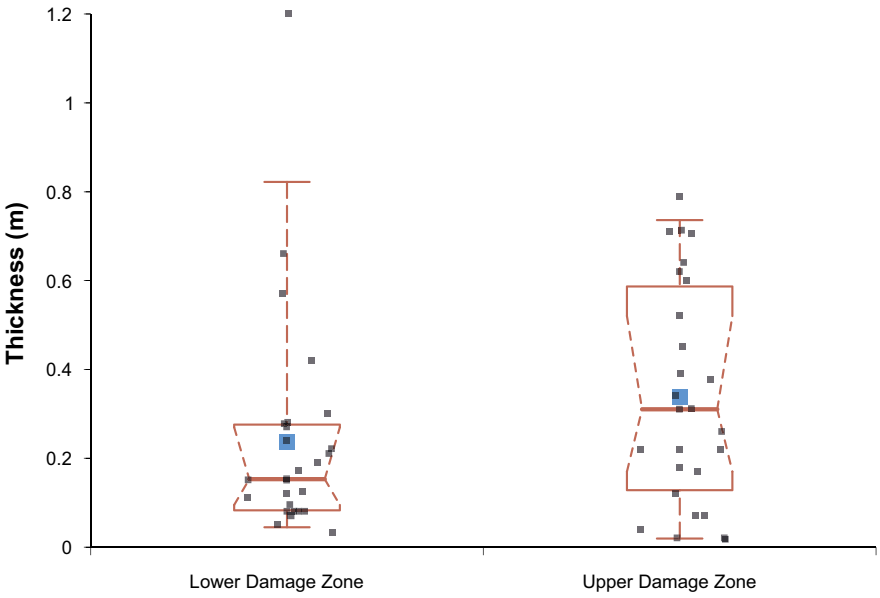

Figure 5-44. *Box-and-whisker plot illustrating the interpreted thicknesses of the upper and lower damage zones of Structure #20). The teal dot represents the mean value for each sample, and the red line the median value.*

As noted in Section 4.6, there is a strong association between Structure #20 and dikes of fine-grained granite. The mapping of Structure #20 in the TASS tunnel provided additional insight as to the nature of the relationship. The authors have developed a tentative hypothesis to describe the timing of the intrusion and its relationship to Structure #20. Intrusion of the fine-grained granite appears to be coincident with the presence of a ductile shear zone precursor to Structure #20. Horizontal expansion of the granite dike is stopped by the ductile precursor structure, and smaller subsidiary dikes of fine-grained granite are emplaced along the ductile structure. Later brittle-ductile and brittle deformation events are now complicated by the interplay of rocks with different rheologies (fine-grained granite versus Äspö diorite), which serves to further focus deformation along the old ductile precursor.

Overall, the general features of Structure #20 found in the TASS tunnel are consistent throughout the tunnel intercept (ductile shear zone with multiple brittle reactivation). Whole rock chemistry of the core of the deformation zone showed variations related to the proportion of the dominant minerals. Extent of wall rock alteration varied along the tunnel intercept. Mylonite thickness was relatively consistent at ~ 5–10 cm, but in some parts (e.g. in the tunnel roof) a splay of epidote-rich mylonite/cataclasite run off from the core (a couple of decimetres to a metre away) and then reunites with the core a couple of metres away along strike. The localisation of the ductile shear zone to a fine-grained granite body (or dike), is another feature that is observed in a minor part of the Structure #20 intercept in the TASS tunnel.

The general features of Structure #20 are (in order of formation):

- Ductile origin; abundant mylonite (epidote- and quartz-dominated occasionally with abundant mica) is as a rule present as numerous parallel shear bands in the core of the deformation zone and a few kinematic indicators were observed (e.g. C-S fabric, σ-type porphyroblasts/mantled porphyroclasts, and oblique foliation). Sinistral strike-slip and dip-slip dominates.
- Cataclasite, often epidote-rich, with related offset of mylonite is indicated. At least two generations of cataclasite were observed.
- Several calcite veins occur in fractures re-activating the mylonite/cataclasite, but the ones analysed for stable isotopes all showed similar signatures, i.e. Paleozoic brine type signature. However, older and younger calcites are indicated (especially younger euhedral calcite in presently open fractures). Presence of older calcite is indicated by paragenesis with epidote, which in this area is Proterozoic in age. Paleozoic calcite occurs together with fluorite, chlorite, clay minerals, adularia and pyrite. The number of calcite-filled/coated fractures varies along strike.

ANOVA

Effect	SS	DF	MS	F	p-value
Model	0.1372	1	0.1372	2.26	0.1384 [1]
Error	3.1510	52	0.0606		
Total	3.2882	53	0.0620		

H0: $\mu_1 = \mu_2 = \mu...$

The mean of the populations are all equal.

H1: $\mu_i \neq \mu_j$ for at least one i,j

The mean of the populations are not all equal.

[1] Do not reject the null hypothesis at the 5% significance level.

Kruskal-Wallis test

Thickness (m) by Damage Zone	n	Rank sum	Mean rank
Lower Damage Zone	27	320.3	11.86
Upper Damage Zone	27	320.3	11.86

H statistic	2.59
X^2 approximation	2.59
DF	1
p-value	0.1076 [1]

H0: $\theta_1 = \theta_2 = \theta...$

The median of the populations are all equal.

H1: $\theta_i \neq \theta_j$ for at least one i,j

The median of the populations are not all equal.

[1] Do not reject the null hypothesis at the 5% significance level.

Figure 5-45. *Results of ANOVA (upper) and Kruskal-Wallis testing of the thickness of the upper and lower damage zones, respectively. The null hypothesis is that there is no difference between the two sample sets. A significance level of 5% was used for both tests.*

On the mostly smooth fracture surfaces of the presently open fractures, calcite was observed (partly euhedral, several generations observed) as well as abundant chlorite and clay minerals (illite or mixed-layer clay) and scattered occurrences of cubic fluorite and pyrite. Chlorite and clay minerals were mostly present in a thin smooth cover on the fracture surface, although euhedral individual crystals were observed as well. Striations were observed on chlorite and clay minerals (also on calcite). Roughness of coatings varies, and clay mineral abundance varies indicating heterogeneous retention properties along the zone. Wall rock minerals and epidote existed in minor clay mineral-rich (gouge) parts (not as frequently found as reported in Andersson et al. (2002a). The size of euhedral minerals such as calcite varied along strike indicating that the aperture of the open fractures varies noticeably.

6 Integrated description of Structure #20

The primary goal of this study was to produce an integrated description of a deformation zone at the centimetre to decimetre length scales, by combining observations from cored boreholes, image logging, tunnel mapping, fracture mineralogical sampling, hydraulic testing and hydraulic pressure responses. The resulting composite description includes comments on the lithologies associated with the deformation zone, a description of the visible fracturing, descriptions of relationships in the ductile fabric at macro and micro scales, the hydraulic connectivity and hydraulic properties of the deformation zone, and detailed mineralogical descriptions of brittle and ductile fabrics. The primary target of this study was Structure #20 of the TRUE Block Scale experiment.

6.1 Lithology

The dominant lithology of Structure #20 is that of its host rocks; i.e. a mix of Äspö diorite and fine-grained granite (Section 4.2). The structure itself consists of a mix of fault rock, including mylonite, cataclasite, fault gouge, and occasional breccia, and of various open, partly open, and sealed fractures. The brittle components of Structure #20 are hosted inside an older, re-activated ductile shear zone characterized by moderate to intense mylonitization. Relative to the rest of the TASS tunnel and the rock mass sampled by the TRUE Block Scale boreholes, the Äspö diorite within the damage zone of Structure #20 tends to have smaller feldspar phenocrysts, a generally more fine-grained groundmass, and a pervasive foliation that increases in intensity closer to the observed core of Structure #20.

Structure #20 shows at least a weak association with fine-grained granite intrusions. During the initial tunnel mapping process (Hardenby and Sigurdsson 2010), the rock around the Structure #20 intercept was classified as “hybrid rock”, representing a significant degree of intermingling and partial re-crystallization of Äspö diorite and fine-grained granite. Termination relationships (Figure 6-1) indicate that, while brittle fracturing has localized along the shear zone/dike contact, the lateral spread of the initial intrusion was limited by the presence of the Structure #20 ductile precursor. This provides constraints on the age of the ductile precursor. It also suggests that paying attention to igneous intrusions is necessary, as they may follow pre-existing ductile shear zones or may be coincident with ongoing ductile shearing.

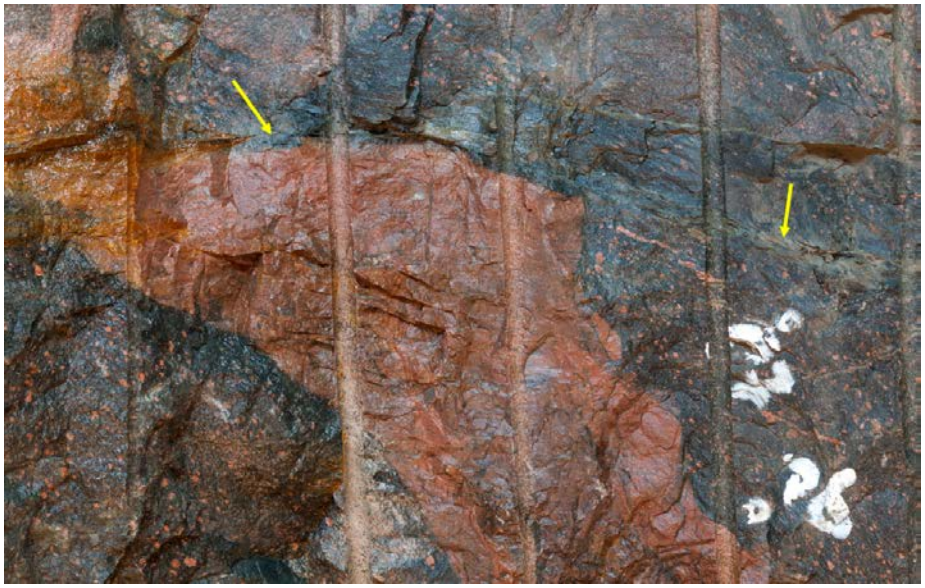

Figure 6-1. *Localization of Structure #20 (yellow arrows) in relation to a dike of fine-grained granite exposed at chainage 76+00 in the TASS tunnel.*

6.2 Fracturing

Effectively, there are three categories of fracturing associated with deformation zones similar to Structure #20, which are also assumed to be applicable to deformation zones in general within the Äspö/Laxemar/Simpevarp region:

- Brittle deformation in the core of the deformation zone, expressed as a mix of sealed and open fractures;
- Increased fracture intensity in the damage zones surrounding the deformation zone cores. This category also includes sealed fracture networks seen around the deformation zone that likely represent a mix of healed veins and diffuse strain during multiple periods of deformation along Structure #20; and
- Epidote-filled fractures that form so-called “marker beds” for Structure #20.

At the macro (centimetre to decimetre) scale, fracturing within the core of Structure #20 is confined to one to three open, well-developed fractures with one or more generations of mineral infilling. The open fractures generally are oriented subparallel to the ductile fabric in the deformation zone; this is visible mainly in thin section (Section 5.5). Surprisingly, kinematic indicators such as slip fibres or slickensides are rare at this scale. Open fracture orientations within the Structure #20 core are almost uniformly along-strike with the larger-scale structure, especially in the pilot boreholes for the TASS tunnel (Figure 6-2). The presence of multiple open fractures within the deformation zone core indicates a level of structural (and hydraulic) complexity that must be accounted for in site-descriptive modelling and analysis of long-term safety. Specifically, it puts constraints on available surface area for transport calculations, as well as potentially limiting permeability perpendicular to the plane of the deformation zone.

Most of the fractures associated with Structure #20 are sealed fractures; the presence of sealed fracture networks (P_{10} values of 10 to 100 fractures/metre, or higher) is a key indicator of the start of the damage zone surrounding Structure #20. This is not to say that sealed fracture networks cannot occur away from deformation zones, but rather that they are a strong piece of evidence in delineating the volume of effect around a deformation zone. They generally show orientations subparallel to the strike of Structure #20, albeit with some minor variability. The increase in sealed fracture intensity is not quite as visible in fracture data from Sicada stored in *p_fract_core*; CFI plots (Section 4.3.2) often show little to no inflection at the interpreted Structure #20 in most of the TRUE Block Scale boreholes (with the exception of KA2511A and KA2563A) and all of the TASS pilot boreholes.

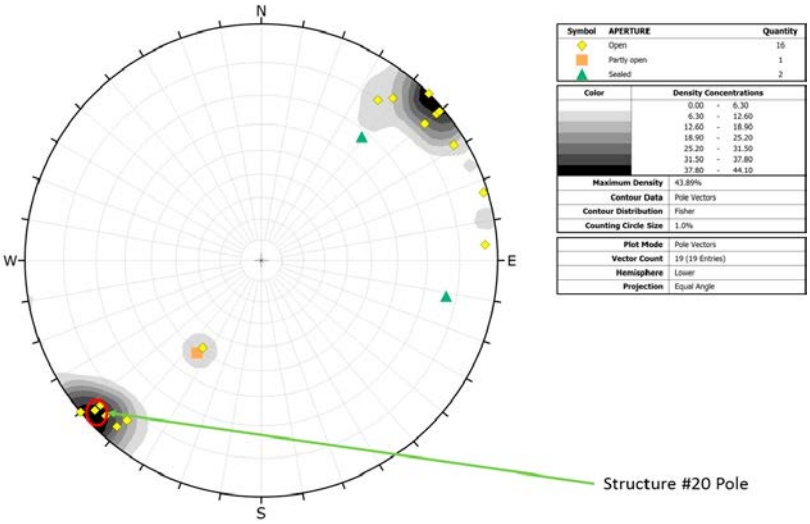

Figure 6-2. *Stereonet of fractures recorded from BIPS imaging (Sicada table p_fract_core) in TASS tunnel pilot boreholes within Structure #20 (Table 4-3). Mean orientation of Structure #20 from Hermanson and Doe (2000) is plotted as orange triangle and circled below. Note that only data from the TASS tunnel are included in this figure for clarity; similar results including the TRUE Block Scale boreholes are presented in Chapter 4.*

Where a deflection is seen on the CFI plot, it is most frequently expressed in the intensity of epidote-filled fractures. Fracture morphologies (roughness, aperture, and degree of alteration) were remarkably similar across all boreholes intersecting Structure #20. The sole exception is fracture shape, where the TASS pilot bores were clearly mapped following a different scheme than the TRUE Block Scale boreholes.

It is the authors' opinion that the epidote-filled fractures surrounding the deformation zone are genetically related to Structure #20, at least in terms of their current mineral infillings. It is likely that these structures first started as veins, and were later re-activated, possibly several times, in the brittle regime. These fractures, or at least one period of their re-activation in the brittle regime, post-date the intrusion of the fine-grained granite, based on cross-cutting relationships observed in the TASS tunnel (Figure 6-3). They serve as a useful indicator as to where the start of the damage zone of Structure #20 is located; it would be useful to see if similar structures are noted near other mapped deformation zones at Äspö or in Simpevarp and Laxemar.

Offset of fine-grained granite dikes, with pre-date brittle deformation along the epidote-filled fracture marker beds, but are contemporaneous with ductile shear along the Structure #20 precursor, can be used to make estimates of potential deformation (Figure 6-4). Apparent displacements on the epidote-filled fractures, assuming predominantly strike-slip motion, are on the order of 0.09–0.12 m in the X-Y plane, parallel to the TASS tunnel floor. As the true slip vector is not known, this should serve as an estimate of the lower range of cumulative displacement. It is also important to recognize that, inside the core of Structure #20, much of the brittle strain is accommodated by further deformation of the rock fabric (production of fault gouge, cataclasite, and mylonite), such that the magnitude of displacement in the Structure #20 core is likely smaller than that observed along the brittle fractures in the damage zone.

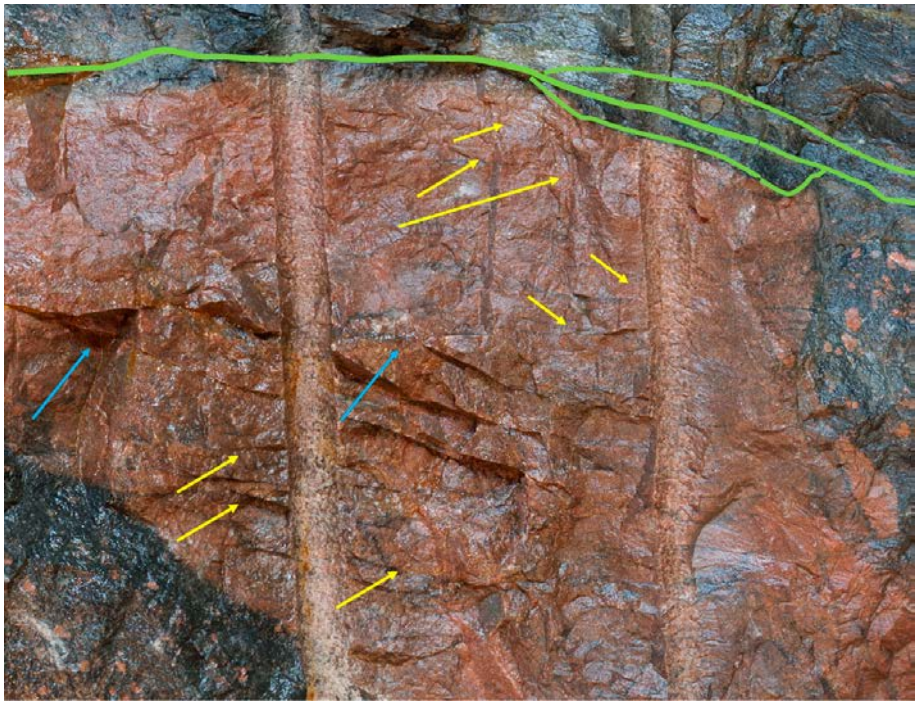

Figure 6-3. *Close up of contact between fine-grained granite and Structure #20. Note the abundance of sealed fractures (yellow arrows) and partially open fractures (blue arrows) inside the fine grained granite. These fractures all have similar orientations to Structure #20, and are likely related to at least one phase of brittle deformation along the deformation zone. The green lines represent the open fractures inside the brittle core of Structure #20.*

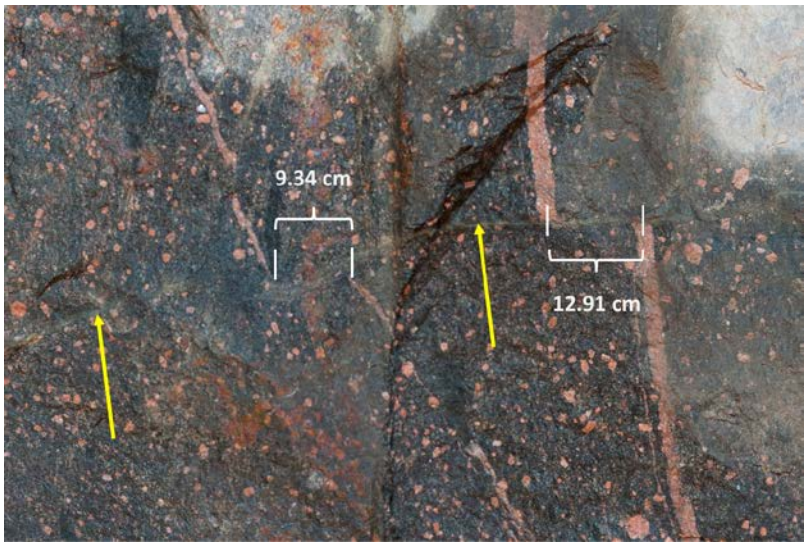

Figure 6-4. *Epidote-filled fractures serving as a "marker beds" for Structure #20 (yellow arrows). Note the left-lateral offset of small dikes of fine-grained granite (white brackets); the same sense of shear is found inside Structure #20. Apparent displacements are measured from tunnel images, where the photographic resolution is on the scale of 0.6 mm per pixel.*

6.3 Structural geology

As previously mentioned in the discussion of Lithology (Section 6.1), Structure #20 as observed today presents as an oblique-slip fault with predominantly sinistral displacements developed from a ductile shear zone pre-cursor. Kinematic indicators in several intercepts (Sections 4-5 and 5-5) also suggest both dextral and pure dip-slip, leading to the conclusion that Structure #20 has been re-activated multiple times in the brittle regime. Faulting has occurred within a zone of previously concentrated ductile deformation, characterized by moderate to intense mylonitization combined with the development of a pervasive foliation. The foliation, which is generally expressed as a preferred alignment of potassium feldspar phenocrysts within Äspö diorite, likely represents the effects of the first post-magmatic metamorphic event after host-rock emplacement. Examination of the Structure #20 intercept with the TASS tunnel (Chapter 5) shows an association between the ductile precursor and a dike of fine-grained granite. The granite either post-dates or occurred coeval with ductile deformation, as the intrusion intersects and then follows Structure #20. However, later brittle deformation on Structure #20 is localized along the Äspö diorite – fine-grained granite boundary (different rheologies).

Structure #20 exhibits a fairly typical deformation zone configuration (Figure 1-2), including a relatively narrow core composed of both ductile and brittle structures, surrounded by a damage zone largely characterized by increased fracture intensity. On average, the total thickness of Structure #20, including the deformation zone core and flanking damage zones, is approximately 0.8 m. The maximum interpreted total thicknesses of Structure #20 generally occur in the TASS tunnel; larger-scale foliation structures and sealed fractures are more readily visible at the tunnel scale than at the borehole scale.

Data recorded from the pilot holes and the walls of the TASS tunnel confirm that the orientation and extent of Structure #20 (transparent blue polygon in Figure 6-5) in the most recent TRUE Block Scale hydrostructural model (Winberg et al. 2000) are a good representation (319/85) of the actual structure geometry when a plane is best-fit to all (TASS and TRUE Block Scale) data. Predicted intercepts in the TASS pilot boreholes based on the TRUE Block Scale model of Structure#20 are only off by 0.2–0.3 m (Table 6-1); the sole exception is in KI0016B01, where we suspect the depths recorded in the drill core box are off by a few metres. This result indicates that, at least over the scale of the investigation area (~ tens of m in length between boreholes in TASS and the TRUE Block Scale rock volume) Structure #20 is largely planar, with only local-scale undulations. The 'best-fit' orientation solution to a single plane, with a bias towards fitting data from the TASS tunnel and nearby boreholes, is 320/83.

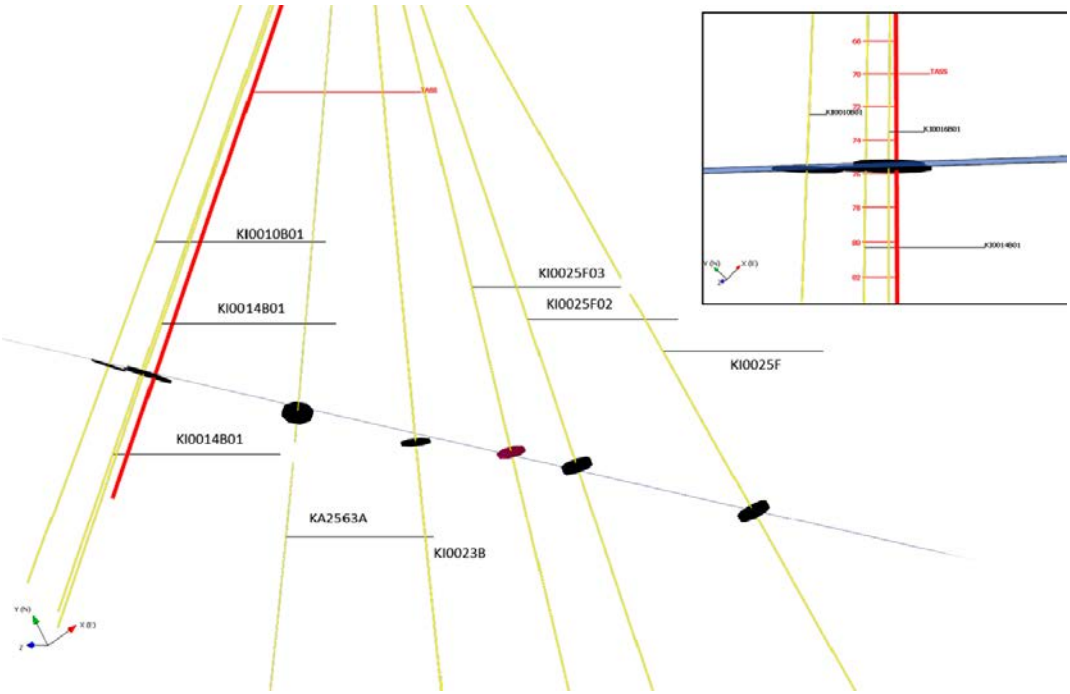

Figure 6-5. *Illustration of Structure #20 intercepts interpreted in the TRUE Block Scale boreholes and the TASS pilot boreholes. View is from above, looking down along dip. Inset shows close-up of interpreted intercepts with the TASS tunnel and TASS pilot boreholes.*

Table 6-1 . Comparison of predicted and actual Structure #20 intercepts based on geological information (Sections 4.6 and 5.6).

Idcode	Measured depth (m) Predicted	Core	BIPS
KI0010B01	74.86	75.1–75.14	75.05–75.19
KI0014B01	72.01	72.16–72.30	72.28–72.42
KI0016B01	70.73	72.58–72.78	70.73–70.91
TASS (centerline)	75.3	75.54–75.81*	N/A

* Based on Blast Hole #13, which is ~ 0.13 cm from the tunnel centre line.

In the boreholes and tunnel sections analyzed as part of this study, the specific structural geological components of Structure #20 consist of, cf. Figure 6-6:

Upper damage zone: The onset of Structure #20, at least locally, is noted by the presence of a series of epidote-filled fractures striking sub-parallel to the deformation zone. The hanging-wall damage zone is defined by a pervasive foliation, a reduction in the grain-size of potassium feldspar phenocrysts, and a trend of increasing sealed fracture intensity towards the deformation zone core. Insome intercepts, sealed fracture networks have been recorded in Sicada in or near the hanging-wall damage zone. Upper damage zone thicknesses are generally in the range of 20 to 40 centimetres, with a significant amount of variability between boreholes and between walls in the TASS tunnel.

Deformation zone core: The deformation zone core primarily consists of one to three open, planar, curved fractures with water seepage and significant mineralization inside a matrix of moderate to intense mylonitization, with pods, lenses and layers of cataclasite. Microtextural analysis of the ductile structures revealed both dip slip and strike slip, the latter mostly sinistral. Occasional fault gouge and breccia are also found, though this is mostly within the TRUE Block Scale borehole array. Note that the deformation zone core is characterized by both brittle and ductile structures, representing its complex deformation history. Open fractures are accompanied by calcite-filled sealed fractures, many of which are oriented sub-parallel to Structure #20. The deformation zone core thickness of Structure #20 averages 0.17 m, and varies in thickness from 0.02 m to 0.68 m.

An important note is that deformation zone core thicknesses calculated from a reinterpretation of BIPS images (Section 4.4.2) are generally much thicker (mean of 0.26 m, maximum of 0.68 m) than those calculated from the physical review of drill cores or from mapping in the TASS tunnel. There is relatively little difference in deformation zone core thickness between borehole data and the TASS tunnel walls (Figure 5-40).

Lower damage zone: The damage zone is highly asymmetric; the lower damage zone is frequently much thinner than the upper damage zone; it is generally 10 to 15 centimetres or less in thickness, although some are thicker (40–70 centimetres). Often the lower damage zone does not exhibit the same ductile precursor characteristics (foliation, changes in phenocryst grain size). It is most frequently delineated by increased sealed fracture intensity, and occasionally by the presence of host-rock alteration (the so-called "red staining"). Sealed fracture intensity in the lower damage zone is highest where Structure #20 intersects dikes of fine-grained granite.

6.4 Mineralogy/geochemistry

Mineralogical analysis of intercepts of Structure #20 in boreholes and the TASS tunnel show similar general features regarding the fracture re-activation history and deformation events. This is evidenced by small deviations of both the fracture mineral assemblages and the whole-rock and mineral chemistry. The overall characteristics were similar but showed some heterogeneity, accordingly:

- Wall rock alteration showed very similar features; alteration of Fe-Mg-minerals, fragmentation of feldspars, re-crystallisation of quartz. The extent of the alteration varied from decimetre to metre scale, depending on the intercepts.
- The thickness and amount of mylonite and cataclasite varied between different intercepts; mylonite thickness ranged from 0.05 m to 0.2 m (Figure 6-6). The proportion of the dominant minerals of the mylonite bands; epidote, quartz and mica, also varied within centimetres.
- The general mineral assemblages were (Figure 6-7), in order of tectonic sequence):
  - Ductile deformation (mylonite)
    - Mylonite was present in all Structure #20 intercepts. A splay of epidote-rich mylonite/ cataclasite intermittently made up the edge of the damage zone.
  - Brittle deformation (cataclasite and extensional fractures)
  - Cataclasite, at least two generations.
    - Multiple fracture zone re-activations are indicated by mineral paragenesis (from hydrothermal [calcite, epidote, quartz, adularia, fluorite, pyrite] to more lower temperatures [calcite, fluorite, chlorite, clay minerals, adularia and pyrite]) and stable carbon and oxygen isotopes in calcite (Proterozoic and Paleozoic fillings dominate). Presently open fractures hold the youngest coatings; calcite (partly euhedral) and abundant chlorite and clay minerals (illite or mixed-layer clay – striated), with minor fluorite, pyrite and quartz. Varying numbers of calcite-filled fractures in different generations between deformation zone intercepts suggest a degree of spatial variability of brittle deformation. Thicknesses of fracture fillings vary considerably between different intercepts (50 μm to 5 mm).
- Mineral coating morphology on the outermost parts of the fractures varied over larger distances, e.g. related to amount of euhedral crystals and fault gouge. The TRUE Block Scale boreholes are featured by higher amounts of loose, fine-grained, fracture coating material than in the TASS pilot boreholes and TASS tunnel intercepts, possibly due to lower drill-core quality in the older TRUE Block Scale cores (grinding and pulverisation of the fracture coatings may have resulted in more fine-grained loose coating material), or that Structure #20 is in fact more gouge-rich in the TRUE Block Scale borehole intercepts. The variation in mineralogy, in particular the clay mineralogy, and the roughness of these coatings would tend to suggest heterogeneous retention properties along a given flow path in the deformation zone.
- The number of presently open fractures also varies and the aperture (as shown by size of euhedral crystals partially covering fracture surfaces) varies between different intercepts and likely influences the hydraulic heterogeneity of the Structure #20 system.

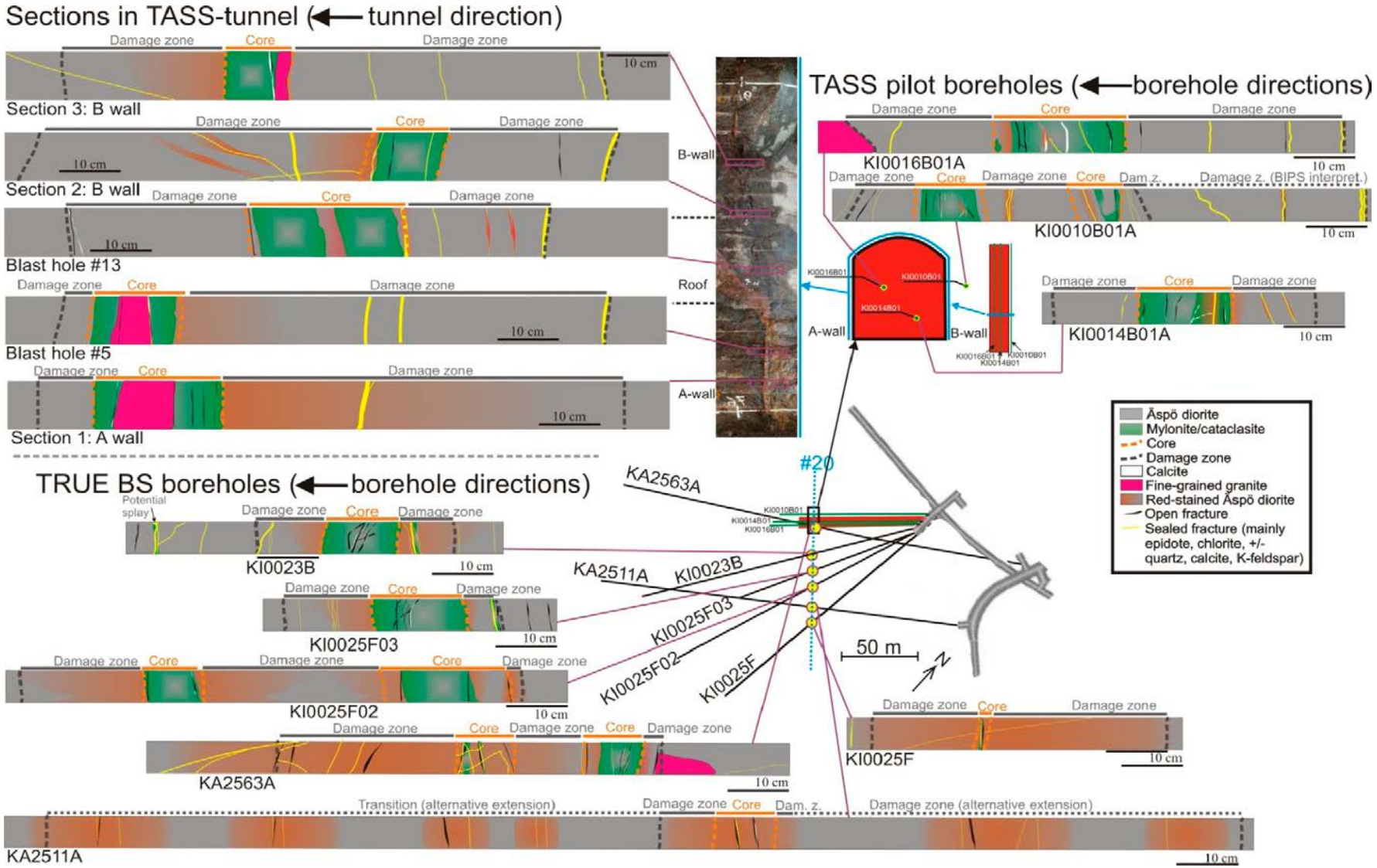

Figure 6-6. *Synthesis of Structure #20 based on mapped borehole and tunnel intercepts (location shown in schematic borehole and tunnel map). Only selected representative sections of the tunnel mapping is shown. Photograph of the tunnel wall projects the whole Structure #20 intercept of the tunnel from B-wall (top – note; upside down with tunnel floor at the very top) roof (centre), A-wall (bottom – with tunnel floor at the lower end).*

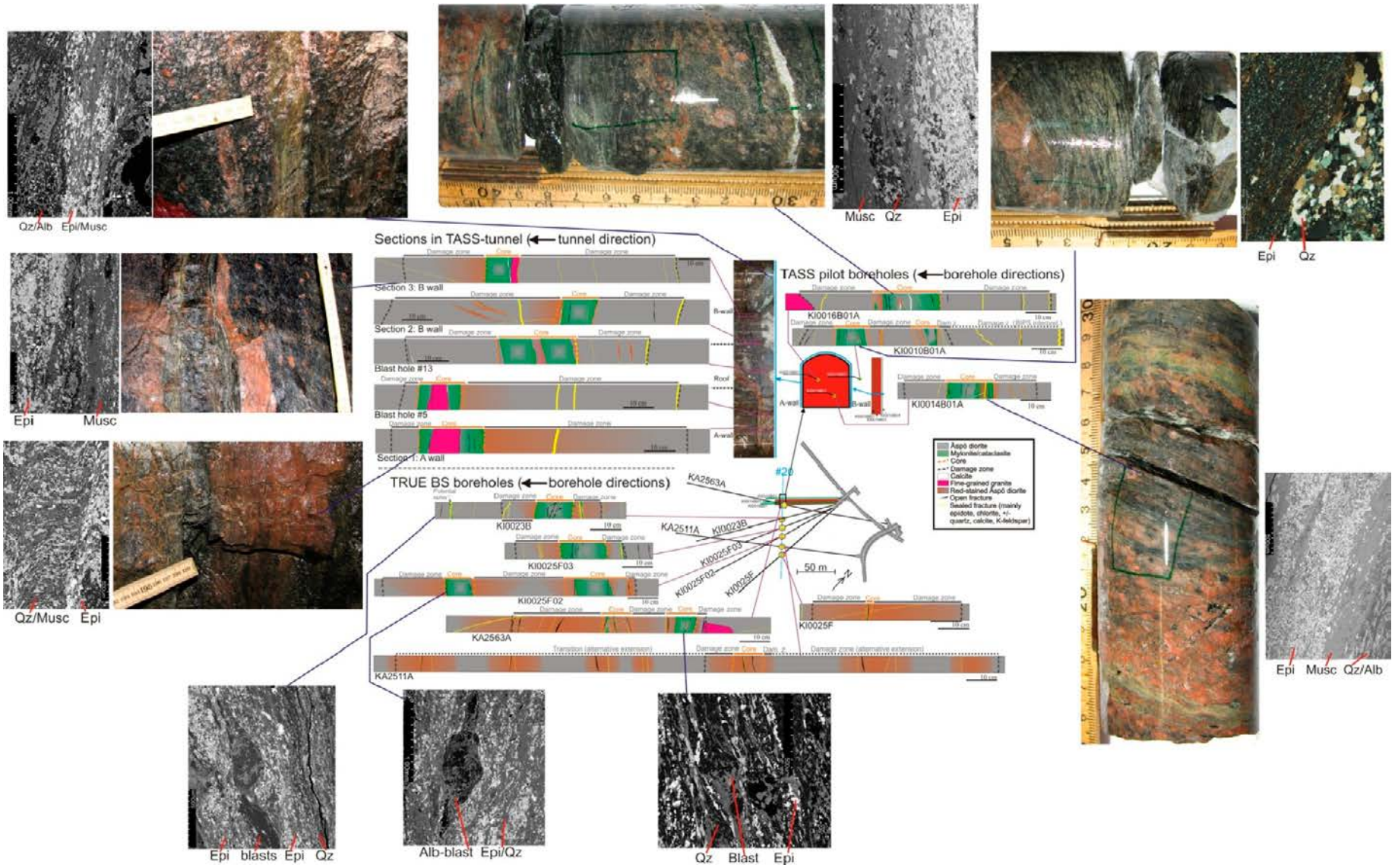

Figure 6-7. *Photographs and/or back-scattered SEM-images of characteristic features of the core of Structure #20 based on the synthesis presented in Figure 6-6.*

6.5 Hydrogeology

The geometry of Structure #20, as modelled by the TRUE Block Scale Project (Andersson et al. 2002a, 2007) was extrapolated from the interior of the TRUE Block Scale volume to intercept the TASS tunnel. The projected intercept was found to compare well with the intercept with the structure interpreted by Hardenby et al. (2008), see also Section 6.3. The intercept was also interpreted from pressure responses observed in the TRUE Block Scale array during drilling of the TASS tunnel pilot borehole KI0010B01. The position of the drill bit in the pilot borehole that produced the pressure responses in the TRUE Block Scale array (Figure 3-3) corresponds well with the geometrically extrapolated intercept. This suggests that Structure #20 can be regarded as an essentially planar structure across its known extent, which is argued on geological grounds in Section 6.3.

Transmissivity data, cf. Table 3-2, evaluated from hydraulic tests performed in the TRUE Block Scale borehole array, the three TASS tunnel pilot boreholes and tests in short TASS grouting holes transecting Feature A were analysed. Statistics of various means of pooling the data were analysed. It was found that the geometric mean and variance of the transmissivity of Structure #20 based on the TASS pilot and probe boreholes (N=6) differ within 45% of the "global mean" established based on all available data on the structure (N=21), cf. Table 3-3. This finding suggests that the statistical sample for Structure #20 from the TASS pilot boreholes (representing a length scale of metres) may be regarded as representative of the "global statistical properties" of the structure (over length scale of several decametres). However, it is noted that the latter relation in no way should be interpreted as a universal law. At best, the relationship is indicative for this type of NW conductive structures (of Structure #20 type) at Äspö (and possibly in the neighbouring Laxemar-Simpevarp area). Corresponding relationships need to be explored site-specifically at depth at Forsmark to fully appraise representativity of a small number of data points related to any given fracture/structure. Furthermore, in a future typical repository (deposition) tunnel situation, access to one single transmissivity data point on a given structure is probably more the rule than the exception. Amongst the cored TASS pilot holes, the three data points span more than two orders of magnitude. This illustrates the effects of structure hydraulic heterogeneity and the uncertainty associated with the representativity of a given hydraulic test result for a given structure. Potentially, an otherwise conductive structure may be intercepted in an impermeable part, where within metres measureable transmissivity (and water flow) would be obtained. It is expected that additional information on heterogeneity in transmissivity of individual structures (fractures and zones) may be obtained from simplified flow and pressure build-up tests conducted in probe and/or grouting holes during tunnel excavation, as exemplified in this study.

6.6 Discussion

6.6.1 Identification of a DZ/MDZ and its characteristics

The purpose of the current work is to document, at a scale of centimetres to decimetres, the characteristics of Structure #20 at the Äspö HRL. This deformation zone, an old ductile shear zone re-activated multiple times in the brittle regime, is likely characteristic of many small-scale faults (so called "minor deformation zones") not only at Äspö, but also in the nearby Simpevarp and Laxemar areas. An analysis of an array of data, including borehole image logs, drill cores, microscopic-scale analysis of deformation, and tunnel mapping all point to the same morphological and hydraulic characteristics:

a. Brittle deformation occurs almost entirely within a ductile precursor. The ductile structure can influence magmatic intrusions (formation of dikes), which then creates zones of rheological contrast that localize brittle deformation.

b. Damage zones, while asymmetric, are almost uniformly indicated by an increase in sealed fracture intensity. Other morphological characteristics, such as changes in grain size or foliation, may not be reliable indicators at locations outside the Äspö/Simpevarp/Laxemar region.

c. The deformation zone core is strongly associated with moderate to intense mylonitization, cataclasite, and minor amounts of clay-rich fault gouge and breccia.

d. There is a strong association between Structure #20 and epidote-filled fractures (minor mylonites/cataclasites), to the point that large, persistent (across multiple boreholes) networks of epidote fractures may serve as "marker beds" for similar structures.

e. Structure geometry inferred from hydraulic connectivity (structure size) assessed from distinct pressure responses in the TRUE Block Scale borehole array during the TASS pilot borehole drilling concur with the existing TRUE Block Scale hydrostructural model, indicating both a relatively planar structure and good in-plane connectivity along strike.

Combining the five primary characteristics of the geology of Structure #20 with knowledge gained during the site descriptive modelling efforts (Fox and Hermanson 2006, Olsson et al. 2007) and with general geological practice, a simple flowchart can be deviseded to distinguish and describe similar structures. Such a flowchart is presented in Figure 6-8; this method is a preliminary method of screening borehole data to determine if a particular fracture intercept is worthy of additional investigation as a potential "large fracture", the latter affecting the positioning of deposition holes/waste canisters through the (Full tunnel Perimeter Intersection) FPI-related design criteria that relate to secondary shear in a fracture as a result of an earthquake, see Munier (2010) for details.

While the overall characteristics (ductile precursor, sealed fracture intensity, and a small number of open, flowing fractures) of structures at the scale of Structure #20 may be similar at Forsmark, the tectonic environment is different enough that conclusions based on size, age relationships, or zone thicknesses should probably need to be evaluated in a similar study there. A suitable structure may exist at the site of the offshore repository for reactor waste (SFR) close to the planned repository site, or a minor deformation zone could be selected for study during the construction of the repository accesses (ramp or central area).

It is noted that the tunnel gives the advantage of a larger observation window of local-scale variability in thickness and heterogeneity, as shown by the detailed mapping of the "inverted cores" made up of the 23 exposed blast holes distributed across the perimeter of the tunnel. However, the mapping effort made here may be regarded as an exception unless extra time and effort is allocated during tunnel excavation. Often, the pace of geologic mapping in the tunnel is dictated by engineering concerns rather than geoscientific needs, resulting in mapping efforts that generalize many important structural features at the expense of limited spatial resolution. Ideally, dedicated campaigns of detailed mapping should be conducted on "type structures" and "type fractures" that can help improve general conceptualizations of these kinds of structures.

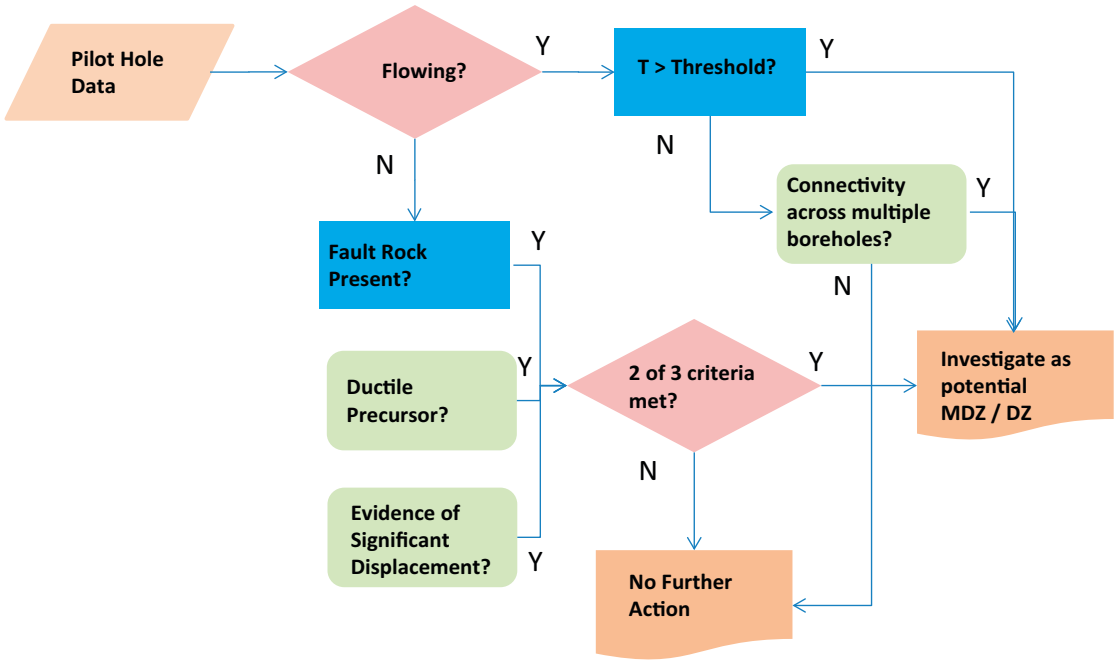

Figure 6-8. *Example of a possible simplified flowchart for determining whether a given fracture is likely to be a feature (MDZ/DZ) similar to Structure #20.*

6.6.2 Implications of structure size and scale of observation

Scale is always an issue in geological modelling, both in how the physical system is represented inside a numerical quantitative model and how primary data are collected to parameterize the underlying conceptual/descriptive and quantitative models. Both issues must be properly addressed in any modelling of a physical system to build confidence in the simulation results.

This work focuses primarily on the collection of data at the centimetre to metre scale. Tunnel maps, which are often constructed at a centimetre-level accuracy using laser scanners or electronic total stations, often impose a truncation limit on fracture mapping (usually on the order of 0.5 to 1.0 metres in terms of trace length). BIPS images, provided they are of high quality with high-quality depth markers, offer the opportunity to characterize fractures, lithology, and deformation features at the centimetre scale. Drill core (and specialized sampling along tunnel walls) allow for the finest resolution, allowing for mapping of geologic structures at the mm to microscopic scale.

The assumed lateral extent of Structure #20, based on geometric interpolation from borehole and tunnel intercepts, is in the range of 77.4 m (Cartesian distance between the most-distant borehole intercepts: KI0010B01 and KI0025F)) to approximately 120 m (the interpreted lateral extent in the X-Y plane in the TRUE Block Scale hydrostructural model (Winberg et al. 2003)). Vertical extent is on a similar scale of 80.5 m (Cartesian distance between the most vertically distant mapped intercepts in boreholes: KA2511A and KI0025F03) to approximately 120 m (interpreted vertical extent in the TRUE Block Scale hydrostructural model). These measurements put Structure #20 firmly in the realm of the so-called “minor deformation zones (MDZ)” and “large fractures” from the Site Descriptive Modelling and safety analysis point of view, respectively. MDZs are hypothesized to exist in the size range of 20 m to ~ 564 m, which represent the largest faults and fractures modelled stochastically during SDM (Fox et al. 2007).

The identification of geological features at the scale of Structure #20 is important both for repository design/construction and safety analysis, where a) such a structure may require pregrouting if the projected water inflow is deemed prohibitive from a practical standpoint, b) their existence and size may affect positioning (and acceptance) of a canister hole (Munier 2010) and c) may (indirectly) affect groundwater flow at a given canister position, thereby potentially affecting the stability of the bentonite buffer (Åkesson et al. 2010) which will affect the safety case. Of particular importance to the safety case are two key questions:

- During an earthquake on a distal fault, is the structure projected to intersect a given emplaced canister large enough to produce a movement large enough to breach (shear) the deposition canister?; and
- Is the groundwater inflow rate projected to be large enough to erode the bentonite buffer from a given canister?

The answer to the second question will be addressed through inflow criteria to deposition holes, access tunnels, or pilot boreholes (for the former two) during development of the deposition areas. However, the first question is entirely a function of fault/fracture size (Munier 2010, Fälth et al. 2008). Notable is that nowhere in the morphological characteristics described above is “size” listed as a significant parameter. Even with a deformation zone as well-sampled and well-documented as Structure #20, the true absolute size in terms of vertical and horizontal extents of the structure is not known. This makes development of any sort of size-thickness relationship to estimate the total size of a deformation zone/minor deformation zone uncertain. A more valid strategy may be to attempt to measure past displacements as a way of constraining the size of structures at this scale. Significant research has been done in many different terrains around the world coupling fracture and fault size to displacement, see e.g. Bonnet et al. (2001), Kim and Sanderson (2005), Shipton et al. (2006), Childs et al. (2009) and Kolyukhin and Torabi (2012). While kinematic indicators are rare in the drill core data collected from Structure #20, clear offsets in dikes and sealed fractures are visible in the TASS tunnel (Figure 6-4). Similar structures can easily be mapped during deposition tunnel mapping, and, combined with hydraulic interference response monitoring, offer the best hope of delineating more accurately the true extent of faults such as Structure #20.

6.6.3 Geological heterogeneity

In terms of heterogeneity, previous sections have commented that, at the metre to tens of metres scale, Structure #20 is remarkably homogeneous. Projected intercepts with the TASS tunnel, based on the structural model for the TRUE Block Scale rock volume, are only off by a few tens of centimetres, suggesting the overall orientation of Structure #20 is both well-constrained and relatively planar. Structural thickness/width (Figures 5-40 and 5-41), although somewhat variable from method to method, are remarkably similar in terms of their means and medians.

At the decimetre and centimetre scale, the geology of Structure #20 is fairly consistent. Nearly every intercept hosts the same features: two to three open fractures with similar mineralization inside a 10–20 cm thick mylonite. Some variability is seen; in particular, some intercepts suggest the presence of a fault splay (i.e. the core branches off into two different structures). However, the relatively limited incidence of visible splays in the borehole data record suggests that the fault splays may be of limited lateral extent. Assessment of the hydraulic connection between the splays and Structure #20 would necessitate their respective isolation with multi-packer system in available boreholes.The largest degree of heterogeneity along Structure #20 occurs in two areas:

- Thickness of the damage zone surrounding the core; and
- The amount, type, and locations of fault rocks (cataclasite, gouge, and breccia) and mineral coated open fractures within the deformation zone core. E.g. the amounts of clay minerals varied widely and the morphology of the coatings varied from smooth striated to a dominance of euhedral crystals, indicating a large variation in aperture.

The ambiguity in the thickness of the damage zone is somewhat vexing. Because of the very high fracture intensity seen in damage zones around deformation zone cores, they can be a threat to tunnel stability during construction. They also raise the issue of re-activation and local fluid flow due to changes in the in situ stress during excavation. There also seems to be little correlation between boreholes as to the sealed fracture intensity, other than a general increase towards the core of Structure #20, and an overall higher intensity in the fine-grained granite, relative to Äspö diorite. However, nearly all of the fractures observed in the damage zone surrounding Structure #20 in the TASS tunnel appeared to be tightly sealed and dry; the majority of flow appeared to come from the open fractures inside the core. This suggests that, while there is significant heterogeneity at the metre to tens of metre scale in the damage zone, the effect of this heterogeneity on overall performance may not be great.

6.6.4 Revisiting the TRUE Block Scale hydrostructural model

The synthesis of Structure#20 established as part of this study is in the following compared with the original conceptualization (Andersson et al. 2002a, 2007).

The original characterisation was focused on identifying and characterising conductive structures, construction of a “hydrostructural” model of the network of conductive structures to serve in the planning and evaluation of in situ tracer tests. Given the short time duration of the performed tests (days to several months) and the fact that radioactive sorbing tracers were to be employed, efforts were also made to describe the microstructural aspects of conductive structures, governing the exchange of mass between the traced fluid and the rock during the tracer experiments. To this end, descriptive categories of conductive structures (Dershowitz et al. 2003) were developed, where Structure #20 belong to structure Type 1 (fault), characterised by cataclasite, open fractures with fault gouge and a developed altered zone around the structure. In addition, detailed generalised microstructure models were developed on the basis of detailed characterisation of altered wall rock and pore spaces (Andersson et al. 2002a). Porosity conceptualization and quantification were obtained from conventional porosity measurements as well as PMMA impregnations of wall rock and constituents of fault rock. Hydrochemical analyses and microscopy provided additional support to the description. Overall, descriptions of the intact rock and the successively and progressively increased alteration towards the conductive structure and the underlying ductile precursor were only made in a tentative manner.

The new components introduced in this study, apart from contributing information from the TASS tunnel intercept with Structure #20, are the detailed characterization and description of Structure #20, including its damage zone, as introduced in the SDM work in Laxemar/Simpevarp and Forsmark. This has been done not only for the cores of the TASS pilot boreholes but also for the TRUE Block Scale intersections with Structure #20 and the along the visible half pipes of blast holes along the TASS tunnel periphery.

The principal comparative findings are the following;

- The geometrical interpretation of Structure #20 as an essentially planar structure within the TRUE Block Scale rock volume (over a distance of c. 100 m) holds also when extrapolating the structure an additional 50 m towards the TASS tunnel, cf. Section 6.5.
- The conceptualization of Structure#20 shifting from single master to dual master (and back) along its extent is substantiated and further refined by the detailed core interpretation made as part of this study, showing dual cores and associated damage zones, cf. Section 6.4.
- The description of geological, structural and mineralogical heterogeneity and variability on a metre to decametre scale is significantly enhanced through the detailed mapping results, see Figures 6-1 and 6-2 and associated text.
- The results of the detailed geological and structural mapping as presented in the synthesis images in Section 6.4 add additional detail and structural-geological context. The images are, however, compatible with and lend additional support to the original micro-structural conceptualization reported by the TRUE Block Scale and TRUE Block Scale Continuation projects.

6.7 Recommendations

In the following some general recommendations for future characterization and modelling work during detailed site investigations at Forsmark are given on the basis of the present work.

Characterization efforts on individual major structures (MDZs/fractures) of the kind and type described in this report may turn out to be prohibitive in terms of time and costs. However, repeated targeted campaigns on representative type structures (and fractures) (e.g. typical orientations) may provide an important basis for constructing generalised conceptual models and may also help define a data base based on which “large fractures”, related to the FIP-related design criteria, may be identified. Ideally multiple pilot boreholes for a given (deposition) tunnel may help to better address and describe heterogeneity in geological and hydrogeological characteristics of a given structure. At a minimum, targeted simplified hydraulic tests in probe holes may help better elucidate hydrogeological heterogeneity of a given structure. Given the expected low intensity of open and flowing fractures at repository depth in Forsmark (PFL $p_{10,corr} < 0.01$ m^{-1}), it should be possible in practice to conduct such tests, thereby obtaining an improved basis for describing structural hydraulic heterogeneity.

High-resolution photography of the tunnel walls should be added as a key part of the RoCS system for mapping deposition tunnels, drifts, and access tunnels. Once the equipment is set up, the photography process is extremely rapid, and can add a significant amount of value to the mapping and documentation efforts. High-resolution imagery (at least 1 mm per pixel, or better, is desired) draped over the laser swath point clouds should allow for a significant amount of added value geoscience mapping data to occur on the desktop, where it does not hinder the the further pace of tunnel excavation.

UV fluorescent imaging of tunnel walls is a useful method of tracking inflow locations, as well as the extent of fine-grained grout (silica sol colloids) penetration in the fracture system. Provided sufficient amounts were injected, it could also (theoretically) be used to track tracer inflow locations into a tunnel, and address issues of channelization and variable aperture. UV surveillance of the tunnel walls would also provide insight as to the number and distribution of flow paths.

There is an issue of construction sequencing and the order of pilot boreholes affecting the detection of MDZ-sized features. For a given transport tunnel, as many pilot boreholes on potential deposition locations should be drilled as possible before beginning excavation of any deposition tunnels. As hydraulic signals are key to defining the extent and connectivity of MDZ-sized features like Structure #20, it is important to have as wide an area of coverage as possible that is well-instrumented with temporary piezometers. In addition, local disturbances in the flow system will result from pre-grouting and deposition tunnel excavation, making collection of data before commencing construction even more critical.

Observation of kinematic indicators in drill core, image logging, and tunnel mapping will be crucial to the understanding of past brittle deformation on fractures, minor deformation zones, and deformation zones. Recording the direction of slip and potential magnitudes from slickensides, slip fibres and offsets of dikes and vein features should be included as part of any formalized method description for fracture mapping during construction. Not only is understanding past displacement key to assessing performance of a given deposition position, it can also pave the way for a more rational basis for constraining deformation zone size and extent than direct correlations to thickness.

There should be a formalized decision matrix constructed for use by geoscience and engineering staff during detailed site investigations at Forsmark to quickly decide whether a given structure encountered in a pilot borehole or during the excavation of an access tunnel should be investigated in more detail. An example decision tree for Äspö/Laxemar is presented as Figure 6-8; similar flowcharts should be constructed for Forsmark, based on geological and mineralogical data from the site investigations and ongoing construction during expansion of the SFR.

References

SKB's (Svensk Kärnbränslehantering AB) publications can be found at www.skb.se/publications.

Aarland R K, Skjerven J, 1998. Fault and fracture characteristics of a major fault zone in the northern North Sea: analysis of 3D seismic and oriented cores in the Brage Field (Block 31/4). Geological Society of London, Special Publications 127, 209–229.

Almén K-E, Stenberg L, 2005. Äspö Hard Rock Laboratory. Characterisation methods and instruments. Experiences from the construction phase. SKB TR-05-11, Svensk Kärnbränslehantering AB.

Andersson P, Byegård J, Dershowitz, B, Doe T, Hermanson J, Meier P, Tullborg E-L, Winberg A (ed), 2002a. Final report of the TRUE Block Scale project. 1. Characterisation and model development. SKB TR-02-13, Svensk Kärnbränslehantering AB.

Andersson P, Byegård J, Winberg A, 2002b. Final report of the TRUE Block Scale project. 2. Tracer tests in the block scale. SKB TR-02-14, Svensk Kärnbränslehantering AB.

Andersson P, Byegård J, Tullborg E-L, Doe T, Hermanson J, Winberg A, 2004. In situ tracer tests to determine retention properties of a block scale fracture network in granitic rock at the Äspö Hard Rock Laboratory, Sweden. Journal of Contaminant Hydrology 70, 271–297.

Andersson P, Byegård J, Billaux D, Cvetkovic V, Dershowitz W, Doe T, Hermanson J, Poteri A, Tullborg E-L, Winberg A (ed), 2007. TRUE Block Scale continuation project. Final report. SKB TR-06-42, Svensk Kärnbränslehantering AB.

Bonnet E, Bour O, Odling N E, Davy P, Main I, Cowie P, Berkowitz B, 2001. Scaling of fracture systems in geological media. Reviews of Geophysics 39, 347–383.

Bradbury K K, Ferrill D A, Dinwiddie C L, Fedors R W, 2002. Fault zone characteristics and deformation mechanisms of porous, non-welded bishop tuff. American Geophysical Union, Fall Meeting 2002, Abstract #T12G-10.

Childs C, Manzocchi T, Walsh J J, Bonson C G, Nicol A, Schöpfer M P J, 2009. A geometric model of fault zone and fault rock thickness variations. Journal of Structural Geology 31, 117–127.

Cooper H H, Jacob C E, 1946. A generalized graphical method for evaluating formation constants and summarizing well field history. American Geophysical Union Transactions 27, 526–534.

Cvetkovic V, 2010a. Significance of fracture rim zone heterogeneity for tracer transport in crystalline rock. Water Resources Research 46. doi:10.1029/2009WR007755

Cvetkovic V, 2010b. Diffusion-controlled tracer retention in crystalline rock on the field scale. Geophysical Research Letters 37, L13401. doi:10.1029/2010GL0434

Cvetkovic V, Frampton A, 2010. Transport and retention from single to multiple fractures in crystalline rock at Äspo (Sweden): 2. Fracture network simulations and generic retention model. Water Resources Research 46. doi:10.1029/2009WR008030

Cvetkovic V, Cheng H, Byegård J, Winberg A, Tullborg E-L, Widestrand H, 2010. Transport and retention from single to multiple fractures in crystalline rock at Äspo (Sweden): 1. Evaluation of tracer test results and sensitivity analysis. Water Resources Research 46. doi:10.1029/2009WR008013

de la Cruz B, Fernández A, Rivas P, Cózar J, Labajo M A, 2000. Äspö Hard Rock Laboratory. TRUE Block Scale project. Tracer test stage. Mineralogical and geochemical analyses of fracture filling materials (gouge and coatings) from drillcore samples. SKB IPR-01-59, Svensk Kärnbränslehantering AB.

Dershowitz W, Lee G, Geier J, Foxford T, La Pointe P, Thomas A, 1998. FRACMAN version 2.6 – Interactive discrete feature data analysis, geometric modelling and exploration simulation. User documentation. Redmond, WA: Golder Associates, Inc.

Dershowitz W, Winberg A, Hermanson J, Byegård J, Tullborg E-L, Andersson P, Mazurek M, 2003. Äspö Hard Rock Laboratory. Äspö Task Force on modelling of groundwater flow and transport of solutes. Task 6c. A semi-synthetic model of block scale conductivite structures at the Äspö HRL. SKB IPR-03-13, Svensk Kärnbränslehantering AB.

Drake H, Tullborg E-L, 2004. Oskarshamn site investigation. Fracture mineralogy and wall rock alteration. Results from drill core KSH01A+B. SKB P-04-250, Svensk Kärnbränslehantering AB.

Drake H, Tullborg E-L, 2009. Paleohydrogeological events recorded by stable isotopes, fluid inclusions and trace elements in fracture minerals in crystalline rock, Simpevarp area, SE Sweden. Applied Geochemistry 24, 715–732.

Drake H, Tullborg E-L, Mackenzie A B, 2009. Detecting the near-surface redox front in crystalline bedrock using fracture mineral distribution, geochemistry and U-series disequilibrium. Applied Geochemistry 24, 1023–1039.

Dynamic range, n d. In Wikipedia. Available at: http://en.wikipedia.org/wiki/Dynamic_ range#Photography [23 November 2011].

Follin S, Levén J, Hartley L, Jackson P, Joyce S, Roberts D, Swift B 2007. Hydrogeological characterization and modelling of deformation zones and fracture domains, Forsmark modelling stage 2.2. SKB R-07-48, Svensk Kärnbränslehantering AB.

Fox A, Hermanson J, 2006. Identification of additional, possible minor deformation zones at Forsmark through a review of data from cored boreholes. SKB P-06-293, Svensk Kärnbränslehantering AB.

Fox A, La Pointe P, Hermanson J, Öhman J, 2007. Statistical geological discrete fracture network model. Forsmark modelling stage 2.2. SKB R-07-46, Svensk Kärnbränslehantering AB.

Fox A, Forchhammer K, Pettersson A, La Pointe P, Lim D-H, 2012. Geological discrete fracture network model for the Olkiluoto site, Eurajoki, Finland. version 2.0. Posiva 2012-27, Posiva Oy, Finland.

Funehag J, Emmelin A, 2011. Injekteringen av TASS-tunneln. Design, genomförande och resultat från förinjekteringen. SKB R-10-39, Svensk Kärnbränslehantering AB (in Swedish).

Fälth B, Hökmark H, Munier R, 2010. Effects of large earthquakes on a KBS-3 repository. Evaluation of modelling results and their implications for layout and design. SKB TR-08-11, Svensk Kärnbränslehantering AB.

Gaich A, Pötsch M, Schubert W, 2006. Basics and application of 3D imaging systems with conventional and high-resolution cameras. In Tonon F, Kottenstette J (eds). Laser and photogrammetric methods for rock face characterization: report on a workshop, Golden, Colorado, 17–18 June 2006. Alexandria, VA: American Rock Mechanics Association, 33–48.

Handy M R, Hirth G, Bürgmann R, 2007. Continental fault structure and rheology from the frictional-to-viscous transition downward. In Handy M, Hirth G, Hovius N (eds). Tectonic faults: agents of change on a dynamic earth. Cambridge, MA: MIT Press, 139–181.

Hardenby C, Sigurdsson O, 2010. Äspö Hard Rock Laboratory. The TASS-tunnel. Geological mapping. SKB R-10-35, Svensk Kärnbränslehantering AB.

Hardenby C, Sigurdsson O, Hernqvist L, Bockgård N, 2008. Äspö Hard Rock Laboratory. The TASS-tunnel project ”Sealing of tunnel at great depth”. Geology and hydrogeology – Results from thge pre-investigations based on the boreholes Kl0010B01, Kl0014B01 and Kl0016B01. SKB IPR-08-18, Svensk Kärnbränslehantering AB.

Hermanson J, 2001a. Äspö Hard Rock Laboratory. TRUE Block Scale project. October 1997 structural model; Update using characterisation data from KA2511A and Kl0025F. SKB IPR-01-41, Svensk Kärnbränslehantering AB.

Hermanson J, 2001b. Äspö Hard Rock Laboratory. TRUE Block Scale project. Preliminary characterisation stage. September 1998 structural model; Update using characterisation data from Kl0023B. SKB IPR-01-42, Svensk Kärnbränslehantering AB.

Hermanson J, Doe T, 2000. Äspö Hard Rock Laboratory. TRUE Block Scale project. Tracer test stage. March'00 structural and hydraulic model based on borehole data from Kl0025F03. SKB IPR-00-34, Svensk Kärnbränslehantering AB.

Hermanson J, Follin S, Wei L, 1997. Äspö Hard Rock Laboratory. TRUE Block Scale experiment. Input data for discrete fracture network modelling of the TRUE Block Scale site. Part 1 – Structural analysis of fracture traces in boreholes KA2563A and KA3510A and in the TBM tunnel. SKB IPR-01-70, Svensk Kärnbränslehantering AB.

High-dynamic-range imaging, n d. In Wikipedia. Available at: http://en.wikipedia.org/wiki/High_dynamic_range_imaging [22 November 2011].

Kemeny J, Turner K, Norton B, 2006. LIDAR for rock mass characterization: hardware, software, accuracy and best practices. In Tonon F, Kottenstette J (eds). Laser and photogrammetric methods for rock face characterization: report on a workshop, Golden, Colorado, 17–18 June 2006. Alexandria, VA: American Rock Mechanics Association, 49–62.

Kim Y-S, Peacock D C P, Sanderson D J, 2004. Fault damage zones. Journal of Structural Geology 26, 503–517.

Kim Y-S, Sanderson D J, 2005. The relationship between displacementand length of faults: a review. Earth Science Reviews 68, 317–334.

Kolyukhin D, Torabi A, 2012. Statistical analysis of the relationship between fault attributes. Journal of Geophysical Research 117, B05406. doi:10.1029/2011JB008880

Landström O, Tullborg E-L, Eriksson G, Sandell Y, 2001. Effects of glacial/post-glacial weathering compared with hydrothermal alteration – implications for matrix diffusion. Results from drill core studies in porphyritic quartz monzodiorite from Äspö SE Sweden. SKB R-01-37, Svensk Kärnbränslehantering AB.

La Pointe P R, 2010. Techniques for identification and prediction of mechanical stratigraphy in fractured rock masses. In Proceedings of 44th U.S. Rock Mechanics Symposium and 5th U.S.–Canada Rock Mechanics Symposium, Salt Lake City, Utah, 27–30 June 2010. Alexandria, VA: American Rock Mechanics Association, ARMA 10-296.

La Pointe P, Fox A, Hermanson J, Öhman J 2008. Geological discrete fracture network model for the Laxemar site. Site descriptive modelling, SDM-Site Laxemar. SKB R-08-55, Svensk Kärnbränslehantering AB.

Magnor B, Hardenby C, Kemppainen K, Eng A, 2006. Rock Characterization System –RoCS. Final report – feasibility study, phase I. State-of-the-art in 3D surveying technology. SKB IPR-06-07, Svensk Kärnbränslehantering AB.

Mattsson K-J, Eklund S, Ehrenborg J 2007. Oskarshamn site investigation. Boremap mapping of core drilled MDZ boreholes KLX22A, KLX22B, KLX23A and KLX23B. SKB P-06-243, Svensk Kärnbränslehantering AB.

Moye D G, 1967. Diamond drilling for foundation exploration. In Civil Engineering Transactions Paper 2150. Presented at Institute of Engineers (Australia) Site Investigation Symposium, September 1966. Available at: http://www.daniel-moye.org/written_works/selected_technical_papers/diamond_drilling/

Munier R, 2010. Full periometer intersection criteria. Definitions and implementations in SR-Site. SKB TR-10-21, Svensk Kärnbränslehantering AB.

Munier R, Stanfors R, Milnes A G, Hermanson J, Triumf C-A, 2003. Geological Site Descriptive Model. A strategy for the development during site investigations. SKB R-03-07, Svensk Kärnbränslehantering AB.

Olsson M, Markström I, Pettersson A, Sträng M, 2009. Examination of the Excavation Damaged Zone in the TASS tunnel, Äspö HRL. SKB R-09-39, Svensk Kärnbränslehantering AB.

Olsson T, Stanfors R, Sigurdsson O, Erlström M, 2007. Oskarshamn site investigation. Identification and characterization of minor deformation zones based on lineament interpretation. SKB P-06-282, Svensk Kärnbränslehantering AB.

Platt J P, Behr W M, 2011. Grainsize evolution in ductile shear zones: implications for strain localization and the strength of the lithosphere. Journal of Structural Geology 33, 537–550.

Poteri A, Billaux D, Dershowitz W, Gómez-Hernández J J, Cvetkovic V, Hauutojärvi A, Holton D, Medina A, Winberg A (ed), 2002. Final report of the TRUE Block Scale project. 3. Modelling of flow and transport. SKB TR-02-15, Svensk Kärnbränslehantering AB.

Rhén I, Forsmark T, Hartley L, Jackson P, Roberts D, Swan D, Gylling B 2008. Hydrogeological conceptualization and parameterization. Site descriptive modelling, SDM-Site Laxemar. SKB R-08-78, Svensk Kärnbränslehantering AB.

Rouhiainen P, 2008. The Posiva Flow Log Difference Flowmeter (PFL DIFF), developed investigation equipment in the nuclear branch. In Proceedings of 33rd International Geological Congress, Oslo, 6–14 August 2008.

Shipton Z K, Soden A M, Kirkpatrick J D, Bright A M, Lunn R J, 2006. How thick is a fault? Fault displacement-thickness scaling revisited. In Abercrombie R, McGarr A, Di Toro G, Kanamori H (eds). Earthquakes: radiated energy and the physics of faulting. Washington, DC: American Geophysical Union. (Geophysical Monograph 170), 193–198.

SKB, 2008. Site description of Forsmark at completion of the site investigation phase, SDM-Site Forsmark. SKB TR-08-05, Svensk Kärnbränslehantering AB.

SKB, 2009. Site description of Laxemar at completion of the site investigation phase, SDM-Site Laxemar. SKB TR-09-01, Svensk Kärnbränslehantering AB.

SKB, 2011. Long-term safety for the final repository for spent nuclear fuel at Forsmark. Main report of the SR-Site project. SKB TR-11-01, Svensk Kärnbränslehantering AB.

Thiem G, 1906. Hydrologische Methoden. Leipzig: Gebhardt. (In German.)

Turner A K, Kemeny J, Slob S, Hack R, 2006. Evaluation and management of unstable rock slopes by 3-D laser scanning. In Culshaw M G, Reeves H J, Jefferson I, Spink T W (eds). 10th International congress International Association of Engineering Geology and The Environment (IAEG2006); Engineering geology for tomorrow's cities, Nottingham, UK, 6–10 September 2006. London: Geological Society of London, Paper 404.

Viola G, Venvik Ganerød G, 2008. Oskarshamn site investigation. Structural characterisation of deformation zones (faults and ductile shear zones) from selected drill cores from the Laxemar area. SKB P-08-07, Svensk Kärnbränslehantering AB.

Wahlgren C-H, Curtis P, Hermanson J, Forssberg O, Öhman J, Drake H, Fox A, Triumf C-A, Mattsson H, Thunehed H, Juhlin C, 2008. Geology Laxemar. Site descriptive modelling, SDM-Site Laxemar. SKB R-08-54, Svensk Kärnbränslehantering AB.

Wilcoxon F, 1945. Individual comparisions by ranking methods. Biometrics Bulletin 1, 80-83.

Winberg A, Andersson A, Hermanson J, Byegård J, Cvetkovic V, Birgersson L, 2000. Äspö Hard Rock Laboratory. Final report of the first stage of the tracer retention understanding experiments. SKB TR-00-07, Svensk Kärnbränslehantering AB.

Winberg A, Andersson P, Byegård J, Poteri A, Cvetkovic V, Dershowitz B, Doe T, Hermanson J, Gómez-Hernández J J, Hautojärvi A, Billaux D, Tullborg E-L, Holton D, Meier P, Medina A, 2003. Final report of the TRUE Block Scale Project. 4. Synthesis of flow, transport and retention in the block scale. SKB TR-02-16, Svensk Kärnbränslehantering AB.

Åkesson M, Kristensson O, Börgesson L, Dueck A, Hernelind J, 2010. THM modelling of buffer, backfill and other system components. Critical processes and scenarios. SKB TR-10-11, Svensk Kärnbränslehantering AB.